OPTO-MICROFLUIDIC DEVICES WITH FEMTOSECOND LASER MICROFABRICATION

by

© Daiying Zhang

A Dissertation submitted to the

School of Graduate Studies

in partial fulfillment of the requirements for the degree of

Doctor of Philosophy

Department of Physics and Physical Oceanography

Memorial University of Newfoundland

June 2016

St. John's Newfoundland and Labrador

ABSTRACT

Opto-microfluidics is a novel technology that integrates optical devices and systems with microchannels to investigate the properties of fluids. Opto-microfluidic devices have been increasingly recognized as important miniaturized devices for optical measurements, biological analyses, and chemical syntheses. These devices significantly reduce reagent consumption, waste production, analysis time and labour costs. Common fabrication techniques include soft lithography, microelectromechanical systems (MEMS) and hot embossing.

In this dissertation, opto-microfluidic devices fabricated by two-photon polymerization (TPP) technique with femtosecond lasers and standard soft lithography are proposed. After analyzing the fabrication properties of the femtosecond laser, we choose optimal parameters to fabricate optical structures in photoresist material SU-8, and integrate them with microchannels which are produced by a standard soft lithographic technique. Diffractive grating, Mach-Zehnder interferometer (MZI) and optical microring resonators based refractive index (RI) and temperature sensors are designed, fabricated and demonstrated. The sensitivities in different conditions are thoroughly investigated. By combining fluid mechanics and optics, two functional opto-microfluidic devices realizing simultaneous particle sorting and RI sensing are successfully proved. In these devices, filters fabricated by femtosecond lasers are used to sieve and control the flow of particles in suspension, and then the purified liquid is induced into the optical structures to measure the RI. The opto-microfluidic devices described in this dissertation verify the practicability and effectiveness as a lab-on-a-chip platform.

ACKNOWLEDGEMENTS

I would like to thank my supervisor, Dr. Qiying Chen, for his support and encouragement in the past four years. I have learned so much from him personally and academically during these four years. I would also like to thank Dr. Liqiu Men for valuable discussion, which provided me broader views in my research field and inspired many novel ideas. I would like to thank former member of the group, Dr. Ping Lu, for his helpful suggestions.

I would like to thank my course instructors, Dr. Martin Plumer, Dr. John Whitehead, Dr. Guy Quirion and Dr. John Lewis, for their interesting lectures, and my committee members Dr. Anand Yethiraj and Dr. Ivan Saika-Voivod for the suggestions from annual graduate progress meetings. The fellowships from the School of Graduate Studies, my supervisor, and the Department of Physics and Physical Oceanography are greatly appreciated. I also thank Memorial University for awarding me the A.G. Hatcher Memorial Scholarship in 2012 that acknowledged my achievement during my Ph.D. Program.

Finally, I would like to thank my parents, my brother and my sister-in-law for their everlasting help and support.

Table of Contents

List of Tables

List of Figures

List of Abbreviations

TPP	Two-photon polymerization
3D	Three-dimensional
2D	Two-dimensional
TPA	Two-photon absorption
RI	Refractive index
OPA	One-photon absorption
UV	Ultraviolet
PAG	Photoacid generator
PC	Photonic crystal
DFB	Distributed feedback
IPA	Isopropyl alcohol
rpm	Rounds per minute
NA	Numerical aperture
SEM	Scanning electron microscope
MEMS	Microelectromechanical systems
PDMS	Polydimethylsiloxane
PMMA	Poly (methyl methacrylate)
SMF	Single-mode fiber
OSA	Optical spectrum analyzer
RF	Radio frequency
RIU	Refractive index unit
MZI	Mach-Zehnder interferometer
PS	Polystyrene
TE	Transverse-electric
TM	Transverse-magnetic
DEP	Dielectrophoresis
Q factor	Quality factor

Chapter 1 Introduction

1.1 Opto-microfluidics

Optofluidics refers to a platform of integrated optical devices and systems that performs investigation on the properties of fluids. By combining microfluidic and optical technologies, optofluidic devices integrate a roomful of laboratory equipment into a palm-size chip to carry out optical measurements, biological analyses and chemical syntheses. Microfluidic and optofluidic devices significantly reduce reagent consumption, waste production, analysis time and labour costs. There is no distinct boundary between microfluidics and optofluidics because many techniques and applications are shared by these two disciplines. We use the term “opto-microfluidics” to refer to the research that takes advantage of both optics/photonics and microfluidics. A few monographs provide good reviews of the history and development in the field of opto-microfluidics [1-6].

1.2 Two-photon polymerization

Lithography has been demonstrated as an advanced microfabrication technique for microelectronics, opto-microfluidics and biomedicine. Various two-dimensional (2D) microdevices, such as the integrated semiconductor and capillary electrophoresis chips, have been applied in industry and medicine. However, as a planar technique, lithography lacks the capabilities to fabricate three-dimensional (3D) microstructures. Although layer-by-layer assembly was proposed to produce 3D structures by stacking planar 2D patterns [7, 8], it is very difficult and time-consuming to precisely align the micro/nano-structures.

Holographic lithography was developed to create periodic 3D microstructures, in which periodic interference patterns such as a hexagonal periodic structure [9], and face-centered-cubic-type structure [10] are printed into the photoresist by multi-laser beam irradiation. However, this type of 3D microstructure is limited to patterns of interference. To achieve arbitrary 3D microstructures, microfabrication by two-photon polymerization (TPP) with a femtosecond laser is adopted in this study.

1.2.1 Two-photon absorption

Two-photon absorption (TPA) is a nonlinear process by which an atom or molecule simultaneously absorbs two photons to jump from the ground state to an excited electronic state (Fig. 1-1). The sum of the energies of the two photons equals the transition energy. The TPA process relates to the imaginary part of the third-order susceptibility in the material polarization. The polarization of material can be expressed as [11]:

$$P = P_0 + \varepsilon_0 \chi^{(1)} E + \varepsilon_0 \chi^{(2)} E^2 + \varepsilon_0 \chi^{(3)} E^3 + \ldots \tag{1.1}$$

where E is the electric field, $\chi^{(m)}$ is susceptibility of the m^{th} tensor, and ε_0 is the electric permittivity of the free space. The real part of the third-order susceptibility $\chi^{(3)}_{real}$ is related to the nonlinear refraction, and the imaginary part of the third-order susceptibility $\chi^{(3)}_{imag}$ is related to the nonlinear absorption (TPA). The energy absorption can be described as:

$$\frac{dW}{dt} = \frac{8\pi^2 \omega}{n^2 c^2} I^2 \chi^{(3)}_{imag} \tag{1.2}$$

where n is the refractive index (RI) of the material, c is the speed of light in a vacuum, ω is the frequency of light, and I is the intensity of the light.

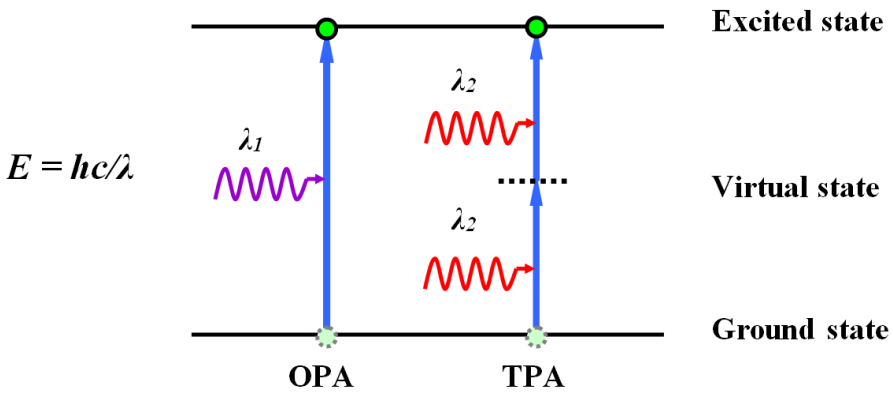

Figure 1-1 Schematic diagram of one-photon absorption (OPA) and two-photon absorption (TPA)

The TPA process was first proposed theoretically by Maria Göppert-Mayer in her doctoral dissertation in 1931 [12]. However, Eqn. (1.2) shows that TPA depends on the square of the light intensity (I^2), and is therefore several orders of magnitude weaker than the one-photon absorption (OPA) at low photon intensities. High photon intensities, which are defined as the number of photons observed per unit time in a unit solid angle, are required to excite TPA. Therefore, TPA was not implemented until the invention of the laser thirty years later. In 1961, Kaiser *et al.* first proved that two-photon fluorescence was excited in a CaF_2:Eu^{2+} crystal [13]. When a laser beam is focused into the two-photon material, the excitation only occurs within a 3D localized spot (focal point) which has the greatest density (Fig. 1-2) [14]. Denk *et al.* utilized this rule to construct a two-photon laser scanning fluorescence microscope in 1990 [15]. Since then, TPA based on optical

power limiting [16], fluorescence imaging techniques [17, 18], 3D data storage [19], photodynamic therapy [20], and microfabrication [21] have been reported.

Figure 1-2 Observation of fluorescence excitation through the path of a laser beam

1.2.2 Two-photon materials and fabrication

The first two-photon microfabrication was reported by Maruo *et al.* in 1997. A Ti: sapphire laser was used to fabricate spiral structures, and the width of the spiral wire was 1.3 μm [21]. Complex 3D microstructures and devices have been fabricated by TPA, such as a microbull [22], woodpile [23], microrotor [24, 25], microchain [26], and microlens [27].

Figure 1-3 illustrates a typical microfabrication system with a femtosecond laser which is used in our lab. The Ti: sapphire femtosecond laser with a laser wavelength of 800 nm and a repetition rate of 80 MHz is focused on a sample by an objective lens. A variable attenuator, consisting of a half-wave plate and a polarizer, is placed in the path of

the beam to control and continuously adjust the output power of the laser. A shutter triggered by a computer program is used to control the exposure time of the sample to laser irradiation. A power meter monitors the change of the laser power in real time through a beam splitter. By moving the translation stages (*X*, *Y*, *Z* directions) programmed by the computer, thereby adjusting the focal points in 3D, the desired features are fabricated. After exposure to the lasers, a development process is employed to wash away any unhardened materials with one or more solvents (generally ethanol), leaving only the created microstructures (Fig. 1-4). The smallest reported feature size can be made as small as 65 nm, which is much smaller than the diffraction limit, by using femtosecond laser pulses at 520 nm [28].

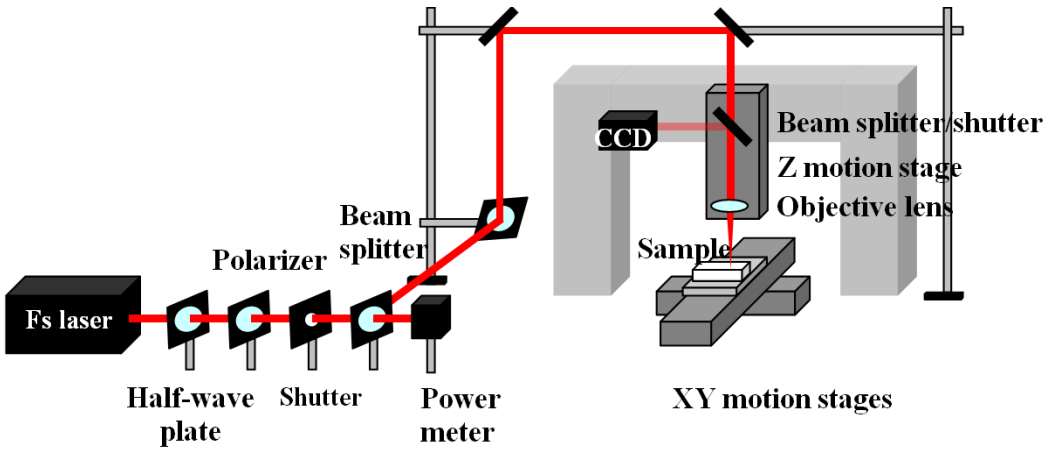

Figure 1-3 Schematic illustration of a femtosecond laser microfabrication system

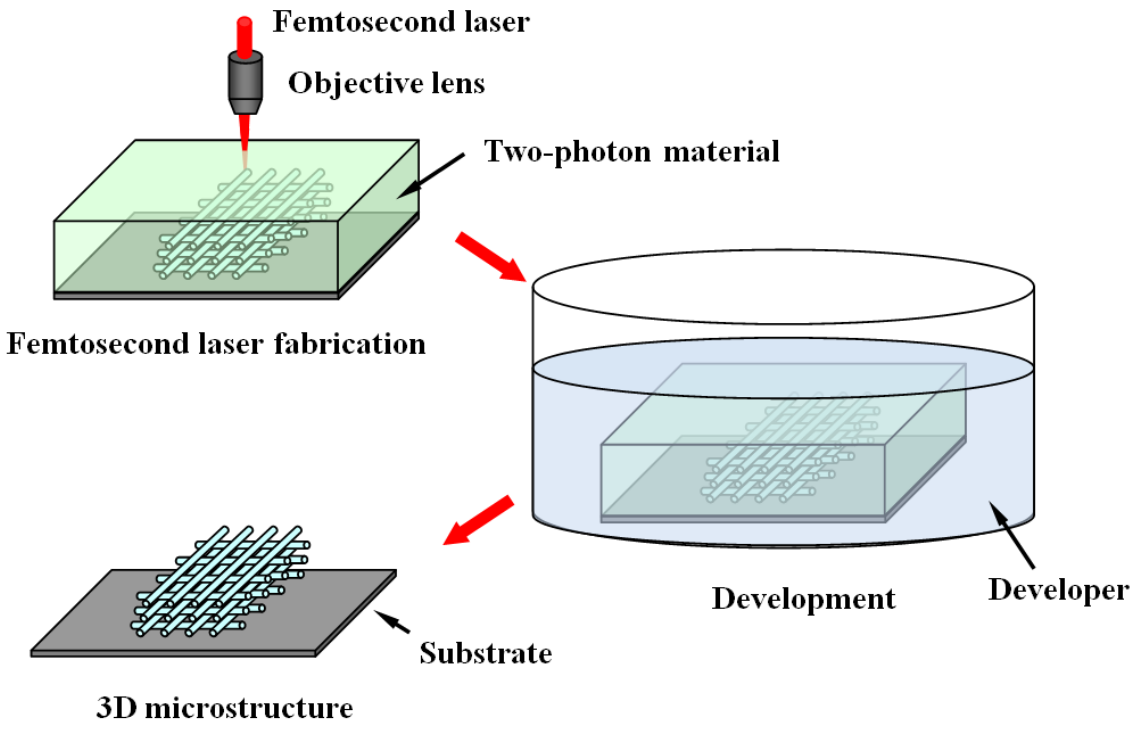

Figure 1-4 Schematic illustration of 3D microfabrication with TPP technique

Various polymerizable materials have been synthesized and applied. Negative- and positive-tone photoresists are two types of photosensitive materials that are used to construct microstructures with the TPP technique. The difference between the negative and positive-tone photoresists is that the unexposed portion can be dissolved into the photoresist developer and exposed portion is insoluble for a negative-tone photoresist as shown in Fig. 1-4, whereas for a positive-tone photoresist, the unexposed portion is insoluble and the exposed portion can be dissolved into the photoresist developer. Table 1-1 lists some reported commercial photosensitive materials for TPP. SU-8 and Ormocers are two leading classes of negative-tone materials which have been widely applied for two-photon fabrication. Both materials show strong absorption in the ultraviolet (UV) region and high transparency in the visible and near infrared ranges. SU-8 is an epoxy-

based negative photoresist, which has eight epoxy groups per monomer and contains a triaryl sulfonium salt photoacid generator (PAG). Under laser exposure, the PAGs absorb enough photon energy to generate strong catalyzed acid (polymerization does not take place during laser irradiation). During the sequent baking process, the acid diffuses in the photoresist to help open up the epoxy ring and gain much higher cross-linking. Then the unexposed resist is washed away by a nonpolar solvent due to the fact that the uncrosslinked resist has a low molecular weight, generating a negative structure [29]. Because the crosslinking occurs during the post-baking process and there is no RI modification before this moment, online monitoring is not possible. Liquid Ormocers can completely overcome this disadvantage. Ormocers are organic-inorganic hybrid polymers containing a highly crosslinkable organic network such as acrylates or epoxides as well as inorganic components which are often used as photocurable dental composites. Direct laser irradiation induces cross-linking of organic groups attached to an inorganic backbone. In this case, TPP is formed in real-time without a post-baking process. However, UV post-curing is needed to harden the structure after development and rinse processes [23].

Table 1-1 A list of commercial two-photon polymerizable materials

Resin	Manufacturer	Type of material	Type of exposure	Ref.
SU-8	MicroChem	Epoxy	Negative	29, 30
Ormocer	Micro resist technology GmbH	Inorganic-organic hybrid	Negative	23
SCR500	Japan Synthetic Rubber Co.	Urethane acrylate	Negative	21, 22, 27,28
IPG	RPO Inc.	Inorganic-organic polysiloxane	Negative	31
LN1	Sartomer	Urethane acrylate	Negative	32
SR348	Sartomer	Ethoxylated bisphenol A dimethacrylate	Negative	33
Nopcocure 800	Japan Synthetic Rubber Co.	Acrylic acid ester	Negative	24
NOA 63/68	Norland Products	Mercapto-ester polyurethane	Negative	24, 25
SCR701	D-MEC Co.	Epoxy	Negative	34
SZ2080	IESL-FORTH	zirconium–silicon hybrid	Negative	35
AZ	MicroChemicals GmbH	Undisclosed	Positive	36
S1800	Shipley	Undisclosed	Positive	36, 37

1.2.3 Applications of two-photon polymerization for microfabrication

The unique capability to fabricate and control 3D structures on the micro/nanoscale using the TPP technique has found a wide range of applications, especially in biomedical

science [38-43]. Gittard *et al.* proposed multifocus TPP technology for producing medical devices [44]. The multibeam system can simultaneously produce multiple micro-scale structures which greatly improve the efficiency of fabrication.

TPP microfabrication has also been applied in the fabrication of photonic crystals (PCs), which are periodic optical nanostructures for controlling and manipulating the flow of photons. 3D woodpile structures with different periodicities in different two-photon polymerizable materials have been reported, and their exposure conditions, optical properties (transmission and photonic band gaps) and shrinkage were investigated [23,26,28,32,45]. Compared with the holographic patterning, two-photon fabrication possesses a significant advantage of ease in the integration of defects or cavities at an arbitrary location of a PC. Sun *et al.* demonstrated a missing "logs" resonance cavity within a PC [46]. More complex crystal geometries such as the diamond-lattice [47], spiral-architecture [48], slanted pore structure [49] and quasicrystal [50] were reported.

Uses of the TPP technique in different optical applications have also received significant attention, for example, for various microoptical elements [51, 27]. Klein *et al.* fabricated suspended waveguides, couplers, Y-splitters, and MZIs between the ends of optical fibers [52]. The integration of convex and Fresnel lenses, gratings and solid immersion lenses on the tip of an optical fiber were reported [53]. A fiber optical device based on microring resonators fabricated on the side of optical fibers was demonstrated by Sherwood *et al.* [54]. Distributed feedback (DFB) dye lasers were achieved by fabricating Bragg gratings in dye-doped TPP materials [55, 56].

Microfluidics has significantly benefited from the availability of the two-photon fabrication technique. Various fabrication techniques for microchannels were developed. Kumi *et al.* produced master structures with two-photon fabrication for microchannels with different cross-sections [57]. 2D and 3D flow systems were developed by directly exposing channel walls on a glass substrate [29]. Microchannels were also achieved by the TPP-assisted ablation technique in which a polymerized rib was generated by TPP during the first laser scan and a polymerized rib with a channel was ablated during the second laser scan [58]. Single-step self-enclosed microchannels were reported by Jariwala *et al.* Two parallel paths were scanned by the femtosecond laser. When the paths were close enough, a channel was formed by self-linking on the top of polymerized ribs [59]. In addition, functional 3D components created in the microfluidic system were reported. Light-drived microrotors such as microwheels [25, 60] and micropumps [34, 61] were directly fabricated into the microchannels. These microdevices are potential manipulation tools for biomolecules such as DNA and proteins. 2D and 3D filtration networks were integrated into the microfluidic system to separate impurities and cells with different sizes [62-64]. Wu *et al.* also reported an ‘‘OFF’’ and ‘‘ON’’ functional microvalve which was controlled by different water flow directions [64].

1.3 Motivation and contributions

As mentioned above, the femtosecond laser induced TPP technique is a promising approach for fabrication of micro/nanoscale structures. Several achievements basing on TPP have been reached, such as PCs, microoptical elements and microfluidics. However, this technique is still in its infancy. New functional devices fabricated by TPP with the

advantages of high precision, flexibility and three dimension is expected to develop and apply in different fields. The goal of this thesis is to design various novel opto-microfluidic devices with femtosecond laser induced TPP technique. These opto-microfluidic devices are targeted to sensing applications such as RI and temperature measurement which will have great potential applications of clinical diagnostics, molecular analysis and chemical synthesis.

In this thesis, the fabrication and characterization of femtosecond laser induced TPP is explored in Chapter 2, diffractive grating based, Mach–Zehnder Interferometer based and microring resonance based opto-microfluidic sensors are designed and tested in Charpter 3-5. Charpter 6 demonstrates the feasibility of an opo-microfluidic device for simultaneous particle sorting and RI sensing.

The research in this thesis first successfully applies two-photon polymerization technique to opto-microfluidic devices; designs unique single-waveguide based Mach–Zehnder Interferometer sensors and achieves RI sensing and temperature testing; and realizes simultaneous particle sorting and optical measurement.

Chapter 2 Characterization of microfabrication with two-photon polymerization technique

In this charpter, the characterization of the TPP fabrication is investigated. The detailed fabrication process and effects of focusing condition, scan speed, exposure time and pulse energy on the the diameter of a voxel are discussed. The study in this chapter provides basic guideline on how to choose optimal fabrication parameters to obtain designed patterns.

2.1 Fabrication processes

In the following sections, SU-8 from Microchem®, USA is used for fabricating various optical components. Due to weak adhesion strength between the glass and SU-8, rigorous procedures must be implemented to avoid SU-8 lift-off. Table 2-1 lists the relevant fabrication processes. A glass slide as the substrate is first cleaned in acetone, isopropyl alcohol (IPA) and distilled water with an ultrasonic cleaner (Branson® 8510, USA) for 10 minutes, respectively, to remove the dust and grease. After drying with pressurized air, the glass slide is dehydrated in a 200 ^{o}C oven (Thermolyne® 1400, USA) overnight. SU-8 resist is deposited on the glass slide, following a two-step spin-coating process: 10 second spread spinning at 50 rounds per minute (rpm) first and then ramping to 3000 rpm for 30 s as the final spin (Headway Research, Inc., USA). After the spin-coating, the film is pre-baked at 65 ^{o}C (Sybron® nuovaII stir plate, USA) for 1 min followed by a soft baking at 95 ^{o}C (Sigma Systems, USA) for 3 min to evaporate the solvent. The spinning and baking time described above is for a 2 μm film of SU-8-2 resist. Other SU-8 series

such as SU-8-2075 and SU-8-3050 have different recommended spin rates and baking times which have been specified in the data sheets issued by Microchem Company. Laser exposure is performed with a femtosecond laser, and two post-exposure baking are adopted for crosslinking the exposed regions: 1 min at 65 ^{o}C and 1 min at 95 ^{o}C. The two-step post-baking is used to minimize stress and resist cracking. The post-baked film is immersed into the SU-8 developer to dissolve the unexposed regions, rinsed with IPA and dried with high-speed spinning. Lastly, hard baking is adopted to reinforce the structures.

Table 2-1 Processes of microfabrication with TPP technique

Steps	Materials/Conditions	Time
Substrate cleaning	Acetone Isopropyl alcohol (IPA) Distilled water	10 min 10 min 10 min
Substrate dehydration	200 ^{o}C	12 h
Spinning	500 rpm 3000 rpm	10 s 30 s
Soft-baking	65 ^{o}C 95 ^{o}C	1 min 3 min
Laser exposure	Femtosecond laser	Variable
Post exposure baking	65 ^{o}C 95 ^{o}C	1 min 1 min
Development	Developer	1 min
Rinsing	Isopropyl alcohol (IPA)	30 s
Hard baking	95 ^{o}C	2 h

2.2 Voxel characterization

Depending on the different applications of the TPP, voxels (volumetric pixel) of different sizes are needed in various structures. The size of a voxel determines the minimum unit of a microstructure. Lee *et al.* proved that the voxel size depends on many parameters as shown in Eqns. (2.1) and (2.2) [65, 66].

$$d = \frac{\lambda}{\pi \tan\left(\sin^{-1}(NA/n)\right)} \times \left[\ln\left(\frac{4\pi^2 P^2 \cdot t \cdot \left[\tan\left(\sin^{-1}(NA/n)\right)\right]^4}{E_{th} \cdot \lambda^4} \right) \right]^{\frac{1}{2}} \tag{2.1}$$

$$l = 2z = \frac{2\lambda}{\pi \left[\tan\left(\sin^{-1}(NA/n)\right)\right]^2} \times \left[\left(\frac{4\pi^2 P^2 \cdot t \cdot \left[\tan\left(\sin^{-1}(NA/n)\right)\right]^4}{E_{th} \cdot \lambda^4} \right)^{\frac{1}{2}} - 1 \right]^{\frac{1}{2}} \tag{2.2}$$

where d and l are the diameter and longitudinal dimension of a voxel, respectively, E_{th} is the exposure threshold for TPA, λ is the wavelength of the femtosecond laser, n is the RI of the resin, P is the laser power, t is the exposure time, and NA is the numerical aperture of an objective lens. Therefore, voxel size can be controlled by choosing optimized exposure parameters, such as laser power, exposure time and NA.

In this section, a film with a thickness of about 1.0 μm is produced on the glass substrate. The diameter of a voxel is studied at different laser powers, focus locations, exposure times and numerical apertures (NA). In the following simulation, the exposure threshold E_{th} of SU-8 for TPA is 3.20 TW/cm^2 [67], λ is 800 nm, n is 1.580 (at 800 nm), P is 20 - 60 mW, and NA is 0.8 for the 50× objective lens and 0.95 for the 100× objective

lens. Considering the step of the motion stage (500 nm/step) used in this study, the exposure time t for a line scan is $t = 500/v$ (ms), where v is the scan speed with a unit of nm/ms (or equivalently μm/s).

2.2.1 Effect of focusing condition

Lines are fabricated by adjusting the focusing of the femtosecond laser. Figure 2-1(a) shows scanning electron microscope (SEM) images of lines fabricated by a laser energy of 0.500 nJ/pulse through a 2× beam expander (Linos 2× - 8×) and an objective lens with a magnification of 50×. The scan speed is 20 μm/s. The lines will lift off the surface when the laser beam is focused too much above or below the film surface. Figure 2-1(b) shows an enlarged image of lines which are fabricated by focusing the laser beam on the location 1 μm above the surface. The lines become wobbly due to the fact that the line-shaped coating almost lifts off the substrate. Figure 2-1(c) shows the results of measured diameters. The width of the line increases with the improvement in focusing, and reaches the maximum when the laser beam is focused on the film surface. Figure 2-2 gives SEM images of lines fabricated by a laser energy of 0.500 nJ through an objective lens with 100× magnification. The scan speed is 20 μm/s. The diameter reaches its maximum when the laser beam is focused exactly on the film surface.

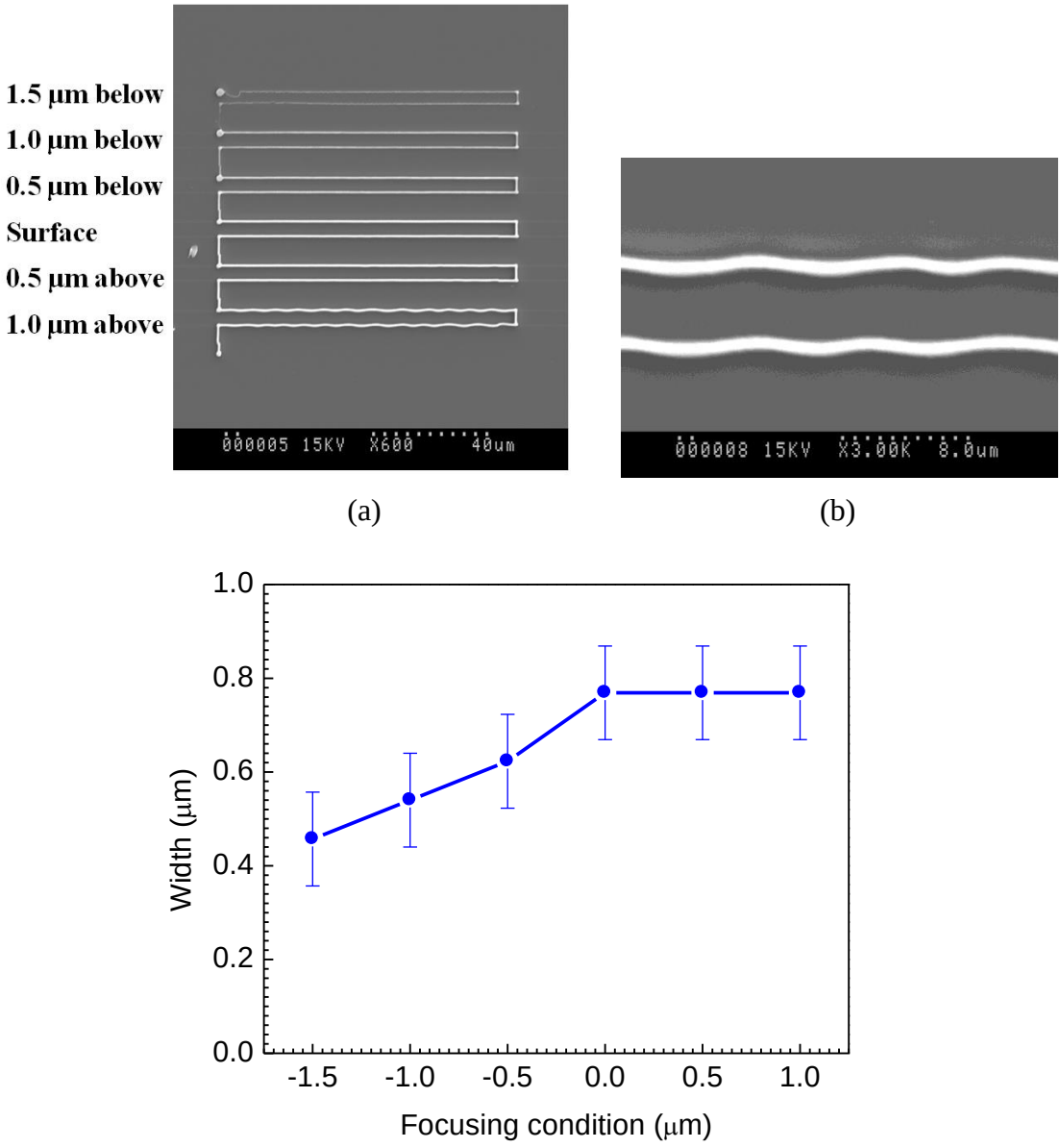

Figure 2-1 Lines exposed by femtosecond lasers of different focusing conditions: (a) an SEM image of lines, (b) an SEM image of lines with a focus at 1.0 μm above the interface, and (c) dependence of the width of line on focus condition. The laser pulses (0.500 nJ/pulse) are focused by an objective lens with a magnification of 50× (0.8 NA). The scan speed is 20 μm/s.

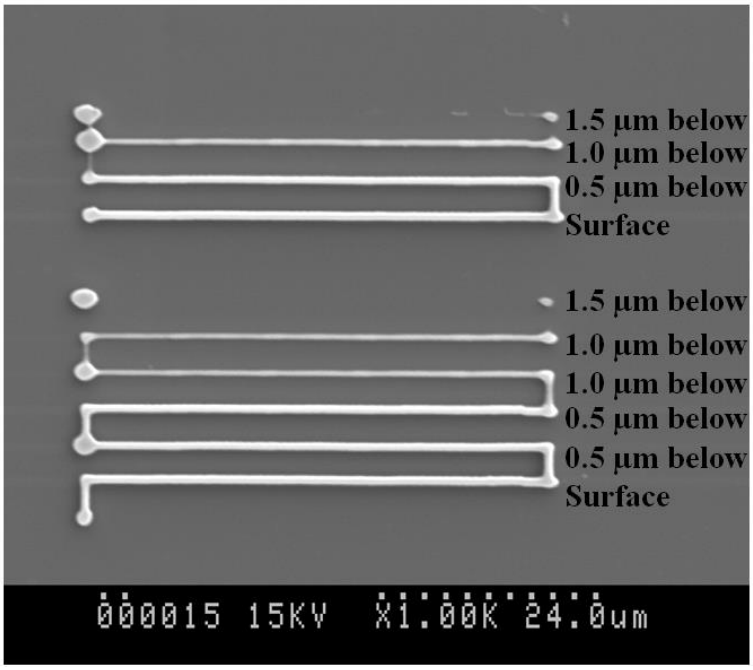

(a)

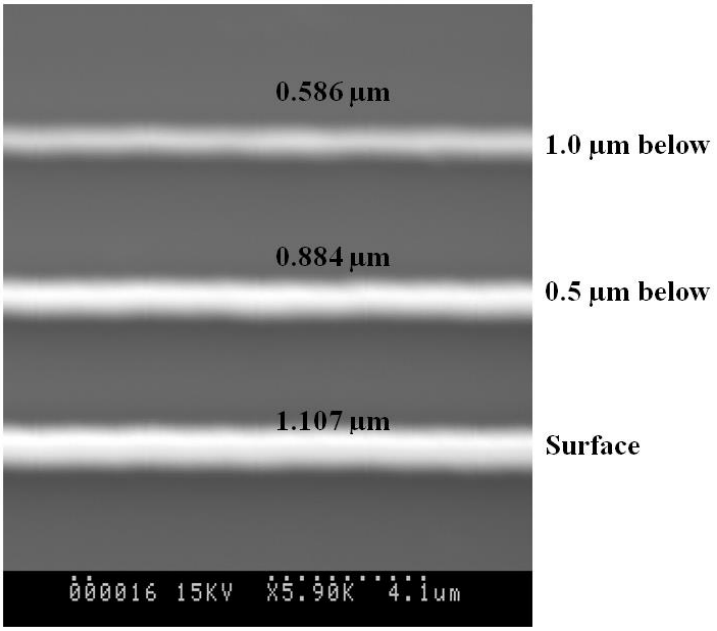

(b)

Figure 2-2 Lines exposed by femtosecond lasers of different focusing conditions: (a) an SEM image of lines, and (b) an enlarged SEM image for the first three lines in (a). The laser pulses (0.500 nJ/pulse) are focused by an objective lens with a magnification of 100× (0.95 NA). The scan speed is 20 μm/s.

2.2.2 Effect of scan speed

Lines are fabricated with a femtosecond laser of different scan speeds. Figure 2-3(a) shows a SEM image of lines fabricated by a laser energy of 0.500 nJ through a 2× beam expander and an objective lens with 50× magnification. The laser beams are focused on the film surface. The scan speed increases from 2 μm/s to 300 μm/s. A slower scan speed means longer exposure time. Therefore, a higher scan speed achieves a narrower line. We also notice that the lines change into separated dots when the scan speed is larger than 80 μm/s. This is caused by the mechanism of the step motion stage. Therefore, the scan speed will be smaller than 80 μm/s to obtain homogeneous lines in the following sections. Figure 2-3(b) presents the dependence of the width on the scan speed. The theoretical result is calculated according to Eqn. (2.1). Figure 2-4 shows a SEM image of lines fabricated by a laser energy of 0.500 nJ through an objective lens with 100× magnification and the dependence of the width on the scan speed. The scan speed increases from 2 μm/s to 60 μm/s. Similar results are obtained, which have showed that the width of the line decreases with the increase of the scan speed.

2.2.3 Effect of exposure time

Dots are fabricated with a femtosecond laser of different exposure times which are controlled by a shutter (Uniblitz® VCM-D1). Figure 2-5 describes a SEM image of dots which are fabricated with a laser energy of 0.500 nJ through a 2× beam expander and an objective lens with 50× magnification and the dependence of the diameter on the exposure time. The exposure time varies from 100 ms to 3000 ms. Seven dots are fabricated with the same exposure time which are shown in the same row. The theoretical

result is obtained according to Eqn. (2.1). The diameter of the dot increases with the increase of the exposure time.

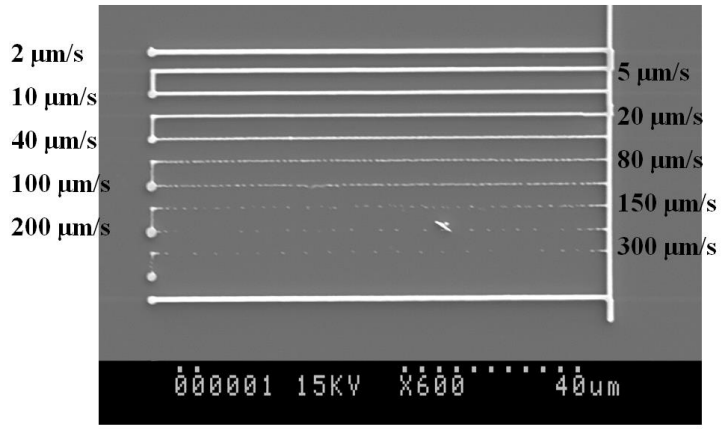

(a)

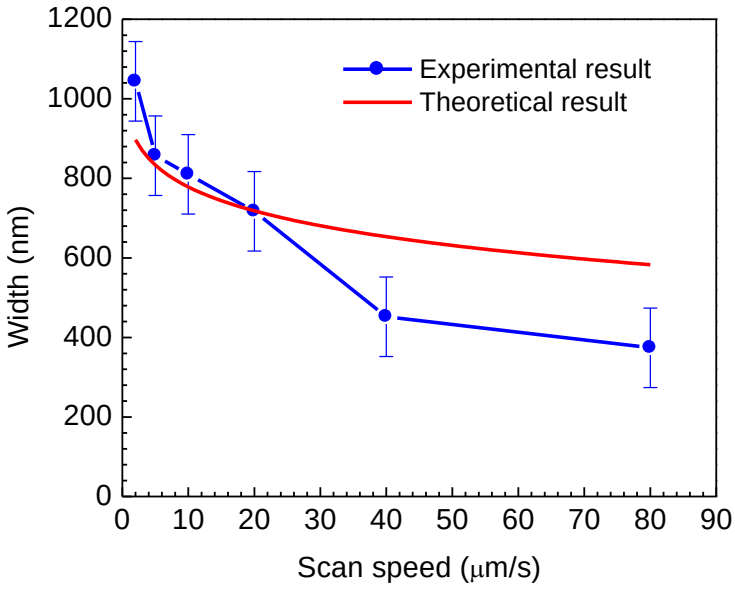

(b)

Figure 2-3 Lines exposed by femtosecond lasers of different scan speeds: (a) an SEM image of lines, and (b) dependence of the width on the scan speed. The laser pulses (0.500 nJ/pulse) are focused by an objective lens with a magnification of 50× (0.8 NA). The theoretical result is obtained according to Eqn. (2.1).

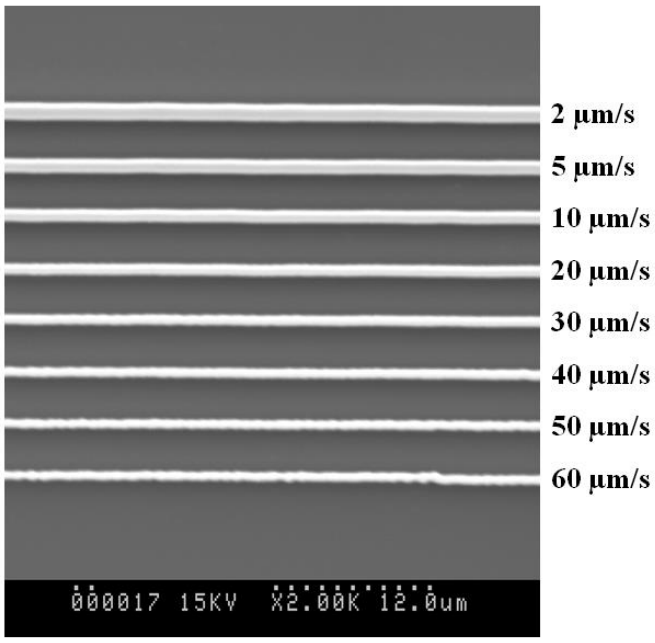

(a)

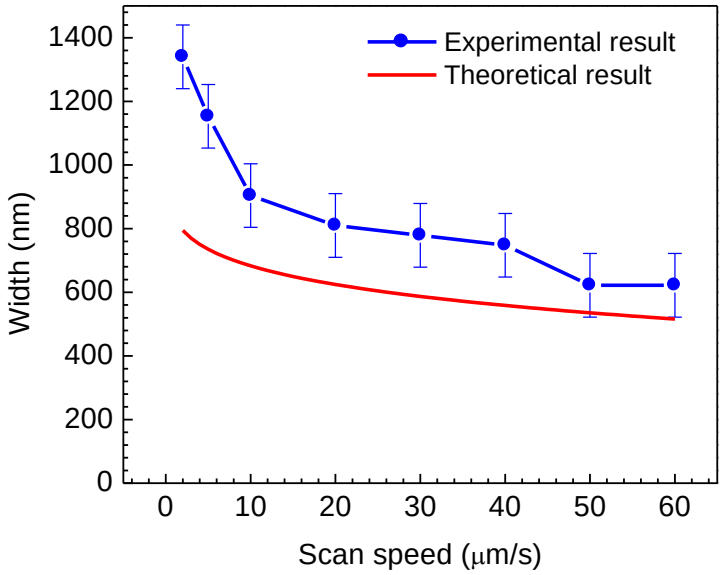

(b)

Figure 2-4 Lines exposed by femtosecond lasers of different scan speeds: (a) an SEM image of lines, and (b) dependence of the width on the scan speed. The laser pulses (0.500 nJ/pulse) are focused by an objective lens with a magnification of 100× (0.95 NA). The theoretical result is obtained according to Eqn. (2.1).

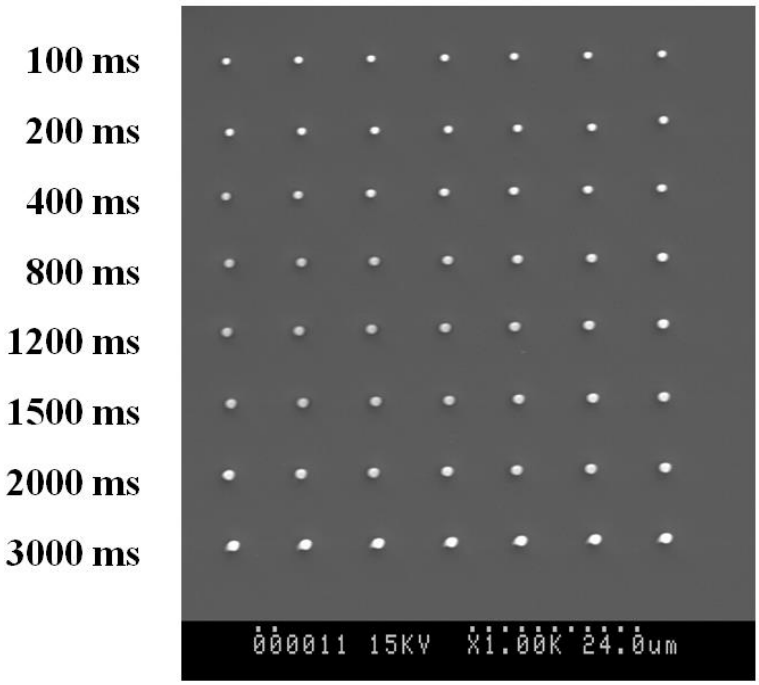

(a)

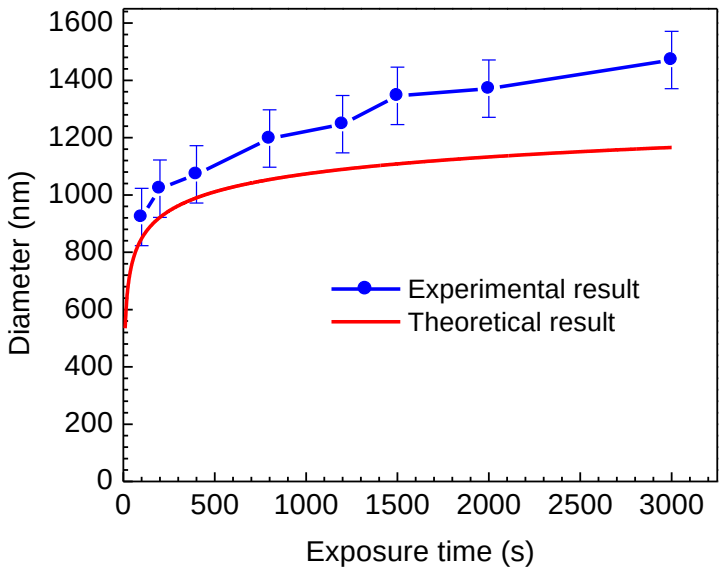

(b)

Figure 2-5 Dots exposed by femtosecond lasers of different exposure times: (a) an SEM image of dots, and (b) dependence of the diameter on the exposure time. The laser pulses (0.500 nJ/pulse) are focused by an objective lens with a magnification of 50× (0.8 NA). The theoretical result is obtained according to Eqn. (2.1).

2.2.4 Effect of pulse energy

Lines are fabricated with different femtosecond laser energies. Figure 2-6 describes a SEM image of lines which are fabricated by laser beams through a 2× beam expander and an objective lens with 50× magnification and the dependence of the width on the pulse energy. The scan speed is 20 μm/s. The pulse energy varies from 0.375 nJ/pulse to 0.875 nJ/pulse. Low pulse energy (< 0.375 nJ) cannot expose SU-8. High pulse energy (> 0.750 nJ) will ablate the SU-8 film and ruin the sample. In the available pulse energy range, the width of the line increases with the increase of the pulse energy.

In conclusion, the characterization of TPP using a femtosecond laser has been carried out in this chapter. The diameters of voxels fabricated at different fabrication conditions have been measured. The experimental results do not agree well with the simulation results based on Eqn. (2.1). The reason might be that the exposure threshold E_{th} of SU-8 for TPA is referenced from Ref. 67. The actual value might be a little different from that value. Following the experimental results obtained here, the diameter of voxel can be increased by using large pulse energy, long exposure time, or slow scan speed.

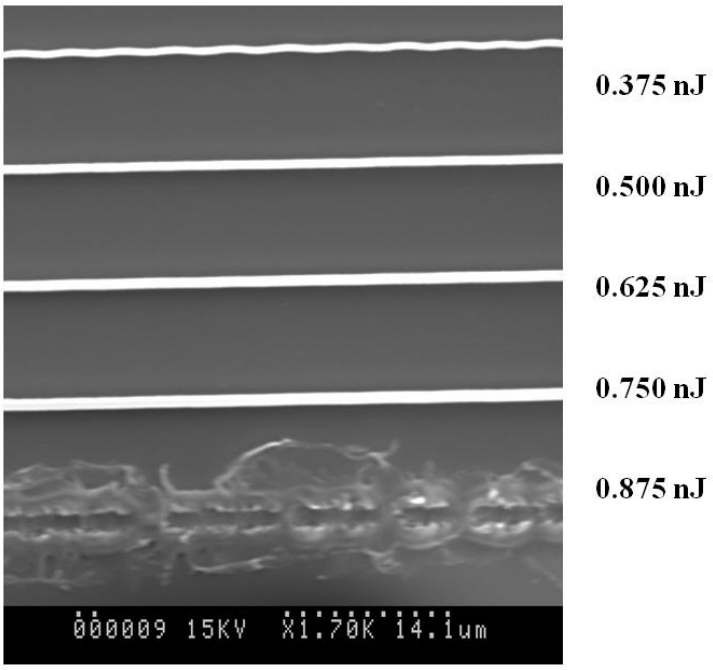

(a)

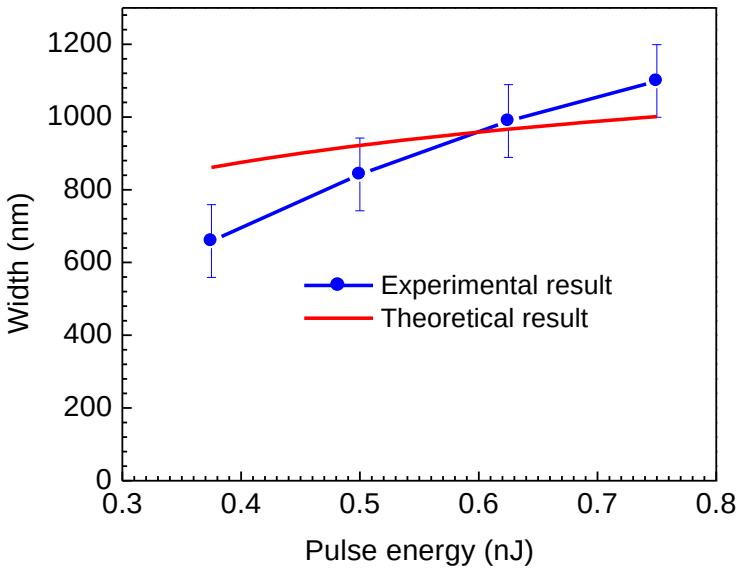

(b)

Figure 2-6 Lines exposed by femtosecond lasers of different pulse energies: (a) an SEM image of lines, and (b) dependence of the width on the pulse energy. The laser pulses are focused by an objective lens with a magnification of 50× (0.8 NA). The scan speed is 20 μm/s. The theoretical result is obtained according to Eqn. (2.1).

Chapter 3 Grating-based opto-microfluidic devices

3.1 Introduction

In this chapter, a diffractive grating is introduced. The fabrication process and the diffraction characterization are studied. Colour filters are realized by fabricating gratings with different thicknesses. RI sensing is also implemented by monitoring the transmission spectra of the zeroth order diffraction light. The effects of the resonance order and grating thickness on the sensitivity are discussed.

3.1.1 Theory

In optics, grating is a kind of periodic structure which diffracts light in different directions. A typical binary dielectric grating consists of alternating regions of high and low RI dielectric materials as shown in Fig. 3-1, in which Λ is the grating pitch, d is the thickness of the grating, n_1 and n_2 are the RIs of these two dielectric materials, and a and b are the widths of the two regions, respectively.

Assuming a planar wave passes through a grating, the transmission function $\tau(x)$ is described as:

$$\tau(x)=\begin{cases} e^{i\varphi_1} \\ \mathrm{e}^{i\varphi_2} \end{cases} \quad \text{for} \quad \begin{matrix} n\Lambda < x < n\Lambda + a \\ n\Lambda + a < x < n\Lambda + \Lambda \end{matrix} \quad n = 0, \pm 1, \pm 2, \pm 3, ... \pm \frac{N}{2} \qquad (3.1)$$

where N+1 is the number of grating lines, and φ_1 and φ_2 are the phases of light that passes through the high RI region n_1 and low RI region n_2. Therefore, the phases can be expressed as:

$$\varphi_1 = 2\pi \frac{n_1 d}{\lambda}$$
$$\varphi_2 = 2\pi \frac{n_2 d}{\lambda} \tag{3.2}$$

where λ is the wavelength of light.

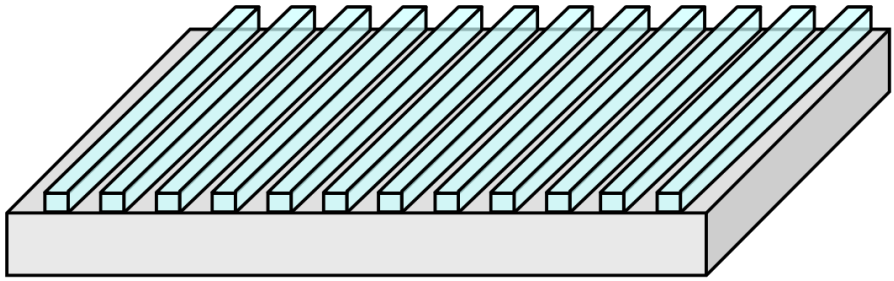

(a)

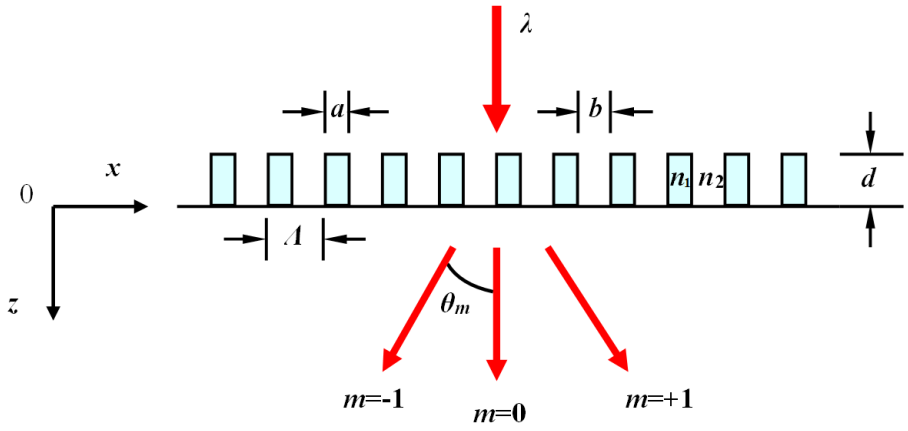

(b)

Figure 3-1 Schematic illustration of a guided-mode resonance grating: (a) the 3D view, and (b) the side view

The Fraunhofer (far-field) complex-amplitude distribution *U(f)* can be calculated by Fourier transformation of the transmission function at the frequency of $f = \frac{x}{\lambda z}$ [68]

$$U(f) = \int_{-(N+1)\Lambda/2}^{(N+1)\Lambda/2} \tau(x) e^{-i2\pi xf} dx = \sum_{m=-\infty}^{\infty} \delta(f - \frac{m}{\Lambda}) \frac{1}{\Lambda} \int_{-\frac{\Lambda}{2}}^{\frac{\Lambda}{2}} \tau(y) e^{-i2\pi yf} dy \tag{3.3}$$

where x is the coordinate along the grating direction, $\tau(x)$ is the transmission function, Λ is the grating pitch, m is the diffraction order, and $y = x - m\Lambda$.

Since the frequency f is equal to $\frac{m}{\Lambda}$, the intensity of the m^{th} order is

$$I_m(f) = |U_m(f)|^2 = \frac{1}{\Lambda^2} \left| \int_{-\frac{\Lambda}{2}}^{\frac{\Lambda}{2}} \tau(y) e^{-i2\pi ym/\Lambda} dy \right|^2 \tag{3.4}$$

Therefore, the intensity of the zeroth diffraction order ($m = 0$) is

$$\begin{aligned} I_0 &= 1 - 2\frac{a}{\Lambda}(1 - \frac{a}{\Lambda}) + 2\frac{a}{\Lambda}(1 - \frac{a}{\Lambda})\cos\delta\varphi \\ &= 1 - 2\frac{a}{\Lambda}(1 - \frac{a}{\Lambda}) + 2\frac{a}{\Lambda}(1 - \frac{a}{\Lambda})\cos[\frac{2\pi}{\lambda} d(n_1 - n_2)] \end{aligned} \tag{3.5}$$

where $\delta\varphi = \varphi_1 - \varphi_2$ is the phase difference.

3.1.2 Fabrication and applications

To date, various fabrication techniques have been proposed to obtain binary dielectric gratings, such as laser machining [69,70], microelectromechanical systems (MEMS) [71,72], soft lithography [73,74], and hot-embossing [75,76]. Figure 3-2 depicts a schematic illustration of various fabrication techniques. During laser micromachining

processes, a high power laser beam is focused on the surface of a planar material such as a metal, ceramics, polymer or glass, and then ablated periodic grooves are fabricated by controlling the movements of the laser beam (Fig. 3-2(a)). MEMS are the fabrication technique which originated from semiconductor device fabrication. There are three basic processes in MEMS technology: A structural layer such as silicon, polymer or metal film and a sacrificial layer such as photosensitive film are first deposited on the substrate sequentially; a grating pattern is transferred to the sacrificial layer by a lithographic technique; the grating structure is produced in the structural layer using a selective etching process (Fig. 3-2(b)). The soft lithographic technique emerged in the 1980s, and underwent rapid development in the 1990s [77]. Elastomeric materials, most notably polydimethylsiloxane (PDMS), are poured on the grating master, which is usually fabricated by laser micromachining or the MEMS technique, to form grating structures (Fig. 3-2(c)). Hot-embossing is a type of stamping technique, in which heat and forces are applied on the substrate and master to emboss the plastic material, commonly polycarbonate or polymethyl methacrylate (PMMA) (Fig. 3-2(d)).

With the development of microfluidic and optofluidic techniques, a novel type of droplet or bubble grating was proposed [78-81]. The design for the formation of a droplet or bubble grating in a microfluidic chip is shown in Fig. 3-3. Immiscible liquids or gas are infused into a microchannel and then generate an interface at the T-junction. The high resistance to the continuously flowing fluid separates the dispersed liquid or gas into an array of periodic droplets or bubbles.

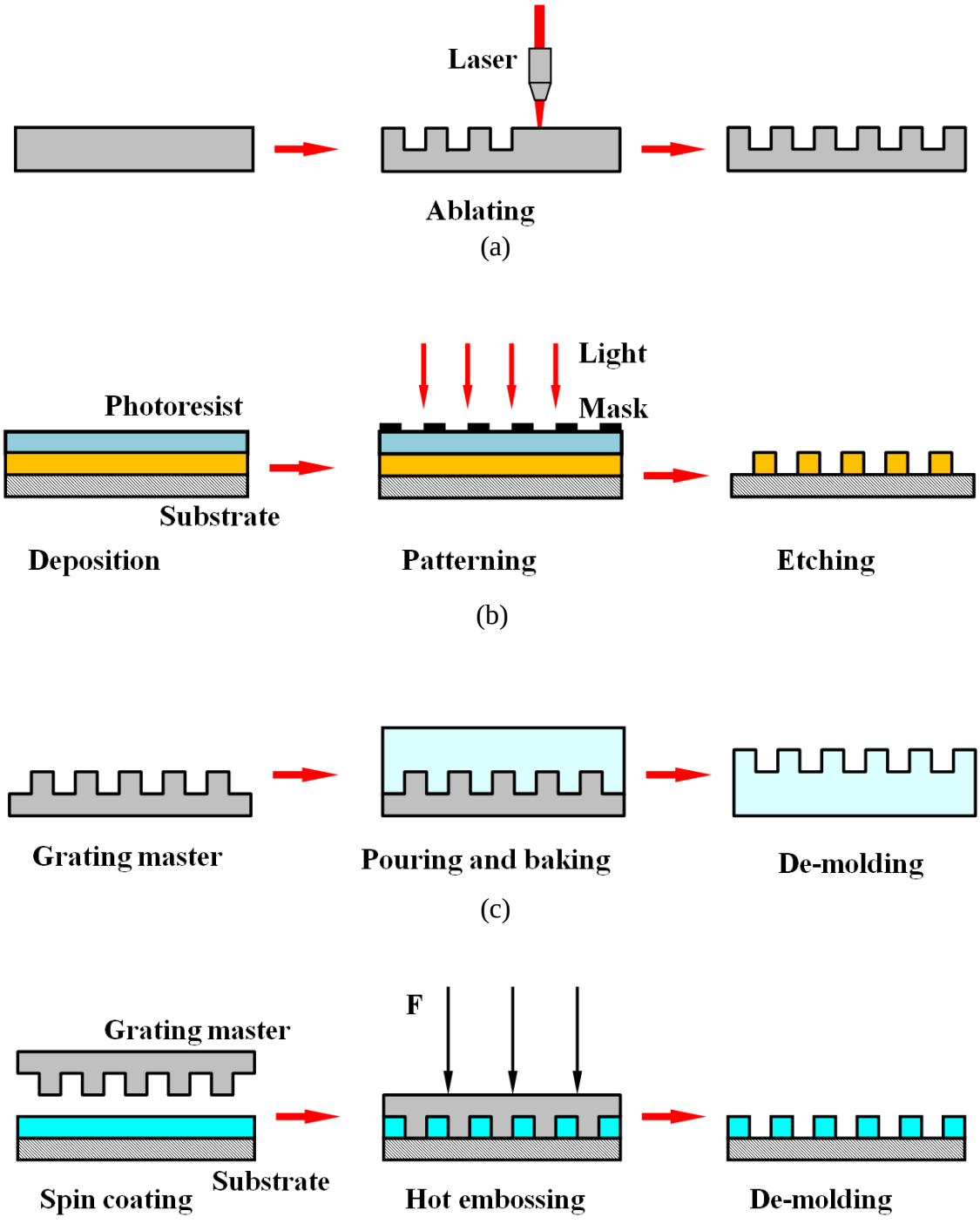

Figure 3-2 Schematic illustration of different fabrication processes: (a) laser micromachining, (b) MEMS, (c) soft lithography, and (d) hot-embossing.

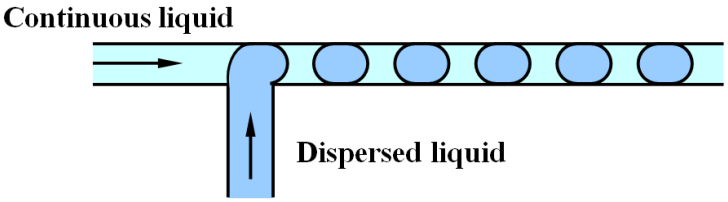

Figure 3-3 Schematic illustration of a droplet grating

As an important optical component, diffraction grating has been widely used as a wavelength separation device in spectroscopy. Diffraction grating is also used in laser pulse stretching and compression. In addition, diffraction gratings can also work as optical filters, beam splitters and optical couplers. Here, we just focus on the applications of the binary dielectric grating in microfluidics and optofluidics. As shown in Eqn. (3.5), the diffraction intensity is related to the thickness of the grating and the RIs of the periodic regions. The microfluidic refractometers were designed to measure the RI of a liquid in the microchannel. Schueller *et al.* replicated a series of microchannels on PDMS and sealed them with a glass slide to form a PDMS-air (liquid)-PDMS grating (Fig. 3-4). Transmission intensities changed according to the RI of the liquid in the microchannel [82]. Yu *et al.* used immersion oil and a $CaCl_2$ solution to generate a microfluidic droplet grating. RIs of the $CaCl_2$ solutions were derived from the diffraction intensities [80]. Lei *et al.* integrated a grating on the tip of a multimode fiber, and inserted the fiber into a microchannel to test the RI of the fluid [83]. Another application of such microfluidic grating is the colour filter [80, 84]. By simply adjusting the RI of the fluid, different colours in the zeroth order are observed by a charge coupled device (CCD) camera when the white light passes through the grating. As a kind of “soft” elastomeric material,

PDMS will deform when a force is applied on them. Based on this phenomenon, Grzybowski *et al.* proposed a type of pressure sensor, in which strain was imposed on a PDMS grating, and a decrease of the grating thickness was induced. Pressure was calculated by monitoring transmission intensities [68]. Hosokawa *et al.* presented a microfluidic pressure sensor using the deformation of a PDMS microchannel grating to achieve the pressure in the microchannel [85]. Besides the applications of diffraction light mentioned above, a droplet signal generator [79] and microfluidic grating dye laser [86-88] were also reported. In the dye laser design, dye solutions flow in the microchannel. After the dye was excited by the pump light, the laser was generated from the laser cavity consisting of a grating and a waveguide.

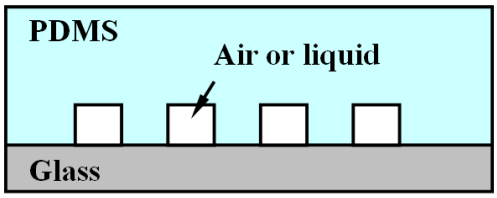

Figure 3-4 Schematic illustration of a microchannel grating

3.2 Grating characterization

SU-8 gratings are fabricated using a femtosecond laser by scanning lines one by one. The most important advantage of this method is the flexibility. It is easy to write gratings with different periodicities Λ, thicknesses d, and widths a by simply adjusting the laser power, scan speed, and focusing condition. Figures 3-5 and 3-6 show the SEM images of gratings with the periodicities of 5 μm and 3 μm, respectively. The laser beam is focused by a 50×

objective lens with NA of 0.8, laser power of 0.625 nJ/pulse, and scan speed of 20 μm/s. The size of the gratings is 200 μm × 200 μm.

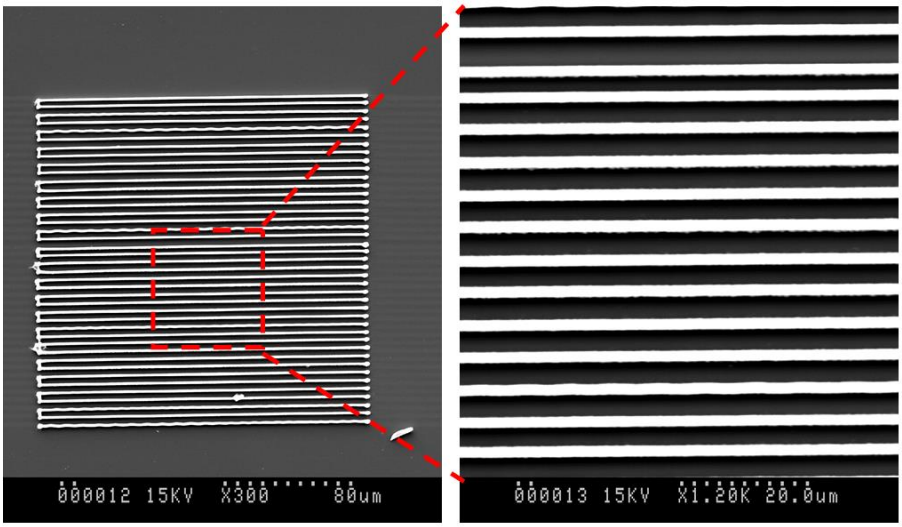

Figure 3-5 SEM images of a grating with a periodicity of 5 μm. The size of the grating is 200 μm × 200 μm.

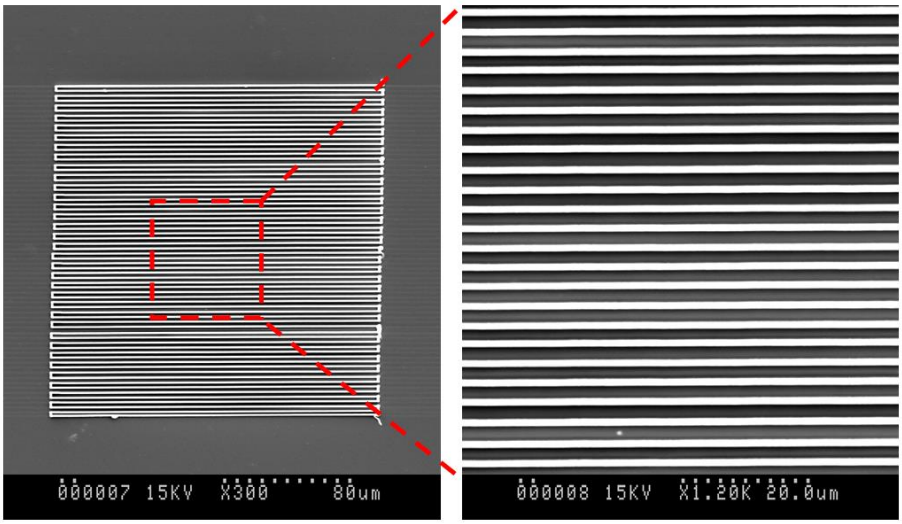

Figure 3-6 SEM images of a grating with a periodicity of 3 μm. The size of the grating is 200 μm × 200 μm.

According to the grating equation:

$$\Lambda \sin \theta_m = m\lambda \quad \text{(normal incident)} \tag{3.6}$$

where θ_m is the angle between the m^{th} order diffracted ray and zeroth order diffracted ray, the diffracted angle depends on the wavelength and the periodicity. If a white beam passes through the grating, components of light with a single wavelength are separated into different directions, thus producing a dispersion spectrum. Figure 3-7 shows an experimental setup for observing the diffraction patterns. Two light sources are used in this setup. One is the ANDO® white light source with three adjustable wavelength ranges (400-1800 nm, 700-1800 nm, and 1000-1800 nm). The other one is an He-Ne laser with a wavelength of 632.8 nm. A single mode fiber (SMF) (Corning SMF28e) transfers the light beam from the light source to the grating. Through an objective lens, a CCD camera captures the diffraction patterns. Here, we use two types of CCD cameras. One is a Panasonic (Japan) GP-KR222 color digital camera which is sensitive to visible light, and the other one is a Hamamatsu system (Japan) including a camera head C2741-03 and controller C2471 which is sensitive from visible to near-infrared light. Figure 3-8 presents diffraction patterns captured by the Panasonic camera. The periodicities of the gratings are 2 μm and 3 μm, respectively. Both patterns are detected at the same site. m = 0, ±1 orders are shown on the screen for the grating with a periodicity of 2 μm (Fig. 3-8(a) and (c)), and m = 0, ±1, ±2 orders are observed on the screen for the grating with a periodicity of 3 μm (Fig. 3-8(b) and (d)). The light with a shorter wavelength (blue colour) is closer to the zeroth order point than the longer wavelength light (red colour) for the same diffraction order which means that the short wavelength light has a smaller diffracted

angle. The diffracted light is closer to the center in a long period grating than in a short period grating at the same diffraction order which means a longer period grating has a smaller diffracted angle. In addition, Figure 3-8(b) shows that the light with a longer wavelength in the first order partly overlaps with the smaller wavelength light in the second order. Figure 3-9 exhibits another diffraction patterns detected by the Hamamatsu system. The same results are obtained as mentioned above.

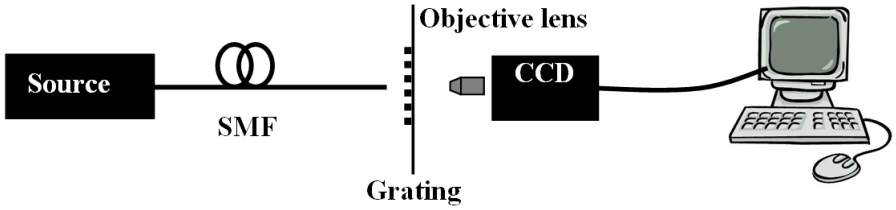

Figure 3-7 Experimental setup for the observation of diffraction patterns

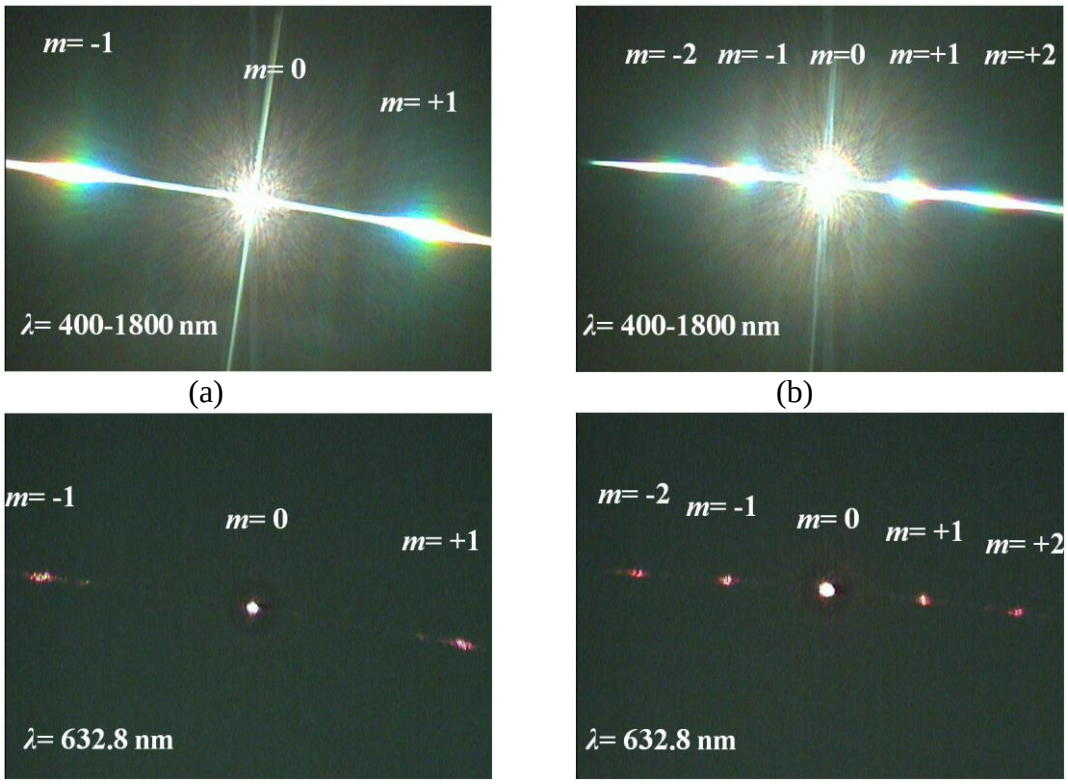

Figure 3-8 Diffraction patterns observed with a Panasonic CCD camera: (a) and (c) Λ = 2 μm, and (b) and (d) Λ = 3 μm.

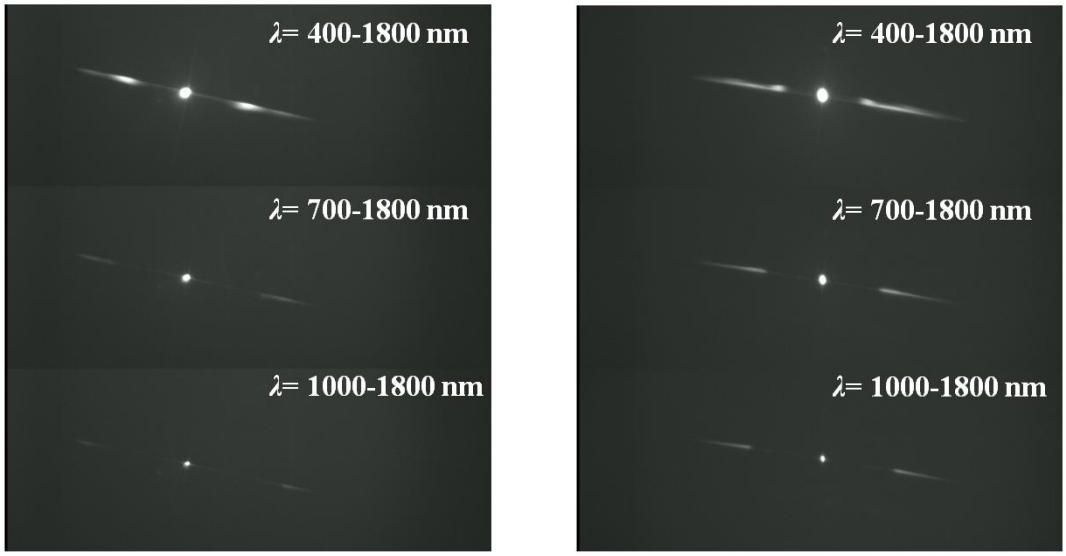

Figure 3-9 Diffraction patterns observed with a Hamamatsu system: (a) Λ = 2 μm, and (b) Λ = 3 μm.

3.3 Colour filters

The white light, which is a broadband light source, consists of monochromatic light of different wavelengths. Figure 3-10 shows a CIE 1931 colour space chromaticity diagram [89]. The blue numbers along the outer curved boundary correspond to the wavelengths of the monochromatic light. The co-ordinates are calculated from ratios of the *XYZ* tristimulus values[1]. The chromaticity diagram describes the colours observed by human eyes when monochromatic light mix together with different intensities.

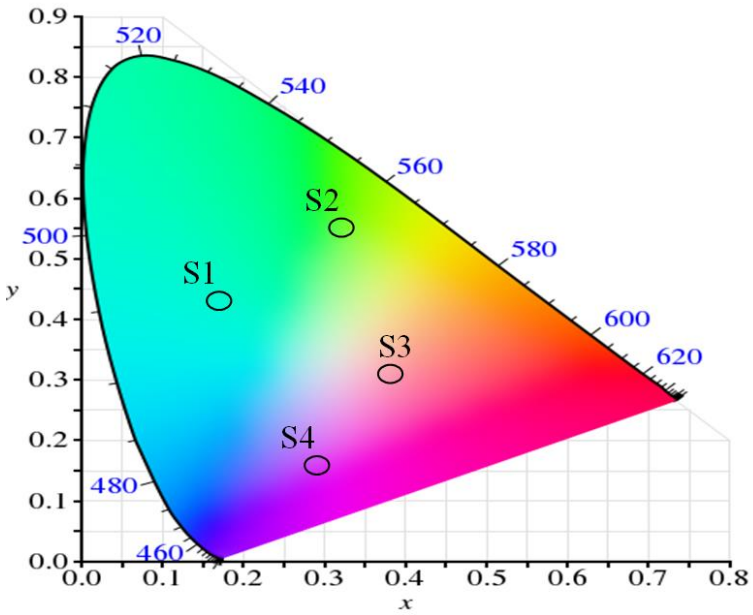

Figure 3-10 The CIE 1931 colour space chromaticity diagram. S1-S4 are the colours shown in Fig. 3-13.

[1] The human eye has three kinds of cones on the retina. They are especially sensitive to red (*X*), green (*Y*) and blue (*Z*), respectively. All colours are mixtures of these three colours. The *XYZ* tristimulus values are calculated using a colour-mapping function.

Based on the Eqn. (3.5), we know that the intensity of the zeroth order relates to the duty cycle a/Λ and is a cosine function of $1/\lambda$. Figure 3-11 shows calculated curves of I_0 in the wavelength range of 350 - 1750 nm at different ratios of a/Λ. The thickness d is 1.50 μm, n_1 is 1.596 (RI of SU-8 at 633 nm) [90], and n_2 is 1.000 (air). Multiple periods are observed in spectral curves. The extinction ratio reaches its maximum at a/Λ = 0.5 and then diminishes with either an increase or decrease of a/Λ. However, wavelengths of peaks and valleys are independent of the grating's periodicity Λ. Therefore, gratings with periodicities of 2, 5, 8 or 10 μm are employed to investigate the spectrum characterization of the zeroth order in this section.

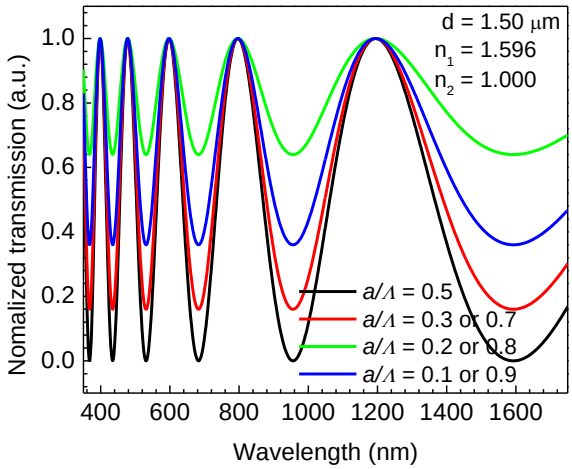

Figure 3-11 Simulation on the transmission spectra of the zeroth order in different duty cycles according to Eqn. (3.5). The SU-8 grating is surrounded by air and the thickness of the SU-8 grating d is 1.50 μm.

If the phase differences satisfy $\delta\varphi = \frac{2\pi}{\lambda} d(n_1 - n_2) = (2n+1)\pi$, then

$$\lambda = \frac{n_1 - n_2}{2n+1} d \qquad (I_0\text{=minimum}) \tag{3.7}$$

where n is the order of the resonance mode. This means that this monochromatic light is filtered out.

Grating colour filters are designed according to Eqn. (3.7). An SMF replaces the CCD camera to collect the zeroth diffracted light and transfer it to an optical spectrum analyzer (OSA) (Ando AQ-6315). As shown in Fig. 3-12, the top SMF and the sample are both mounted on separate *XYZ* motion stages. At first, the top fiber directly aligns with the bottom fiber without the sample by adjusting the *XYZ* motion stages. This process is monitored by a Newport® dual-channel power meter (2832-C, USA) which is connected to the bottom fiber. When a maximal reading is shown on the power meter which means the alignment is achieved, we substitute the power meter with the OSA, measure the spectrum of the light source I_s, and then insert the sample between the two fibers to measure the spectrum of zeroth order diffracted light I. Normalized light intensity (grating efficiency) can thus be obtained by calculating I/I_s.

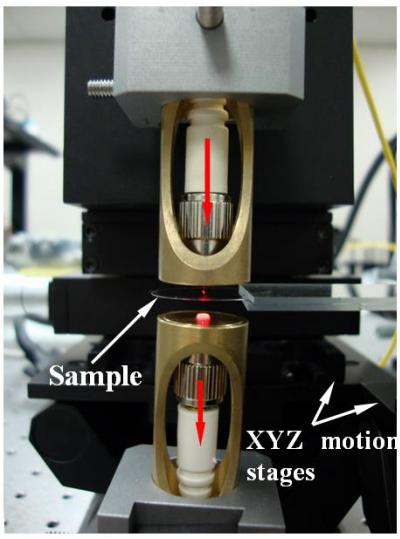

Figure 3-12 Photograph of an experimental setup for color filters

Four groups of data are shown in Fig. 3-13. The colour images are captured by Leica DMR microscope (Canada). The blue curves show the measured normalized spectra of the zeroth order diffracted light from different samples. The red curves are the simulation results calculated with MATLAB software according to Eqn. (3.5). In the simulation, a/Λ is 0.5, n_1 is 1.596, and n_2 is 1.000. Due to the fact that the RI changes slightly with different wavelengths, there is a small discrepancy between the experimental data and simulation results. For the S1 sample with a graing thickness of 1.57 μm, the transmission spectrum shows the highest intensity at 491.8 nm which responses to a cyan colour for human eyes. For the S2 sample with a graing thickness of 1.76 μm, the highest intensity is shown at 550.5 nm which responses to a green colour for human eyes. When the grating thickness increases to 1.84 μm (S3), the peak moves to 566.1 nm which responses to a yellow colour for human eyes. The peak is 648.5 nm which responses to a red colour for human eyes for the S4 sample with a graing thickness of 2.15 μm. The grating samples with different thicknesses present different colours under microscope which match the chromaticity diagram depending on the spectra. We also notice that Figure 3-13(d) has a smaller extinction ratio than (a), (b) and (c) due to its smaller duty cycle. The peak wavelengths λ_{peak} with the same resonance mode are marked with pink stars. The linear relationship between the peak wavelength λ_{peak} and thickness d is demonstrated in Fig. 3-14. Peak shifts to a longer wavelength region as the thickness increases.

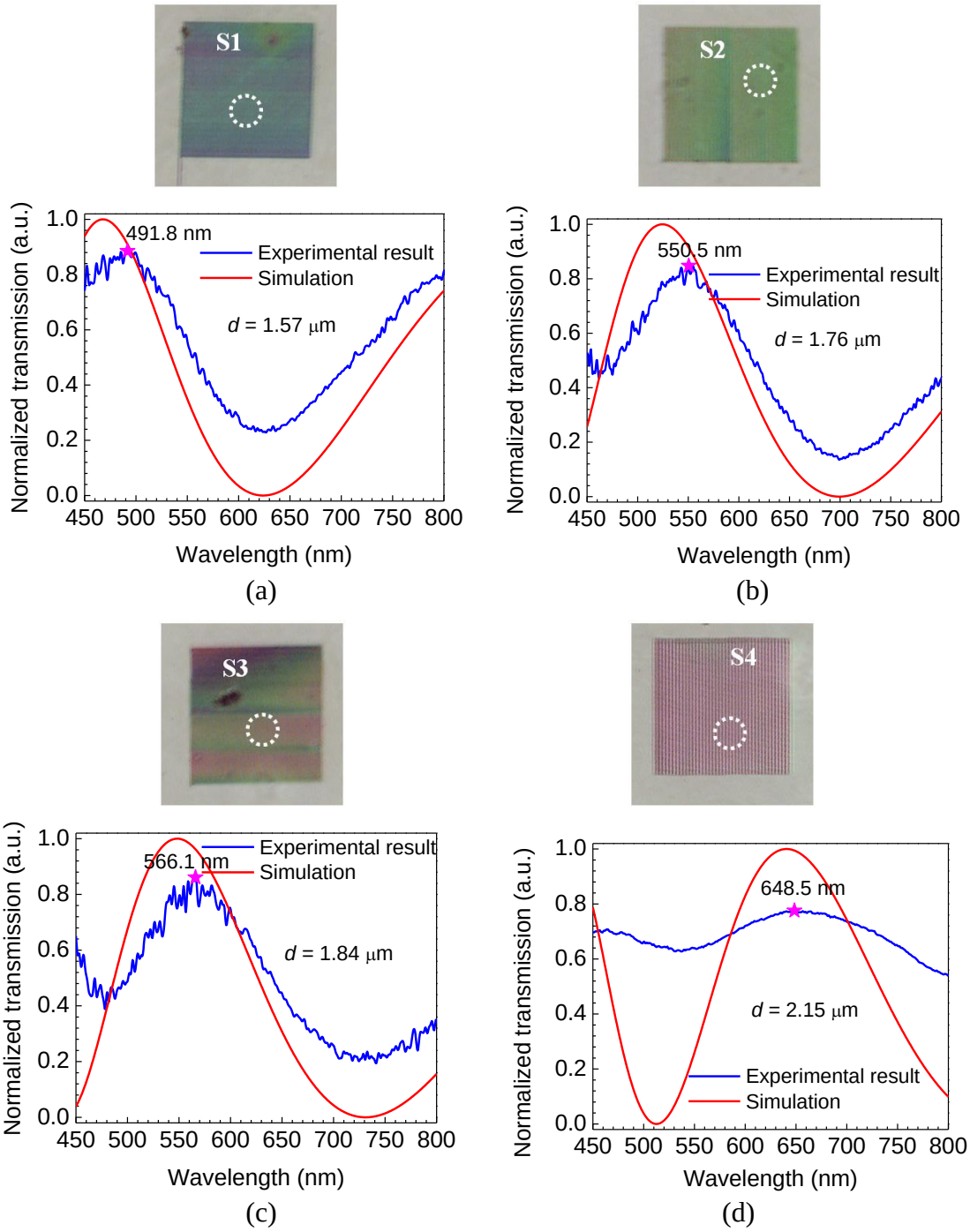

Figure 3-13 Comparison between the experimental and simulation results. The thicknesses of the four samples are about 1.57, 1.76, 1.84, and 2.15 μm, respectively. Λ of (a), (b) and (c) is 2 μm and (d) is 5 μm. The simulation results are calculated with MATLAB software according to Eqn. (3.5), in which a/Λ is 0.5, n_1 is 1.596, and n_2 is 1.000.

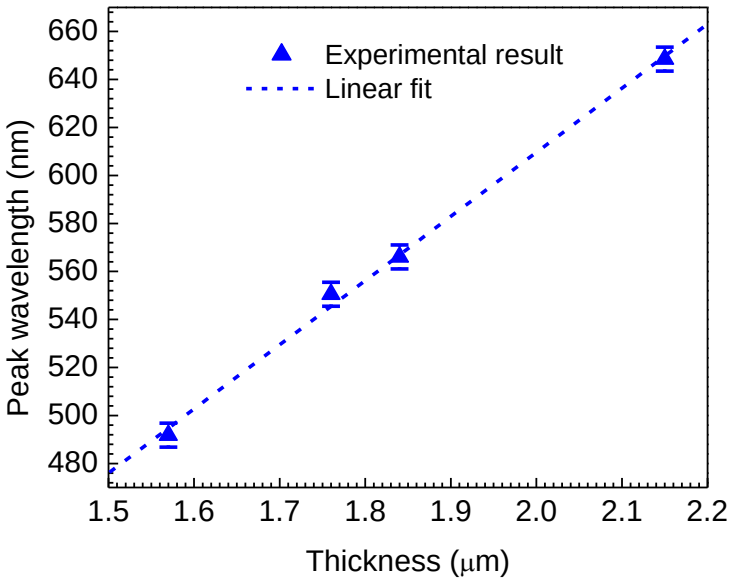

Figure 3-14 Dependence of the peak wavelength on grating thickness for samples in Fig. 3-13

In conclusion, colour filters are achieved with SU-8 gratings fabricated by a femtosecond laser. Colours from gratings of different thicknesses are observed through microscope. Compared with other grating-based colour filters reported in some papers [80, 84], the grating fabrication technique adopted in this study is much simpler. In addition, we demonstrate the practicability of such colour filters by identifying accurate spectral specifications with an OSA.

3.4 Grating-based refractive index sensor

3.4.1 Fabrication and experimental setup

In this section, standard soft lithography is used to produce PDMS microchannels. Microchannel patterns are designed by AutoCAD software as shown in Fig. 3-15(a), and saved as an eps file. The file is resized by PhotoShop software and printed on transparent

plastic film with a resolution of 1200 dpi ×1200 dpi. SU-8-2075 with a thickness of 75.00 μm is spin-coated on a glass substrate. After soft baking, the sample is aligned with the mask and exposed to UV light (28 mJ/cm^2) for 18 s. SU-8 masters are obtained after post-exposure baking and development. Figure 3-15(b) shows an SU-8 master. PDMS prepolymer and curing agent (Dow Corning Sylgard-184, USA) are mixed in a mass ratio of 10:1, degassed in a vacuum desiccator for 1 hour, poured on the master which is placed in a folded aluminium foil plate, and cured at 95 ^{o}C on a hotplate for 1 hour. Molds are then peeled off from the master, trimmed, and punched with a 22 gauge needle (ID 0.413 mm, OD 0.718 mm) for access holes.

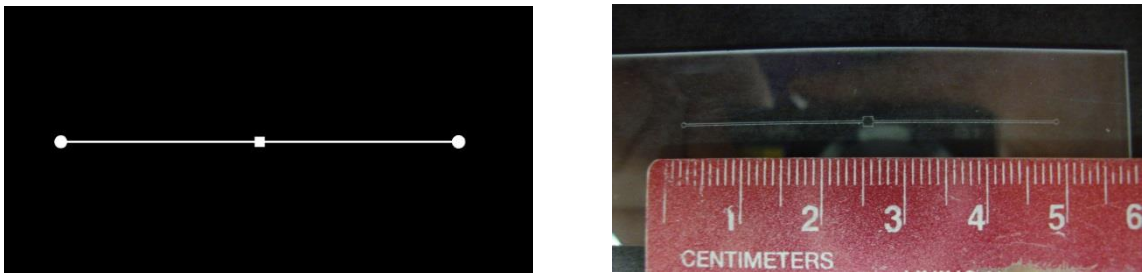

(a) (b)

Figure 3-15 SU-8 master fabrication: (a) a designed mask structure, and (b) a fabricated SU-8 master on a glass substrate

An SU-8 grating is first fabricated on a glass substrate, as shown in Fig. 3-16(a). The glass substrate and PDMS mold are treated with a plasma cleaner (PDC-001, Harrick Plasma, USA) for 40 s at a high radio frequency (RF), and then quickly attached together with a force to achieve irreversible bonding as shown in Fig. 3-16(b). The sample is baked at 95 ^{o}C for 12 hours to strengthen the bonding. Two capillary tubes (Upchurch Scientific® PEEK tubing, USA, ID 100 μm, OD 360 μm) are inserted into the access

holes and sealed by UV glue (DYMAX® 3013, USA). One end of a tube is inserted and sealed in a 22 gauge needle. The schematic illustration of the experimental setup is depicted in Fig. 3-16(c). An arc lamp of a higher power (Newport® 69907, USA) is used as the light source. The white light is focused on the grating through an objective lens with 20× magnification and 0.46 NA. A syringe (BD Luer-Lok™ 1mL, USA) driven by a syringe pump (Chemyx® Fusion 400, USA) smoothly pushes a liquid into the microchannel. Figure 3-16(d) is a photo of the experimental setup.

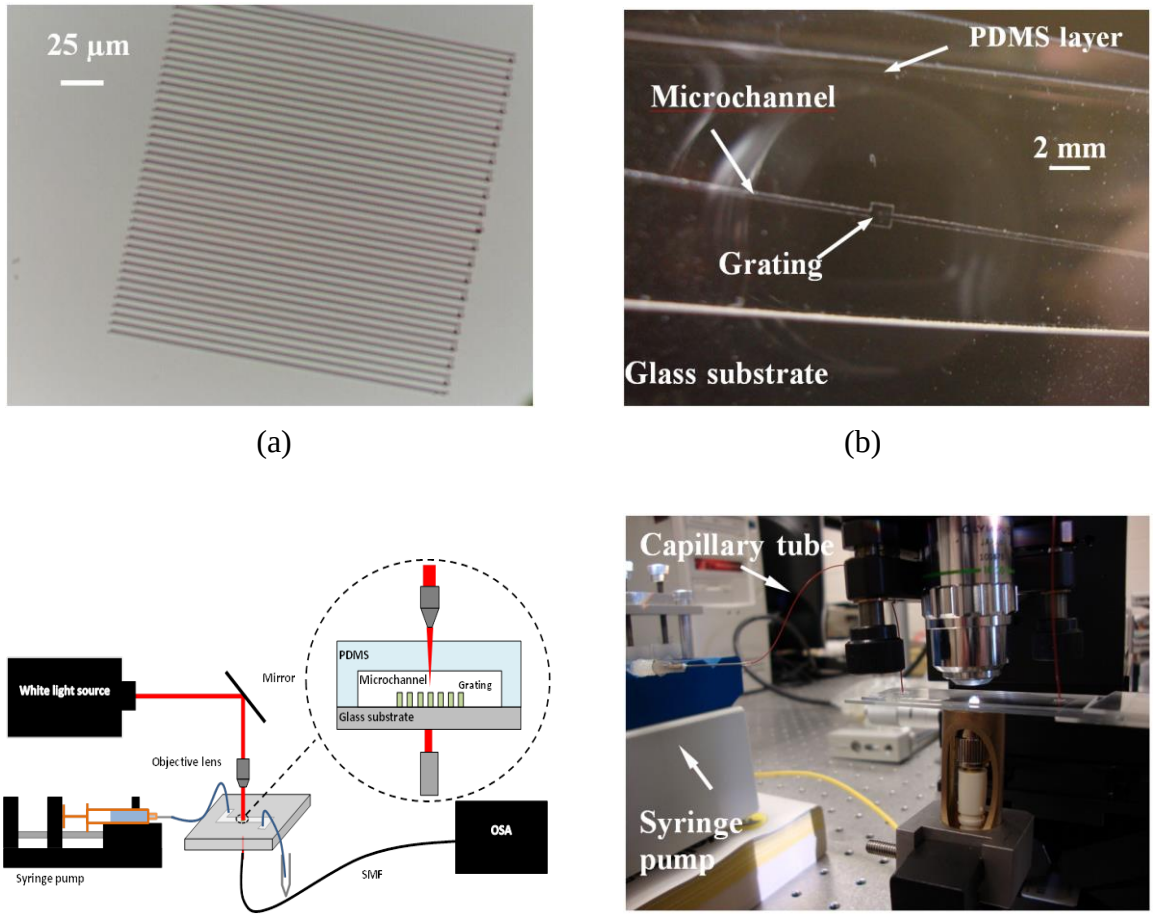

(a) (b)

(c) (d)

Figure 3-16 Grating based RI sensor: (a) an SU-8 grating on a glass substrate, (b) a substrate covered by a PDMS layer, (c) a schematic illustration of an experimental setup, and (d) a photo of the experimental setup.

3.4.2 Characterization of opto-microfluidic refractive index sensor

Comparing to the grating for colour filtering, the grating for RI sensing discussed in this section should be thicker. As a result, more periods can be found in the spectral curve. According to Eqn. (3.2), the phase difference for peaks can be expressed as follows:

$$\delta\varphi = 2\pi d(n_{SU-8} - n_2)/\lambda = 2\pi n \tag{3.8}$$

where n is the order of resonance mode. Since both the peaks and valleys should be monitored in this study, Eqns. (3.7) and (3.8) can be re-arranged as:

$$\delta\varphi = \frac{2\pi d(n_{SU-8} - n_2)}{\lambda} = \pi q \qquad \begin{array}{ll} \text{for peaks} & q \text{ is even} \\ \text{for valleys} & q \text{ is odd} \end{array} \tag{3.9}$$

Figure 3-17 shows a spectral curve with a grating thickness of 2.15 μm in the air. Four peaks and valleys can be found in the curve. If the RI of the fluid n_2 in the microchannel continuously changes, phase shifts occur, which correspond to the peak shifts in the spectral curve.

So
$$\lambda = 2d(n_{SU-8} - n_{Liquid})/q = \frac{2dn_{SU-8}}{q} - \frac{2d}{q}n_{Liquid} \tag{3.10}$$

$$\begin{aligned} \Delta\lambda = \lambda' - \lambda &= \frac{2d(n_{SU-8} - n'_{Liquid})}{q} - \frac{2d(n_{SU-8} - n_{Liquid})}{q} \\ &= -\frac{2d}{q}(n'_{Liquid} - n_{Liquid}) = -\frac{2d}{q}\Delta n \end{aligned} \tag{3.11}$$

where $\Delta n = n'_{\text{Liquid}} - n_{\text{Liquid}}$.

The slope of the peak shift is expressed as:

$$k = -\frac{2d}{q} \tag{3.12}$$

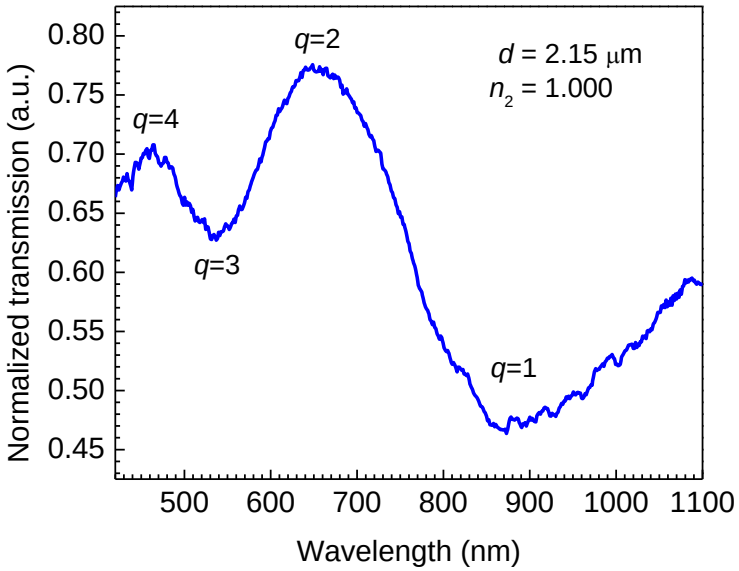

Figure 3-17 Transmission spectrum of the zeroth order signal from an air-surrounded grating with a thickness of 2.15 μm.

When saline solutions with different concentrations, which possess different RIs [91], are infused into the microchannel, the zeroth order transmission spectra are recorded and analysed. The simulation on the transmission spectra, experimental transmission spectra, and dependence of peak wavelength on RI for gratings with the thicknesses of 2.15 and 3.60 μm are shown in Figs. 3-18 and 3-19, respectively. The simulation results are calculated according to Eqn. (3.5), in which a/Λ is 0.5 and n_1 is 1.596. It is apparent that a blue shift occurs with the increase of the RI of the fluid.

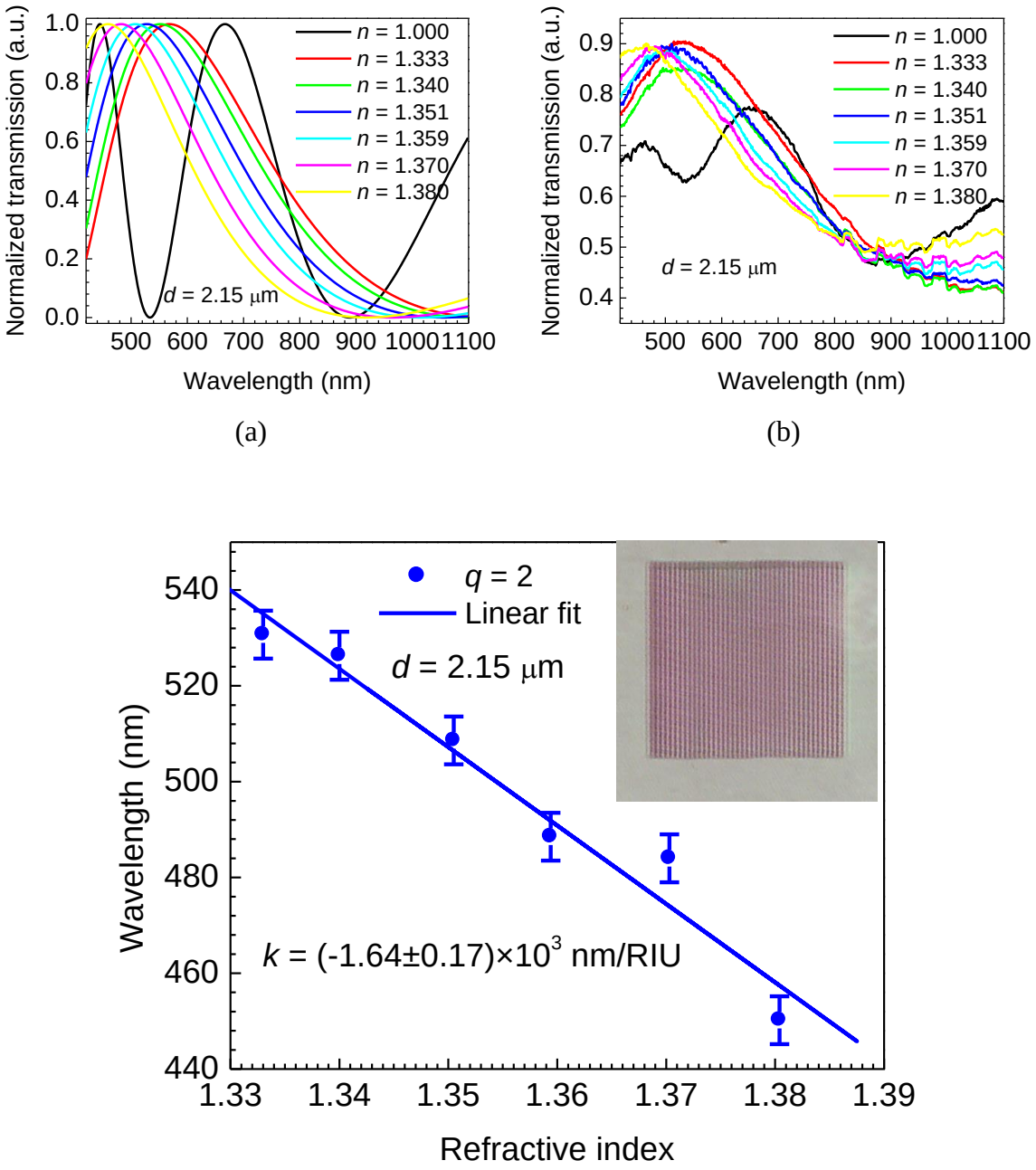

Figure 3-18 RI sensing measurement of a grating with a grating thickness of 2.15 μm: (a) simulation on the transmission spectra of the zeroth order according to Eqn. (3.5), (b) experimental results of the transmission spectra of the zeroth order, and (c) dependence of the peak wavelength on RI. The inset is the morphology of the grating.

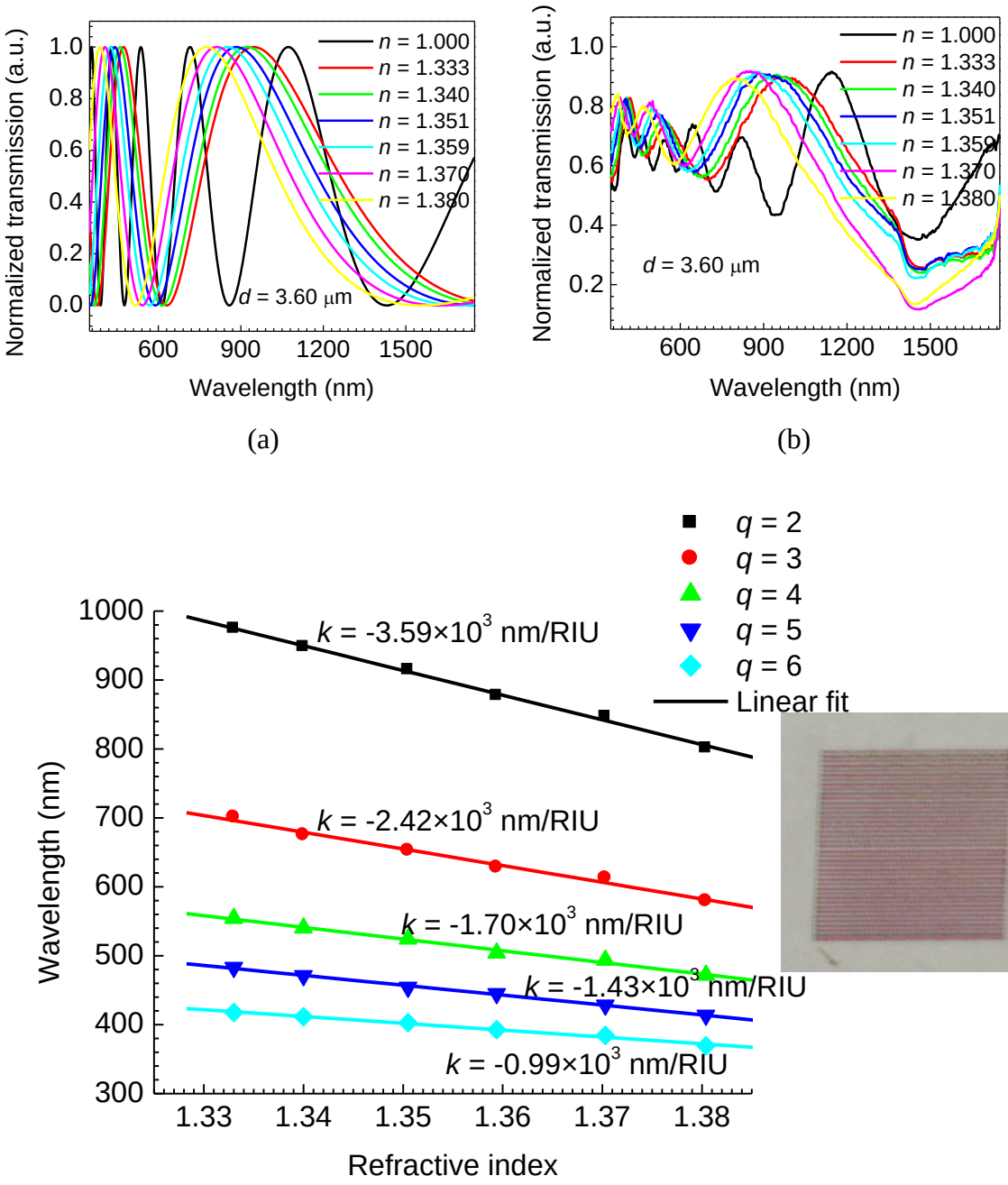

Figure 3-19 RI sensing measurement of a grating with a grating thickness of 3.60 μm: (a) simulation on the transmission spectra of the zeroth order according to Eqn. (3.5), (b) experimental results of the transmission spectra of the zeroth order, and (c) peak wavelengths in different fluidic environments. The inset is the morphology of the grating.

The sensitivity is obtained from the slope of a linear fit. Only one resonance mode (q= 2) is observed for the grating with a thickness of 2.15 μm due to the fact that other transmission spectra of peaks and valleys move out of the range of the OSA, and the sensitivity is (-1.64 ± 0.17)×10^3 nm per refractive index unit (RIU). However, five resonance modes (q= 2 ~ 6) are observed for the grating with a thickness of 3.60 μm. The sensitivity is about -3.59×10^3 nm/RIU for the second-order mode, which decreases to -0.99×10^3 nm/RIU for the sixth-order mode. A relatively high sensitivity can be obtained in the lower order of resonance mode. The sensitivity is also dependent on the thickness of the grating. Figure 3-20 shows the RI sensitivities of different orders in gratings with the thickness range from 2.15 to 6.00 μm. The sensitivity of the grating is inversely proportional to the order of the resonance mode. For the grating with a thickness of 6.00 μm, the sensitivity of the fifth-order mode is -2.31×10^3 nm/RIU, which drops to -1.32×10^3 nm/RIU for the grating with a thickness of 2.85 μm. Thicker grating has a higher sensitivity at the same order of the resonance mode.

In conclusion, grating-based microfluidic RI sensors have been successfully designed and demonstrated. From the studies on the sensitivities in different situations, we find that a thicker grating in a lower order of the resonance mode possesses a higher sensitivity. In addition, unlike some fiber RI sensors in which the RI measurement range is limited by the fiber material, such as n_{max} = 1.460 for a glass fiber [92], the measurement range of the grating RI sensors we developed here is not restricted.

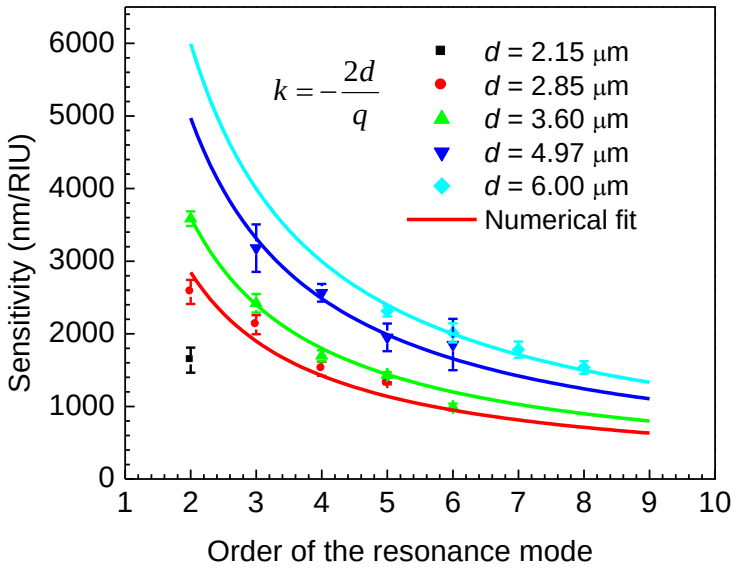

Figure 3-20 RI sensitivities of different orders of the resonance mode in gratings of various thicknesses

Chapter 4 Waveguide-Mach-Zehnder Interferometer based opto-microfluidic devices

4.1 Introduction

In this chapter, five new waveguide based Mach-Zehnder interferometer (MZI) structures are designed to achieve RI and temperature measurement. The effects of the waveguide size, chip length and microchannel length on the sensitivity are analysed both theoretically and experimentally.

4.1.1 Theory

The MZI is a device to detect the relative phase shift variation between two beams which are usually split from a single source. Figure 4-1 depicts a schematic diagram of a typical MZI. The light from the source is split into two beams, which then propagate through two different paths. A delay inserted into one of the paths results in a phase difference. When the two beams are finally recombined, this delay causes a change of the output light intensity.

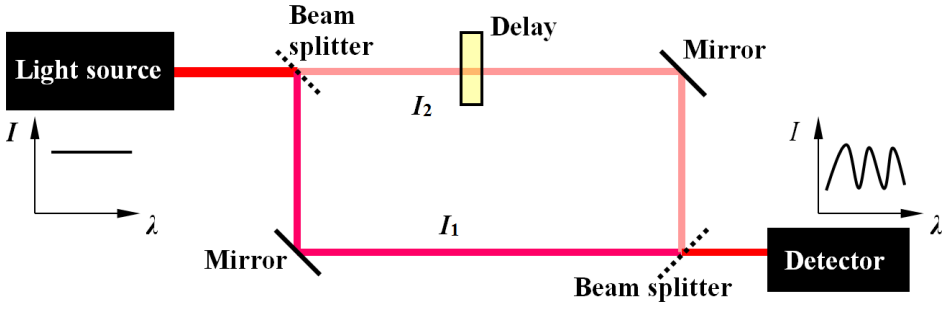

Figure 4-1 Schematic diagram of a typical MZI

The output light intensity can be expressed as follows:

$$I = I_1 + I_2 + 2\sqrt{I_1 I_2}\cos(\delta\varphi) \tag{4.1}$$

where I is the output intensity, I_1 and I_2 are the intensities of the two beams, and $\delta\varphi$ is the phase difference of the two beams.

In opto-microfluidic devices, an MZI structure is typically integrated into an optical waveguide as shown in Fig. 4-2. The signal is first coupled into the waveguide, and then split into two arms. One arm acts as a reference arm to compare the phase difference, and the other arm is used to sense the phase changes due to the variations of the surrounding environment such as temperature [93, 94], concentration [95, 96], and RI [97].

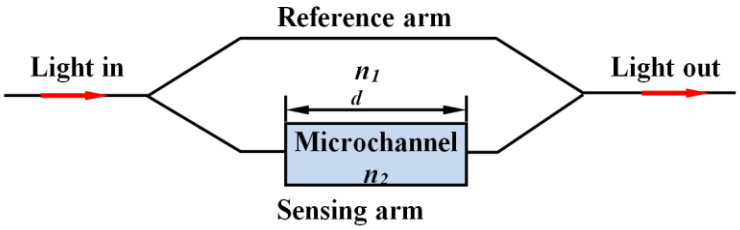

Figure 4-2 Schematic illustration of an opto-microfluidic MZI

In this configuration, the phase difference is

$$\delta\varphi = \frac{2\pi(n_1 - n_2)d}{\lambda} \tag{4.2}$$

where d is the length of the sensing arm, λ is the light wavelength, n_1 and n_2 are the RIs of the two paths, respectively.

4.1.2 Fabrication and applications

The optical waveguide is an important component of the opto-microfluidic MZI. Among various types of optical waveguides prepared, the typical waveguide structures are silicon-based solid core and solid cladding waveguides, which can be fabricated by MEMS. Crespi *et al.* reported an opto-microfluidic MZI in which waveguides were directly written in a bulk fused silica by a Yb:KYW femtosecond laser [95]. Wang *et al.* integrated an opto-microfluidic MZI into a single-mode fiber by ablating half of the core with a femtosecond laser. The remaining half core became the reference arm and the missing part acted as the sensing arm [93]. Without fabricating any waveguide on their MZI, Lapsley *et al.* fabricated a micro-lens to expand the beams to simultaneously pass through a short microchannel and PDMS, and another micro-lens to focus the beams to a fiber. The microchannel and PDMS acted as a sensing arm and reference arm, respectively [96].

One of the applications for opto-microfluidic MZI is RI sensing. When the microchannel (sensing arm) is filled with different liquids, phase differences are induced. RI is measured by monitoring the output intensity [93-96, 98]. Other applications of opto-microfluidic MZIs are in biology. In the design of MZI biochemical sensors, one or several kinds of reagents such as antigens, antibodies and proteins are bound on the sensing arm. When solvents are injected into the microchannel, the chemical or biological reaction, which generates new materials, produces a variation in the RI of the sensing arm. As a result, the types of molecules and the concentrations in the solvents can be determined by the output intensity [97, 99-102].

4.2 Waveguides with hybrid cladding

4.2.1 Waveguide characterization

After the SU-8 thin layer is exposed to the irradiation of femtosecond lasers, an SU-8 core is generated on a glass substrate after baking and developing. In this section, we mix SU-8-2 and SU-8-2075 with a ratio of 8:3, spin-coat the SU-8 with a spin speed of 1400 rpm, and expose SU-8 with a scan speed of 2 - 5 μm/s. As a result, the thickness of the core is about 7.00 μm, and the width of the SU-8 core is about 4.00 - 5.00 μm. A PDMS layer is bonded on the glass substrate via oxygen plasma treatment. A small air gap is formed between the PDMS and the glass as shown in Fig. 4-3(a) - (b). The RIs of the PDMS, SU-8, glass, and air are 1.410, 1.573, 1.510, and 1.000, respectively. The glass substrate is cut into small pieces with a glass cutter. As shown in Fig. 4-3(c), the cross section of the glass substrate is quite smooth, so that a special polishing treatment is not needed. The distribution of the time average of the energy density at wavelength of 1550 nm is simulated using COMSOL software (Fig. 4-4). In this simulation, the size of the core is 4.00 μm×7.00 μm, sizes of the glass and PDMS are both 20.00 μm×10.00 μm, and length of the air gap is 16.00 μm. The simulation result shows that the effective RI for the fundamental mode is 1.560.

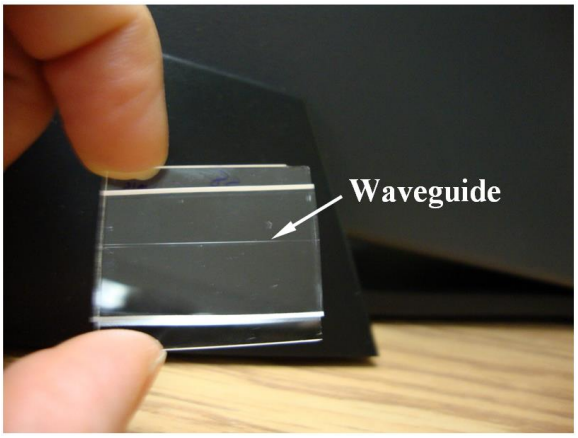

(a)

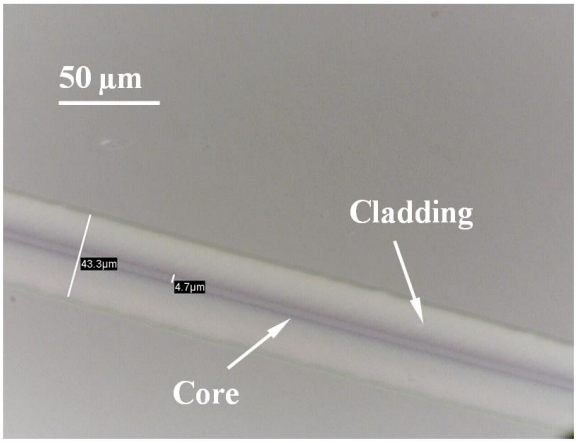

(b)

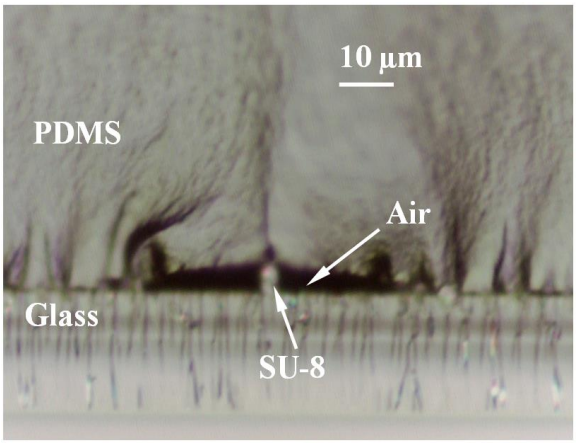

(c)

Figure 4-3 Optical waveguides with an SU-8 core and hybrid cladding: (a) a waveguide chip, (b) the top view of the waveguide, and (c) the cross section of the waveguide.

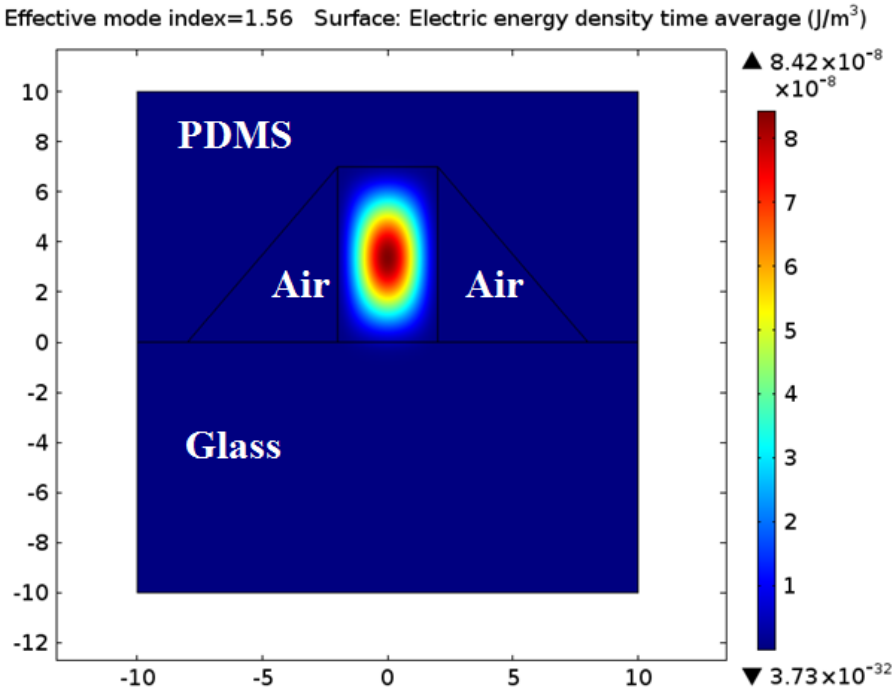

Figure 4-4 Simulation on the time average of the energy density for the fundamental mode at the wavelength of 1550 nm. The size of the core is 4.00 μm×7.00 μm, the sizes of the glass and PDMS are both 20.00 μm×10.00 μm, and length of the air gap is 16.00 μm.

The waveguide chip is placed on a platform, and an SMF couples light from an Er^{3+} dual-band broadband source (MPB Technologies EBS-7210) into the waveguide via a butt coupling method. A CCD camera with an objective lens (50×, 0.8 NA) is first used to collect the output light. Maximum output, which shows as a bright dot on the screen, is obtained by adjusting the *XYZ* motion stages below the fiber, illustrated in Fig. 4-5(a). Figure 4-5(b) shows a near field image on the cross section of a waveguide. The result agrees with the simulation. Then the CCD camera is replaced with another SMF which connects with a power meter on the other end. The maximum power shown on the power meter should be achieved by slowly adjusting the location of the SMF on the collecting side. Last, the power meter is replaced with the OSA.

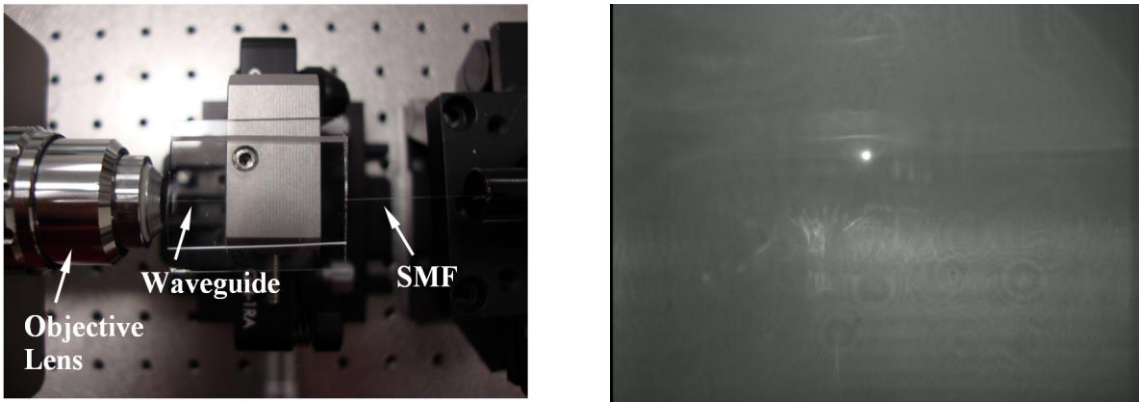

(a) (b)

Figure 4-5 Waveguide characterization: (a) an experimental setup for butt coupling, and (b) a near field image on the cross section of a MZI based waveguide

4.2.2 MZI characterization

For a Corning SMF28e, the core is a cylinder with a diameter of 9 μm for its cross section. In contrast, the core of an SU-8 waveguide is a rectangle with a cross section of 5.00 μm × 7.00 μm (width × height). Therefore, when an SMF is carefully adjusted to the location between the SU-8 layer and glass layer, as shown in Fig. 4-6(a), most of the light is simultaneously coupled into the core and the glass layer, whereas very little light is scattered into the PDMS layer. Interference occurs at the other side of the waveguide when the transmitted light is collected by another SMF. Figure 4-6(b) shows a near field image on the cross section of an MZI chip. The bright dot is the output from the waveguide, the bright background comes from the transmitted light of the glass substrate, and the dark background originates from the PDMS layer.

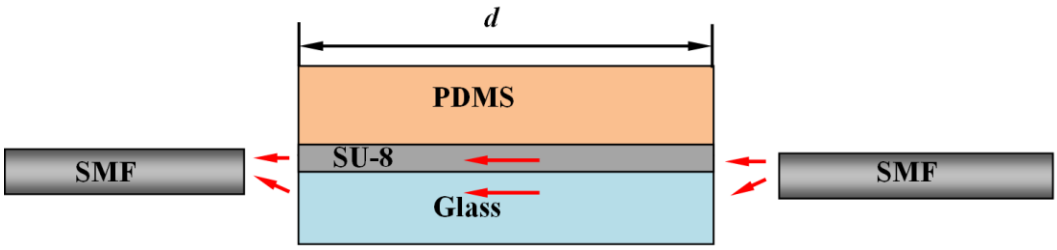

(a)

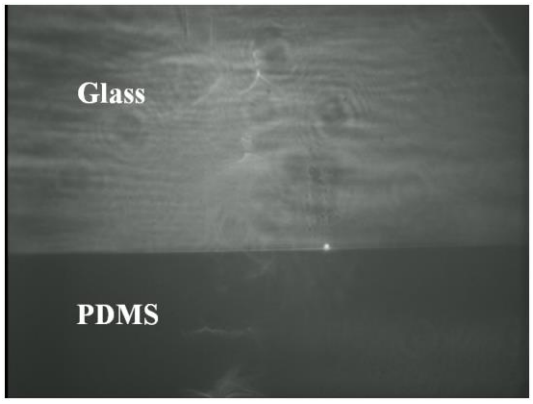

(b)

Figure 4-6 MZI characterization: (a) a schematic illustration of the MZI chip, and (b) a near field image of the cross section of an MZI chip

Therefore, the phase difference is

$$\delta\varphi = \frac{2\pi(n_{SU-8} - n_{Glass})d}{\lambda} \tag{4.3}$$

where $n_{\text{SU-8}}$ is the effective RI of the SU-8 core ($n_{\text{SU-8}}$=1.560), n_{Glass} is the RI of the glass (n_{Glass}=1.510), and d is the length of the chip. As shown in Eqn. (4.3), the phase difference relates to the length of the chip. Figure 4-7 shows the transmission spectra of MZI chips with different chip lengths. More interference fringes are shown in the spectrum for the chip of 46.50 mm in length. The reason is that the chip with a longer

length results in a larger phase difference, and thus generates a shorter interference periodicity.

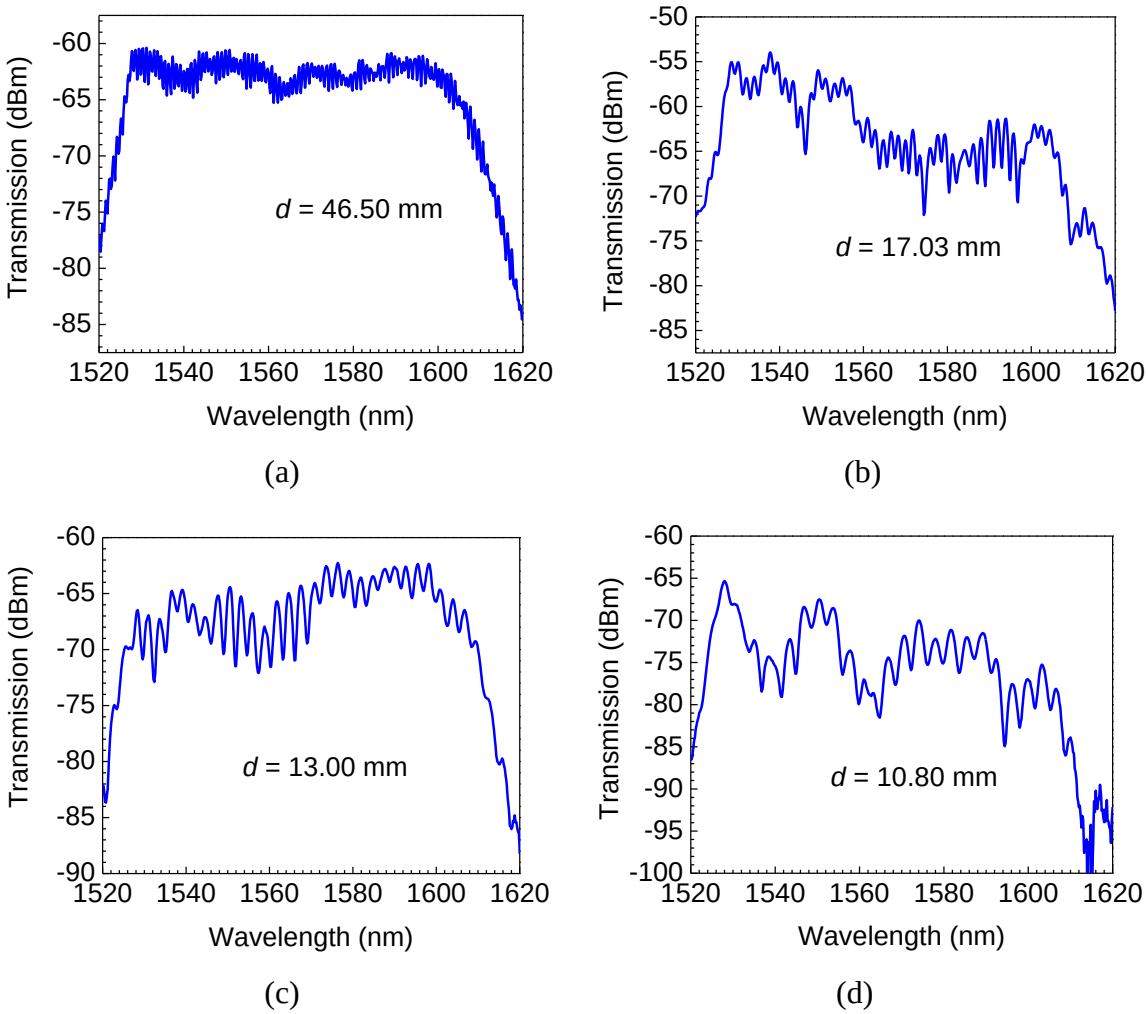

Figure 4-7 Transmission spectra of MZI chips with different chip lengths

4.2.3 Mach-Zehnder Interferometer-based refractive index sensor

An RI sensor is produced by attaching a PDMS layer with a microchannel on top of the SU-8 core (Fig. 4-8(a)). Liquids with different RI values can be injected into the microchannel. As a result, the SU-8 core in the microchannel has different effective RIs

depending on the liquid claddings. Figure 4-8(b) shows the photo of an MZI sensor chip. Table 4-1 shows the effective RIs of the cores with sizes of 4.00 μm×7.00 μm and 3.00 μm ×4.18 μm surrounded by NaCl solutions with different concentrations, which are calculated by the COMSOL software. A smaller core has a lower effective RI value, and the effective RI of the core increases with the increase of the liquid RI.

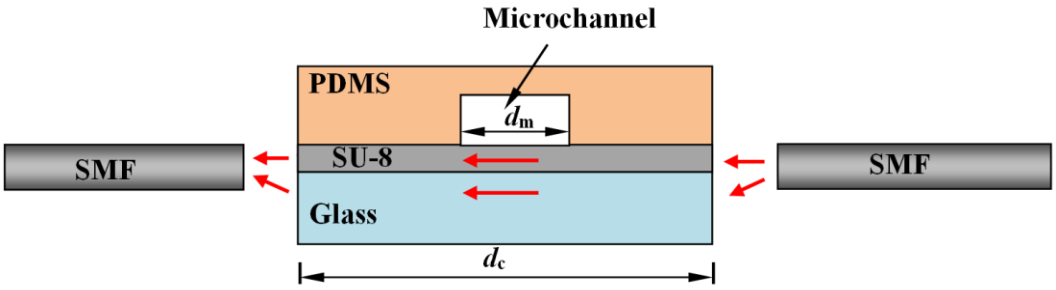

(a)

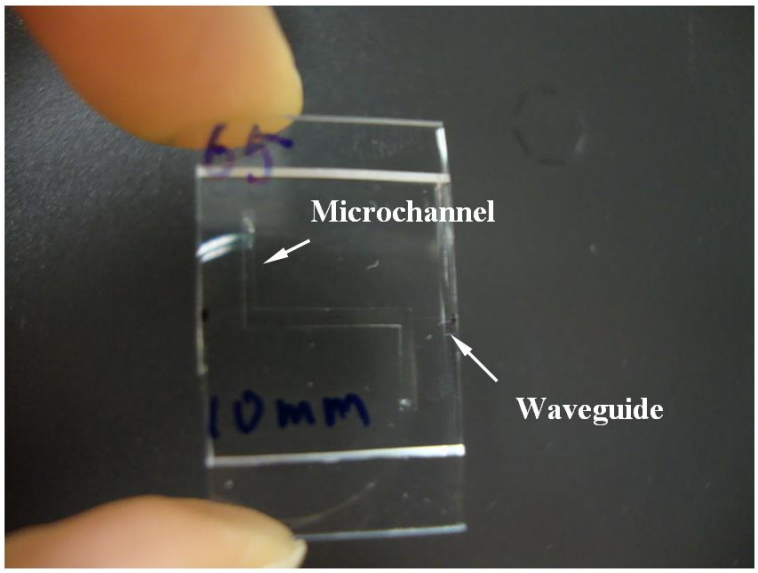

(b)

Figure 4-8 MZI sensor: (a) a schematic illustration of an MZI sensor, and (b) an MZI sensor chip

Table 4-1 Effective refractive indices of NaCl solutions with different concentrations

NaCl solution concentration (wt%)	Air	Distilled water	4.0%	6.8%	9.8%
RI of salt solution [91]	1.000	1.333	1.340	1.345	1.350
Effective RI of core (4.00 ×7.00 μm^2)	1.559823	1.560726	1.560763	1.560791	1.560819
Effective RI of core (3.00×4.18 μm^2)	1.548132	1.550289	1.550375	1.550439	1.550505
NaCl solution concentration (wt%)	12.5%	15.0%	18.0%	21.0%	24.0%
Salt solution RI	1.355	1.359	1.365	1.370	1.376
Effective RI of core (4.00×7.00 μm^2)	1.560848	1.560872	1.560909	1.560941	1.560981
Effective RI of core (3.00×4.18 μm^2)	1.550572	1.550628	1.550714	1.550789	1.550881

The phase difference between the SU-8 core and glass can be expressed as:

$$\delta\varphi = 2\pi \frac{n_{eff} d_m + n_{effair}(d_c - d_m) - n_{Glass} d_c}{\lambda} \tag{4.4}$$

where n_{eff} is the effective RI of the core in the microchannel, n_{effair} is the effective RI of the core outside of the microchannel, d_m is the length of the microchannel, and d_c is the length of the chip. When the phase difference satisfies the condition:

$$\delta\varphi = 2m\pi \tag{4.5}$$

where m is the order of the MZI resonance mode, the attenuation peak wavelength λ_m can be expressed as:

$$\lambda_m = \frac{n_{eff} d_m + n_{effair}(d_c - d_m) - n_{Glass} d_c}{m} \tag{4.6}$$

The peak shifts can be described as:

$$\begin{aligned} \delta\lambda_{m,n} &= \lambda_{m,n'} - \lambda_{m,n} \\ &= \frac{n'_{eff} d_m + n_{effair}(d_c - d_m) - n_{Glass} d_c}{m} - \frac{n_{eff} d_m + n_{effair}(d_c - d_m) - n_{Glass} d_c}{m} \\ &= \frac{(n'_{eff} - n_{eff}) d_m}{m} = \frac{\delta n_{eff,n} d_m}{m} \end{aligned} \tag{4.7}$$

where $\delta n_{eff,n} = n'_{eff} - n_{eff}$.

An MZI sensor chip with a chip length of 14.97 mm, core size of 4.00 μm ×7.00 μm, and the microchannel length of 4.00 mm is fabricated. The sensing results are shown in Fig. 4-9. The simulation on the transmission spectra in Fig. 4-9(a) is carried out using MATLAB software according to Eqns. (4.1), (4.4) and (4.7). The experimental results in Fig. 4-9 (b) are obtained by infusing different salt solutions into the microchannel. The transmission spectrum is recorded and the peak shift is measured in turn. The peak moves toward the longer wavelength side with the increase of the liquid RI. The comparison of the experimental and simulation results on the dependence of the peak shift on RI is shown in Fig. 4-9(c). Distilled water (n = 1.333) is used as the reference solution ($\delta\lambda$ = 0) for these measurements. The experimental sensitivity (slope) is 45.7 ± 1.7 nm/RIU, and the simulation on the sensitivity is 43.6 nm/RIU. The experimental result agrees with the simulation result very well.

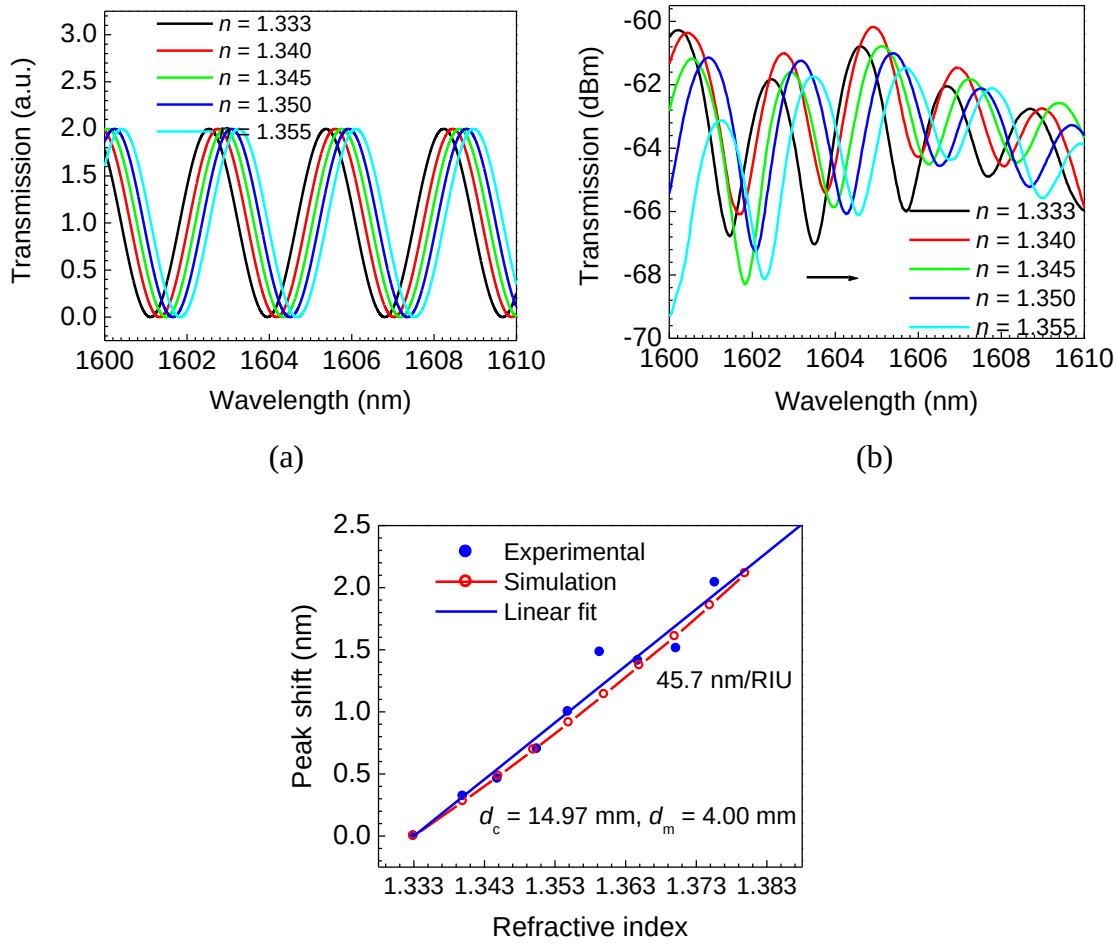

Figure 4-9 RI sensing measurement of an MZI chip with a chip length of 14.97 mm and microchannel length of 4.00 mm: (a) simulation on the transmission spectra of the MZI sensor in solutions of different RIs, (b) experimental measured transmission spectra of the MZI sensor in solutions of different RIs, and (c) comparison of the experimental and simulation results on the dependence of the peak shift on RI. The simulation is carried out using MATLAB software according to Eqns. (4.1), (4.4) and (4.7).

As shown in Eqn. (4.7), the phase shift depends on the order of the resonance mode and length of the microchannel. Therefore, the sensitivity varies depending on the chip length and microchannel length. Figure 4-10 describes the peak shifts in the MZI chips with the same microchannel length (6.00 mm), core size (4.00 μm ×7.00 μm), and

different chip lengths. The sensitivity is 94.0 nm/RIU in the chip with a chip length of 11.78 mm, and decreases to 35.5 nm/RIU in the chip with a chip length of 20.71 nm. Figure 4-11 presents the peak shifts in the MZI chips with the same chip length (about 15.00 mm), core size (4.00 μm ×7.00 μm), and different microchannel lengths. The sensitivity is 26.0 nm/RIU in the chip with a microchannel length of 2.00 mm, and increases to 96.8 nm/RIU in the chip with a microchannel length of 8.00 mm. Both simulations are carried out using MATLAB software according to Eqn (4.7), and distilled water (n = 1.333) is used as the reference solution ($\delta\lambda$ = 0) for above measurements.

According to the simulation in Table 4-1, the core with a smaller size has a smaller effective RI in the same environment. Therefore, different sizes of core are fabricated by adjusting the spin rate of the spin-coater and the scan speed of the femtosecond laser. Cores with the sizes of 4.85 μm×5.55 μm, 4.00 μm×5.55 μm, 3.35 μm×5.19 μm, and 3.00 μm×4.18 μm are achieved. Figures 4-12(a) and (b) present the transmission spectra of MZIs with core sizes of 4.00 μm×5.55 μm and 3.00 μm×4.18 μm, respectively. The periodicities are 1.26 and 1.40 nm, respectively. The smaller core has a wider interference pattern due to the fact that the smaller core has a smaller effective RI than the larger core if they are made of the same material. The sensitivities of MZIs with different core sizes are measured. As shown in Fig. 4-12(c), the sensitivity of MZI increases from 32.5 to 122.4 nm/RIU when the core size drops from 4.85 μm×5.55 μm to 3.00 μm×4.18 μm. MZI with a smaller core is much sensitive to changes in the environment. Distilled water (n = 1.333) is used as the reference solution ($\delta\lambda$ = 0) for these measurements.

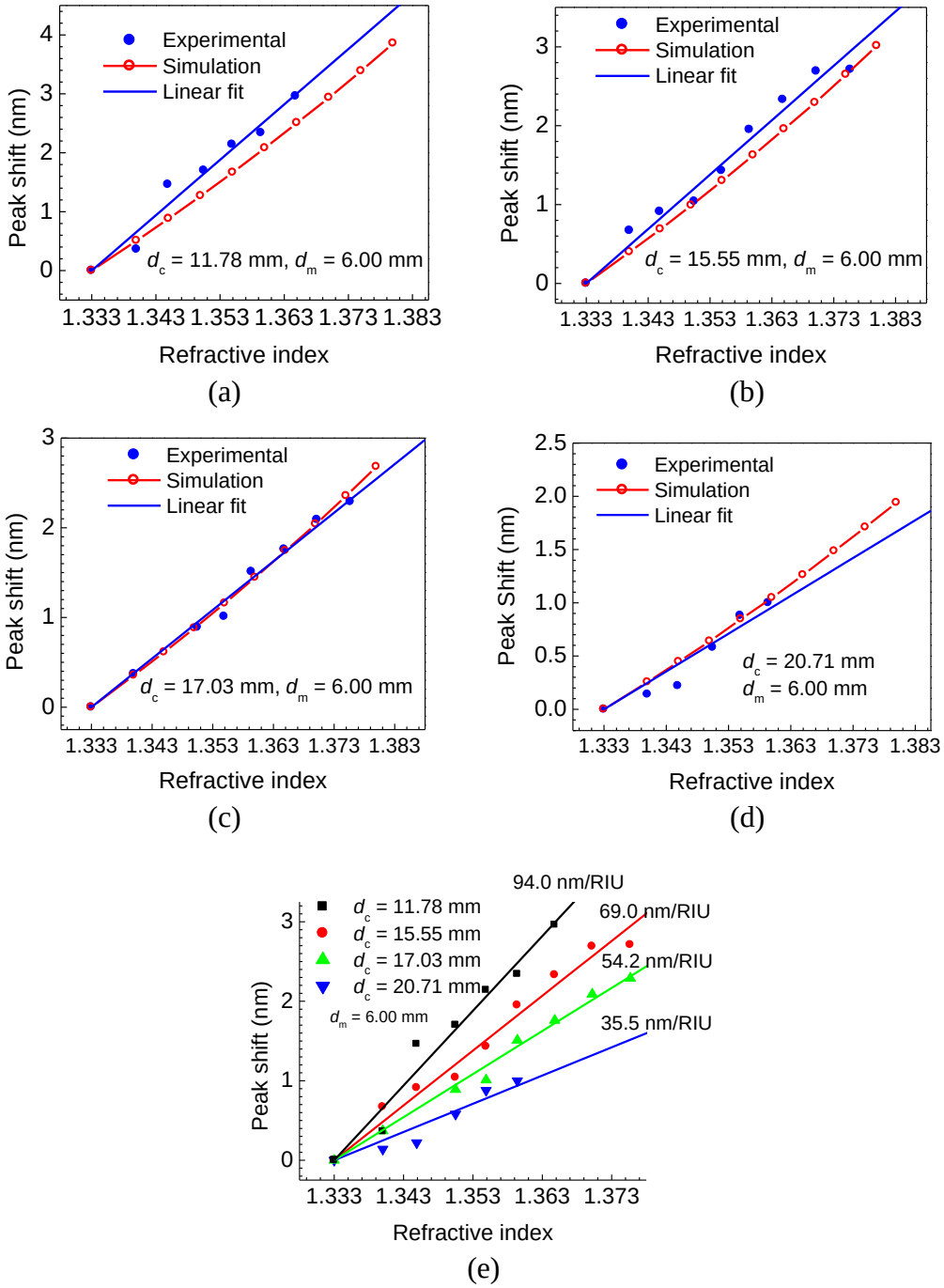

Figure 4-10 Effect of chip length on RI sensing: (a)-(d) comparison of MZI peak shifts between the experimental data and simulation, and (e) comparison of MZI peak shifts with the same microchannel length and different lengths of chips. The simulation is carried out using MATLAB software according to Eqn (4.7). The length of microchannels is 6.00 mm. The lengths of the chips are 11.78, 15.55, 17.03, and 20.71 mm, respectively.

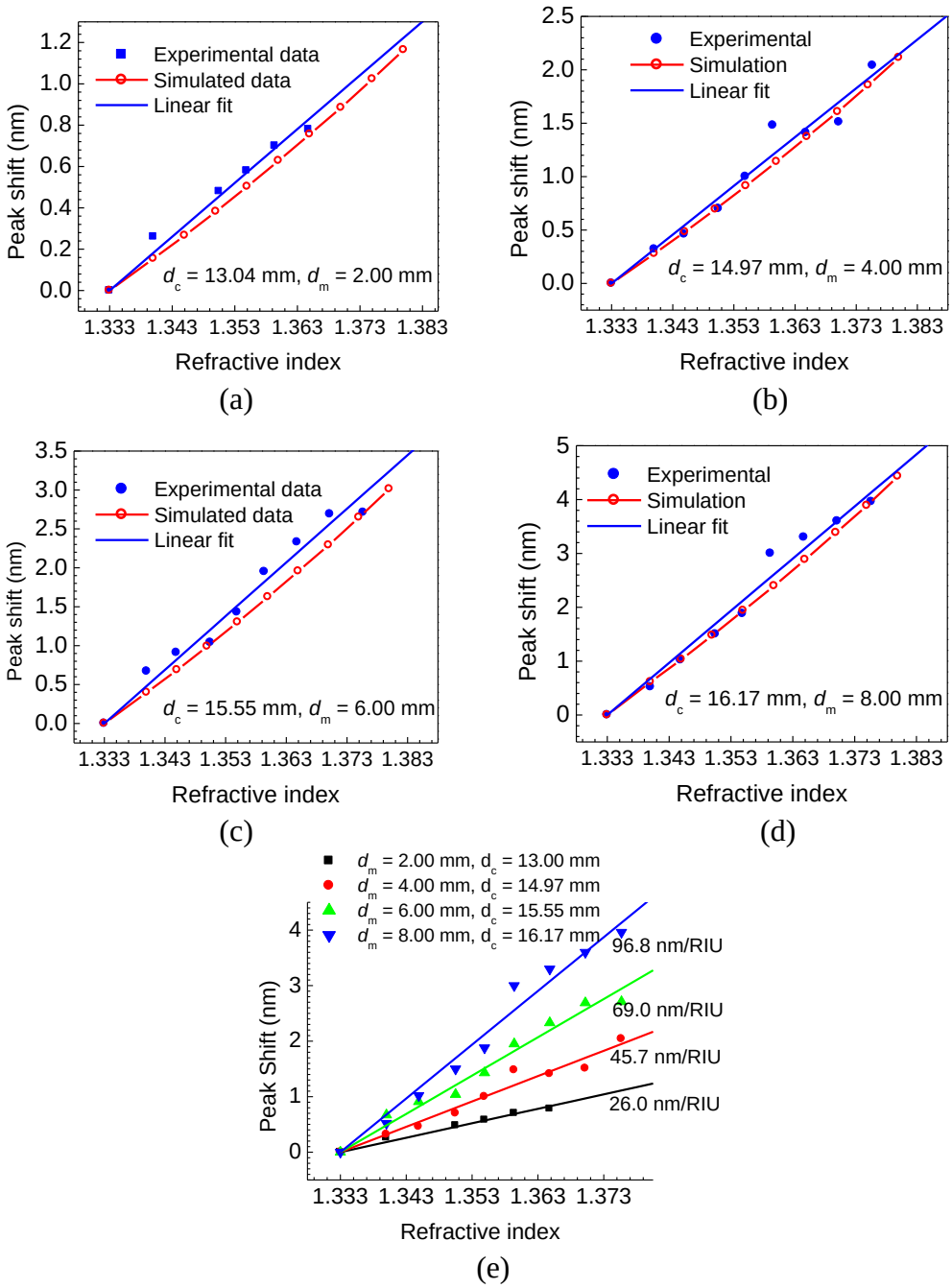

Figure 4-11 Effect of microchannel length on RI sensing: (a)-(d) comparison of MZI peak shifts between the experimental data and simulation, and (e) comparison of MZI peak shifts with the same length of chips and different lengths of microchannels. The simulation is carried out using MATLAB software according to Eqn (4.7). The length of chips is about 15.00 mm. The microchannel lengths are 2.00, 4.00, 6.00, and 8.00 mm, respectively.

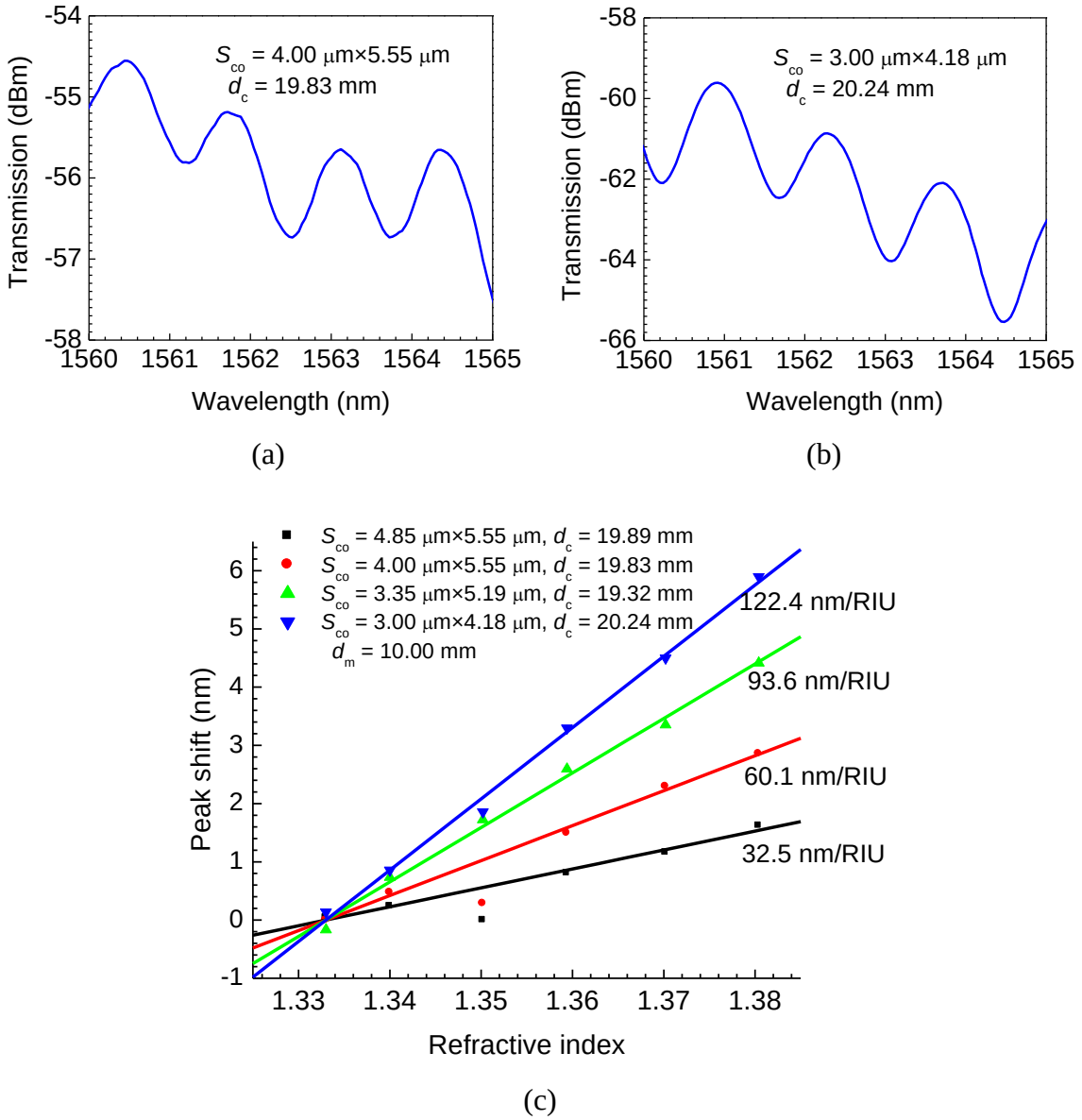

Figure 4-12 Effect of core size on RI sensing: (a) and (b) transmission spectra of MZIs with different core sizes, and (c) dependence of the peak shift on RI

In conclusion, we have successfully designed and fabricated opto-microfluidic MZI sensors based on a waveguide with hybrid cladding. This type of sensor can be used to measure the RI of any liquid below 1.573 (RI of SU-8 at 1550 nm). The experimental results nicely agree with the simulation based on Eqn (4.7). In addition, investigation on

the influence of the sensitivities of the opto-microfluidic MZI sensors demonstrates that an MZI sensor with a shorter chip length, longer microchannel and smaller core size can achieve a higher sensitivity which is better for sensor applications.

4.3 Waveguides with solid cladding

4.3.1 Waveguide characterization

SU-8, SU-8-2000 and SU-8-3000 series are members of photoresist material SU-8 family from Microchem. Figure 4-13 shows the RIs of photoresists at different wavelengths according to the data sheet listed on the website of the manufacturer. The SU-8 series has the highest RI (n = 1.575 at 1550 nm), and the SU-8-2000 and SU-8-3000 series have the lower RIs. In each SU-8 series, SU-8 photoresists with different viscosities can be selected to obtain the desired film thickness. Therefore, in this section, we use SU-8-2 of SU-8 series and SU-8-3050 of SU-8-3000 series for the core and cladding materials, respectivitly. The core is first fabricated on the glass substrate by femtosecond laser exposure, baking and development. Then SU-8-3050 is spin-coated on the chip with a spin rate of 3000 rpm for 120 s. The SU-8-3050 is baked on a hotplate at 50 ^{o}C for 12 hours. The thickness of the SU-8-3050 layer is about 20.00 μm. In order to obtain a thinner cladding thickness, a mixture of SU-8-3050 and SU-8-2 with the volume ratio of 2:1 is also used as the cladding material. In the following experiments, if the cladding thicknesses are less than 20.00 μm, it means that the cladding is the mixture of SU-8-3050 and SU-8-2.

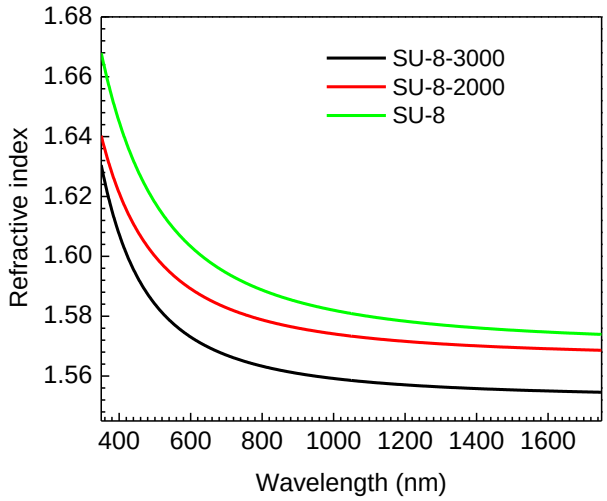

Figure 4-13 Refractive indices of different SU-8 series

The cladding is aligned with a slot mask fabricated by a femtosecond laser (1 kHz, 0.3 mJ, 800 nm and 67 fs) and exposed to a mercury lamp for 25 s. After the chip is baked and developed, a waveguide structure is left on the glass substrate. A PDMS layer is bonded on the glass substrate via oxygen plasma treatment. Finally, the glass substrate is cut into small pieces with a glass cutter. Figure 4-14(a) and (b) illustrate a waveguide chip and the top-view of the waveguide, respectively. The width of the cladding is 300.00 μm. The thin line in the middle of the cladding is the core. Figure 4-14(c) is the morphology of the cross section of the chip. The thickness of the cladding is about 20.00 μm.

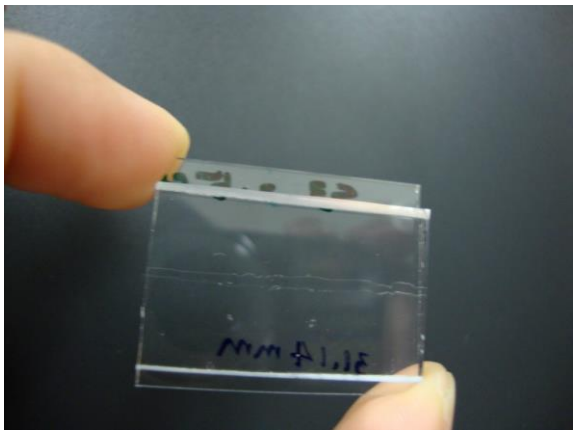

(a)

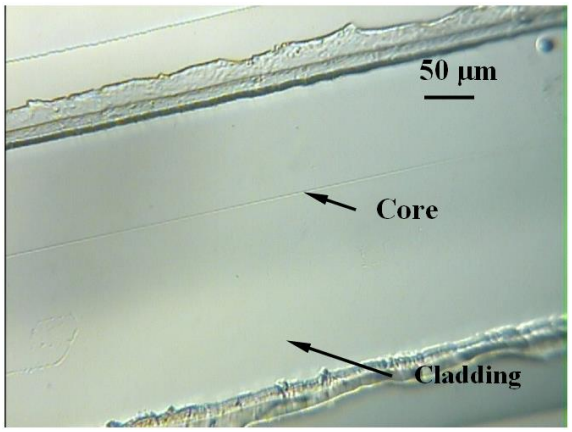

(b)

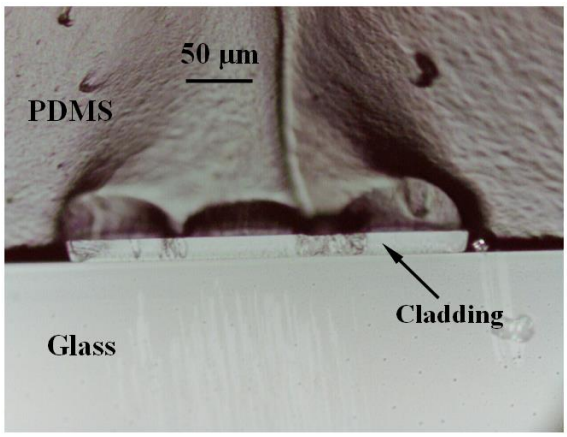

(c)

Figure 4-14 Waveguide with an SU-8 core and cladding: (a) a waveguide chip, (b) the top view of the waveguide, and (c) the cross section of the chip

4.3.2 MZI characterization

Similar to the MZI structure shown in the section 4.2, an SMF couples light from an Er^{3+} dual-band broadband source into the waveguide via the butt coupling method, shown in Fig. 4-15(a). Split beams pass through the core and the cladding, respectively. Interference occurs at the other side of the waveguide when the transmitted light is coupled into another SMF. Figure 4-15(b) presents a near field image on the cross section of the MZI chip. The rectangular-shaped white line comes from the beam passing through the cladding, and the bright dot in the middle of the white line comes from the beam passing through the core.

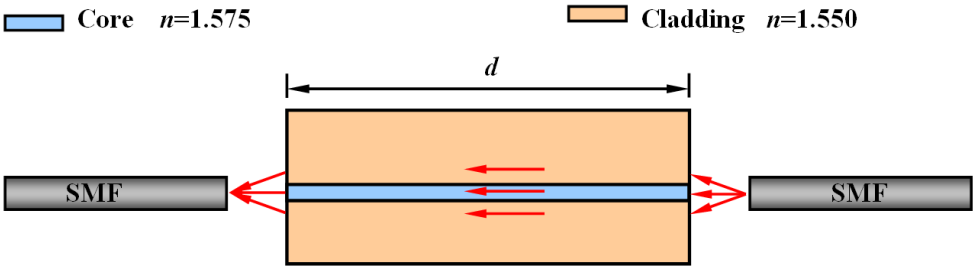

(a)

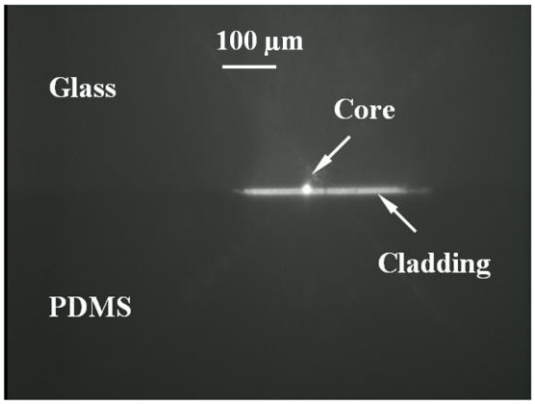

(b)

Figure 4-15 MZI characterization: (a) a schematic illustration of a MZI structure, and (b) a near field image on the cross section of a MZI chip

The phase difference can be expressed as:

$$\delta\varphi = \frac{2\pi(n_{eff-co} - n_{eff-cl})d}{\lambda} = \frac{2\pi\Delta n_{eff}\, d}{\lambda} \tag{4.8}$$

$$I = I_1 + I_2 + 2\sqrt{I_1 I_2}\cos(\delta\varphi) \tag{4.9}$$

where $n_{eff\text{-}co}$ is the effective RI of the core, $n_{eff\text{-}cl}$ is the effective RI of the cladding, Δn_{eff} is the RI difference between the core and cladding, and d is the length of the chip. As Eqn. (4.8) shows, the phase difference depends on the length of the chip. Figure 4-16 shows the transmission spectra of MZI chips with different chip lengths. A chip with a longer length induces a larger phase difference, and thus generates a shorter interference periodicity. This result is similar to the results obtained in section 4.2.

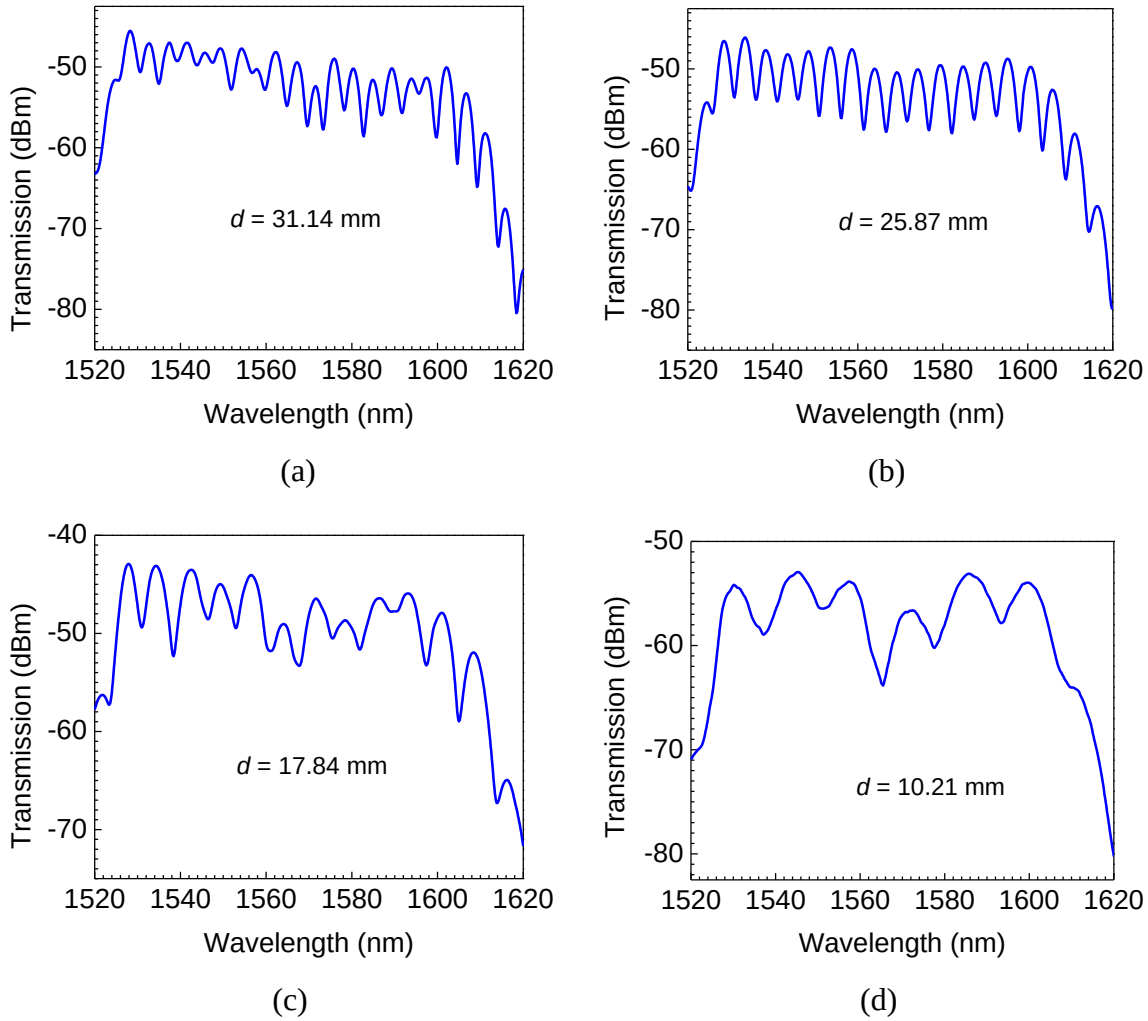

Figure 4-16 Transmission spectra of MZIs with different chip lengths

4.3.3 MZI-based refractive index sensor

When the phase difference satisfies the condition:

$$\delta\varphi = 2m\pi \tag{4.10}$$

where m is the order of the MZI resonance mode, the peak wavelength λ_m can be expressed as:

$$\lambda_m = \frac{\Delta n_{eff} d}{m} \tag{4.11}$$

An RI sensor can be fabricated by attaching a PDMS layer with a microchannel on the top of an SU-8 waveguide (Fig. 4-17). Liquids with different RIs can be injected into the microchannel. As a result, the effective RI of the cladding changes depending on the liquids, whereas the effective RI of the SU-8 core is hardly affected by the liquid. Therefore, Eqn. (4.11) can be shown as:

$$\delta\lambda_{m,n} = \lambda_{m,n'} - \lambda_{m,n} = \frac{(\Delta n_{eff,n} d + \delta n_{eff,n} L)}{m} - \frac{\Delta n_{eff,n} d}{m} = \frac{\delta n_{eff,n} L}{m} = \frac{\delta n_{eff,n} \lambda_{m,n}}{\Delta n_{eff,n}} \frac{L}{d} \tag{4.12}$$

where $\delta n_{eff,n} = n'_{eff} - n_{eff}$, n_{eff} is the effective RI of the cladding, d is the length of the chip, and L is the length of the microchannel.

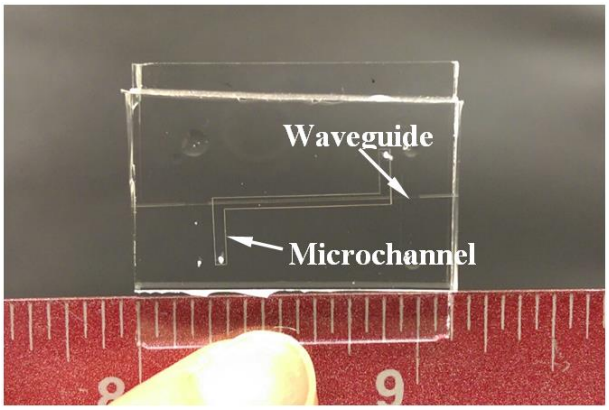

Figure 4-17 MZI chip for RI sensing

Figure 4-18(a) shows the transmission spectra of an MZI chip with a core size of 4.00 μm×6.50 μm×20.03 mm (width × height × length), cladding size of 300.00 μm ×10.00 μm ×20.03 mm and microchannel length of 16.00 mm in different liquid

environment. A blue shift occurs with the decrease of liquid RI. Figure 4-18(b) exhibits the dependence of the peak shift on RI. The sensitivity is -119.6±6.8 nm/RIU.

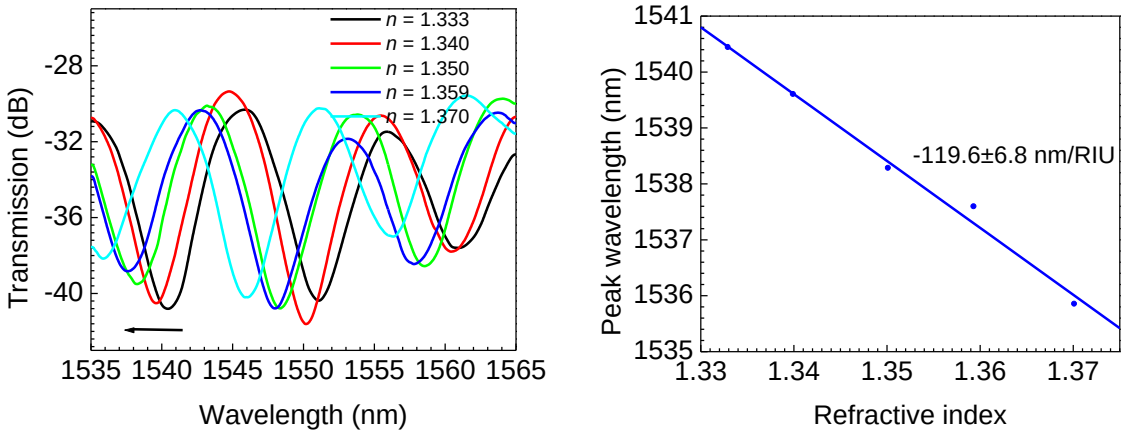

(a) (b)

Figure 4-18 RI sensing measurement of an MZI chip with a core size of 4.00 μm ×6.50 μm ×20.03 mm, cladding size of 300.00 μm ×10.00 μm ×20.03 mm, and microchannel length of 16.00 mm: (a) transmission spectra of MZI in different liquid environments, and (b) dependence of the peak shift on RI.

4.3.3.1 Effect of cladding thickness

Waveguides with different cladding thicknesses are fabricated on the glass substrates. The cladding thickness is controlled by adjusting the spin speed of the spin-coater. As shown in Eqn. (4.12), the peak shift relates to the effective RI difference of the cladding $\delta n_{eff,n}$. Figure 4-19(a) simulates the effective RI of the cladding with the cladding thickness of 10.00 – 20.00 μm. The effective cladding RI increases with the increase of the cladding thickness. Therefore, the MZI with a thicker cladding has a larger phase difference and a smaller intensity periodicity than the thinner cladding has. The result is demonstrated by Fig. 4-19(b). For the waveguide with a cladding thickness of 10.00 μm, the periodicity is 11.68 nm which decreases to 7.19 nm for the waveguide with a cladding thickness of

18.50 μm. Figure 4-19(c) simulates the effective cladding RIs with the cladding thickness of 10.00 μm and 20.00 μm in different solutions. The cladding with the thickness of 10.00 μm is more sensitive to the changes of the solution. The experimental results in Fig. 4-19(d) prove that the chip with a thinner cladding has a higher sensitivity. All chips have the same core size of 4.00 μm × 6.50 μm, cladding width of 300.00 μm, and chip length of 22.80 mm. Distilled water (n = 1.333) is used as the reference solution ($\delta\lambda$ = 0) for these measurements.

4.3.3.2 Effect of chip length

Two groups of MZIs with cladding thicknesses of 18.50 and 10.00 μm, and a cladding width of 300.00 μm are measured. The chip lengths are 32.00, 28.00, 22.00, and 20.00 mm, respectively, in each group. The microchannel length is 16.00 mm, and the cross section of the core is about 4.00 μm ×6.50 μm. The experimental results are shown in Fig. 4-20. If the microchannel length is the same, the sensitivity increases with the decrease of the chip length. In addition, the finding that an MZI chip with a thinner cladding possesses a higher sensitivity than the MZI chip with a thicker cladding at the same chip length is demonstrated again.

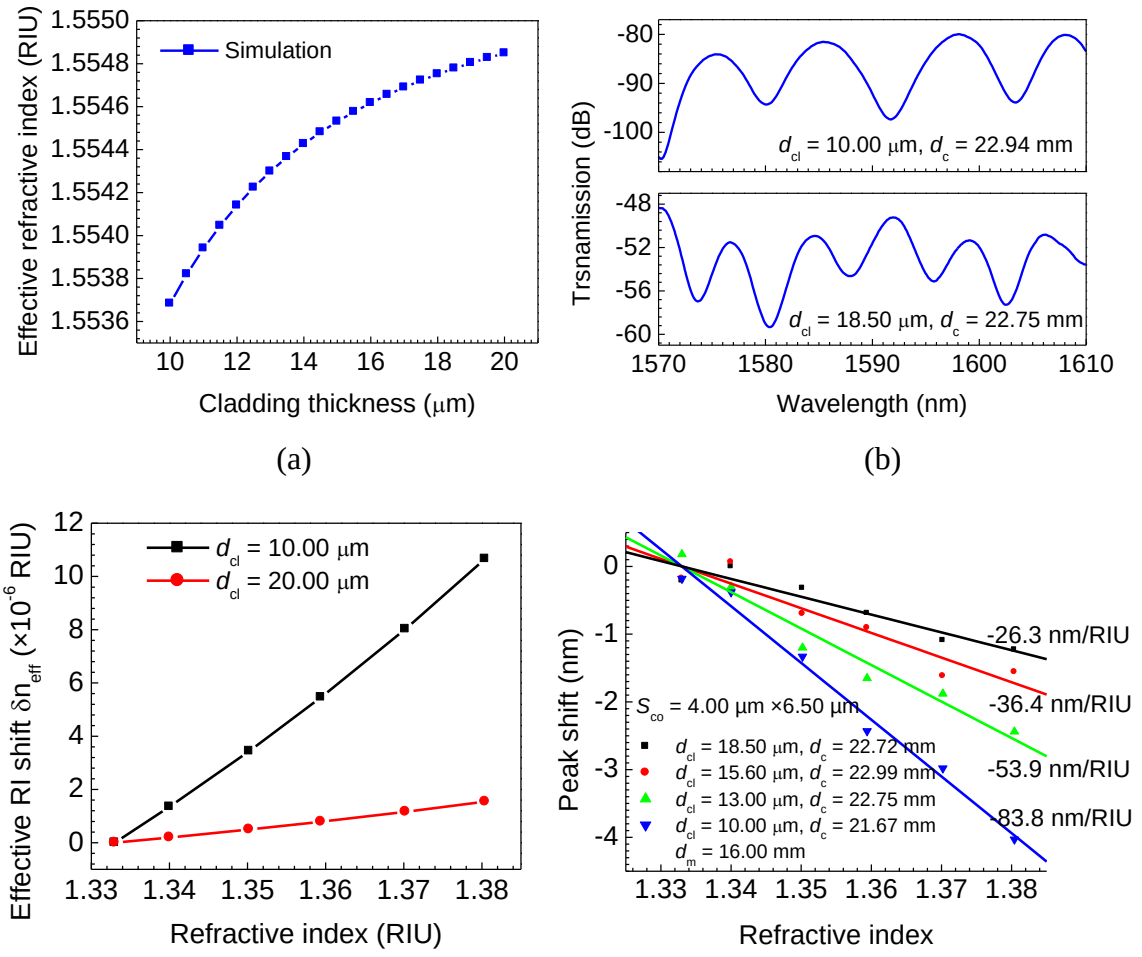

Figure 4-19 Effect of cladding thickness on RI sensing: (a) simulation on the effective RIs of the cladding with different cladding thicknesses, (b) transmission spectra of MZIs with the cladding thickness of 18.50 and 10.00 μm, respectively, (c) simulation on the effective cladding RIs with the cladding thickness of 10.00 μm and 20.00 μm in different solutions, and (d) dependence of the peak shift on RI. The width of the cladding is 300.00 μm.

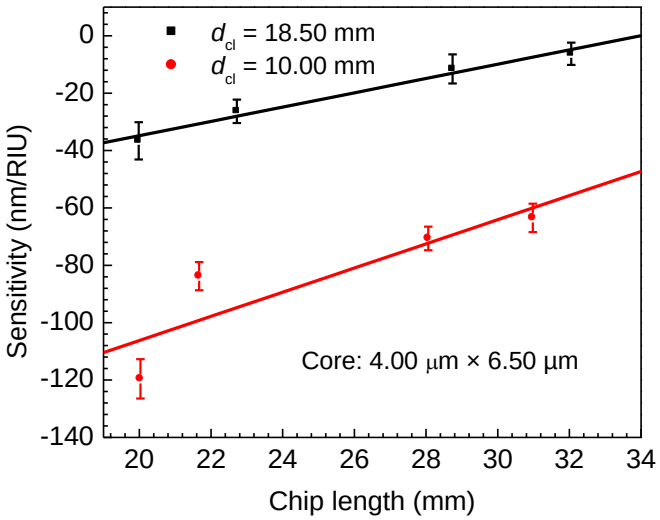

Figure 4-20 Dependence of the sensitivity on chip length. The core size is 4.00 μm×6.50 μm. The black squares show the sensitivities of MZIs with the cladding size of 300.00 μm×18.50 μm. The red dots show the sensitivities of MZIs with the cladding size of 300.00 μm ×10.00 μm. The microchannel length is 16.00 mm.

4.3.3.3 Effect on the core size

In this section, different core sizes of MZI are produced by adjusting the scan speed of the femtosecond laser. The sizes of the core are 5.00 μm ×5.50 μm×22.66 mm, 4.00 μm×5.50 μm×22.38 mm, 3.20 μm×5.50 μm×22.45 mm, and 2.80 μm×5.50 μm×22.92 mm, respectively. The cross section of the cladding, which is made of mixed SU-8-3050, is 125.00 μm×11.50 μm. Figure 4-21(a) simulates the effective RI of a core with a core width of 2.80 – 5.00 μm. The effective RI increases with the increase of the core width. Therefore, according to the simulation, the MZI chip with a larger core has a larger phase difference and a smaller intensity periodicity. As shown in Fig. 4-21(b) and (c), the intensity periodicities are 11.12 and 12.62 nm for the MZIs with the core sizes of 5.00 μm×5.50 μm and 2.80 μm×5.50 μm, respectively. Dependence of the peak shift on RI is

shown in Fig. 4-21(d). Distilled water (n = 1.333) is used as the reference solution ($\delta\lambda$ = 0) for these measurements. The sensitivity slightly increases with the decrease of the core size. The sensitivities in this group are larger than the values in Fig. 4-20 due to the fact that the width of the cladding has been reduced from 300.00 to 125.00 μm.

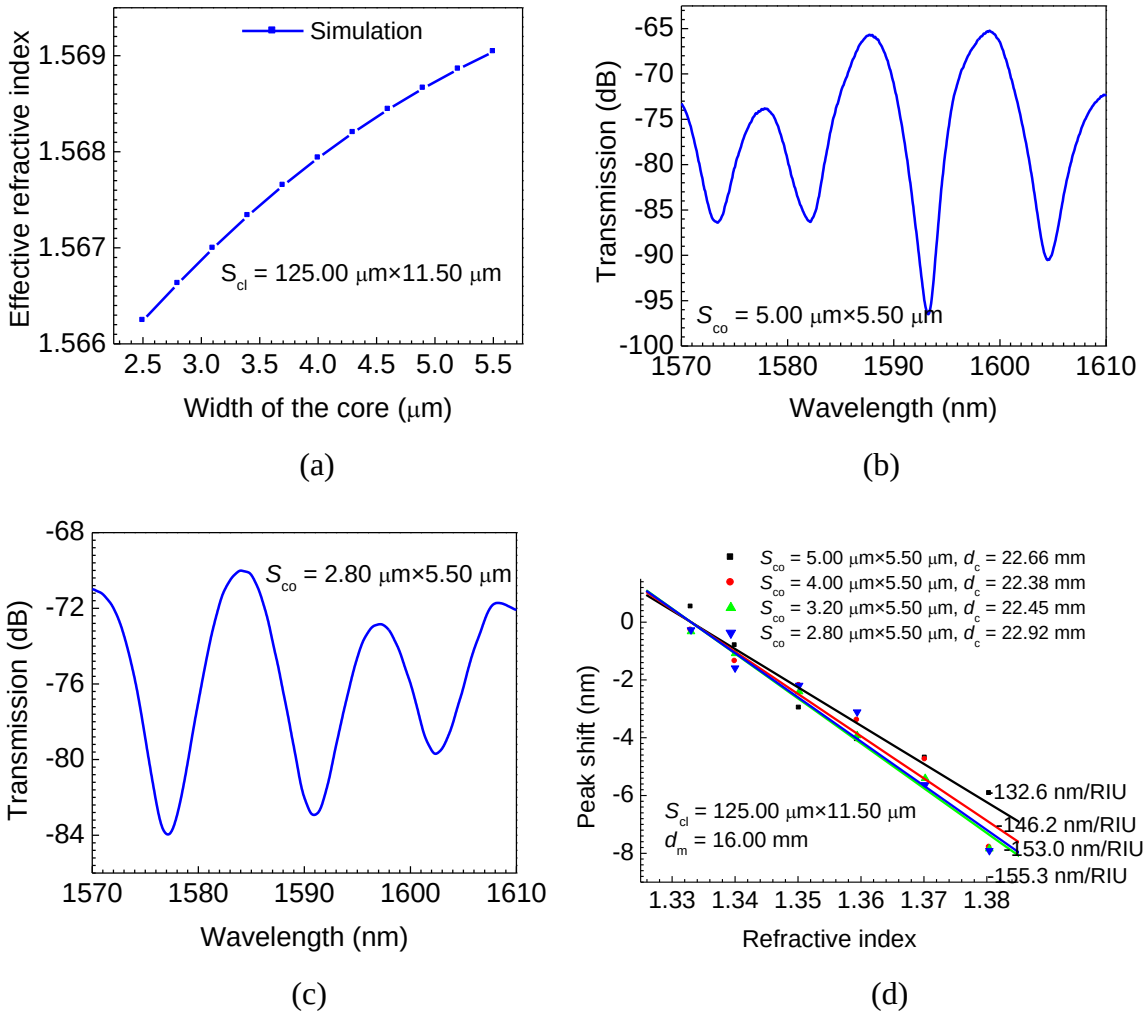

Figure 4-21 Effect of core size on RI sensing: (a) simulation on the effective RIs of the core in different core widths and same core height of 5.50 μm, (b) and (c) transmission spectra of MZIs with different sizes of core, and (d) dependence of the peak shift on RI. All MZI chips have a cladding cross section of 125.00 μm× 11.50 μm and microchannel length of 16.00 mm.

4.3.4 Mach-Zehnder Interferometer-based temperature sensor

If the environmental temperature of the waveguide rises, both the effective RIs of the cladding mode and core mode change. If the change is different ($\delta n_{eff,T}$), the attenuation peak wavelength shift $\delta\lambda_{m,T}$ is:

$$\delta\lambda_{m,T} = \lambda_{m,T'} - \lambda_{m,T} = \frac{(\Delta n_{eff,T} + \delta n_{eff,T})d}{m} - \frac{\Delta n_{eff,T} d}{m} = \frac{\delta n_{eff,T} d}{m} \tag{4.13}$$

where $$\delta n_{eff,T} = (\frac{dn}{dT}_{core} - \frac{dn}{dT}_{cladding})\Delta T$$

dn/dT is the thermo-optic coefficient of the material, $\Delta T = T' - T$, and $\Delta n_{eff,T}$ is the RI difference of core and cladding at the starting temperature *T*.

Therefore, the shift in the peak wavelength can be expressed as:

$$\delta\lambda_{m,T} = \frac{(\frac{dn}{dT}_{core} - \frac{dn}{dT}_{cladding})d}{m}\Delta T = \frac{(\frac{dn}{dT}_{core} - \frac{dn}{dT}_{cladding})\lambda_{m,T}}{\Delta n_{eff,T}}\Delta T \tag{4.14}$$

A mini hotplate is attached to the bottom of the chip and installed on the platform. The microchannel is empty (air). The chip is heated from 19.2 ^{o}C to 73.2 ^{o}C with a step of 2 ^{o}C. At each step, the transmission spectrum is recorded when the chip reaches the thermodynamic equilibrium. Figure 4-22(a) exhibits the transmission spectra of an attenuation valley at different temperatures. The core size is 4.00 μm ×5.50 μm ×22.88 mm, which is made of SU-8-2, the cladding size is 125.00 μm ×10.00 μm ×22.88 mm, which is made of a mixture of SU-8-3050 and SU-8-2 with a volume ratio of 2:1, and the microchannel length is 16.00 mm. It can be observed that the valley shifts towards the

longer wavelength region with the increasing temperature. SU-8 material has a high negative thermo-optic coefficient of about -1.86×10^{-4} K^{-1} [103]. This result means that the cladding is more sensitive to the temperature change than the core. The sensitivity of the valley is analyzed using a linear fit, and a good linear function is exhibited as 0.465±0.006 nm/^{o}C.

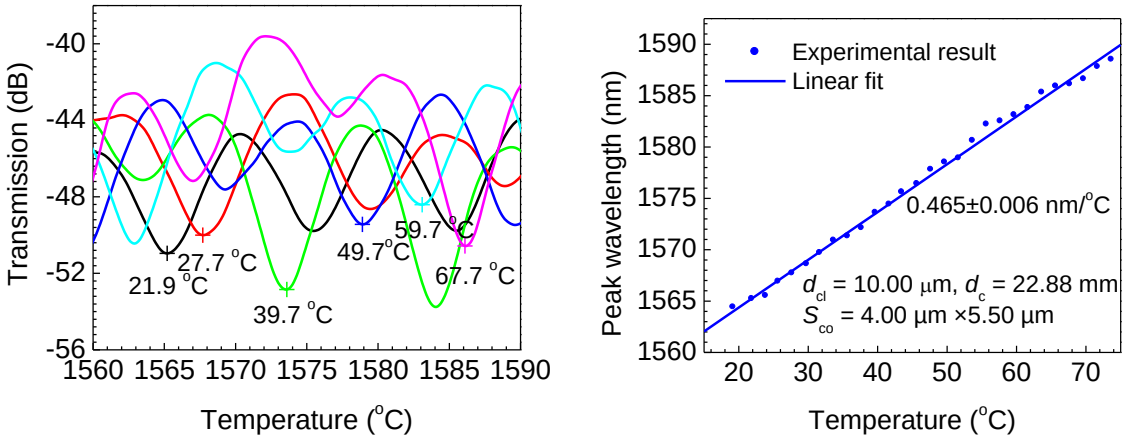

(a) (b)

Figure 4-22 Temperature sensing measurement of an MZI chip with a core size of 4.00 μm ×5.50 μm ×22.88 mm, cladding size of 125.00 μm ×10.00 μm ×22.88 mm, and microchannel length of 16.00 mm: (a) transmission spectra of MZI in different temperatures, and (b) dependence of the peak shift on temperature.

According to Eqn. (4.14), the temperature sensitivity relates to the thermo-optic coefficient difference, RI difference of core and cladding, and wavelength except chip length. Four chips with the same cladding size of 300.00 μm×10.00 μm and core size of 4.00 μm ×6.50 μm are investigated. Their lengths are 20.30, 22.94, 28.00 and 30.98 mm, respectively. Distilled water is infused into the microchannel. Figure 4-23(a) presents the dependence of the peak shift on temperature at different chip lengths. 24.7 ^{o}C is used as the reference temperature ($\delta\lambda$ = 0) for these measurements. The sensitivity of the MZI

chip with a length of 30.98 mm is 0.459 nm/^{o}C, and becomes 0.471 nm/^{o}C when the chip length is 20.30 mm. The sensitivity is almost unchanged as shown in Fig. 4-23(b). The small discrepancy is caused by the difference of the peak wavelength λ.

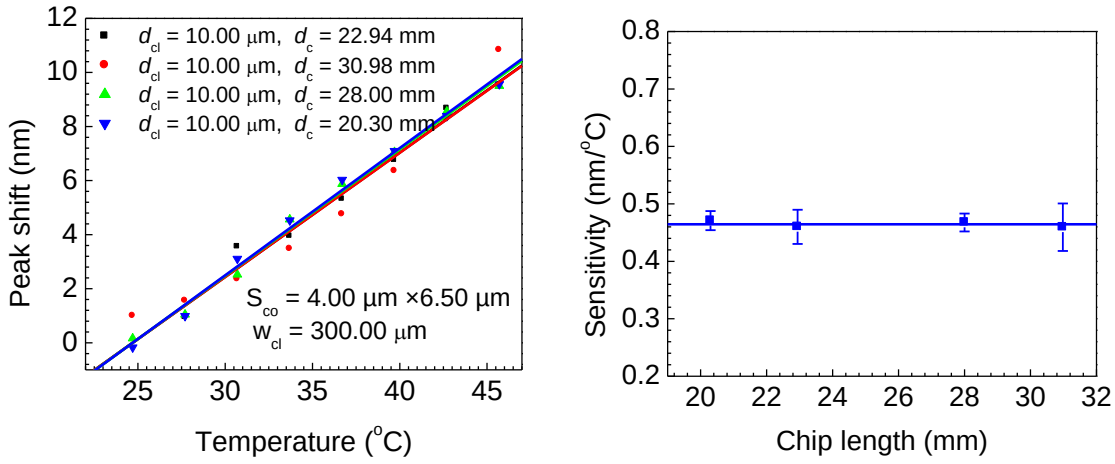

(a) (b)

Figure 4-23 Effect of chip length on temperature sensing: (a) dependence of the peak shift on temperature for chips of different length, and (b) dependence of the sensitivities on chip length

Taking the thermo-optic coefficient of the mixed SU-8 material as -1.86×10^{-4} K^{-1}, the effective RIs of cladding at different temperatures have been calculated with COMSOL software, which are shown in Fig. 4-24(a) for claddings with thicknesses of 10.00 μm and 20.00 μm. The thicker cladding has a higher effective RI and a larger effective thermo-optic coefficient than the thinner one. Therefore, according to the simulation, the MZI chip with a thicker cladding should have a higher sensitivity. The experimental results for the effects of cladding thickness are shown in Fig. 4-24(b), in which the chips have a core size of 2.80 μm ×3.60 μm, cladding width of 125.00 μm, and the cladding thicknesses of 10.07, 11.31, 17.65, and 21.84 μm, respectively. Distilled

water is infused into the microchannel. 21.7 ^{o}C is used as the reference temperature ($\delta\lambda$ = 0) for these measurements. The sensitivity of MZI with a thickness of 10.07 μm is 0.837 nm/^{o}C, which increases to 0.950 nm/^{o}C when the thickness is increased to 21.84 μm. The sensitivity increases with the increase of the cladding thickness, which agrees with the simulation.

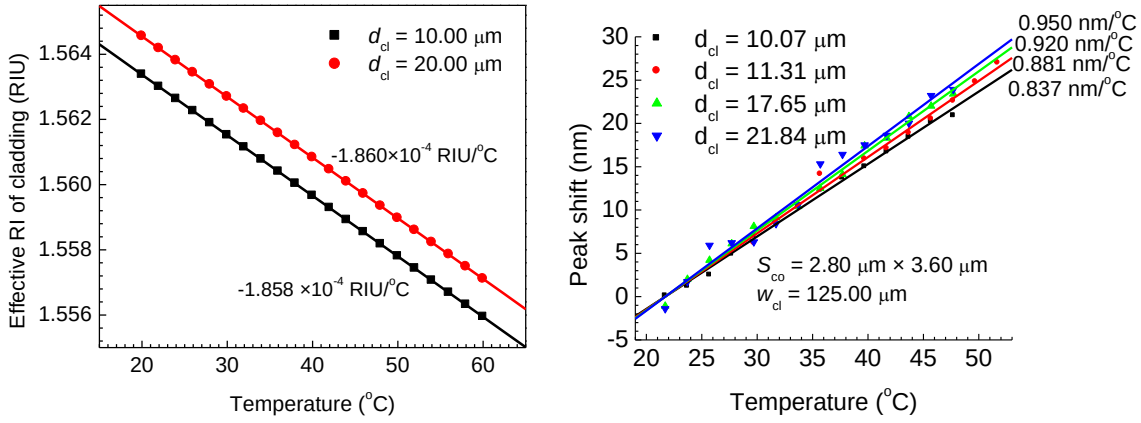

(a) (b)

Figure 4-24 Effect of cladding thickness on temperature sensing: (a) COMSOL simulation on the effective RIs of the cladding at different temperatures, and (b) dependence of the peak shift on temperature at different cladding thicknesses. The core sizes are 2.80 μm ×3.60 μm, the width of the cladding is 125.00 μm.

Taking the thermo-optic coefficient of the SU-8-2 material as -1.86×10^{-4} K^{-1}, the effective RIs of the core at different temperatures have been calculated with COMSOL software, which are shown in Fig. 4-25(a) for cores with the sizes of 5.00 μm×5.50 μm and 2.80 μm × 5.50 μm. The cladding is set to be 125.00 μm×11.50 μm. A smaller core has a lower effective RI and a larger effective thermo-optic coefficient than a bigger one. In the experiments, MZI chips with the cores of 5.00 μm×5.50 μm×22.66 mm, 4.00 μm×5.50 μm×22.38 mm, 3.20 μm×5.50 μm×22.45 mm, and 2.80 μm×5.50 μm×22.92

mm are fabricated. The size of cladding, made of mixed SU-8-3050 and SU-8-2 with a volume ratio of 2:1, is 125.00 μm×11.50 μm. Distilled water is infused into the microchannel. The experimental results in Fig. 4-25(b) show that the sensitivity of MZI with a core size of 5.00 μm×5.50 μm is 0.414 nm/^{o}C which increases to 0.849 nm/^{o}C when the core size decreases to 2.80 μm×5.50 μm. 24.7 ^{o}C is used as the reference temperature ($\delta\lambda$ = 0) for these measurements. The sensitivity increases with the decrease of the core size, which is manifested from the fact that the sensitivity increases from 0.460 nm/^{o}C in Figs. 4-22 and 4-23 to 0.900 nm/^{o}C in Fig. 4-24. According to the simulation, if the cladding and core have the same thermo-optic coefficient, the temperature sensitivity should increase with the increase of the core size. However, the experimental result is the opposite. Therefore, we conclude that the SU-8-3050 material must have a higher thermo-optic coefficient than SU-8-2 material has. This is reasonable due to the fact that SU-8-2 and SU-8-3050 are made with different solvents. Figure 4-26 shows the sensitivities of MZIs with the core sizes of 5.00 μm×6.50 μm×17.59 mm, 4.00 μm×6.50 μm×17.59 mm, and 3.20 μm×6.50 μm×17.59 mm, respectively. The size of cladding, which is made of SU-8-3050, is 300.00 μm×20.00 μm×17.59 mm. 24.7 ^{o}C is used as the reference temperature ($\delta\lambda$ = 0) for these measurements. In this situation, the sensitivities are almost independent of the core size and smaller than those in Fig. 4-24. Although the SU-8-3050 material has a higher thermo-optic coefficient, as concluded above, the lower RI of SU-8-3050 makes the higher Δn_{eff} dominate in Eqn. (4.14), and causes smaller sensitivities.

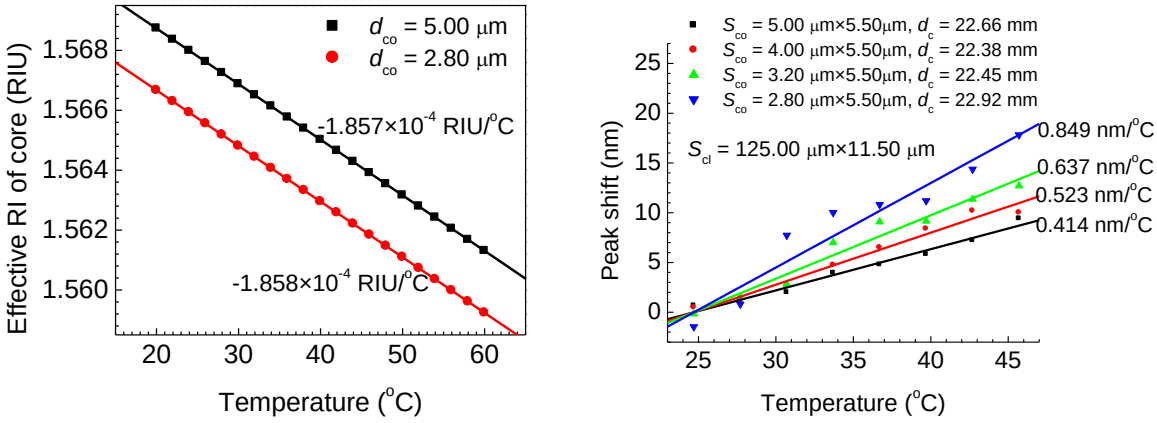

(a) (b)

Figure 4-25 Effect of core size on temperature sensing: (a) simulation on the effective RIs of the core with the cross sections of 5.00 μm×5.50 μm and 2.80 μm×5.50 μm in different temperatures, and (b) dependence of the peak shift on temperature for the MZI chips with different core sizes. The cross section of the cladding is 125.00 μm×11.50 μm.

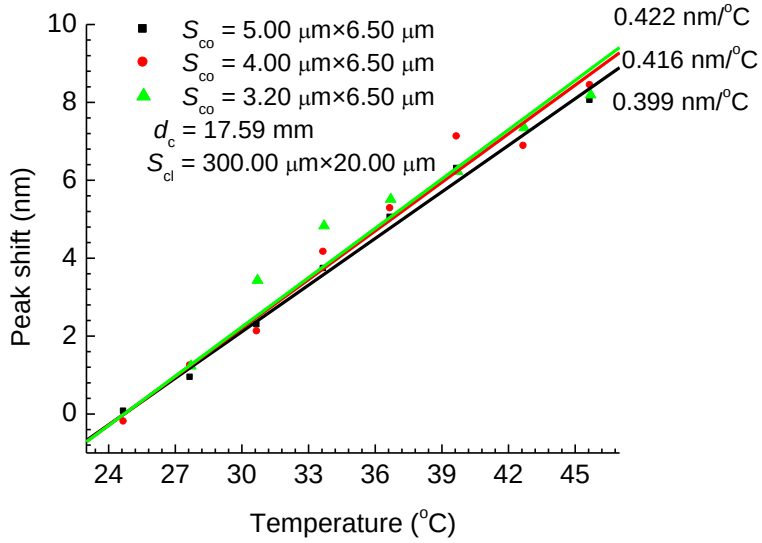

Figure 4-26 Dependence of the peak shift on temperature for MZIs with different core sizes. The cross section of the cladding is 300.00 μm×20.00 μm.

4.3.5 Refractive index calibration

As mentioned in the previous section, the interference fringes are affected by the RI of the solution as well as the temperature. Therefore, a disturbance of temperature will influence the accurate measurement of analytes. Figure 4-27 (a)-(d) presents the transmission spectra of a MZI chip with a chip length of 28.77 mm under different environmental conditions. The core is made of SU-8-2 with a cross section of 2.80 μm×3.85 μm, and the cladding is made of mixed SU-8-3050 and SU-8-2 with a volume ratio of 2:1. The cross section of the cladding is 125.00 μm×10.00 μm, and the size of the microchannel is 1.00 mm×75.00 μm×16.00 mm. The same interference order is selected for monitoring in this study. The valley wavelength is 1538.3 nm in distilled water at 25.7 ^{o}C, and shifts to 1549.9 nm at 39.7 ^{o}C (red shift). When an NaCl solution with an RI of 1.359 is infused into the microchannel, the valley wavelength shifts to 1547.6 nm at 39.7 ^{o}C. When an NaCl solution with an RI of 1.380 is infused into the microchannel, the valley wavelength shifts to 1530.4 nm at 21.7 ^{o}C. Figure 4-27(e) describes the dependence of the shift of the transmission peak wavelength on the RI and temperature for the same interference order. Distilled water (n = 1.333) and 21.7 ^{o}C are used as the reference solution and temperature ($\delta\lambda$ = 0) for these measurements, respectively. The sensitivity for temperature sensing is 0.837 nm/^{o}C, and the sensitivity for RI sensing is -83.0 nm/RIU. Figure 4-27(f) shows the peak shifts in response to RI and temperature changes. In order to measure the accurate RI of a solution, the peak shift caused by temperature disturbance must be considered. The total wavelength shift can be expressed as:

$$\Delta\lambda = 0.837\Delta T - 83.0\Delta n \tag{4.15}$$

where -83.0Δn is the peak shift caused by RI change, and 0.837ΔT is the peak shift caused by temperature change. If the temperature is known, the RI of liquid can be calibrated by this equation. The concentration can also be calibrated with the same method. Figure 4-28(a) presents the sensing measurement of the RI and temperature for the same chip in the sucrose solutions. Distilled water (C = 0 ^{o}Bx) and 21.7 ^{o}C are used as the reference solution and temperature ($\delta\lambda$ = 0) for these measurements, respectively. Figure 4-28(b) shows the peak shifts in response to RI and temperature changes. The wavelength shift can be expressed as:

$$\Delta\lambda = 0.837\Delta T - 0.146\Delta C \tag{4.16}$$

In conclusion, we have successfully designed and fabricated an opto-microfluidic MZI sensor based on a waveguide, in which SU-8-2 is used as the core material and SU-8-3050 or mixed SU-8-3050 is used as the cladding material. This sensor can be used to measure the environmental temperature and the RI of liquids below 1.575 (RI of SU-8). The RI sensitivity changes depending on the thickness of the cladding, length of chip, and size of core. The temperature sensitivity changes depending on the materials of the core and cladding, size of core, and cladding thickness. In addition, this type of MZI exhibits pronounced spectral interference fringes (larger extinction ratio) than the MZI in the last section due to the stronger transmission in the cladding.

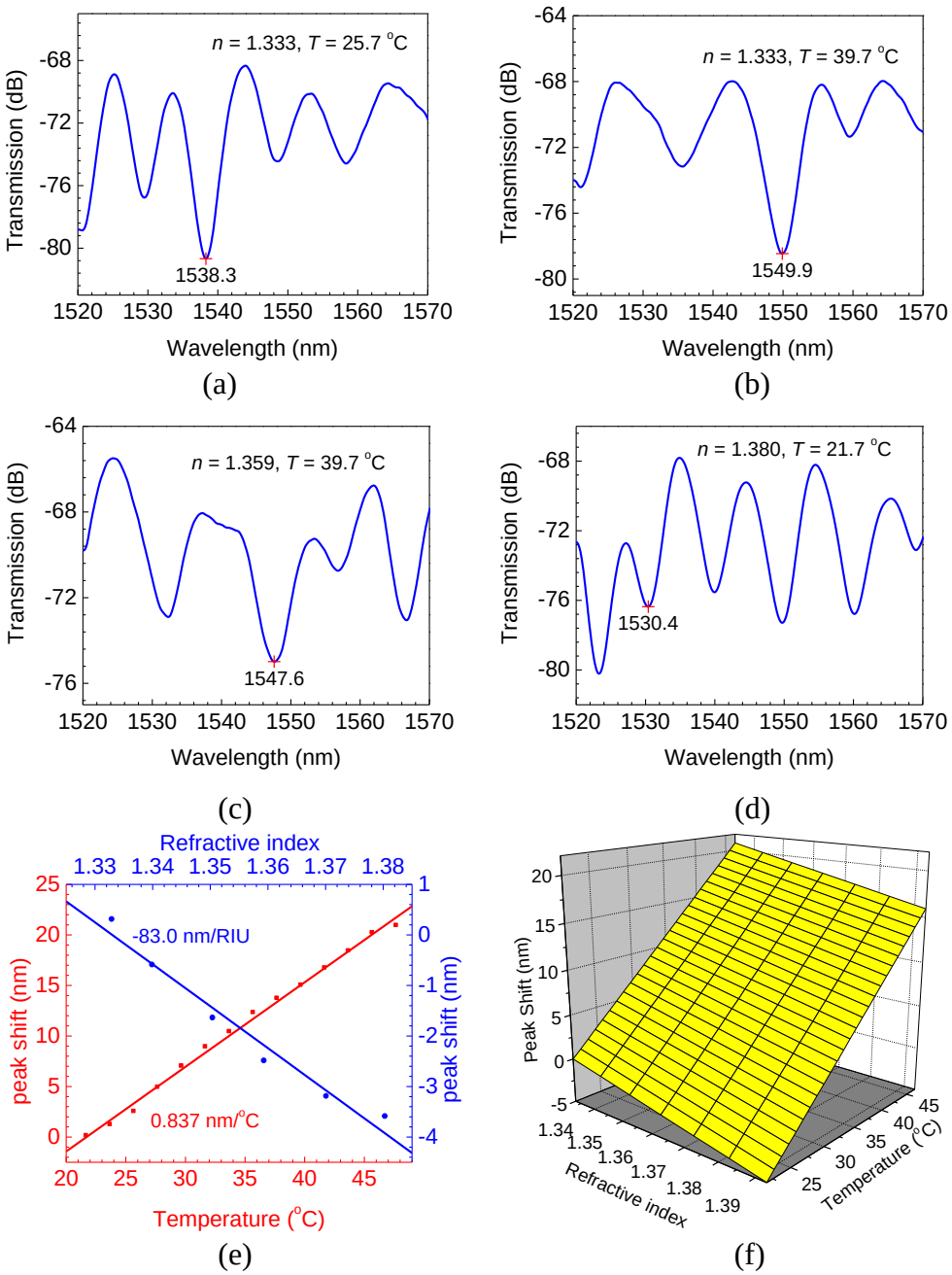

Figure 4-27 Sensing measurement of the RI and temperature for an MZI chip with the chip length of 28.77 mm, core cross section of 2.80 μm×3.85 μm, cladding cross section of 125.00 μm×10.00 μm, and microchannel size of 1.00 mm×75.00 μm×16.00 mm: (a)-(d) transmission spectra of the MZI under different environmental conditions, (e) dependence of the shift of the transmission peak wavelength on RI and temperature for the same interference order, and (f) peak shifts in response to RI and temperature changes.

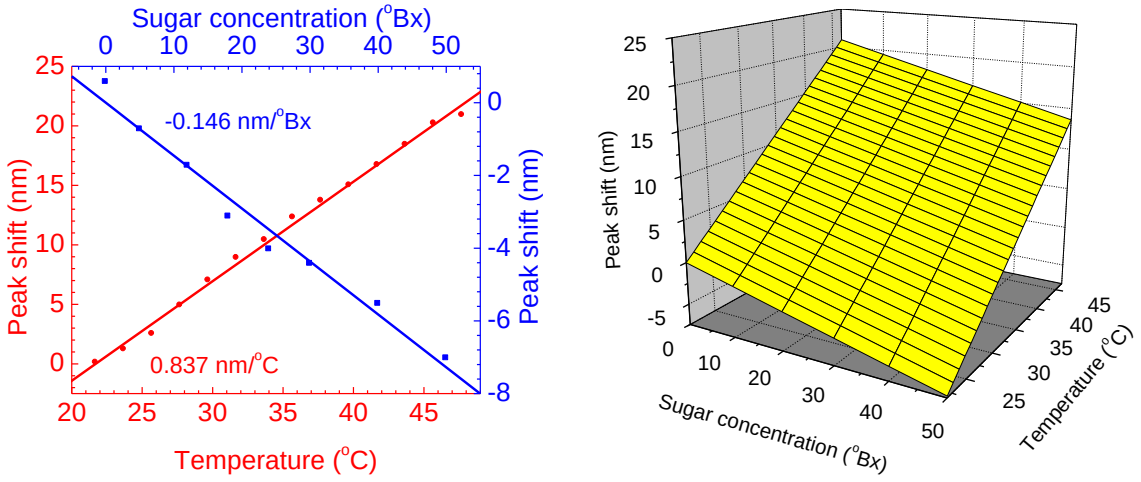

(a) (b)

Figure 4-28 Sensing measurement of the RI and temperature for an MZI chip with the chip length of 28.77 mm, core cross section of 2.80 μm×3.85 μm, cladding cross section of 125.00 μm×10.00 μm, and microchannel size of 1.00 mm×75.00 μm×16.00 mm: (a) dependence of the shift of the transmission peak wavelength on concentration and temperature for the same interference order, and (b) peak shifts in response to RI and temperature changes

4.4 Waveguide with cores of different sizes

4.4.1 MZI characterization

In this section, we use the same core and cladding as mentioned in the last section as the main components of MZI. However, the size of the core purposely changed by adjusting the scan speed or adopting multiple scans. Figure 4-29 depicts a schematic illustration for the MZI structure. Light is first coupled into a wide core by an SMF and propagated to a connector which is a core of much wider size to expand the light. Then the light is separated into three paths after it leaves the connector. One beam propagates along the core and two beams spread along the cladding. Interference occurs at the other side of the waveguide when the transmitted beams are coupled into another SMF. In order to prevent

the input light from coupling into the SU-8 cladding from the SMF, only a small part of the wide core is coved with the SU-8 cladding and most of the wide core is bald (air cladding).

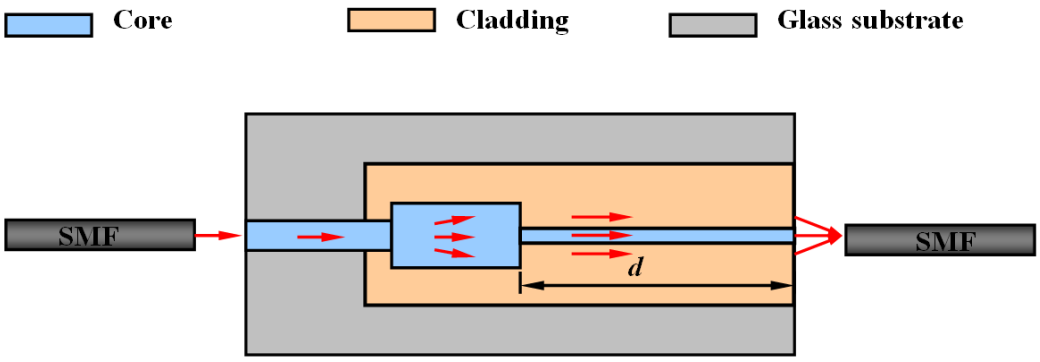

Figure 4-29 Schematic illustration of an MZI structure with a connector

Figure 4-30(a) is the morphology of a connector. The connector with a size of 300.00 μm× 20.00 μm× 6.50 μm (length × width × height) is fabricated by a multiple-scan, the wide core with a width of 6.20 μm is fabricated with a scan speed of 1 μm/s, and the thin core with a width of 4.00 μm is fabricated by a scan speed of 5 μm/s. Figure 4-30(b) is the COMSOL simulation on the light intensity distribution of this connector. It shows that the beam is expanded from 6.20 μm to 20.00 μm after it leaves the connector.

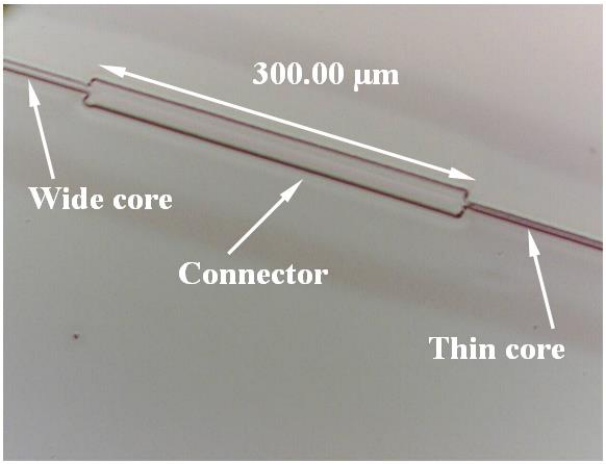

(a)

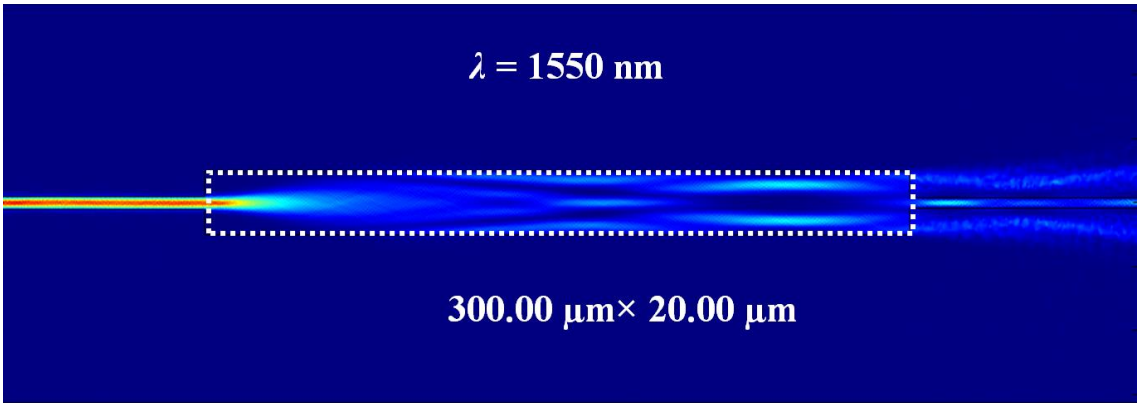

(b)

Figure 4-30 Connector chatacterization: (a) the morphology of a connector with the size of 300.00 μm× 20.00 μm× 6.50 μm, and (b) a COMSOL simulation on the light intensity distribution of the connector

The phase difference equations are the same with the Eqns. (4.5) and (4.6). Here, *d* is the length of the thin core (sensing arm). Figure 4-31 shows the transmission spectra of the MZI chips with different thin core lengths. All chips have a connector with a size of 300.00 μm× 30.00 μm× 5.50 μm, wide core with a width of 5.00 μm, thin core with a width of 3.20 μm, and cladding with a cross section of 300.00 μm×20.00 μm. The MZI

chip with a longer sensing arm induces a larger phase difference, and generates a shorter interference periodicity. This result is the same as those in section 4.2.2 and 4.3.2.

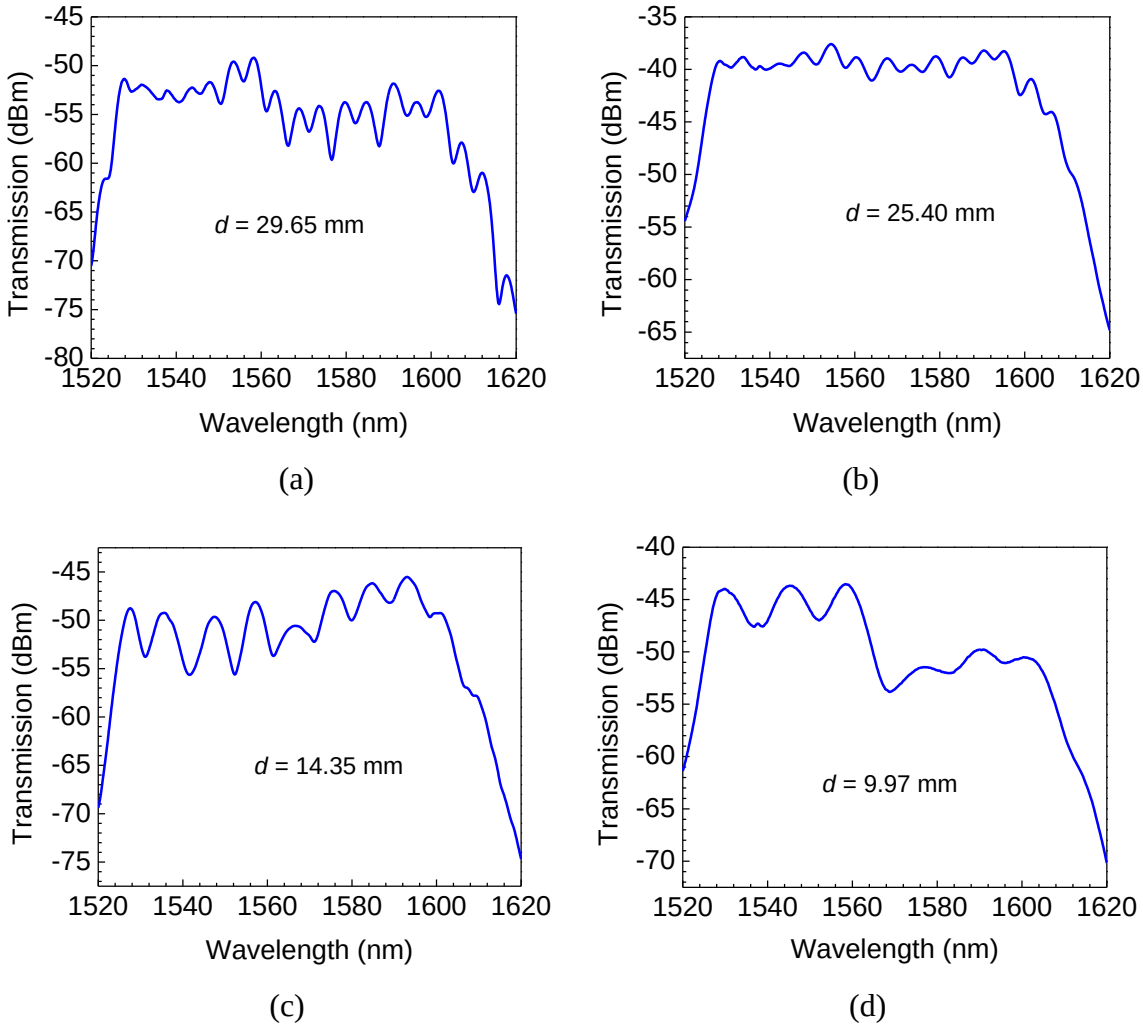

Figure 4-31 Transmission spectra of MZIs with different thin core lengths. All chips have a connector size of 300.00 μm× 30.00 μm× 5.50 μm, wide core with a width of 5.00 μm, thin core with a width of 3.20 μm, and cladding cross section of 300.00 μm×20.00 μm.

In this design, the MZI is an asymmetric structure. Figure 4-29 depicts a schematic illustration in which light is coupled into the waveguide from the wide core side to the thin core side. In fact, the light can also be coupled into the waveguide from the thin core

side to the wide core side. Figure 4-32 presents transmission spectra of an MZI chip when light is coupled from different directions. When the light is coupled from the thin core side, the transmission intensity is weaker than the intensity coupled from the wide core side due to the fact that more light is lost in the cladding in this situation. However, light coupling directions do not affect the phase difference of the MZI. As shown in Fig. 4-32, the two interference patterns are the same.

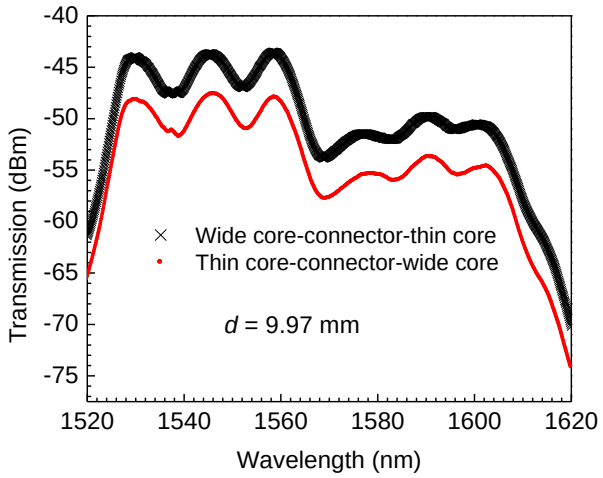

Figure 4-32 Transmission spectra of an MZI obtained from different coupling directions

4.4.2 Refractive index and temperature measurement

For many applications, RI and temperature measurement is extremely important, which is studied here. The RI and temperature sensing results are shown in Figs. 4-33 and 4-34. In Fig. 4-33, the core of the MZI chip is made by SU-8-2 with a thin core length of 18.33 mm, cross section of the wide core of 5.00 μm×5.50 μm, and cross section of the thin core of 3.20 μm×5.50 μm. The cladding is made of mixed SU-8-3050 and SU-8-2 with a volume ratio of 1:1 (n = 1.565 at 1550 nm) and a cross section of 125.00 μm×10.50 μm.

The size of the microchannel is 1.00 mm×75.00 μm×10.00 mm. The same interference order is selected for monitoring in this study. Figure 4-33(a) - (d) show that the peak wavelength is 1553.92 nm in distilled water at the temperature of 24.7 ^{o}C, which shifts to 1565.6 nm at 36.7 ^{o}C (red shift). When an NaCl solution with an RI of 1.359 is infused into the microchannel, the peak wavelength shifts to 1551.92 nm at 24.7 ^{o}C and 1562.8 nm at 36.7 ^{o}C (blue shift). Figure 4-33(e) describes the dependence of the shift of the transmission peak wavelength on RI and temperature for the same interference order. Distilled water (n = 1.333) and 21.7 ^{o}C are used as the reference solution and temperature ($\delta\lambda$ = 0) for these measurements, respectively. The sensitivity for the temperature sensing is 1.023 nm/^{o}C, and the sensitivity for the RI sensing is -97.9 nm/RIU. Figure 4-33(f) shows peak shifts in response to RI and temperature changes. Therefore, the total wavelength shift $\Delta\lambda$ can be expressed as:

$$\Delta\lambda = 1.023\Delta T - 97.9\Delta n \tag{4.17}$$

where ΔT is the change of the temperature, and Δn is the change of the RI.

Figure 4-34 presents the measurements on another MZI chip. The core of the MZI chip is made by SU-8-2 with a thin core length of 19.05 mm, cross section of the wide core of 5.00 μm×5.50 μm, and cross section of the thin core of 3.20 μm×5.50 μm. The cladding is made of mixed SU-8-3050 and SU-8-2 with a volume ratio of 2:1 (n = 1.562 at 1550 nm) and a cross section of the cladding of 125.00 μm× 11.50 μm. The size of the microchannel is 1.00 mm×75.00 μm×16.00 mm. Distilled water (n = 1.333) and 24.7 ^{o}C are used as the reference solution and temperature ($\delta\lambda$ = 0) for these measurements,

respectively. Figure 4-34(a) shows that the sensitivity for temperature sensing is 0.636 nm/^{o}C, and the sensitivity for RI sensing is -178.8 nm/RIU. Figure 4-34(b) shows peak shifts in response to RI and temperature changes. Therefore, the total wavelength shift can be expressed as:

$$\Delta\lambda = 0.636\Delta T - 178.8\Delta n \tag{4.18}$$

A comparison on the experimental results in Fig. 4-33 and Fig. 4-34 indicates that the first MZI chip has a higher temperature sensitivity due to a smaller RI difference between the cladding and core (Δn_{eff}), whereas the second MZI chip has a higher RI sensitivity due to a larger ratio of the microchannel length to the chip length (L/d).

In conclusion, opto-microfluidic MZI sensors based on a waveguide of cores of different sizes have been proposed and demonstrated. Linear responses of peak wavelength to RI and temperature have been found. The effects of RI difference between the cladding and core (Δn_{eff}) and the ratio of microchannel length to chip length (L/d) have been discussed. The MZI sensor with a smaller RI difference between the cladding and core (Δn_{eff}) and a larger ratio of microchannel length to chip length (L/d) exhibits a higher sensitivity which is preferred for sensor applications.

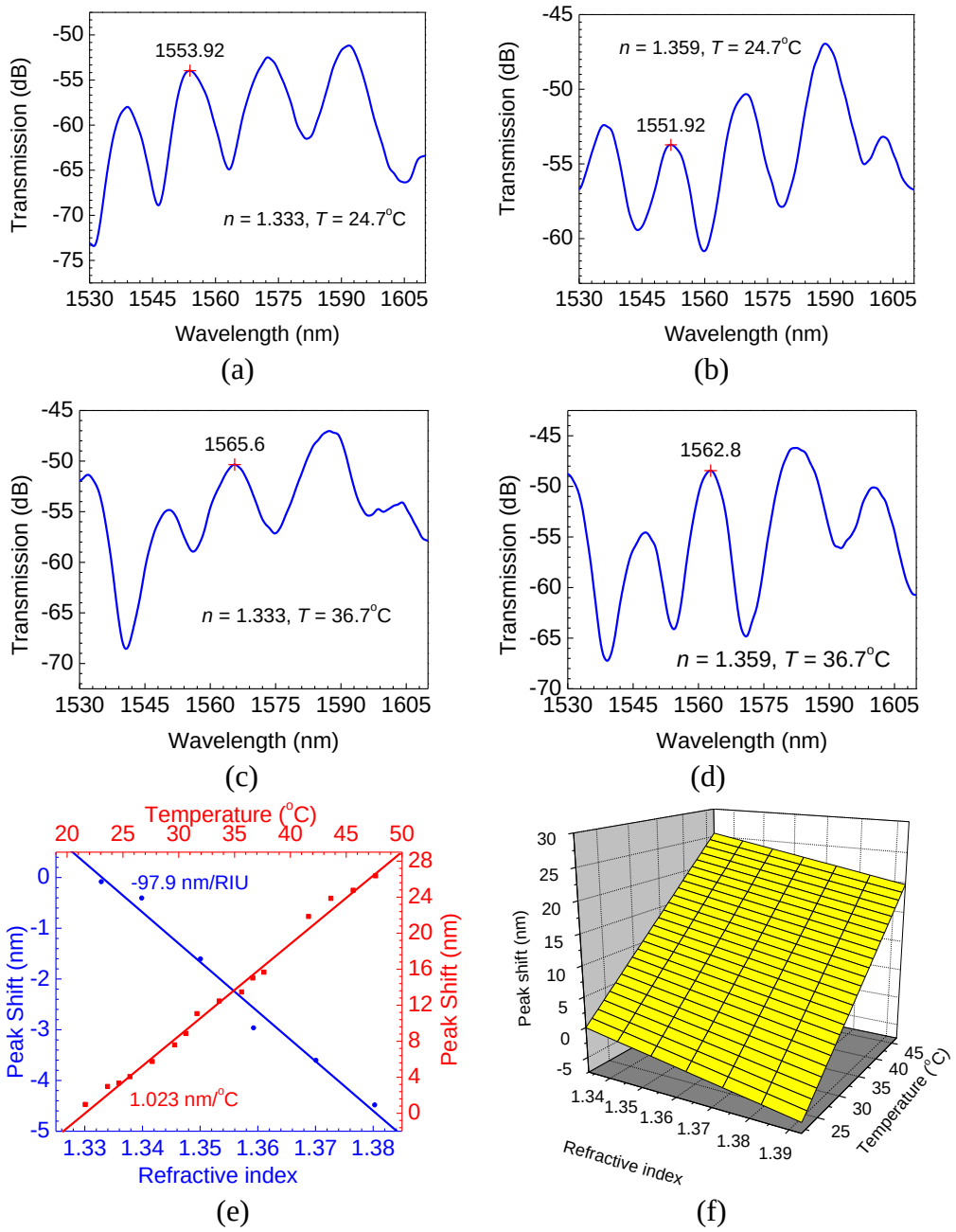

Figure 4-33 Sensing measurement of the RI and temperature for an MZI chip with a thin core length of 18.33 mm, cross section of the wide core of 5.00 μm×5.50 μm, cross section of the thin core of 3.20 μm×5.50 μm, cladding cross section of 125.00 μm×10.50 μm and the microchannel size of 1.00 mm×75.00 μm×10.00 mm: (a)-(d) transmission spectra of the MZI under different environmental conditions, (e) dependence of the shift of the transmission peak wavelength on RI and temperature for the same interference order, and (f) peak shifts in response to RI and temperature changes

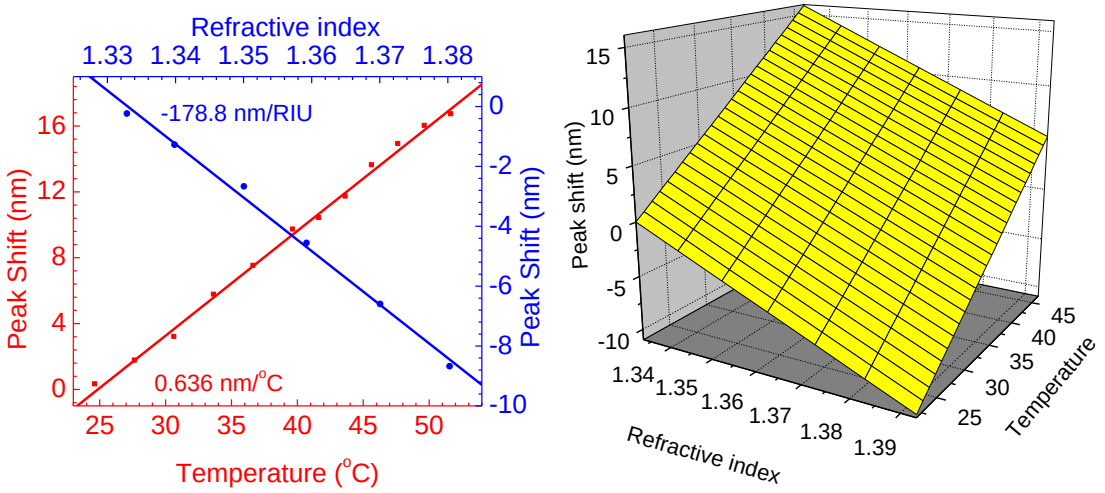

(a) (b)

Figure 4-34 Sensing measurement of the RI and temperature for an MZI chip with a thin core length of 19.05 mm, cross section of the wide core of 5.00 μm×5.50 μm, cross section of the thin core of 3.20 μm×5.50 μm, and cladding cross section of 125.00 μm×11.50 μm: (a) dependence of the shift of the transmission peak wavelength on RI and temperature for the same interference order, and (b) peak shifts in response to RI and temperature changes. The size of the microchannel is 1.00 mm×75.00 μm×16.00 mm.

4.5 Waveguide with symmetrical core

In this section, MZIs with two connectors will be investigated. One of the connectors is used to spread beams into the cladding and the other one is used to collect beams from the cladding. Figure 4-35 gives a schematic illustration of an MZI with a symmetrical core. Tapered SMFs with a focused spot size of 2.5 μm (OZ Optics, Canada) couple beams in and out of the wide cores. In order to prevent SMFs from directly coupling light into, or collecting light from, the cladding as in the MZI structure in section 4.3, SU-8 cladding is designed to cover only part of the wide core at both sides. Therefore, only the light in the wide core is propagated into the MZI structure, spread and collected at the other end. In addition, the uncollected beams in the cladding are scattered into the air before they propagate into the SMF. Figure 4-36 presents a COMSOL simulation result on the light

intensity distribution for an MZI with a connector size of 100.00 μm×30.00 μm (length × width) and thin core length of 600.00 μm between the two connectors. The light is expanded to a wider size in the first connector, and spreaded into the cladding and core. After these beams travel 600.00 μm in the core and cladding, a part of the light propagating in the cladding is coupled into the second connector.

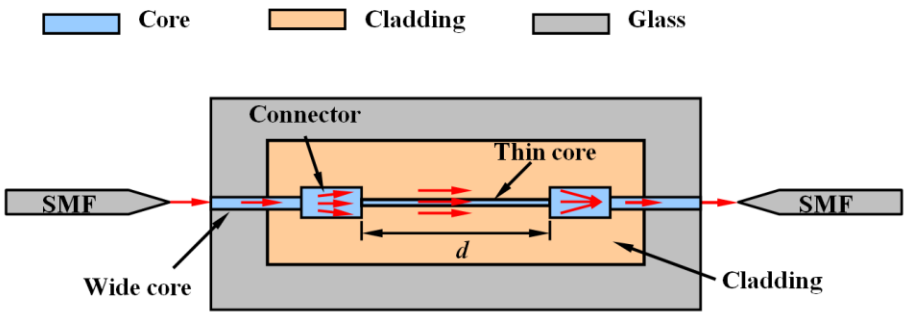

Figure 4-35 Schematic illustration of an MZI with a symmetrical core

Figure 4-37 shows the experimental result and COMSOL simulation on the transmission spectra for an MZI with a thin core length of 20.00 mm between the two connectors. The size of the connector is 300.00 μm×30.00 μm. These two results agree very well. We also notice that the periodicity of the interference in the simulation is a little smaller than the experimental result. The reason is that we use RIs of 1.575 (core RI at 1550 nm) and 1.565 (cladding RI at 1550 nm) for the COMSOL simulation. In fact, the RI varies with the wavelength of the incident light.

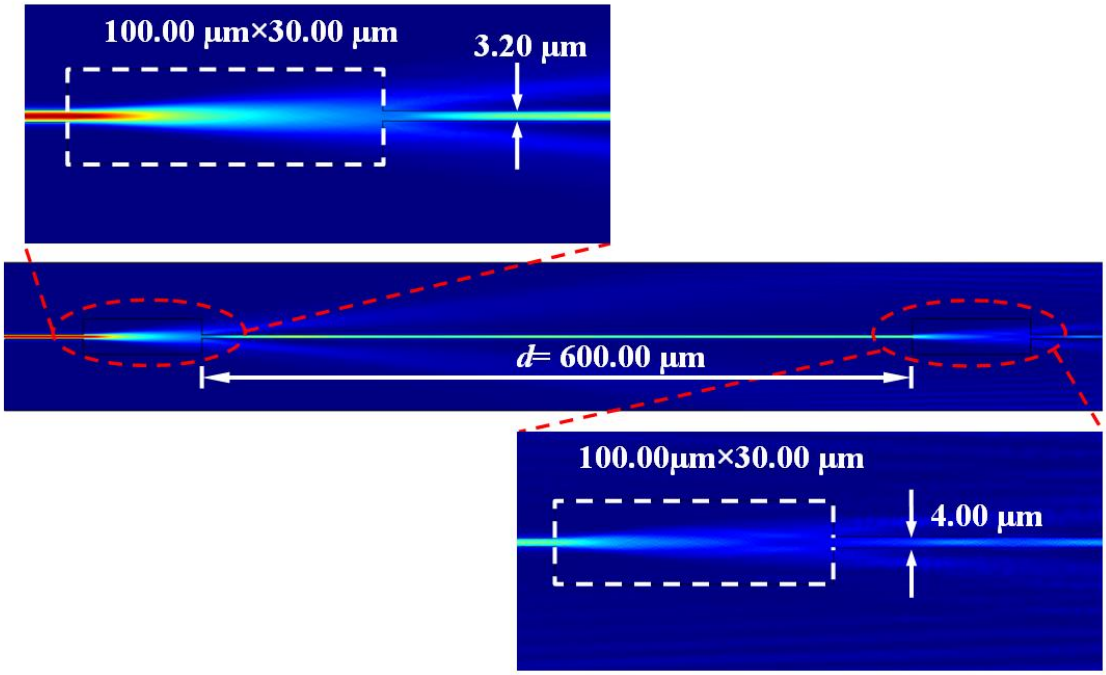

Figure 4-36 COMSOL simulation on the light intensity distribution for an MZI with the connector size of 100.00 μm×30.00 μm, a thin core length of 600.00 μm between the two connectors, width of the thin core of 3.20 μm and width of the wide core of 4.00 μm.

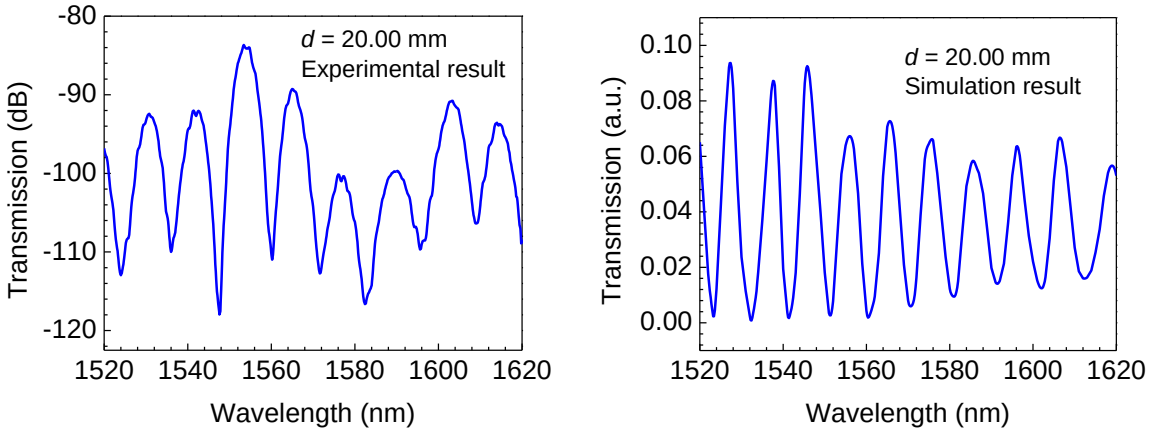

(a) (b)

Figure 4-37 Transmission spectra of an MZI with a thin core length of 20.00 mm: (a) the experimental result, and (b) the COMSOL simulation. The size of the connector is 300.00 μm×30.00 μm.

4.5.1 Characterization of the connectors

The functions of the connectors used in MZIs in this section are to spread and collect beams. The light spreading or collection capability can be calculated according to the NA of an optical fiber which is the maximum angle that an optical fiber can collect or emit light. The equation can be described as follows [104]:

$$NA = n\sin\theta = \sqrt{n_{core}^2 - n_{cladding}^2} \tag{4.19}$$

where n is the RI of the medium outside the fiber and θ is the maximum angle of acceptance. For an MZI connector, the equation is:

$$NA = n_{core}\sin\theta = \sqrt{n_{core}^2 - n_{cladding}^2} \tag{4.20}$$

$$\sin\theta = \sqrt{1 - \frac{n_{cladding}^2}{n_{core}^2}} \tag{4.21}$$

According to Eqn. (4.21), the RIs of the cladding and core affect the maximum angle of acceptance θ which relates to the intensity distribution of light. However, the lengths and widths of the connectors also affect the light intensity distribution. Figures 4-38~4-41 present four kinds of connectors with different lengths, widths and shapes, and their COMSOL simulation on the light intensity distribution, respectively. The rectangular connector with a size of 50.00 μm× 30.00 μm does not expand the beam widely enough, so most of light is coupled into the thin core. On the contrary, the rectangular connector with a size of 300.00 μm× 50.00 μm achieves lesser light coupling into the thin core. The

isosceles triangular connector with a vertex angle of 5.72^{o} contains the beams in the triangular region.

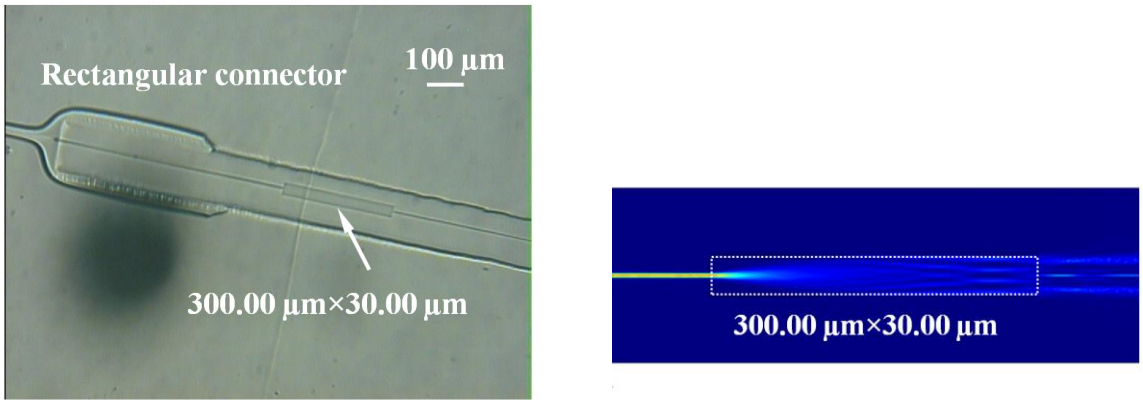

(a) (b)

Figure 4-38 Rectangular connector with a size of 300.00 μm× 30.00 μm: (a) the morphology, and (b) the COMSOL simulation on the light intensity distribution.

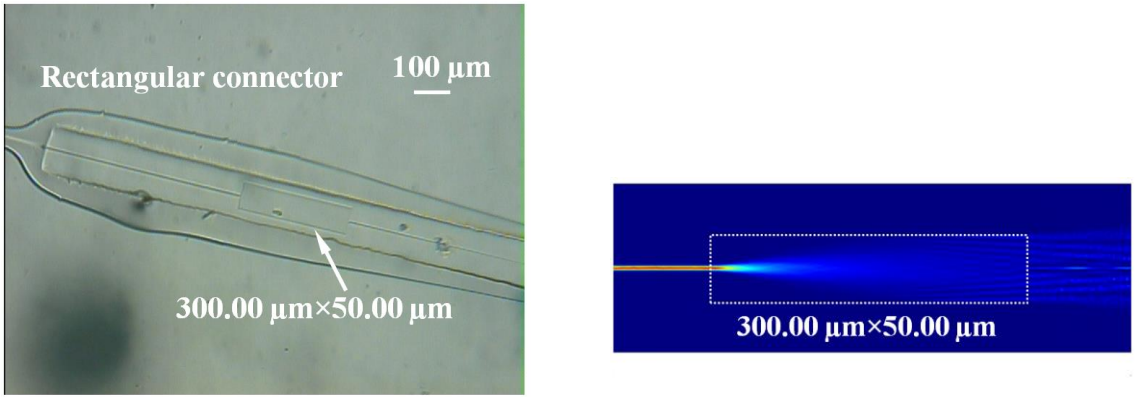

(a) (b)

Figure 4-39 Rectangular connector with a size of 300.00 μm× 50.00 μm: (a) the morphology, and (b) the COMSOL simulation on the light intensity distribution.

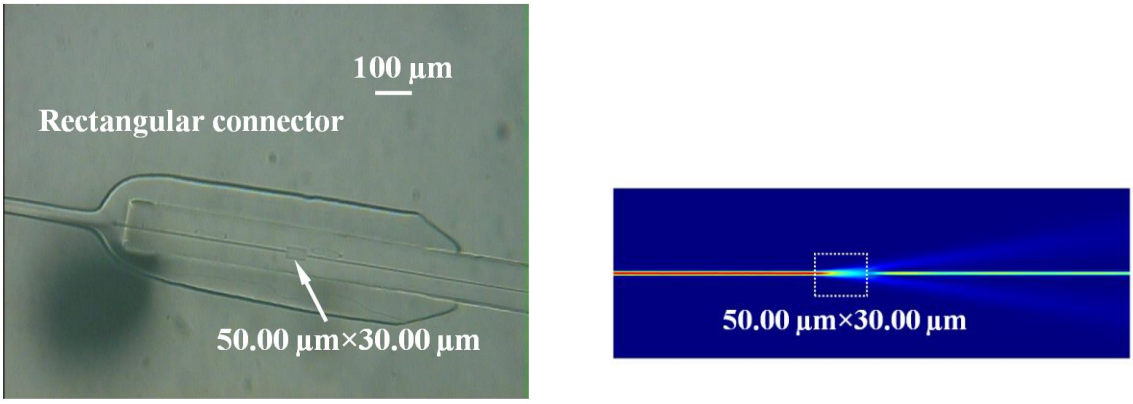

(a) (b)

Figure 4-40 Rectangular connector with a size of 50.00 μm× 30.00 μm: (a) the morphology, and (b) the COMSOL simulation on the light intensity distribution.

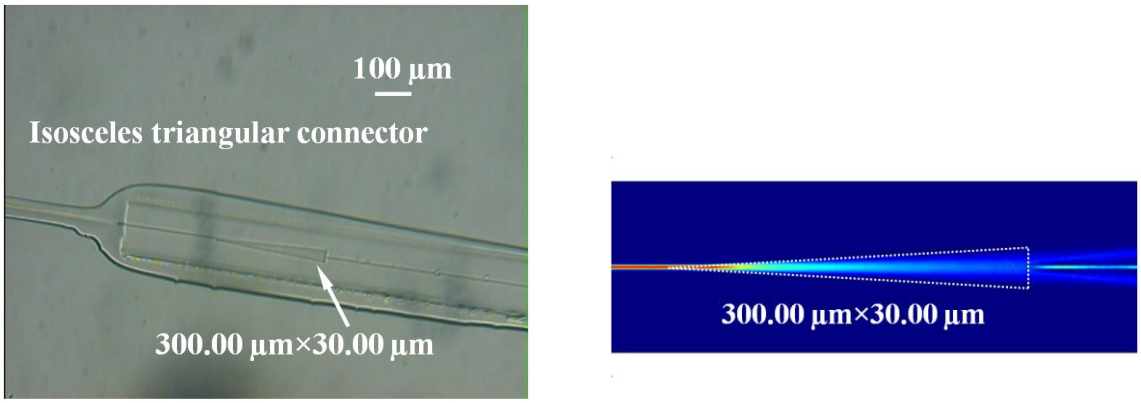

(a) (b)

Figure 4-41 Isosceles triangular connector with a size of 300.00 μm× 30.00 μm: (a) the morphology, and (b) the COMSOL simulation on the light intensity distribution.

Figure 4-42 describes the transmission spectra of MZI chips with different kinds of connectors. All MZI chips have the widths of the wide and thin core of 5.00 and 3.20 μm, respectively, the width of the cladding of 125.00 μm, and a thin core length of 20.00 mm. The connector with a length of 50.00 μm and width of 30.00 μm has the strongest transmission intensity and weakest interference pattern's visibility. According to Eqn. (4.21), the maximum angle of acceptance θ is 6.46^{o} for the cladding RI of 1.565 and

core RI of 1.575. For the connector with a length of 50.00 μm, the beam can be expanded to a width of 11.32 μm. As a result, most of the beam is coupled into the thin core before it is expanded to the whole width of the connector, and only a fraction of the beam is scattered into the cladding, as shown in the simulation in Fig. 4-40(b). Therefore, the interference pattern's visibility is weak and the transmission intensity is strong in this situation. The connector with a length of 300.00 μm and width of 50.00 μm has the weakest transmission intensity and strongest interference pattern's visibility. According to the calculation, the beam can be expanded to the full width of the connector (50.00 μm) at the length of 220.80 μm. As a result, most of the beam is scattered into the cladding instead of coupling into the thin core, as shown in the simulation in Fig. 4-39(b). Therefore, the interference pattern's visibility is stronger and the transmission intensity is weaker in this situation. For the connector with a width of 30.00 μm, the beam can be expanded to the whole width of the connector at a length of 132.50 μm. Therefore, the connectors with the width of 30.00 μm and a length larger than 132.50 μm exhibit almost the same transmission intensity and interference pattern's visibility.

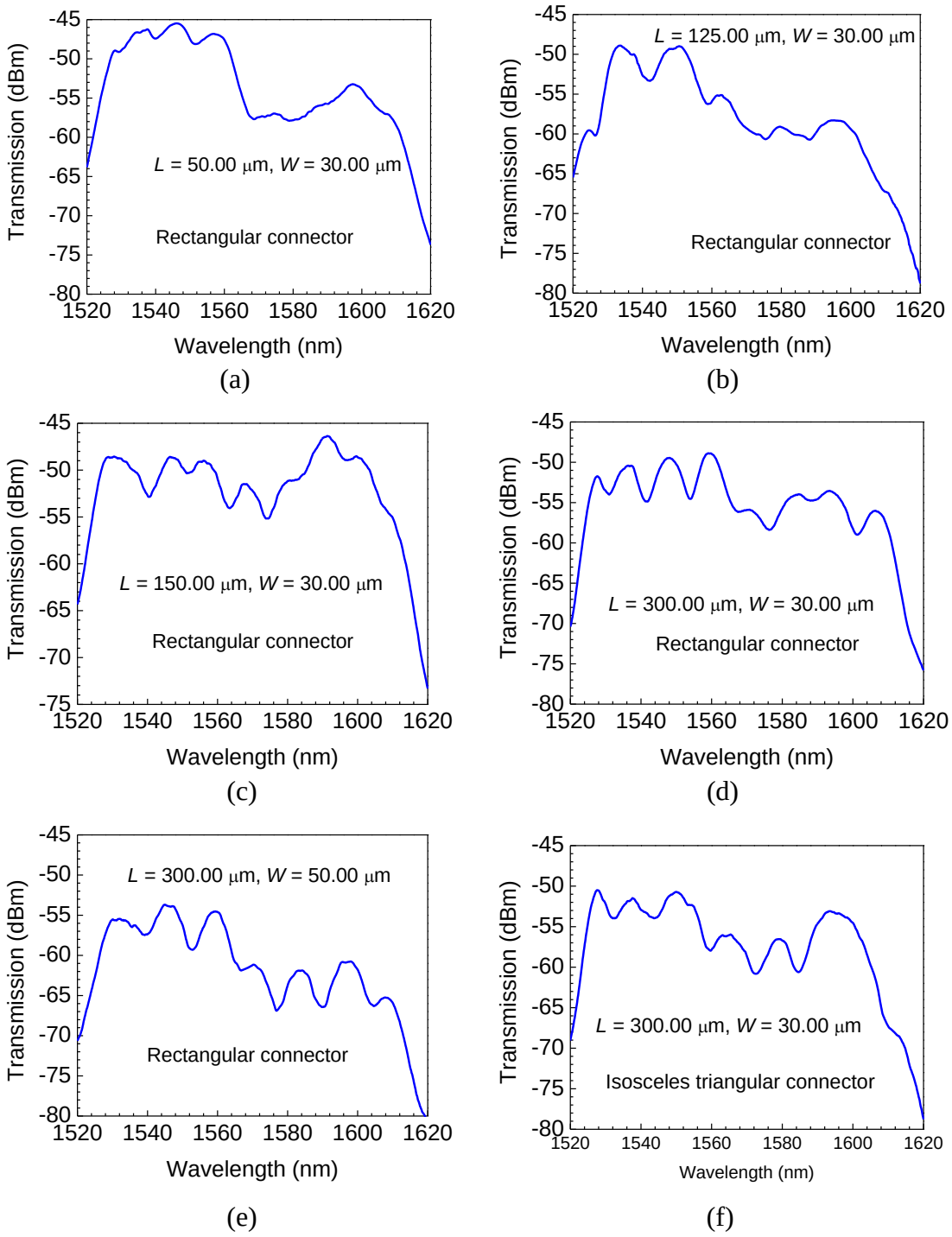

Figure 4-42 Transmission spectra of MZIs with different sizes of connectors. The sizes of the wide and thin core are 5.00 and 3.20 μm, respectively. The cladding width is 125.00 μm and there is a thin core length of 20.00 mm between the two connectors.

4.5.2 Concentration and temperature sensing

Similar to the other types of MZI mentioned above, this kind of MZI can also be used for RI and temperature sensing. A chip with a thin core size of 2.80 μm× 3.70 μm× 20.00 mm, cladding cross section of 125.00 μm× 9.95 μm and connector size of 150.00 μm×30.00 μm has been fabricated. The size of the microchannel is 1.00 mm×75.00 μm×16.00 mm. Figure 4-43 presents a 3D surface profile of one connector observed by a ZYGO nexview^{TM} 3D optical surface profiler. Figure 4-44 shows the dependence of the peak shift on temperature. 21.7 ^{o}C is used as the reference temperature ($\delta\lambda$ = 0) for these measurements. The sensitivity is -0.595 nm/^{o}C.

Salt solutions are infused into the microchannel with a constant temperature of 21.7 ^{o}C. The dependence of the peak shift on NaCl concentration is shown in Fig. 4-45. Distilled water (C = 0 wt%) is used as the reference solution ($\delta\lambda$ = 0) for these measurements. The sensitivity is -0.102 nm/wt%. The relationship between the peak shift in the temperature and NaCl concentration can be described as:

$$\Delta\lambda = 0.595\Delta T - 0.102\Delta C \tag{4.22}$$

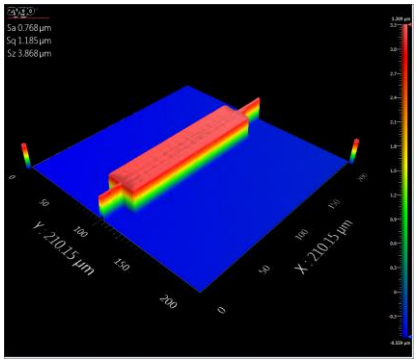

Figure 4-43 3D surface profile of a connector observed by 3D optical surface profiler. The size of the connector is 150.00 μm×30.00 μm×3.70 μm.

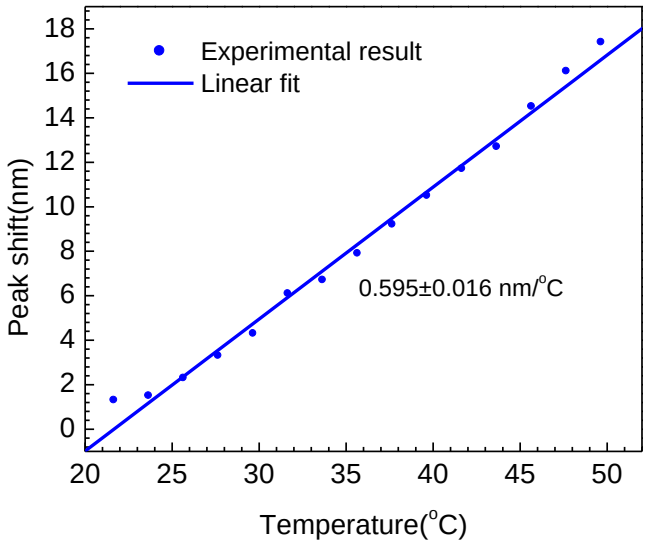

Figure 4-44 Dependence of the peak shift on temperature. The MZI chip has a thin core size of 2.80 μm× 3.70 μm× 20.00 mm, cross section size of the cladding of 125.00 μm× 9.95 μm, and connector size of 150.00 μm×30.00 μm. The size of the microchannel is 1.00 mm×75.00 μm×16.00 mm.

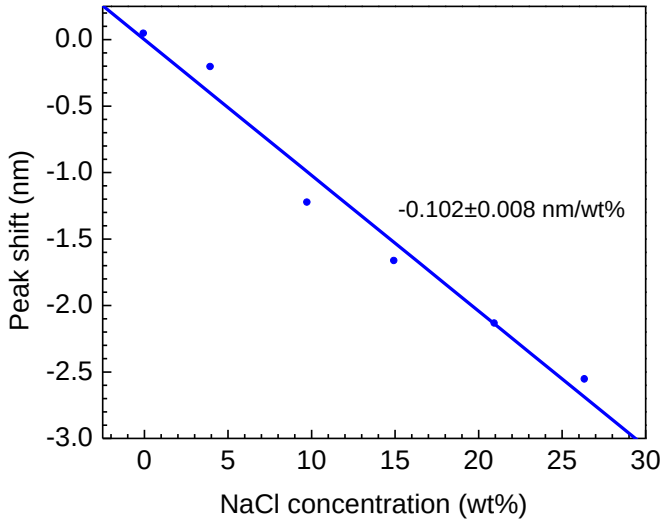

Figure 4-45 Dependence of the peak shift on NaCl concentration. The MZI chip has a thin core size of 2.80 μm× 3.70 μm× 20.00 mm, cross section size of the cladding of 125.00 μm× 9.95 μm, and connector size of 150.00 μm×30.00 μm. The size of the microchannel is 1.00 mm×75.00 μm×16.00 mm.

Sugar solutions are measured using the same chip and processes. Figure 4-46 shows the peak wavelength change as a function of sugar concentration, in which the sensitivity of the sugar concentration is -9.2×10^{-2} nm/^{o}Bx. Distilled water (C = 0 ^{o}Bx) is used as the reference solution ($\delta\lambda$ = 0) for these measurements. The relationship between the peak shift in the temperature and sugar concentration can be described as:

$$\Delta\lambda = 0.595\Delta T - 9.2\times10^{-2}\Delta C \tag{4.23}$$

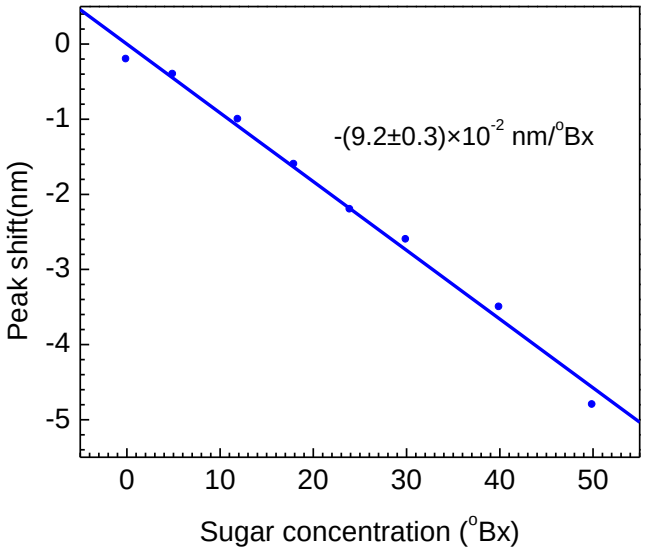

Figure 4-46 Dependence of the peak shift on sugar concentration. The MZI chip has a thin core size of 2.80 μm× 3.70 μm× 20.00 mm, cross section size of the cladding of 125.00 μm× 9.95 μm, and connector size of 150.00 μm×30.00 μm. The size of the microchannel is 1.00 mm×75.00 μm×16.00 mm.

In conclusion, opto-microfluidic MZI sensors based on waveguide with a symmetrical core have been designed and demonstrated. This type of sensor can be used to measure the RI, concentration and temperature of a liquid. The effects of length and width of the connector are discussed in theory and experiment. By choosing the optimum width and length of the connectors, a strong interference pattern can be obtained.

4.6 Waveguide with discontinuous core

In this section, waveguide-MZI based opto-microfluidic devices with discontinuous cores are designed and fabricated. As shown in Fig. 4-47(a), a tapered SMF couples the light into the core. When a beam is transmitted into the gap with a length of *l*, part of the light is recoupled into the core, and the remaining light is scattered into the cladding. Light propagates along different paths with the same path length of *d* (length of the sensing arm). An SMF is used to collect the light that comes out from the core and the cladding to generate interference. Figure 4-47(b) is the morphology of a waveguide with a discontinuous core. The length of the gap is 250.00 μm.

4.6.1 Effect of gap length

Four groups of MZI chips have been prepared with gap lengths of 200.00, 150.00, 100.00, and 50.00 μm, respectively. All MZI chips have a core cross section of 4.00 μm× 4.50 μm, sensing arm of 20.00 mm, and cladding cross section of 125.00 μm× 11.00 μm. Figure 4-48 presents the corresponding transmission spectra of the MZI chips. An MZI chip with a gap length of 200.00 μm manifests the largest extinction ratio. Figure 4-49 shows the COMSOL simulation on the light transmission intensity at different gap lengths at the wavelength of 1561 nm. The simulation results prove that more light is scattered into the cladding layer in the chip with a longer gap. Therefore, a longer core gap induces higher fringe visibility.

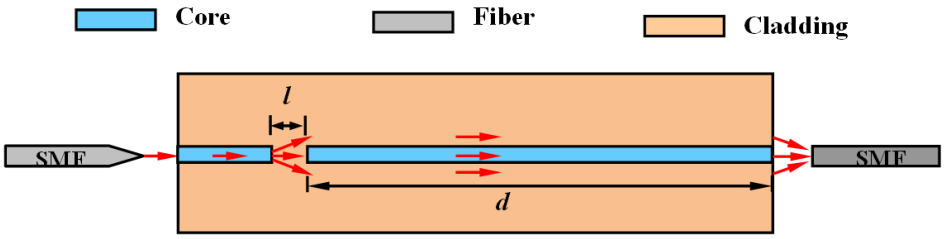

(a)

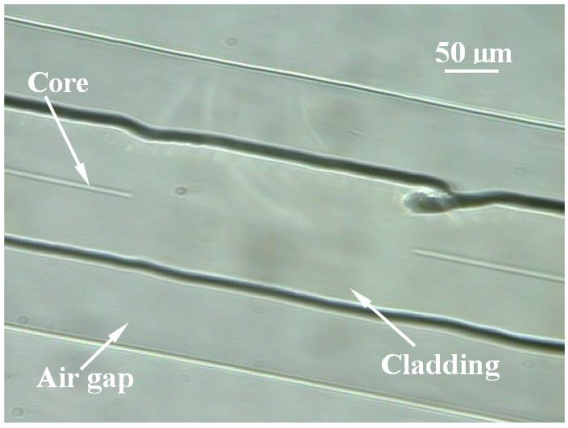

(b)

Figure 4-47 MZI structure with a discontinuous core: (a) a schematic illusion of an MZI structure, and (b) the morphology of a waveguide with a discontinuous core. The gap length is 250.00 µm.

4.6.2 Refractive index/concentration sensing

A chip with a gap length of 150.00 µm, core cross-section of 4.00 µm× 4.50 µm, sensing arm of 21.05 mm, cladding cross section of 125.00 µm × 11.00 µm, and microchannel length of 16.00 mm is employed to sense the RI of the salt solution. Figure 4-50 shows the transmission spectra and dependence of the peak shift on RI. The sensitivity is -159.4 nm/RIU. A chip with a gap length of 200.00 µm, core cross section of 4.00 µm× 4.50 µm, sensing arm of 20.63 mm, cladding cross section of 125.00 µm× 11.00 µm, and microchannel length of 16.00 mm is used to sense the concentration of the $CaCl_2$ solution.

Figure 4-51 shows dependence of the peak shift on $CaCl_2$ concentration. The sensitivity is -4.01 nm/M.

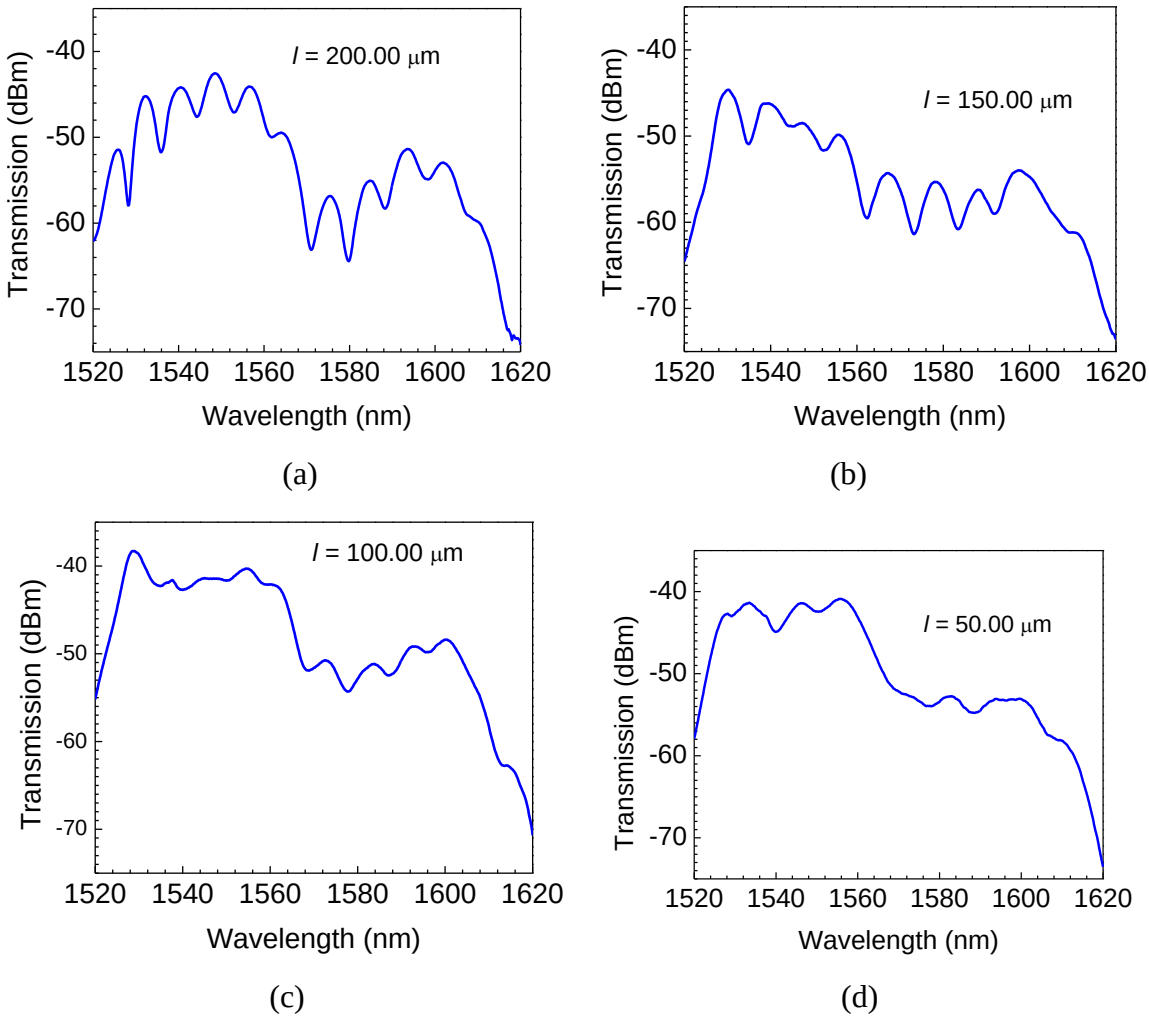

Figure 4-48 Transmission spectra of MZI chips with different gap lengths. All MZI chips have a core cross section of 4.00 μm× 4.50 μm, length of the sensing arm of 20.00 mm, and cladding cross section of 125.00 μm× 11.00 μm.

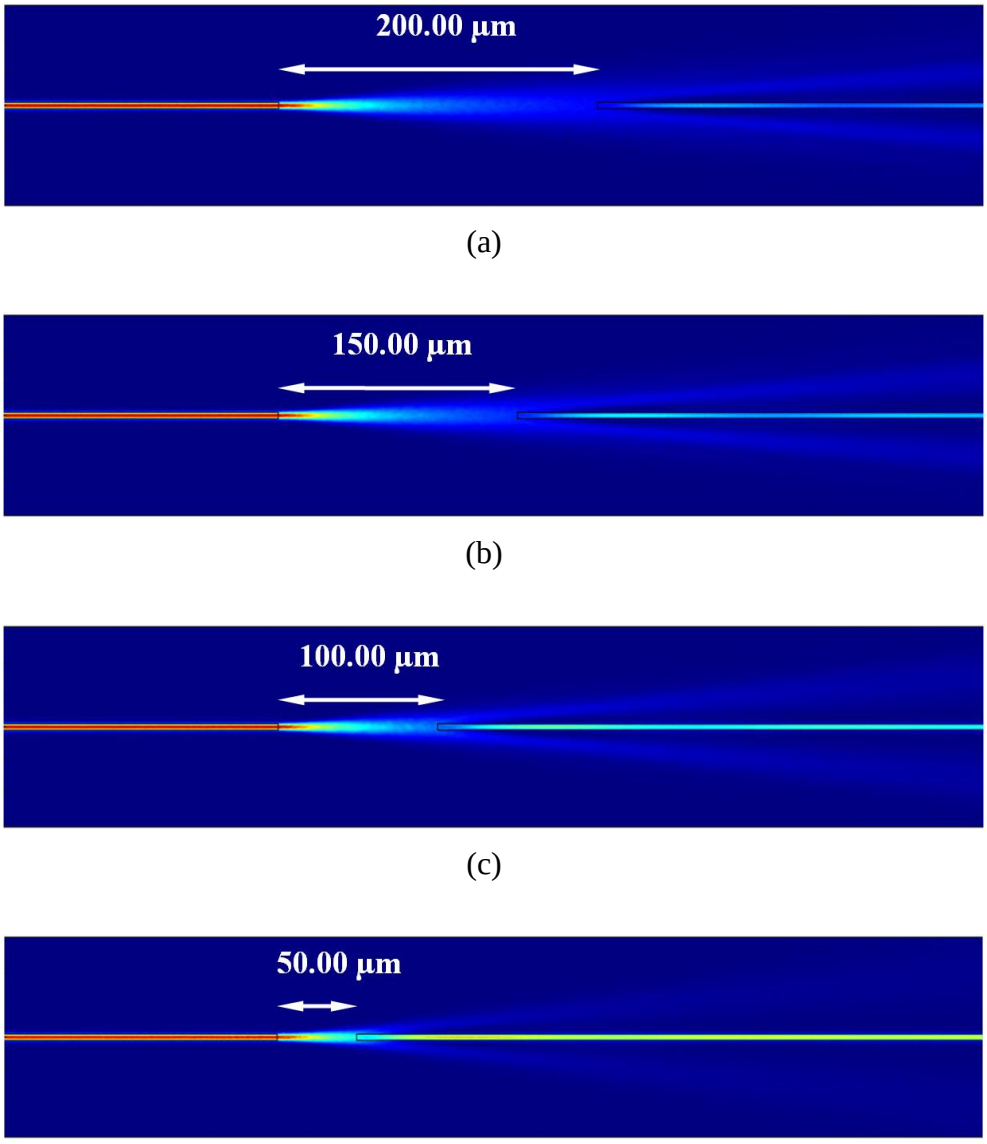

Figure 4-49 COMSOL simulation on the light transmission intensity at different gap lengths.

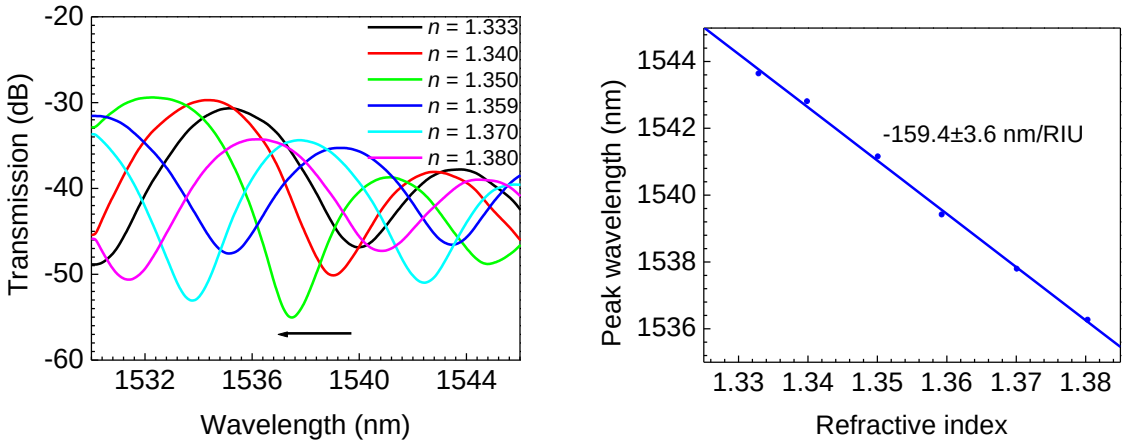

(a) (b)

Figure 4-50 RI sensing measurement of an MZI chip with a gap length of 150.00 μm, core cross section of 4.00 μm× 4.50 μm, sensing arm of 21.05 mm, cladding cross section of 125.00 μm× 11.00 μm, and microchannel length of 16.00 mm: (a) transmission spectra of the MZI in different RI solutions, and (b) dependence of the peak shift on RI.

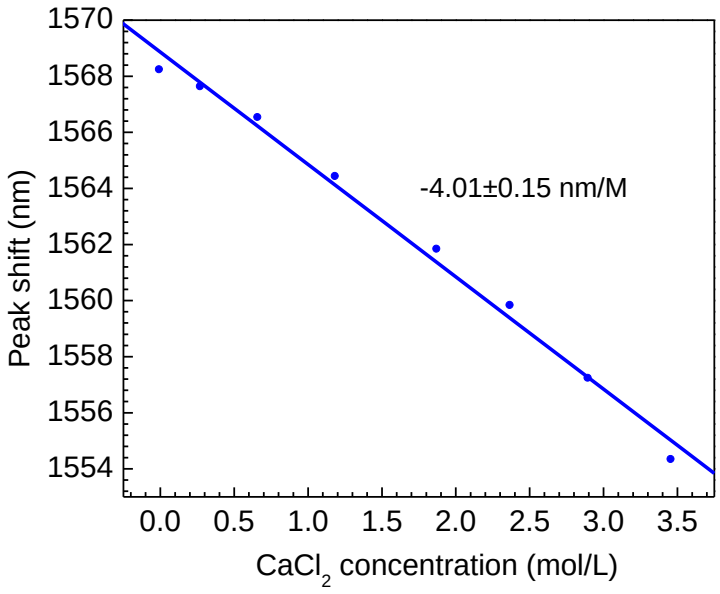

Figure 4-51 Dependence of the peak shift on $CaCl_2$ concentration. The MZI chip has a gap length of 200.00 μm, core cross section of 4.00 μm× 4.50 μm, sensing arm of 20.63 mm, a cladding cross section of 125.00 μm× 11.00 μm, and microchannel length of 16.00 mm.

4.6.3 Temperature sensing

A chip with a gap length of 200.00 μm, core size of 3.20 μm×4.17 μm, cladding size of 125.00 μm×9.88 μm, and sensing arm of 24.29 mm is used for temperature sensing. Figure 4-52 shows the transmission spectra and dependence of the peak shift on temperature. 21.7 ^{o}C is used as the reference temperature ($\delta\lambda$ = 0) for these measurements. The sensitivity is 0.519 nm/^{o}C.

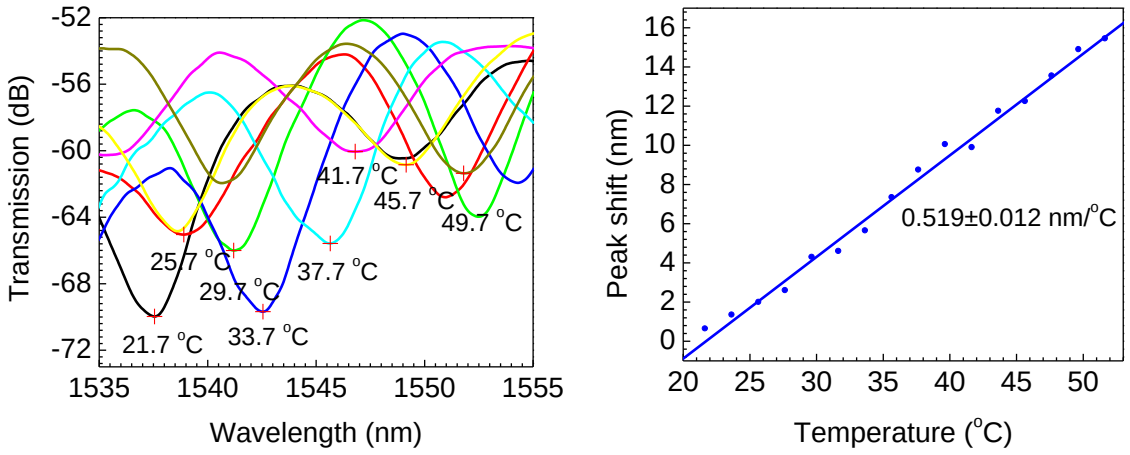

(a) (b)

Figure 4-52 Temperature sensing measurement of an MZI chip with a gap length of 200.00 μm, core size of 3.20 μm×4.17 μm, cladding size of 125.00 μm×9.88 μm, and sensing arm of 24.29 mm: (a) transmission spectra of the MZI at different temperatures, and (b) dependence of the peak shift on temperature.

Due to significant wavelength shifts, temperature sensing characterization over a broader range is studied here. Figure 4-53 shows the transmission spectra at the temperatures of 20 ^{o}C and 182 ^{o}C, respectively. The MZI chip has a core cross section of 4.00 μm×4.50 μm, sensing arm of 20.00 mm, and cladding cross section of 125.00 μm×11.00 μm. The transmission spectrum has a smaller periodicity of interference at a higher temperature than at a lower temperature.

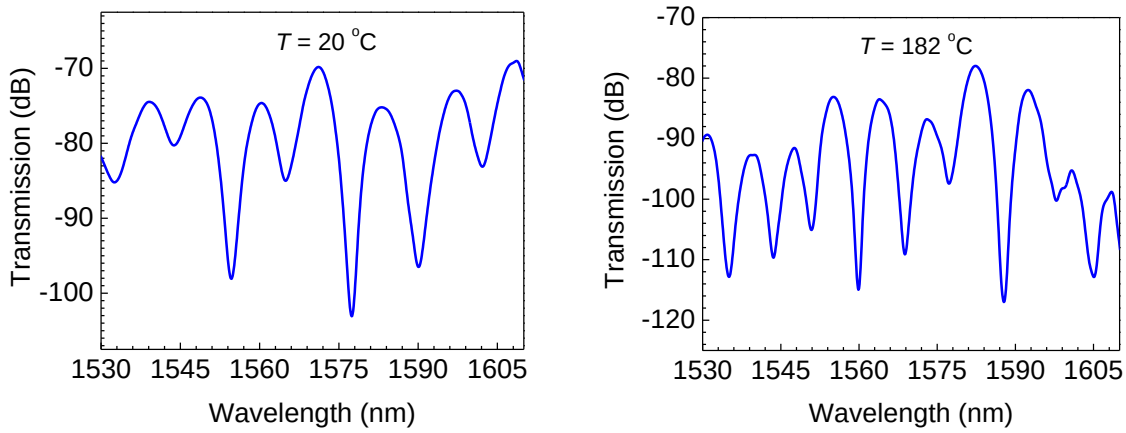

(a) (b)

Figure 4-53 Transmission spectra of an MZI chip with a gap length of 200.00 μm, core cross section of 4.00 μm× 4.50 μm, sensing arm of 20.00 mm, and cladding cross section of 125.00 μm× 11.00 μm at 20 °C and 182 °C.

Due to the large peak shifts over a wide range of temperature sensing, which is out of the range of the light source (1520 - 1620 nm) for a constant peak, we choose multiple peaks with the orders of interference of 136, 137, 138, 144 and 149 to measure the peak shift as shown in Fig. 4-54(a) and link the peak shifts together which will cause a small discrepancy. The experimental results in Fig. 4-54(b) show that the temperature sensitivity is almost constant over the low temperature range (20 - 100 °C), and increases over the high temperature range (>100 °C). 20 °C is used as the reference temperature ($\delta\lambda$ = 0) for these measurements. Considering that the thermo-optic coefficient of material is usually a quadratic function of temperature [105-107], the RI difference of the core and cladding caused by temperature is set as:

$$\delta n_{eff,T} = \left(\frac{dn}{dT}_{core} - \frac{dn}{dT}_{cladding}\right)\Delta T = (a + b \times T + c \times T^2) \times \Delta T \tag{4.24}$$

where *a*, *b*, and *c* are undetermined coefficients. Equation (4.14) can be written as

$$\delta\lambda_T = \frac{(\frac{dn}{dT}_{core} - \frac{dn}{dT}_{cladding})\lambda_{T_{start}}}{\Delta n_{eff,T_{start}}}\Delta T = \frac{(a+bT+cT^2)(T-T_{start})\lambda_{T_{start}}}{\Delta n_{eff,T_{start}}} \quad (4.25)$$

where $\delta\lambda_T$ is the peak shift at the temperature of T, T_{start} is the starting temperature, λ_{Tstart} is the peak wavelength at the starting temperature, and $\Delta n_{eff,Tstart}$ is the effective RI difference between the core and cladding at the starting temperature. In this case, the starting temperature is 20 ^{o}C (293 K), $\Delta n_{eff,Tstart}$ is 5.62×10^{-3} which is calculated by COMSOL, and λ_{Tstart} is 1532.5 nm. A polynomial fit is applied to this experimental data. $\delta n_{eff,T}$ is obtained as follows:

$$\frac{\delta n_{eff,T}}{\Delta T} = \frac{dn}{dT}_{core} - \frac{dn}{dT}_{cladding} = 7.70\times10^{-6} - 4.72\times10^{-8}T + 8.52\times10^{-11}T^2 \quad (4.26)$$

which also proves that the thermo-optic coefficients of the SU-8 series are different. The RI difference between the core and cladding ($\Delta n_{eff,T}$) increases with the increasing temperature. As a result, a larger phase difference between the two arms is induced at a higher temperature and generates a smaller periodicity of the interference in the transmission spectrum.

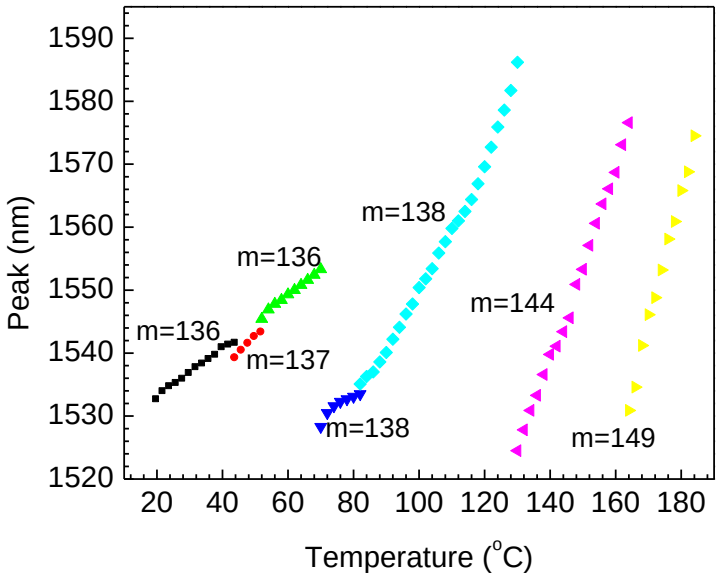

(a)

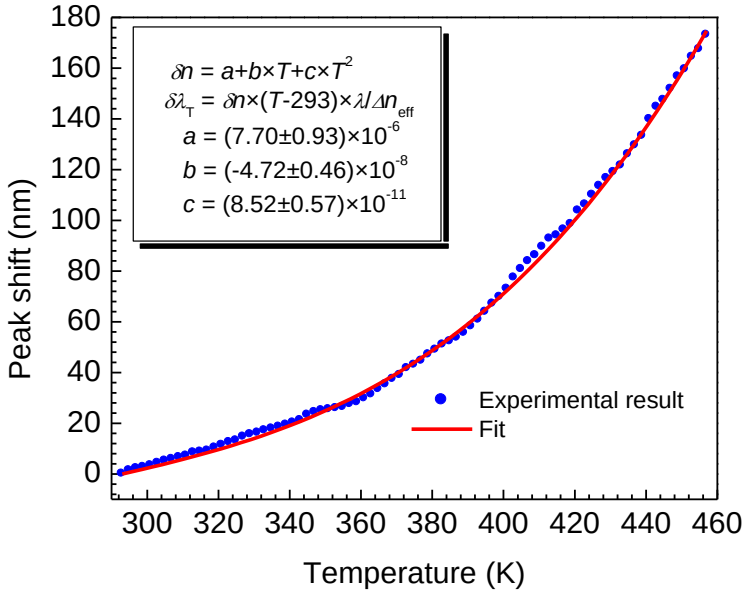

(b)

Figure 4-54 Temperature sensing measurement of an MZI chip with a gap length of 200.00 μm, core cross section of 4.00 μm× 4.50 μm, sensing arm of 20.00 mm and cladding cross section of 125.00 μm× 11.00 μm: (a) peak wavelengths for the peaks with the interference modes of 136, 137, 138, 144 and 149 at different temperatures, and (b) dependence of the peak shift on temperature.

4.6.4 Simultaneous measurement of refractive index and temperature

Figure 4-55 describes transmission spectra of an MZI under different environmental conditions, the dependence of the shift of the transmission peak wavelengths on RI and temperature for the same interference order, and peak shifts in response to RI and temperature changes. The MZI chip has a core cross section of 4.00 μm× 4.50 μm, sensing arm of 20.00 mm, cladding cross section of 125.00 μm× 11.00 μm, and microchannel length of 16.00 mm. Distilled water (n = 1.333) and 21.7 ^{o}C are used as the reference solution and temperature ($\delta\lambda$ = 0) for these measurements, respectively. The total wavelength shift can be expressed as:

$$\Delta\lambda = 0.446\Delta T - 159.4\Delta n \tag{4.24}$$

Figure 4-56(a) presents the dependence of the shift of the transmission peak wavelengths on RI and temperature for another chip. Distilled water (n = 1.333) and 21.7 ^{o}C are used as the reference solution and temperature ($\delta\lambda$ = 0) for these measurements, respectively. This chip has a core cross section of 3.20 μm×4.17 μm, sensing arm of 24.29 mm, cladding cross section of 125.00 μm×9.88 μm, and microchannel length of 16.00 mm. The sensitivity for temperature sensing is 0.519 nm/^{o}C, and the sensitivity for RI sensing is -216 nm/RIU. Figure 4-56(b) shows the peak shifts in response to RI and temperature changes. Therefore, the total wavelength shift can be expressed as:

$$\Delta\lambda = 0.519\Delta T - 216\Delta n \tag{4.25}$$

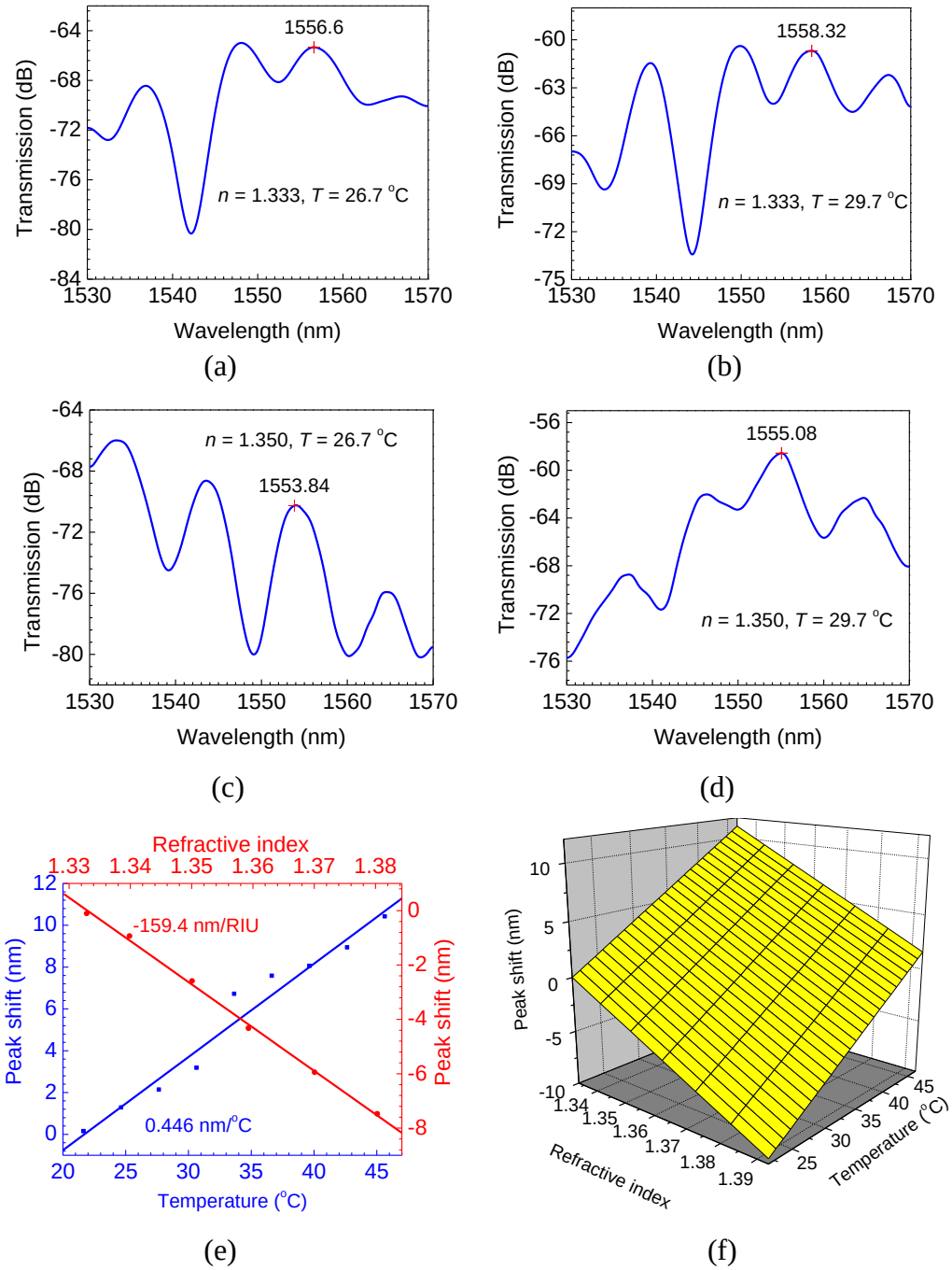

Figure 4-55 Sensing measurement of the RI and temperature for an MZI chip with a core cross section of 4.00 μm× 4.50 μm, sensing arm of 20.00 mm, cladding cross section of 125.00 μm× 11.00 μm, and microchannel length of 16.00 mm: (a)-(d) transmission spectra of the MZI under different environmental conditions, (e) dependence of the shift of the transmission peak wavelengths on RI and temperature for the same interference order, and (f) peak shifts in response to RI and temperature changes.

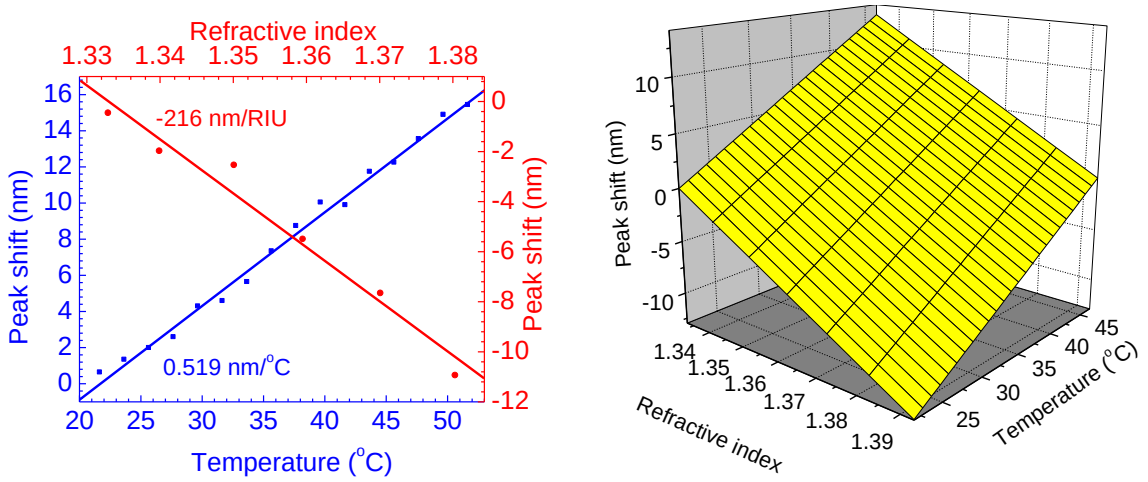

(a) (b)

Figure 4-56 Sensing measurement of the RI and temperature for an MZI chip with a core cross section of 3.20 μm×4.17 μm, sensing arm of 24.29 mm, cladding cross section of 125.00 μm×9.88 μm, and microchannel length of 16.00 mm: (a) dependence of the shift of the transmission peak wavelengths on RI and temperature, and (b) peak shifts in response to RI and temperature changes.

A comparison on the experimental results in Fig. 4-55 and Fig. 4-56 indicates that the second MZI chip has a higher RI sensitivity due to the fact that a thinner cladding layer is more sensitive to the environment (larger $\delta_{neff,n}$), and a higher temperature sensitivity due to a smaller core size (smaller $\Delta_{neff,T}$). Using these two MZI chips, simultaneous measurement of RI and temperature can be achieved. If a solution sample is injected into the two chips, the peak shifts can be tested. The relationship between the peak shift and the changes in the temperature and RI of the liquid can be expressed with a matrix equation:

$$\begin{bmatrix} \Delta T \\ \Delta n \end{bmatrix} = \begin{bmatrix} 0.446 & -159.4 \\ 0.519 & -216 \end{bmatrix}^{-1} \begin{bmatrix} \Delta\lambda_1 \\ \Delta\lambda_2 \end{bmatrix} \tag{4.26}$$

where $\Delta\lambda_1$ and $\Delta\lambda_2$ are the shifts in the interference wavelengths of the chips, respectively.

In order to prove the validity of the chip in Fig. 4-56, water samples of melted iceberg water, pond water and seawater are applied to the chip. The chip temperature is maintained at 21.7 ^{o}C. Distilled water is first infused into the chip for reference, and then water samples are injected into the microchannel. Figure 4-57 describes the experimental results. The RI of the iceberg is about 1.3347 which is a bit higher than distilled water. The RI of the pond water is 1.3360. The RI of the seawater is about 1.3393. By calculation [108], the salinity of seawater is about 3.26% which is reasonable for the seawater.

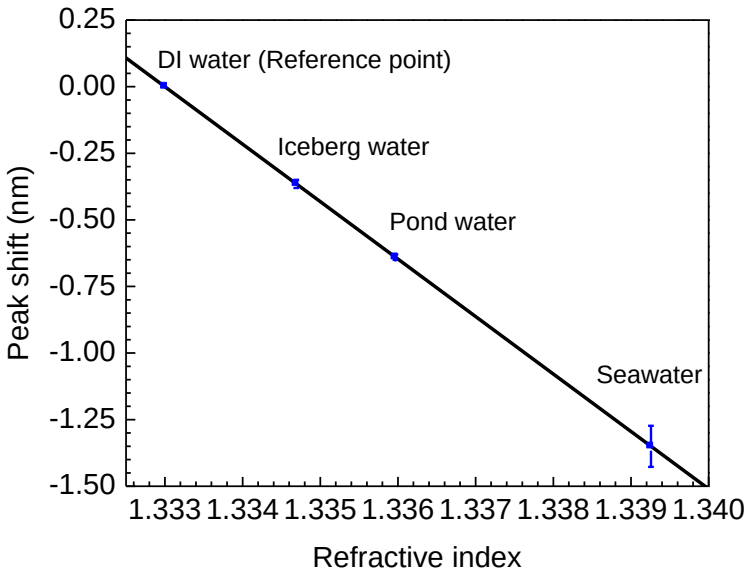

Figure 4-57 RI measurement on different water samples

In conclusion, we have successfully designed and fabricated an opto-microfluidic MZI sensor based on a waveguide with a discontinuous core. The effects of gap length have been investigated. The MZI with a longer gap has a better fringe visibility. Different water samples have been tested with an MZI chip. These results prove the practicability

of opto-microfluidic devices for *in situ* monitoring of salinity with a high sensitivity and low cost. In addition, simultaneous measurement of the temperature and RI of solutions can be achieved by using two MZI chips.

Chapter 5 Optical microring resonator based opto-microfluidic devices

5.1 Introduction

In this chapter, ring-shaped and racetracktrack-shaped resonators are fabricated by femtosecond laser induced TPP technique, which exhibit linear responses to RI and temperature. The effects of the resonator size, resonance wavelength and polarization on the sensitivity are exploded in theory and experiment. Two-ring based and polarization based opto-microfluidic sensors for simultaneous RI and temperature measurements are achieved.

5.1.1 Theory

An optical microring resonator is an arrangement of an optical waveguide with one or several closed loops. When incident light is coupled into the loop from the input bus waveguide (input port), some light with special wavelengths is strongly confined inside the ring over multiple round-trips due to the constructive interference. As a result, the confinement of light causes a sharp drop of electromagnetic energy and generates multiple optical resonance modes in the output spectrum at the through port.

As shown in Fig. 5-1, the interaction between the bus waveguide and ring can be described by the matrix relation:

$$\begin{bmatrix} E_2 \\ E_4 \end{bmatrix} = \begin{bmatrix} t & -\kappa^* \\ \kappa & t^* \end{bmatrix} \begin{bmatrix} E_1 \\ E_3 \end{bmatrix} \tag{5.1}$$

where t and κ are the transmission and cross-coupling coefficients, respectively. E_1 is the electric field intensity of the input light, E_2 is the electric field intensity of the output light, E_4 is the electric field intensity of the cross-coupling light, and E_3 is the electric field intensity of cross-coupling light after a round trip.

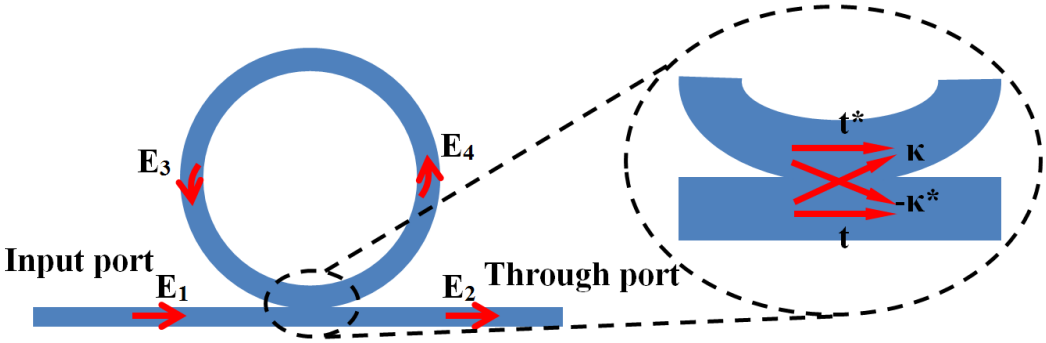

Figure 5-1 Schematic illustration of an optical ring resonator

The round trip in the ring is given by

$$E_3 = \alpha_R e^{j\phi} E_4 \tag{5.2}$$

where α_R is the propagation loss coefficient per round trip of the microring, $\phi = 2\pi n_{eff} L/\lambda$, L is the circumference of the microring, n_{eff} is the effective RI of the microring, and λ is the wavelength of the light.

The ratio of E_2 and E_1 can be derived from Eqns (5.1) and (5.2) to the following form:

$$\frac{E_2}{E_1} = \frac{te^{-j\phi} - \alpha_R(|t|^2 + |\kappa|^2)}{e^{-j\phi} - \alpha_R t^*} \tag{5.3}$$

where $|t|^2$ and $|\kappa|^2$ are the power splitting ratios of the coupler. The transmission T in the output port of the bus waveguide is

$$T = \left|\frac{E_2}{E_1}\right|^2 = \left|\frac{te^{-j\phi} - \alpha_R(|t|^2 + |\kappa|^2)}{e^{-j\phi} - \alpha_R t^*}\right|^2 = \frac{|t|^2 + \alpha_R{}^2(|t|^2 + |\kappa|^2)^2 - 2\alpha_R t_r(|t|^2 + |\kappa|^2)\cos\phi}{1 + \alpha_R{}^2|t|^2 - 2\alpha_R t_r\cos\phi} \quad (5.4)$$

where t_r is the real part of t.

If $|t|^2+|\kappa|^2 = 1$ (lossless coupling) and $|t| = t_r$, Eqn. (5.4) can be expressed as:

$$T = \frac{|t|^2 + \alpha_R{}^2 - 2\alpha_R|t|\cos(\phi)}{1 + \alpha_R{}^2|t|^2 - 2\alpha_R|t|\cos(\phi)} = 1 - \frac{(1-|t|^2)(1-\alpha_R{}^2)}{1 + \alpha_R{}^2|t|^2 - 2\alpha_R|t|\cos(\phi)} \quad (5.5)$$

When $\cos\phi = 1$, the transmission reaches minimum:

$$T = \frac{|t|^2 + \alpha_R{}^2 - 2\alpha_R|t|}{1 + \alpha_R{}^2|t|^2 - 2\alpha_R|t|} = \frac{(\alpha_R - |t|)^2}{(1 - \alpha_R|t|)^2} \quad (5.6)$$

The transmission will be zero if $|t| = \alpha_R$.

The resonance wavelengths which cause minimum transmission are expressed as [109]:

$$m\lambda_m = n_{eff}L = 2\pi n_{eff}R \quad (5.7)$$

where λ_m is the resonance wavelength, m is the mode number of the ring resonator, and R is the radius of the ring resonator.

5.1.2 Fabrication and applications

With the development of micro/nanometer technology, the optical microring resonator received significant attention due to its high quality factor (Q) and sensitivity in the past decade. As an important optical component, various optical microring resonators have been designed for different purposes. According to the shapes of the mirocring, the resonator can be classified as ring-shaped [110, 111], racetrack-shaped [112, 113], slot ring-shaped [114], rectangular-shaped [115], and disk-shaped [116, 117]. Microring resonators can be fabricated with different dielectric materials such as silicon [110, 111, 118], SU-8 [113, 119], PMMA [120], polystyrene (PS) [121], and ultra-fast ceramic [122]. Optofluidic ring resonators which use liquids as optical waveguides were also reported [115, 123]. Depending on the distance between the ring and the bus waveguide, these resonators can also be separated into those with gap coupling [110, 112, 119] and gapless coupling [113, 123]. The gap coupling resonators usually have gaps of several hundred nanometers between the looped waveguide and bus waveguide. Another interesting type of ring resonator is the capillary-based microfluidic structure in which the capillary and the tapered fiber are integrated into a miniaturized chip [124-127]. The capillary works as a ring resonator and light couples between the capillary and the tapered fiber.

Ring resonators are very sensitive to environmental parameters such as temperature, liquid, gas, and coatings. Therefore, one of the important applications of ring resonators is sensing, such as RI detection. According to Eqn. (5.7), when a ring resonator is surrounded by a special liquid, the resonator generates specific resonance wavelengths to

respond to the RI of the liquid. As the liquid RI changes, a shift in the resonance mode can be detected. Based on this principle, a variety of chemical and biological liquids have been measured such as sodium chloride, glucose, DNA and proteins [116, 121, 128, 129]. Yebo *et al.* designed an ethanol vapour sensor by coating a thin layer of ZnO nanoparticles on a ring resonator. The RI of porous ZnO film changes with vapour adsorption which results in a shift of the microring resonance [112]. Temperature sensing is another kind of RI-based detection. The RIs of the dielectric material are different at different temperatures due to the thermo-optic coefficient. Therefore, temperature sensors are fabricated based on a ring resonator [109,130]. Teng *et al.* also devised an athermal ring resonator by overlaying a polymer cladding on the silicon wires [131]. A pressure sensor based on a ring resonator was reported by Zhao *et al.* in which mechanical deformation of the ring resonator induced resonance wavelength shifts [132]. Heavy water has been detected using a ring resonator due to the difference of optical absorption between H_2O and D_2O which gives different Q factors [117]. In addition, by combining with optofluidic technology, ring resonator based dye lasers in which the optical feedback is provided by whisper gallery modes have been reported [124,125]. Compared with conventional dye lasers, these structures possess advantages of simplicity and compactness.

5.2 Ring resonator

5.2.1 Ring resonator simulation

Figure 5-2 shows simulation on the transmission spectra in different values of $|t|^2$ and α_R^2 according to Eqn. (5.5). In the simulation, n_{eff} is 1.5583, and the radius of the ring R is 60.00 μm. Multiple optical resonance modes, which are independent of $|t|$ and α_R, appear in the spectral curves. The interval of the neighbouring resonance wavelength (free spectral range) is about 3.96 nm. The extinction ratio is larger when there is a closer matching between the α_R and $|t|$, and the Q factor rises with the increase of $|t|$ or/and α_R.

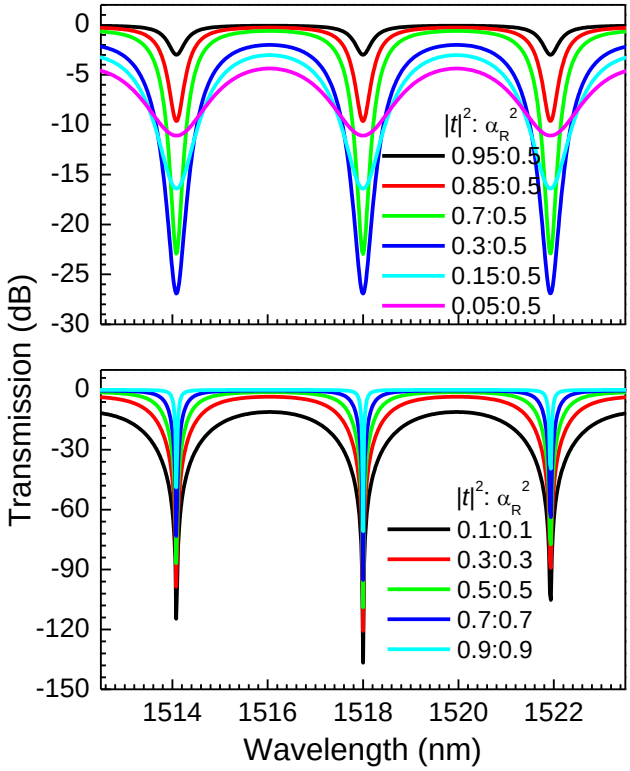

Figure 5-2 Simulation on the transmission spectra in different $|t|^2$ and α_R^2 according to Eqn. (5.5)

Figure 5-3 shows the COMSOL simulation on distribution of the electromagnetic energy of a ring resonator at the wavelengths of 1547 and 1550 nm, respectively. The straight bus waveguide with a width of 4.00 μm adjoins the bottom of a ring waveguide with a width of 4.00 μm and radius of 60.00 μm. The bus waveguide and ring consist of the same material, with an RI of 1.575 (SU-8-2), and surrounded by air. Less electromagnetic energy spreads into the looped waveguide at the wavelength of 1547 nm, whereas most of the electromagnetic energy is coupled and trapped into the looped waveguide at the wavelength of 1550 nm. As a result, a low energy output can be observed in the through port at the wavelength of 1550 nm. Figure 5-4 describes the simulation on the transmission spectrum in the wavelength range of 1535 -1565 nm, in which five optical resonance modes can be observed, including the one at 1550 nm. The free spectral range is about 7.2 nm, and the maximum extinction ratio is about 7.0 dB.

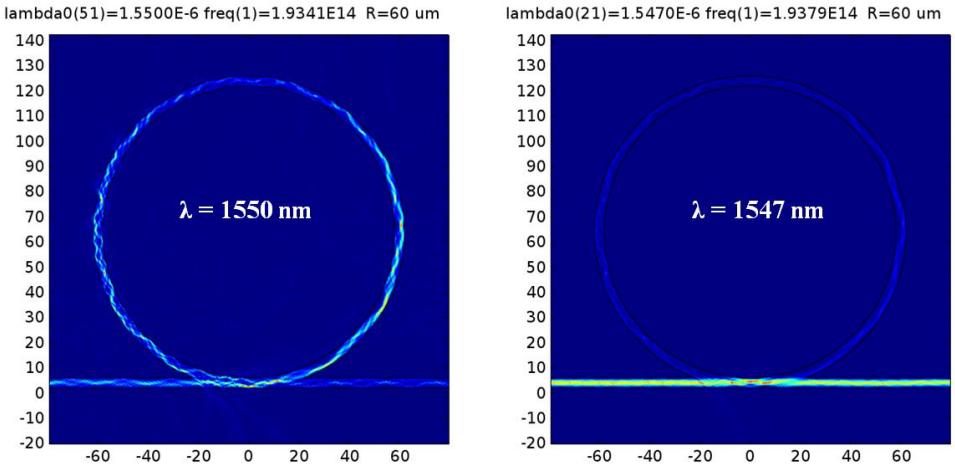

(a) (b)

Figure 5-3 COMSOL simulation on the distribution of the electromagnetic energy at the wavelengths of 1547 and 1550 nm, respectively. The ring resonator has a radius of 60.00 μm and waveguide width of 4.00 μm.

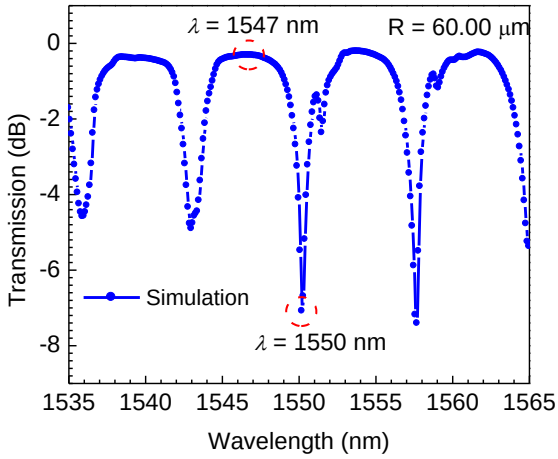

Figure 5-4 COMSOL simulation on the transmission spectrum of a ring resonator with a radius of 60.00 μm and waveguide width of 4.00 μm in the wavelength range of 1535 - 1565 nm

5.2.2 Ring resonator characterization

SU-8-2 is first spin-coated on a cleaned glass slide with a spin speed of 850 rpm for 40 s, and baked on the hotplate at a temperature of 95^{o}C for 50 mins. The thickness of the SU-8 layer is about 4.30 μm. Then a ring-shaped structure and a straight line are scanned by the femtosecond laser with a scan speed of 5 μm/s. The ring structure is left on the glass substrate after the baking and developing processes. As shown in Fig. 5-5(a), a gapless type of ring with a radius of 60.00 μm is produced on the glass slide. The width of the bus waveguide is about 4.20 μm, and the width of the ring waveguide is about 4.50 μm. For protection from dust, the ring is covered with a PDMS layer. The same experimental setup as described in Chapter 4 is adopted to couple light from an Er^{3+} dual-band broadband source into the bus waveguide and transmit it into an OSA. Multiple periodic resonance modes appear in the transmission spectrum as shown in Fig. 5-5(b). According to Eqn. (5.6), the free spectral range can be expressed as:

$$\delta\lambda_m = \lambda_m - \lambda_{m+1} = \frac{\lambda_m}{m+1} \approx \frac{\lambda^2{}_m}{2\pi n_{eff} R} (\text{for } m \gg 1) \tag{5.8}$$

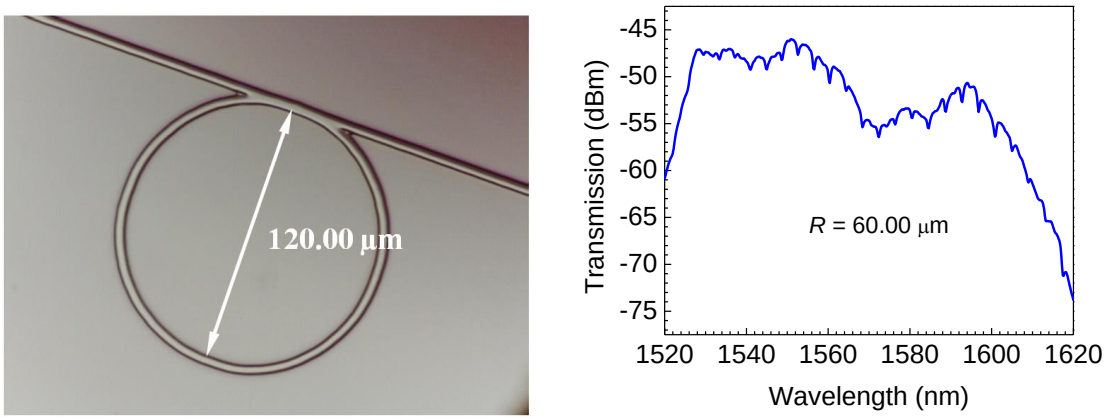

(a) (b)

Figure 5-5 Micro-ring with a radius of 60.00 µm and ring cross section of 4.48 µm×4.23 µm: (a) the morphology, and (b) a transmission spectrum

5.2.1.1 Effect of ring radius

As shown in Eqn. (5.8), the free spectral range is dependent on the radius of the ring. Figure 5-6 presents the transmission spectra of ring resonators with a ring cross section of 4.48 µm×4.23 µm and different radii. The free spectral range decreases with the increase of the radius of the ring. In the ring resonator with a radius of 60.00 µm, the free spectral range is about 3.90 nm, which drops to 1.95 nm in the ring resonator with a radius of 120.00 µm.

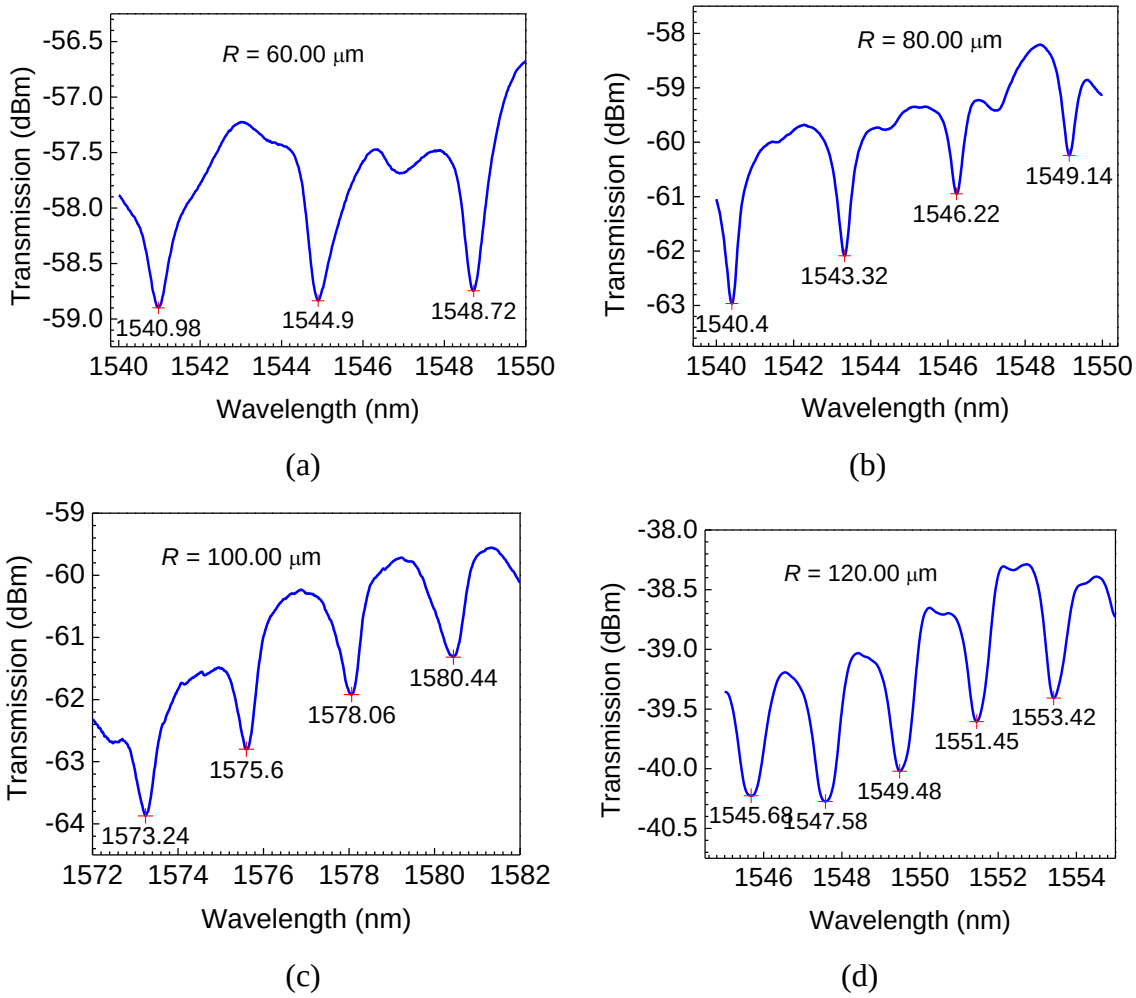

Figure 5-6 Transmission spectra of ring resonators with a ring cross section of 4.48 μm×4.23 μm and different radii

5.2.1.2 Effect of resonance wavelength

The free spectral range is also affected by the resonance wavelength chosen. Figure 5-7 presents two segments of transmission spectra in the ranges of 1460 - 1470 nm and 1570 - 1580 nm for a ring resonator with a radius of 100.00 μm and ring cross section of 4.48 μm×4.23 μm. In the first wavelength range, the free spectral range is about 2.10 nm,

which slightly increases to 2.30 nm in the second wavelength range. Therefore, the free spectral range increases at longer wavelengths.

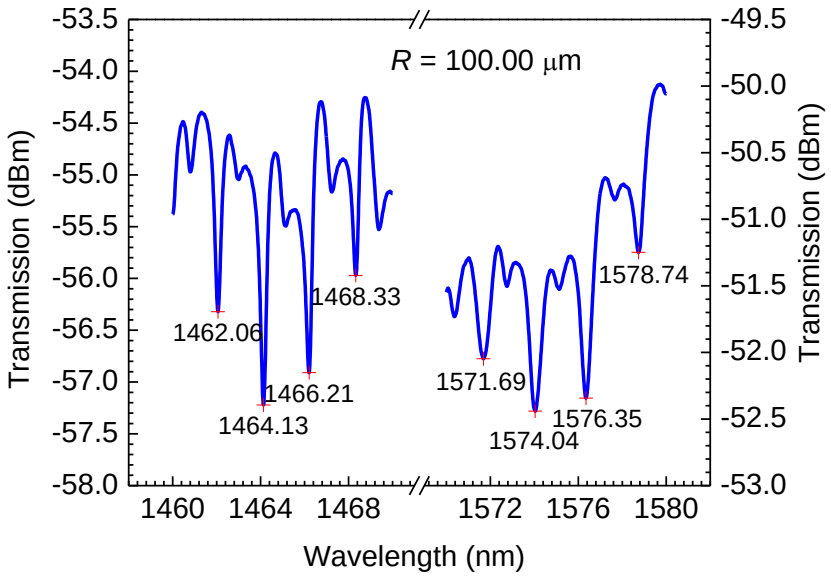

Figure 5-7 Transmission spectra of a ring resonator with a radius of 100.00 μm and ring cross section of 4.48 μm×4.23 μm in different wavelength ranges

5.2.1.3 Effect of core size

In this case, the optical waveguide consists of SU-8-2 core and air cladding. If the core size changes, the effective RI of the waveguide (n_{eff}) will be affected accordingly. Figure 5-8 depicts a group of ring resonators with the same radius (80.00 μm) and different core sizes. The free spectral range is about 2.99 nm in the resonator with a core size of 4.48 μm×4.23 μm, which becomes 3.18 nm in the resonator with a core size of 2.50 μm×2.62 μm. This is reasonable due to the fact that a waveguide with a smaller core has a smaller effective RI as proved in Table 4-1.

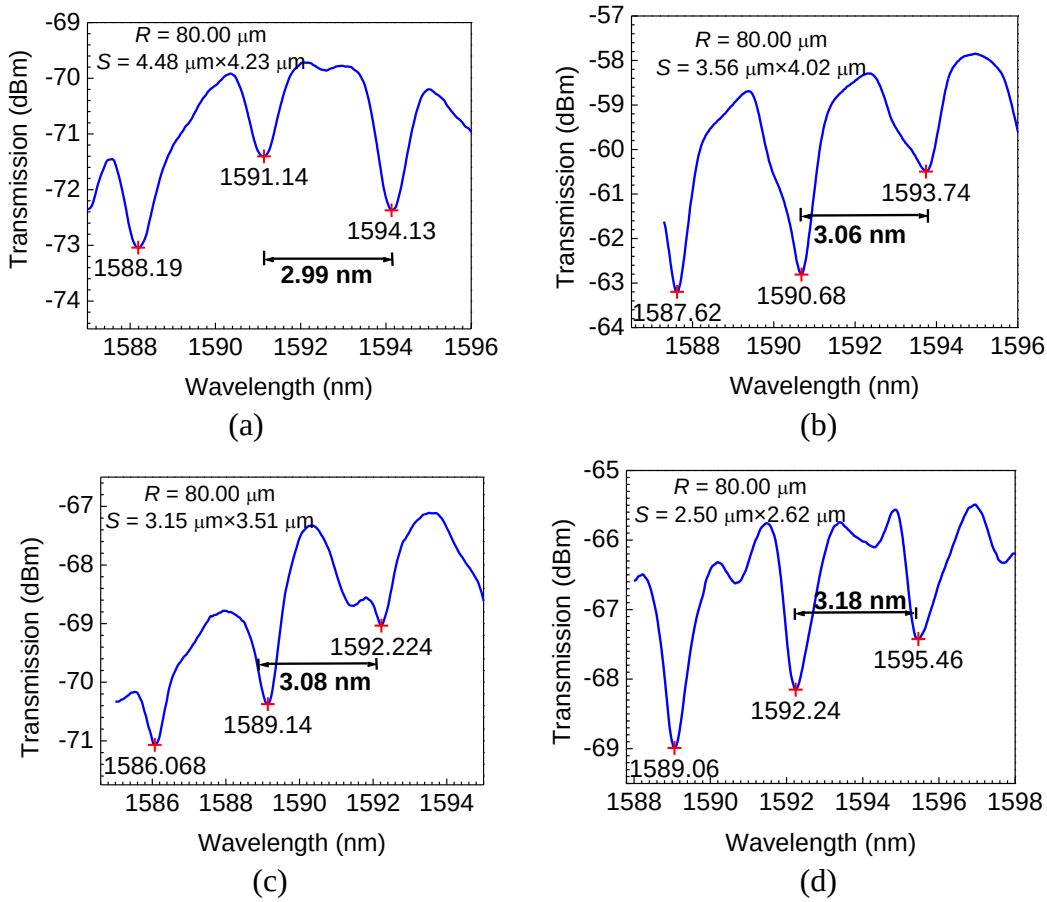

Figure 5-8 Transmission spectra of ring resonators with a radius of 80.00 μm and different core sizes

5.2.1.4 Effect of ring number

A multiple-microring with the same radius is fabricated to test the effect of ring number. Figure 5-9 shows the morphologies and transmission spectra of the ring resonators consisting of one ring and four rings with the radius of 80.00 μm and ring cross section of 4.48 μm×4.23 μm, respectively. The free spectral ranges are not affected by the number of rings, but the full-width half-maximum of the resonance is much wider for the four-ring resonator due to the fact that multiple rings have a larger loss than that of a single-ring resonator.

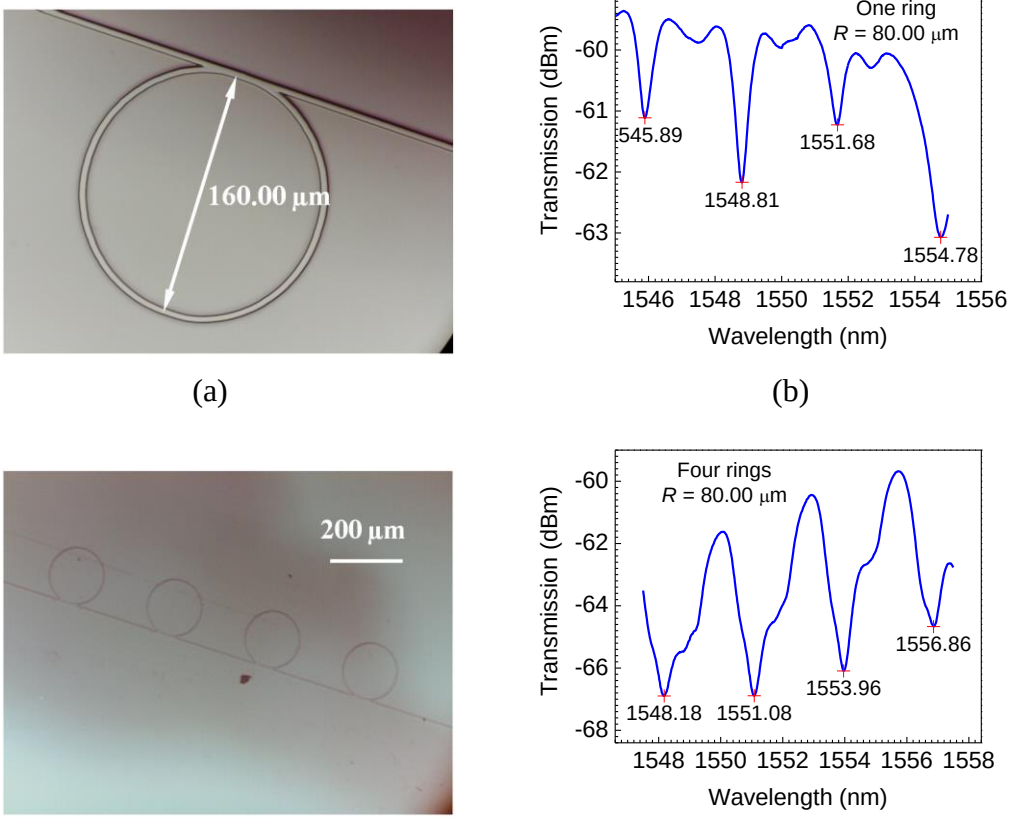

Figure 5-9 Morphologies and transmission spectra of single ring and multiple ring resonators with a radius of 80.00 μm and ring cross section of 4.48 μm×4.23 μm.

5.2.1.5 Effect of polarization

A ring resonator with a rectangular-shaped core is fabricated using a slower scan speed. Transverse-electric (TE) and transverse-magnetic (TM) light transmit in the transverse and horizontal directions along the plane of the ring, respectively. For a rectangular-shaped core, the different lateral boundary conditions for TE and TM modes cause a structural birefringence. As a result, TE and TM light possess different effective RIs. Figure 5-10(a) and (b) show the simulation on TE and TM modes for the waveguide with a cross section of 5.51 μm× 4.13 μm (width × height) at the wavelength of 1550 nm. The

effective RIs of TE and TM modes are 1.5611 and 15610, respectively. In the experiments, a fiber polarizer (Newport®) is connected between the SMF and OSA. The transmitted light with TE or TM mode is obtained by rotating the angle between the SMF and fiber polarizer. Figure 5-10(c) shows the transmission spectra of a ring resonator with the TE mode, TM mode and transmitted light without the polarizer (unpolarised light). The waveguide cross section is 5.51 μm×4.13 μm, and the radius is 80.00 μm. TE and TM modes present different resonance wavelengths due to the different effective RIs, whereas the unpolarised light shows the combination of the resonance wavelengths specific for the TE and TM modes.

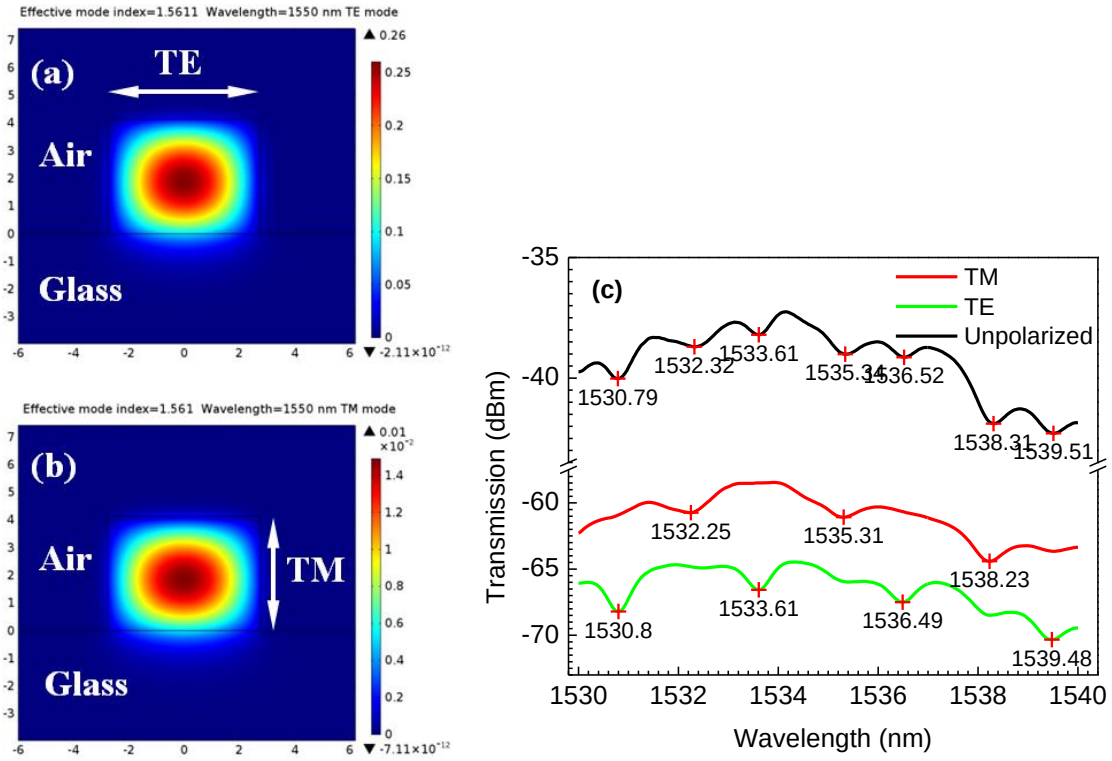

Figure 5-10 Effect of polarization on resonance wavelength: (a) and (b) simulation on TE and TM modes for a waveguide with the cross section of 5.51 μm× 4.13 μm at the wavelength of 1550 nm, and (c) transmission spectra of a ring resonator with a waveguide cross section of 5.51 μm×4.13 μm and radius of 80.00 μm in different polarized modes.

5.2.3 Ring resonator based temperature sensing

Due to the high thermo-optic coefficient of SU-8 material, this type of ring resonator can be used to sense temperature. The resonance peak shift $\Delta\lambda_{m,T}$ is expressed as:

$$\Delta\lambda_{m,T} = \lambda_{m,T'} - \lambda_{m,T} = \frac{2\pi R}{m}(n_{eff,T'} - n_{eff,T}) = \frac{2\pi R}{m}\frac{\delta n}{\delta T}\Delta T = \frac{\lambda_{m,T}}{n_{eff,T}}\frac{\delta n}{\delta T}\Delta T \qquad (5.9)$$

where $\delta n/\delta T$ is the thermo-optic coefficient, and ΔT is the temperature change.

Figure 5-11 shows the transmission spectra at different temperatures and dependence of the peak shift on temperature. The ring resonator has a radius of 60.00 μm and ring cross section of 4.48 μm×4.23 μm. A blue shift occurs as the temperature increases due to the negative thermo-optic coefficient of SU-8 material. The sensitivity is about -9.10×10^{-2} nm/^{o}C.

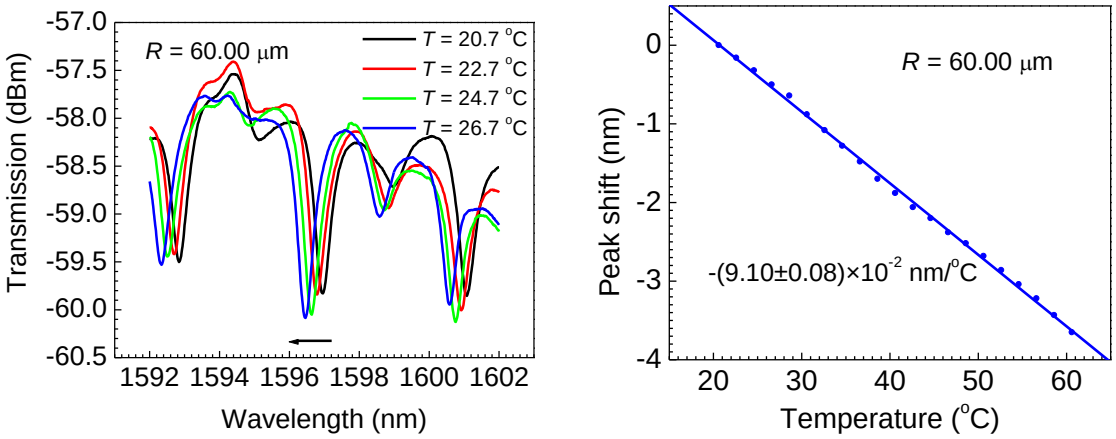

(a) (b)

Figure 5-11 Temperature sensing measurement of a ring resonator with a radius of 60.00 μm and ring cross section of 4.48 μm×4.23 μm: (a) transmission spectra at different temperature, and (b) dependence of the peak shift on temperature

5.2.4 Ring resonator based refractive index sensing

If the ring is covered by a microchannel (Fig. 5-12), the effective RI of the ring resonator can be modified by infusing liquids of different RIs. Therefore, a ring resonator based RI sensor is designed. The equation for RI sensing can be described as follows:

$$\Delta\lambda_{m,n} = \lambda_{m,n'} - \lambda_{m,n} = \frac{2\pi R}{m}(n_{eff,n'} - n_{eff,n}) = \frac{2\pi R}{m}\delta n_{eff,n} = \frac{\delta n_{eff,n}\lambda_{m,n}}{n_{eff,n}} \quad (5.10)$$

where $\delta n_{eff,n}$ is the change of the effective RI of the ring resonator.

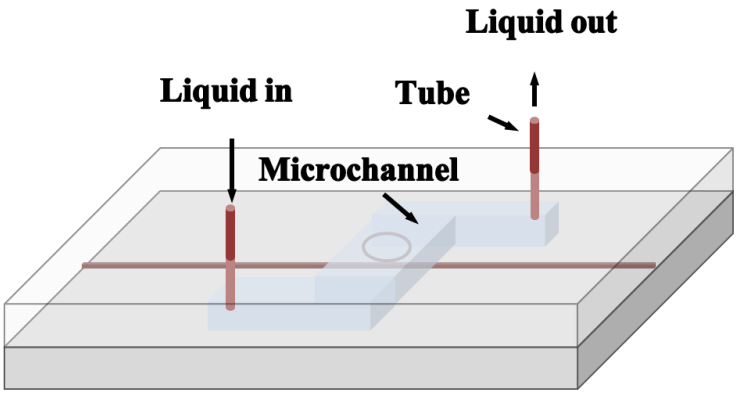

Figure 5-12 Schematic illustration of an optical ring resonator based RI sensor

Figure 5-13 shows the transmission spectra in different RI environment and dependence of the peak shift on the RI in a wavelength range of 1465 - 1470 nm for a resonator with a radius of 100.00 μm and ring cross section of 4.48 μm×4.23 μm. A red shift occurs as the RI increases due to the fact that the effective RI increases with the increase of liquid RI which is proved in Table 4-1. The sensitivity is about 17.56 nm/RIU. In addition, resonance wavelengthes induced by both TE and TM modes can be clearly observed when the resonator is surrounded by liquids with RIs of 1.350 and 1.359,

respectively, whereas the extinction ratios of several resonance (TM mode induced) significatively decrease when liquid with a RI of 1.370 or 1.380 is infused into the microchannel. The reason is that the ring resonator has different transmission coefficients t and propagation loss coefficients α_R for TE and TM modes and these coefficients also change with the environmental parameters such as RI and temperature.

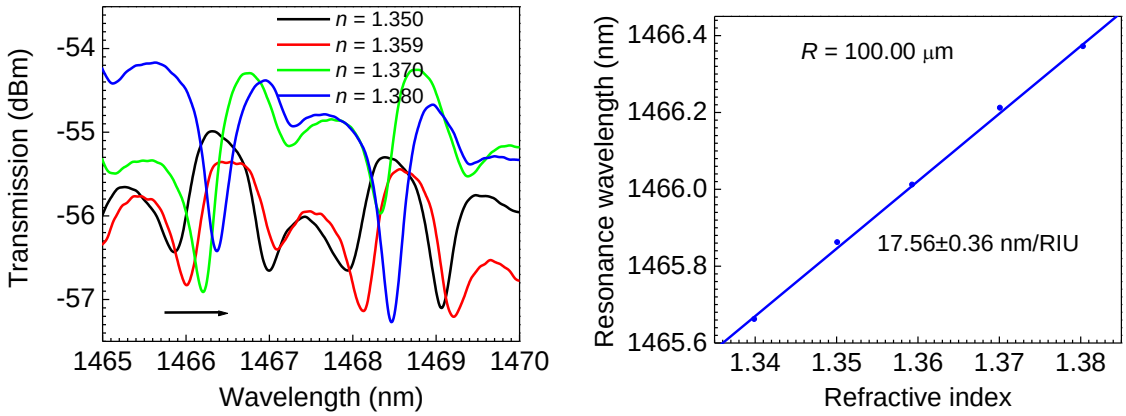

(a) (b)

Figure 5-13 RI sensing measurement of a ring resonator with a radius of 100.00 μm and ring cross section of 4.48 μm×4.23 μm: (a) transmission spectra in different RIs, and (b) dependence of the peak shift on RI

5.2.5 Two-ring based simultaneous refractive index and temperature sensing

5.2.5.1 Two-ring resonator

A two-ring resonator is designed as shown in Fig. 5-14, in which the rings have the same radius. If the rings are covered with different materials such as gas, liquid, or polymer, the two rings will generate different resonance wavelengths which cause an alteration between the two resonance peaks. Two chip samples with a ring radius of 60.00 μm and ring cross section of 4.48 μm×4.23 μm are fabricated. In the first sample, two rings are

both surrounded by air. In the second sample, one of the rings is surrounded by air and the other one is surrounded by PDMS (n = 1.400). Figure 5-15(a) shows the transmission spectrum of the first sample. In this case, two series of resonance wavelengths, which are induced by the two rings, overlap. Figure 5-15(b) shows the transmission spectrum of the second sample. In this situation, the resonance wavelengths of the ring surrounded by air are almost unchanged when they are compared with the first sample, whereas the resonance wavelengths of the ring surrounded by PDMS shift to the red side due to the fact that the effective RI of the ring surrounded by PDMS is larger than that surrounded by air. In addition, the free spectral range of the ring resonator surrounded by air is 3.883 nm which is slightly larger than that of the ring resonator surrounded by PDMS (3.857 nm), as shown in Fig. 5-15(c). The reason is that the ring surrounded by PDMS has a higher effective RI than that of the ring surrounded by air. It has a smaller free spectral range according to Eqn. (5.8). The mode number of the two-ring resonator is also calculated by Eqn. (5.8).

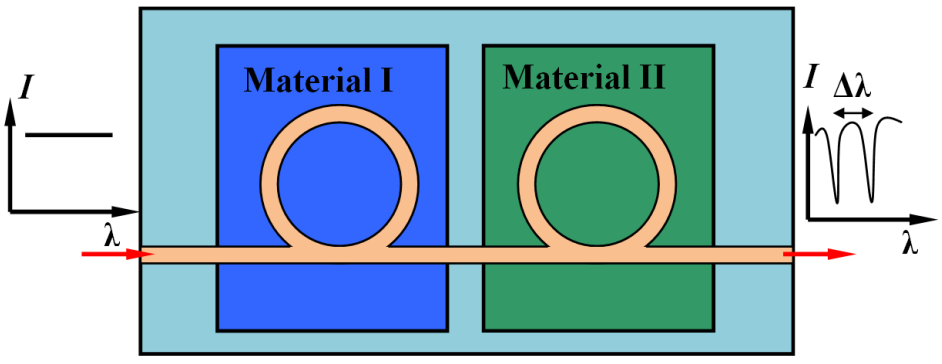

Figure 5-14 Schematic illustration of a two-ring resonator structure

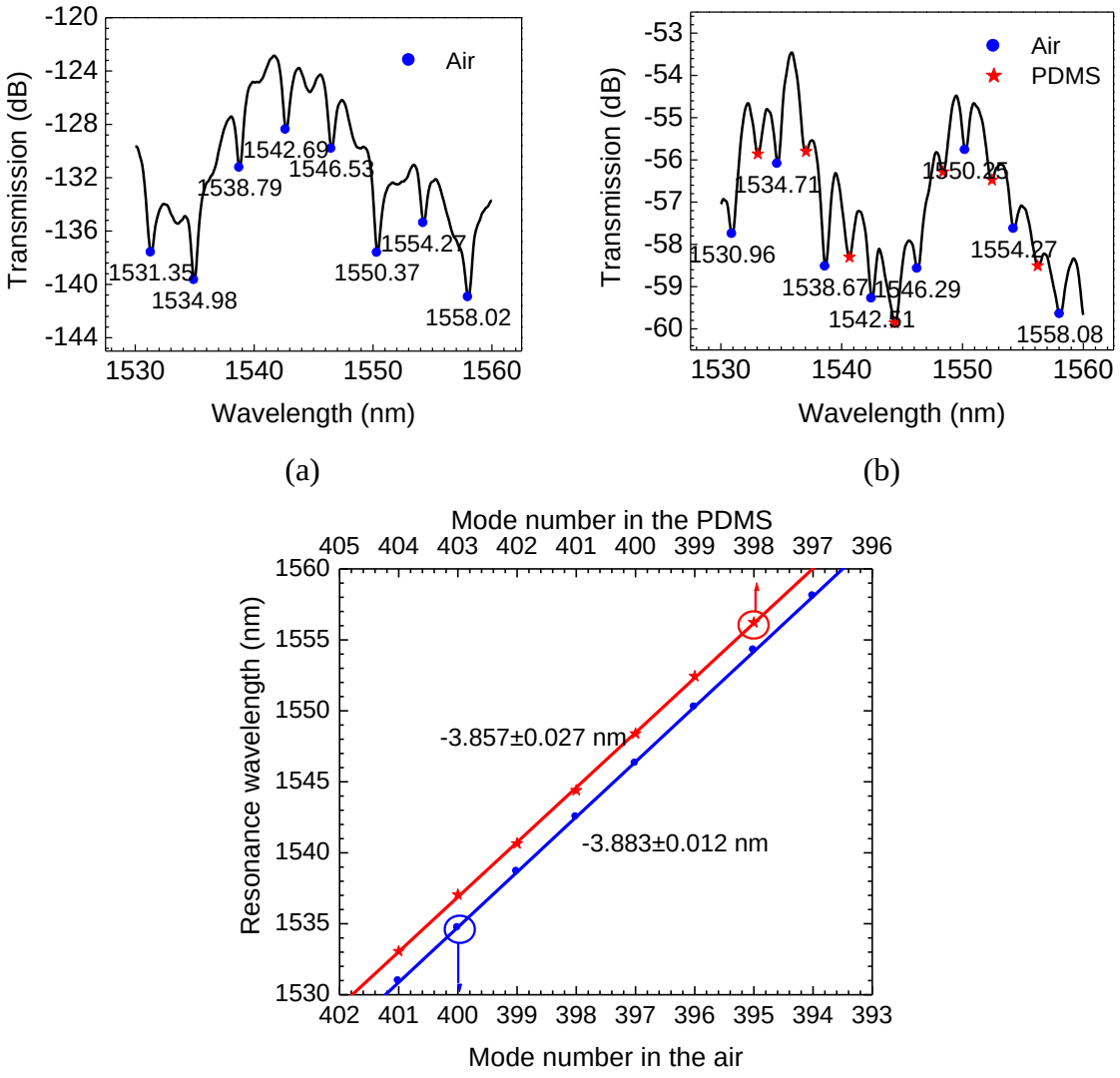

Figure 5-15 Two-ring resonator: (a) a transmission spectrum of a two-ring resonator in which both rings are surrounded by air, (b) a transmission spectrum of a two-ring resonator in which one ring is surrounded by air and the other ring is surrounded by PDMS, and (c) resonance wavelengths induced by two rings. All rings have the same radius of 60.00 μm and ring cross section of 4.48 μm×4.23 μm.

5.2.5.2 Simultaneous refractive index and temperature sensing

In a unique two-ring resonator structure designed and fabricated in this study, illustrated in Fig. 5-16(a), a PDMS layer with a microchannel is employed to cover the two-ring

resonator. In this design, the microchannel covers one of the rings (Fig. 5-16(b)), and the PDMS layer covers the other ring (Fig. 5-16(c)). However, air still surrounds this ring due to an air gap generated between the PDMS and ring. Figure 5-17 presents a transmission spectrum for a two-ring resonator with a radius of 60.00 μm and ring cross section of 4.48 μm×4.23 μm. The chip temperature is maintained at 27.7 ^{o}C, and the microchannel is filled with an NaCl solution with an RI of 1.359. Two series of resonance peaks alternately appear in the transmission spectrum.

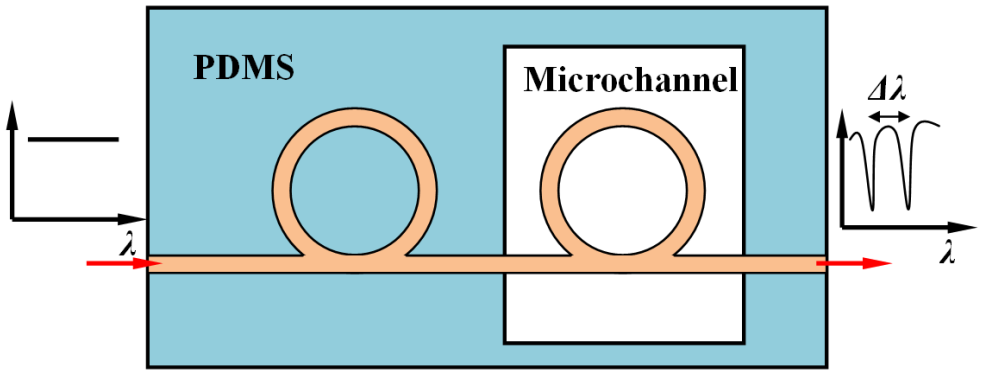

(a)

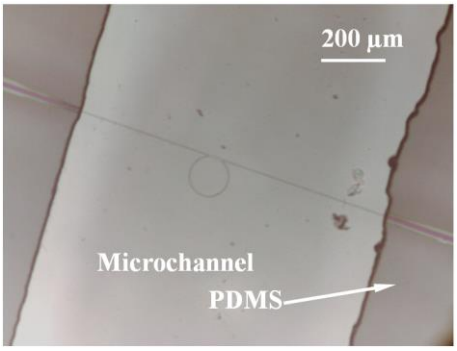

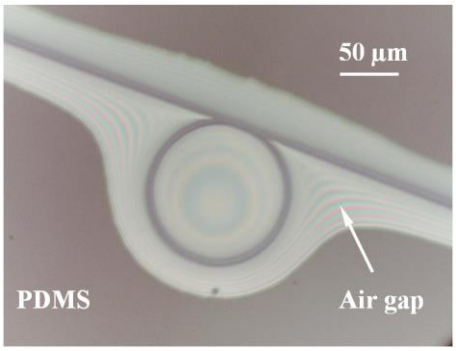

(b) (c)

Figure 5-16 Two-ring resonator sensor: (a) a schematic illustration of a two-ring resonator structure, (b) the morphology of a resonance ring covered by a microchannel, and (c) the morphology of the other resonance ring covered by a PDMS layer. Both resonance rings have a radius of 60.00 μm and ring cross section of 4.48 μm×4.23 μm.

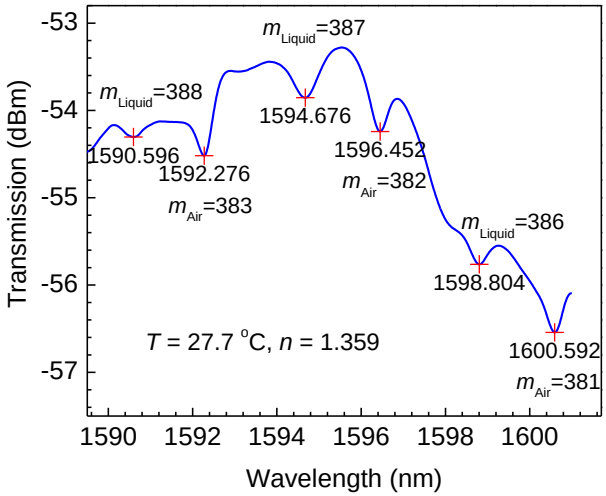

Figure 5-17 Transmission spectrum of a two-ring resonator with a radius of 60.00 μm and ring cross section of 4.48 μm×4.23 μm. One of the rings is covered by PDMS, and the other ring is surrounded by an NaCl solution with an RI of 1.359. The chip temperature is maintained at 27.7 °C.

5.2.5.2.1 Refractive index sensing

NaCl solutions with different RIs are infused into the microchannel in turn to measure the resonance peak shifts. As shown in Fig. 5-18, the resonance wavelengths caused by the ring surrounded by air gap are unchanged, whereas the resonance wavelengths caused by the ring surrounded by liquid appear red shifted with the increasing RI of liquid. The sensitivity of the RI is about 24.2 nm/RIU.

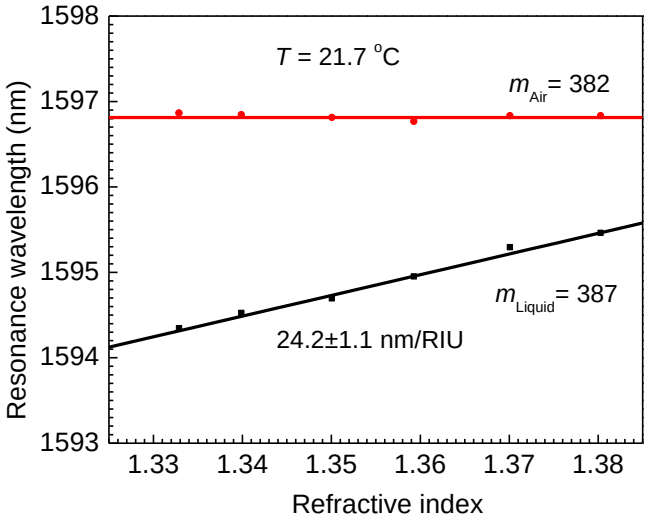

Figure 5-18 Dependence of the peak shift of a two-ring resonator with a radius of 60.00 μm and ring cross section of 4.48 μm×4.23 μm on RI

5.2.5.2.2 Temperature sensing

The microchannel is filled with distilled water. The temperature of the chip is increased by raising the temperature of the hotplate step by step. At each step, the transmission spectrum is recorded when the chip reaches a thermodynamic equilibrium. As shown in Fig. 5-19, both series of resonance wavelengths exhibit blue shifts with simlar sensitivities of -9.10×10^{-2} nm/^{o}C and -9.22×10^{-2} nm/^{o}C, respectively. The experimental results imply that the effective thermo-optic coefficient of a ring resonator $\delta n/\delta T$ will not change in different RI environment.

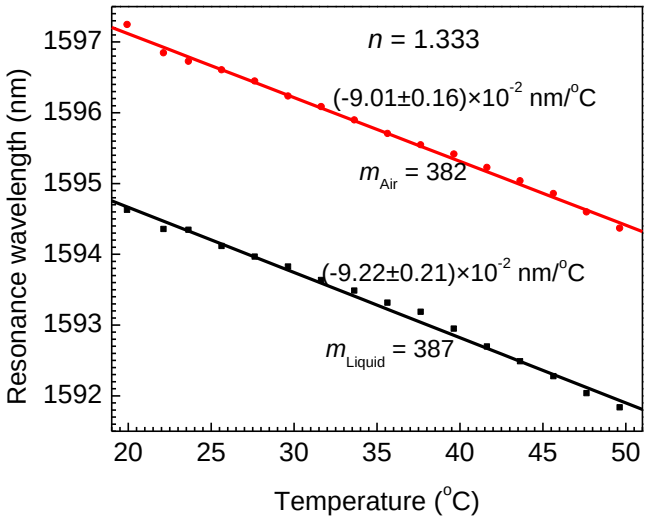

Figure 5-19 Dependence of the peak shift of a two-ring resonator with a radius of 60.00 μm and ring cross section of 4.48 μm×4.23 μm on temperature

5.2.5.2.3 Simultaneous refractive index and temperature sensing

In this case, the ring surrounded by air gap is used for sensing temperature, whereas the ring surrounded by liquid is used for RI sensing. Therefore, the relationship between the shift of the resonance wavelength and the changes in temperature and RI of the liquid can be expressed with a matrix equation:

$$\begin{bmatrix} \Delta T \\ \Delta n \end{bmatrix} = \begin{bmatrix} -9.01\times10^{-2} & 0 \\ -9.22\times10^{-2} & 24.2 \end{bmatrix}^{-1} \begin{bmatrix} \Delta\lambda_{Air} \\ \Delta\lambda_{Liquid} \end{bmatrix} \tag{5.11}$$

where $\Delta\lambda_{Air}$ and $\Delta\lambda_{Liquid}$ are the shifts in the resonance wavelengths of the air gap-surrounded and liquid-surrounded rings, respectively, and ΔT and Δn stand for the changes in temperature and RI, respectively. Figure 5-20 presents transmission spectra of the two-ring resonator under different environmental conditions. The comparision of

actual and test values is listed in Table 5-1. The maxium error is only 0.46% which demonstrates that the experimental results agree with the matrix equation.

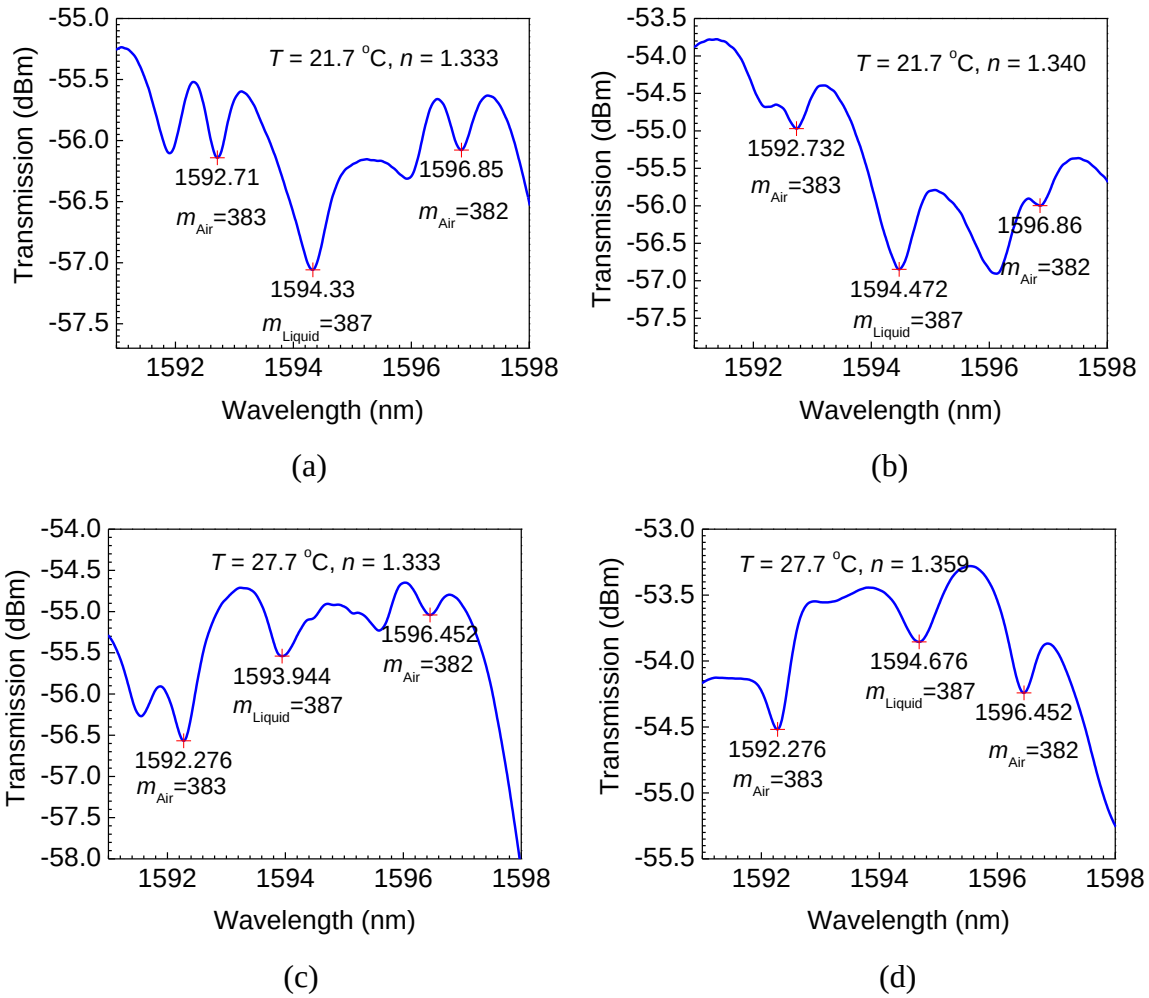

Figure 5-20 Transmission spectra of a two-ring resonator with a radius of 60.00 μm and ring cross section of 4.48 μm×4.23 μm under different environmental conditions.

Table 5-1 Comparison of actual values and test values in different environment for a two-ring resonator with a radius of 60.00 μm

Sample	Actual value		Peak shift		Test value		Error%	
	T(°C)	RI(RIU)	$\Delta\lambda_{Air}$(nm)	$\Delta\lambda_{Liquid}$(nm)	T(°C)	RI(RIU)	T	RI
1 (Ref.)	21.7	1.333	0	0	-	-	-	-
2	21.7	1.340	0.022	0.142	21.46	1.3398	1.1%	0.01%
3	27.7	1.333	-0.434	-0.386	27.52	1.3354	0.65%	0.18%
4	27.7	1.359	-0.434	0.346	27.52	1.3656	0.65%	0.46%

5.3 Racetrack resonator

5.3.1 Racetrack resonator characterization

Racetrack resonator is a type of microring resonator with a racetrack-shaped structure. As shown in Fig. 5-21(a), two half circles connected with two straight lines are designed to generate a looped racetrack waveguide. The radius of the circle is *R*, and the length of the straight line (coupling length) is *L*. A straight bus waveguide is located at the bottom of the looped waveguide with a gap of *G* between the centers of the bus waveguide and the lower straight line. In this case, Eqn. (5.7) can be expressed as:

$$m\lambda_m = (2\pi R + 2L)n_{eff} \tag{5.12}$$

Figure 5-21(b) shows the morphology of a racetrack resonator with a radius of 60.00 μm, coupling length of 30.00 μm, and gap of 4.00 μm. The width of the bus waveguide is about 4.20 μm, and the width of the looped waveguide is about 4.50 μm, which means that the bus waveguide and the looped waveguide are entirely

interconnected. Figure 5-21(c) is a 3D profile of this racetrack resonator observed by a ZYGO nexview^{TM} 3D optical surface profiler (USA), and Figure 5-21(d) is the transmission spectrum of this resonator. Compared with the transmission spectrum of a ring resonator in Fig. 5-5, the racetrack resonator exhibits a higher extinction ratio due to the fact that the longer coupling length induces a smaller transmission coefficient $|t|$ of the resonator which causes a closer matching between α_R and $|t|$.

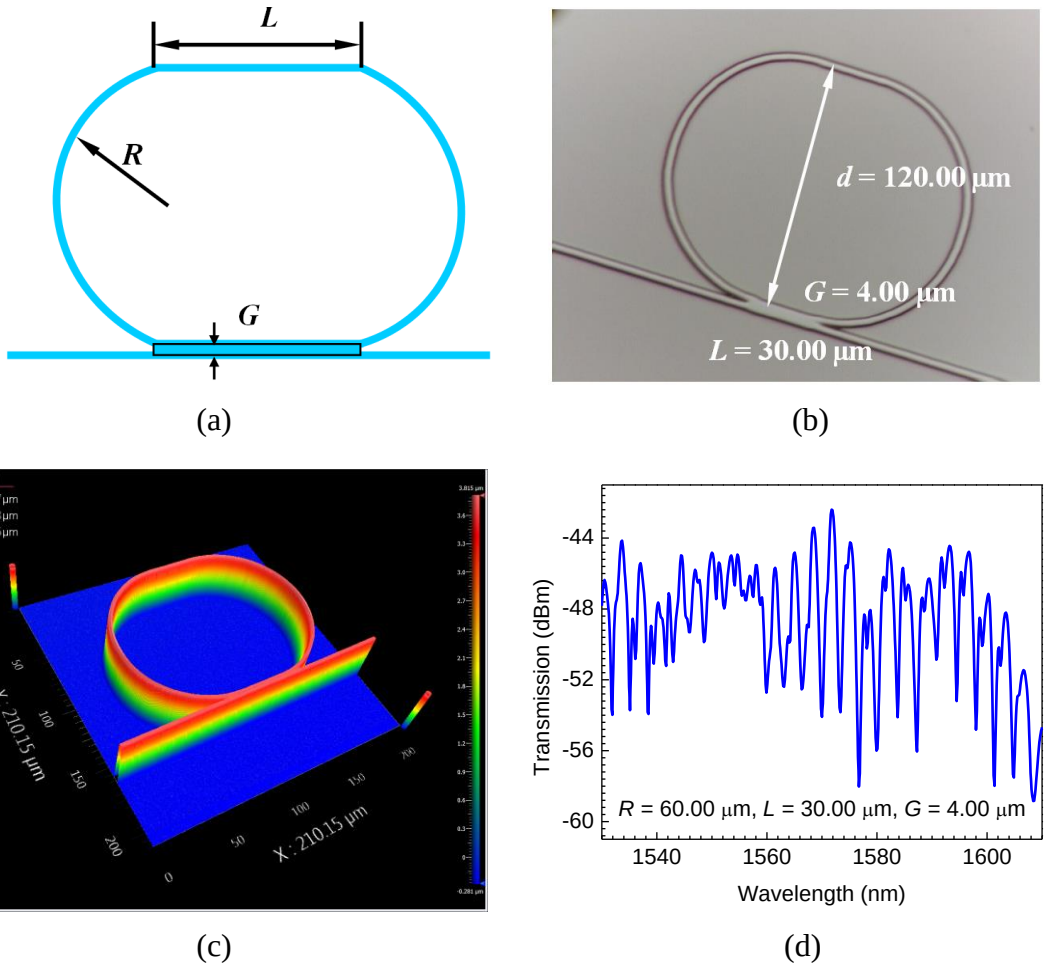

Figure 5-21 Racetrack resonator: (a) a schematic illustration of a racetrack resonator structure, (b) the morphology of a racetrack resonator with a radius of 60.00 μm, coupling length of 30.00 μm, and gap of 4.00 μm, (c) 3D profile of a racetrack resonator observed by a ZYGO 3D optical surface profiler, and (d) transmission spectrum.

Figure 5-22 simulates a transmission spectrum of a racetrack resonator with a radius of 60.00 μm, gap of 4.00 μm, coupling length of 10.00 μm, and width of the waveguide of 4.00 μm in the wavelength range of 1535 - 1565 nm. Four optical resonance modes can be observed. The free spectral range is about 7.0 nm. The insets show the distribution of the electromagnetic energy of the racetrack resonator at the wavelengths of 1547 and 1544.9 nm, respectively. The light propagates along the bus waveguide without influence by the looped waveguide at the wavelength of 1547 nm. However, the majority of the energy is trapped in the looped waveguide at the wavelength of 1544.9 nm which results in a low energy output at the through port.

5.3.1.1 Effect of coupling length

According to Eqn. (5.8), the free spectral range for a racetrack resonator is expressed as:

$$\delta\lambda_m = \lambda_m - \lambda_{m+1} = \frac{\lambda_m}{m+1} \approx \frac{\lambda_m^2}{(2\pi R + 2L)n_{eff}} \qquad \text{for } m \gg 1 \qquad (5.13)$$

in which the free spectral range is dependent on the radius R and coupling length L. If the radius remains a constant, the free spectral range will change with the coupling length. Figure 5-23 presents the transmission spectra of racetrack resonators with a radius of 60.00 μm, width of waveguide of 4.50 μm, gap of 4.00 μm, and different coupling lengths. The free spectral range is about 3.60 nm when the coupling length is 30.00 μm, and drops to 2.80 nm when the coupling length is 90.00 μm. The free spectral range decreases with the increase of the coupling length. In addition, the extinction ratio of the resonance increases with the increase of the coupling length. In the ring resonator, the

maximum extinction ratio is about 5.0 dB as shown in Fig. 5-15. It increases to 12 dB in the racetrack resonator with a coupling length of 10.00 μm, and reaches 30 dB in the racetrack resonator with a coupling length of 30.00 μm.

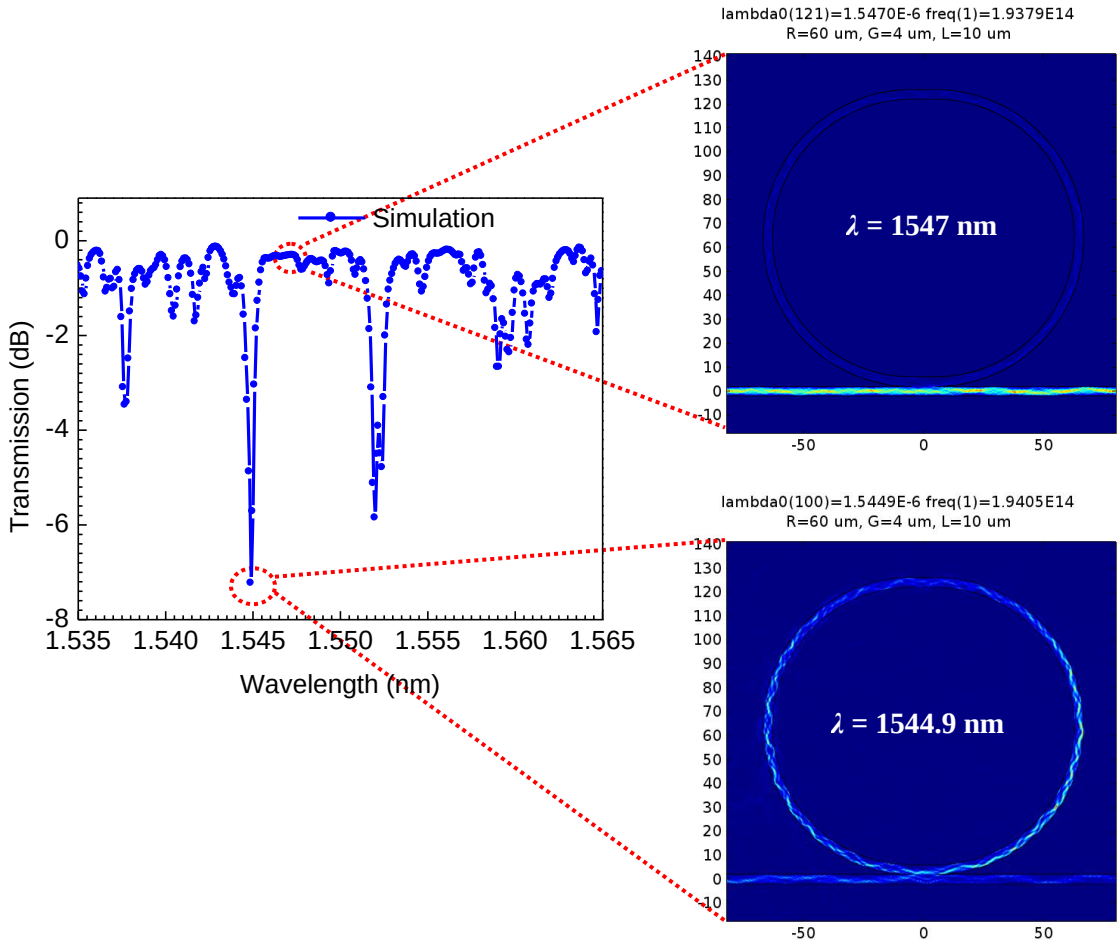

Figure 5-22 COMSOL simulation on the transmission spectrum of a racetrack resonator with a radius of 60.00 μm, waveguide width of 4.00 μm, gap of 4.00 μm and coupling length of 10.00 μm. The insets show the distribution of the electromagnetic energy of the racetrack resonator at the wavelengths of 1547 nm and 1544.9 nm, respectively.

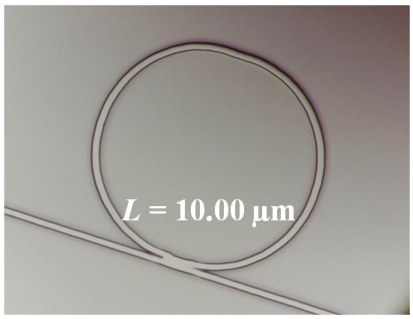

(a)

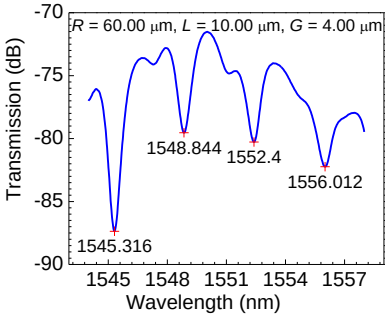

(b)

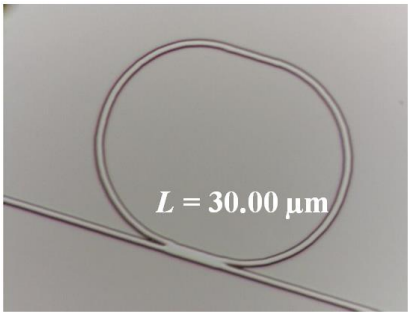

(c)

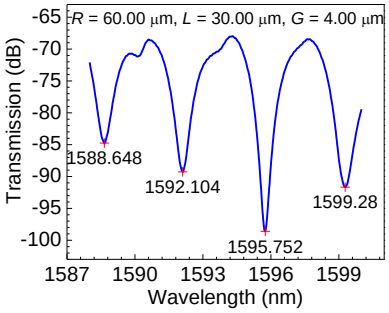

(d)

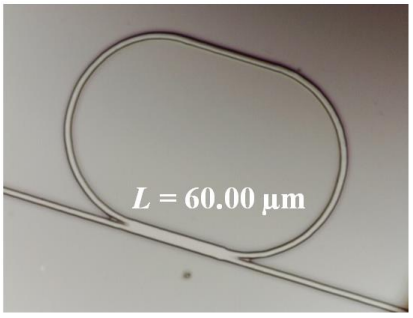

(e)

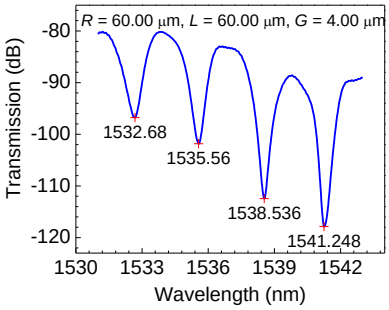

(f)

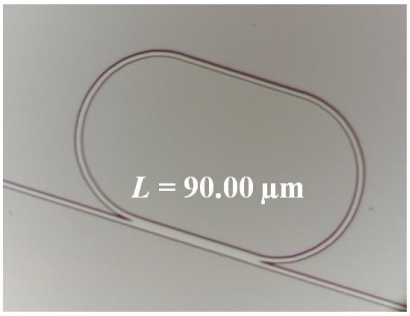

(g)

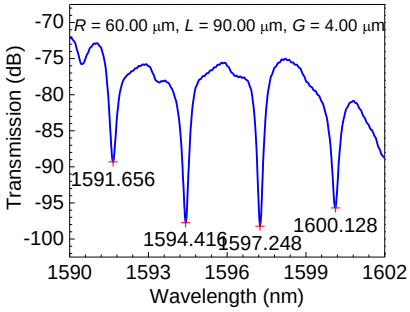

(h)

Figure 5-23 Morphologies and transmission spectra of racetrack resonators with a radius of 60.00 μm, gap of 4.00 μm and different coupling lengths.

5.3.1.2 Effect of resonance wavelength

Figure 5-24 presents two transmission spectra in the wavelength ranges of 1530 - 1540 nm and 1590 - 1604 nm for a racetrack resonator with a radius of 60.00 μm, coupling length of 90.00 μm, and gap of 4.00 μm. In the wavelength range of 1530 - 1540 nm, the free spectral range is about 2.50 nm, which slightly increases to 2.80 nm in the wavelength range of 1590 - 1604 nm. Therefore, the free spectral range increases with the increase of the resonance wavelength.

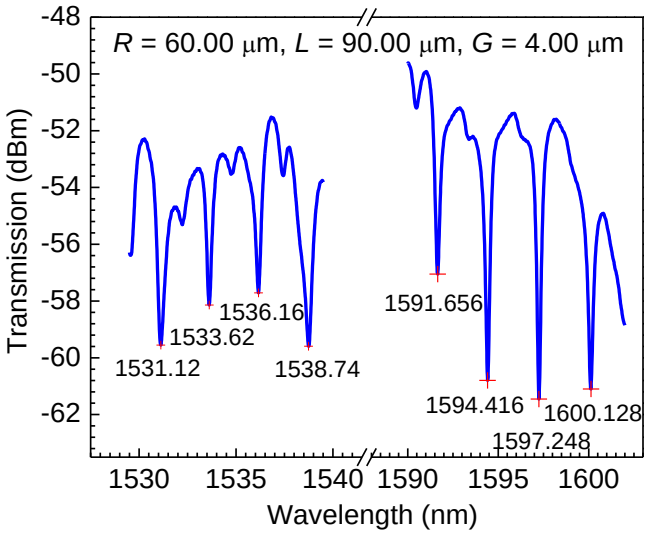

Figure 5-24 Transmission spectra of a racetrack resonator with a radius of 60.00 μm, coupling length of 90.00 μm, and gap of 4.00 μm at different wavelength ranges

5.3.1.3 Effect of gap

For the designed racetrack resonators, the gap (light coupling) region between the bus waveguide and coupling line is fabricated by multiple-scan with the femtosecond laser. Figures 5-25 and 5-26 show the experimental results of the racetrack resonators with a radius of 60.00 μm and different gap distances. Figure 5-27 indicates the extinction ratio

of the resonance in different gap distances. The racetrack resonator with a gap of 4.00 μm reaches a maximum extinction ratio of 30 dB due to the fact that the transmission coefficient $|t|$ has the closest matching with the propagation loss coefficient α_R, whereas the racetrack resonator with a narrower or wider gap has a lower extinction ratio of the resonance.

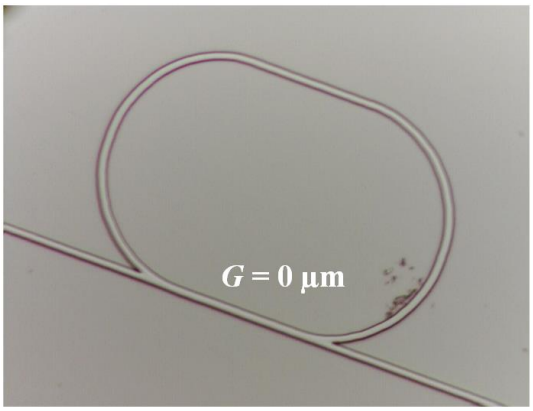

(a)

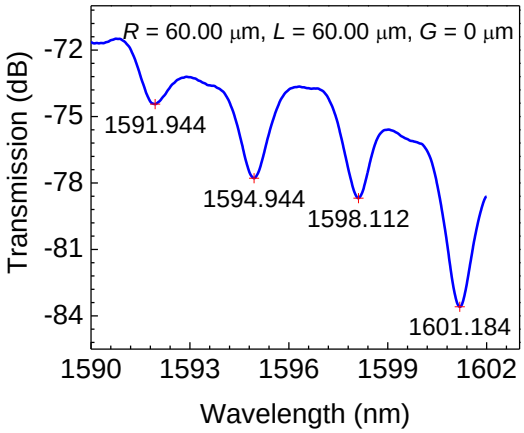

(b)

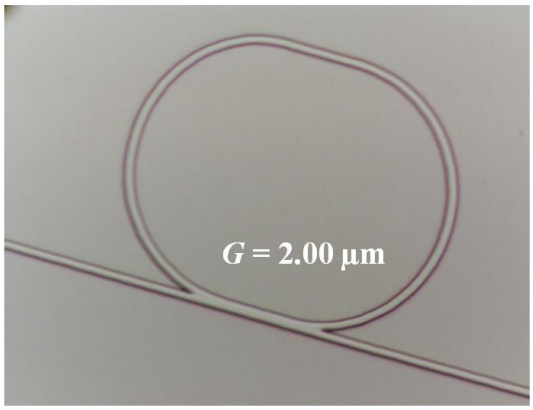

(c)

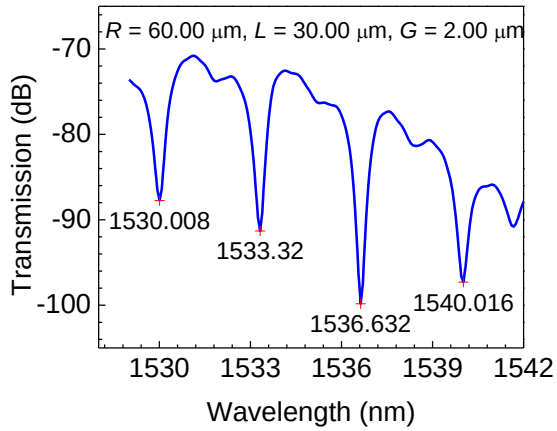

(d)

Figure 5-25 Morphologies and transmission spectra in racetrack resonators with a radius of 60.00 μm and racetrack gaps of 0 and 2.00 μm

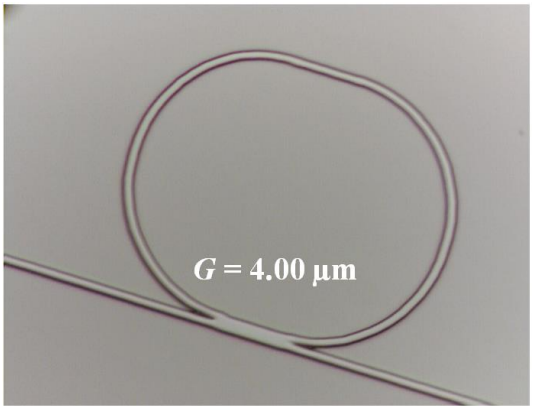

(a)

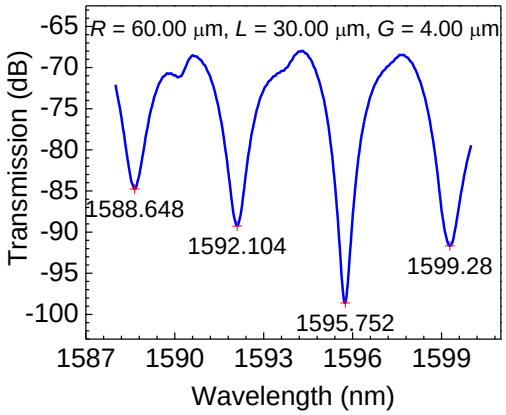

(b)

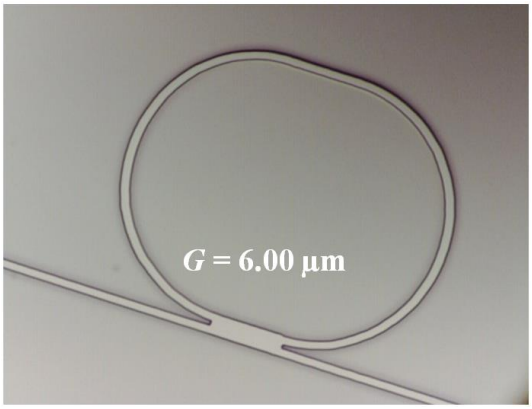

(c)

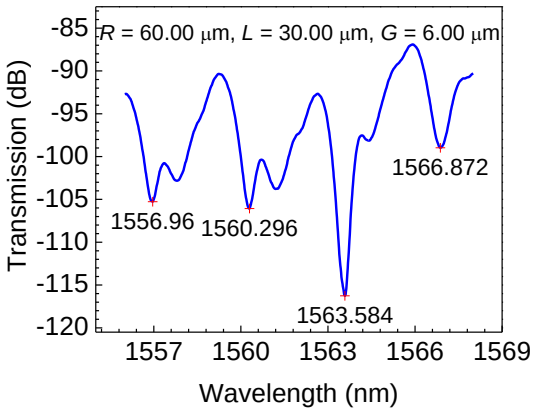

(d)

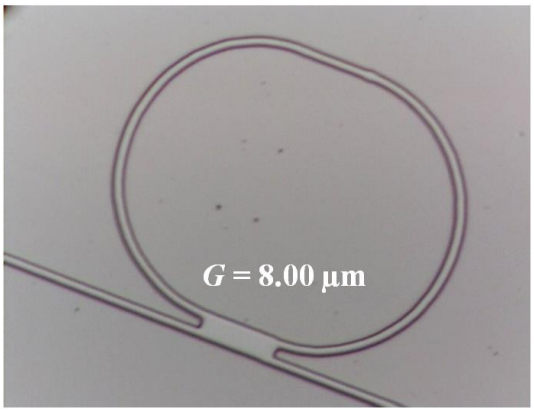

(e)

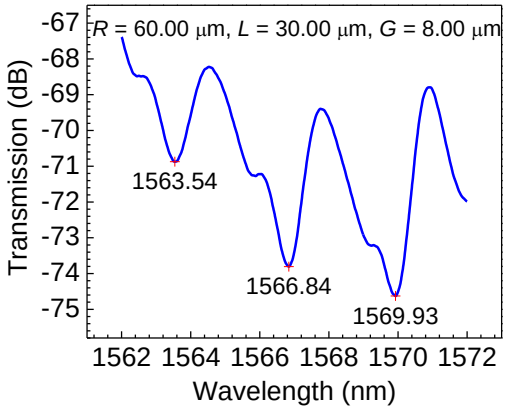

(f)

Figure 5-26 Morphologies and transmission spectra in racetrack resonators with a radius of 60.00 μm and racetrack gaps of 4.00, 6.00 and 8.00 μm

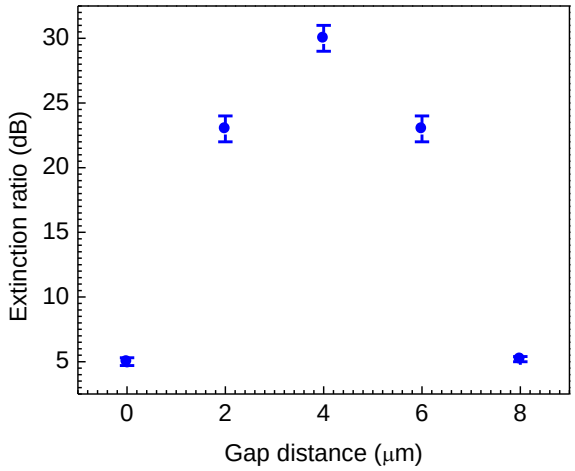

Figure 5-27 Dependence of the extinction ratio of the resonance on gap distance

5.3.1.3 Effect of polarization

The cross section of the racetrack resonator is usually about 4.50 μm×4.15 μm (width × height) after an 850 rpm spin-coat and scanning with a speed of 5 μm/s. Figure 5-28 describes the simulation on the field distribution of TE and TM modes for this core surrounded by air at the wavelength of 1550 nm. The effective RIs of TE and TM modes are 1.5583 and 1.5586, respectively. The TM mode has a slightly larger effective RI than the TE mode. As a result, when the unpolarised light is coupled into the bus waveguide, two series of racetrack resonances are induced by the TE and TM modes. In Fig. 5-29, TM and TE resonances sequentially appear in a transmission spectrum of a racetrack resonator with a radius of 60.00 μm, gap of 4.00 μm, and coupling length of 90.00 μm. The free spectral range of the TE mode is 2.623 nm which is almost the same as that of the TM mode (2.621 nm).

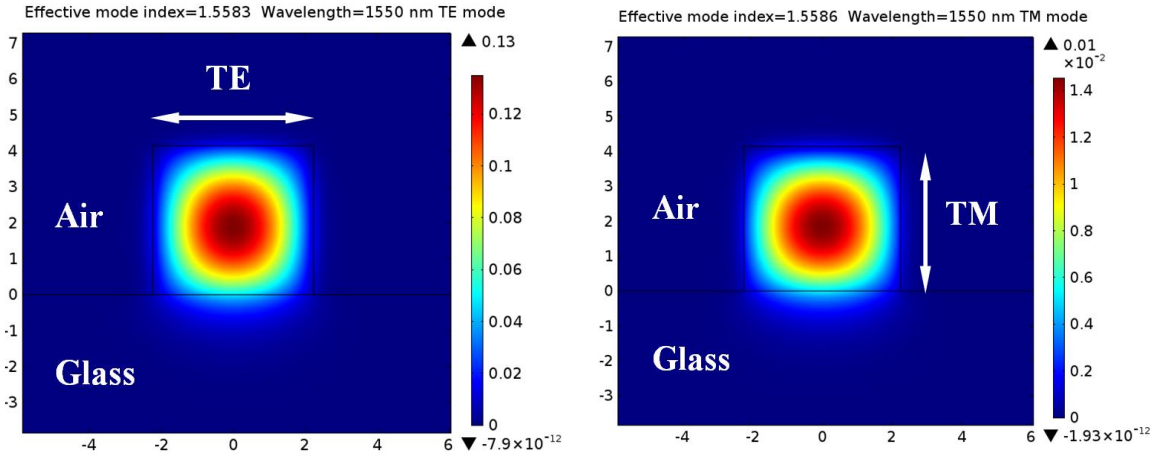

(a) (b)

Figure 5-28 COMSOL simulation on the field distribution of TE and TM modes. The core with a cross section of 4.50 μm×4.15 μm is surrounded by air. The light wavelength is 1550 nm. The effective RIs are 1.5583 and 1.5586, respectively.

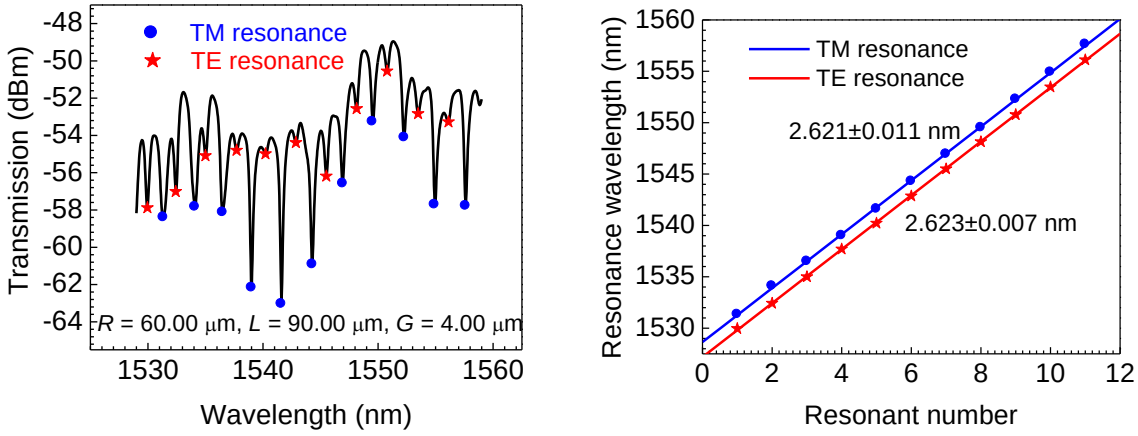

(a) (b)

Figure 5-29 Transmission spectrum (a) and free spectral range (b) of a racetrack resonator with a radius of 60.00 μm, gap of 4.00 μm, and coupling length of 90.00 μm.

5.3.2 Racetrack resonator based temperature sensing

Similar to the ring resonator, the resonance peak shift $\Delta\lambda_m$ of a racetrack resonator can be expressed as:

$$\Delta\lambda_m = \lambda_{m,T'} - \lambda_{m,T} = \frac{2\pi R + 2L}{m}(n_{eff,T'} - n_{eff,T}) = \frac{2\pi R + 2L}{m}\frac{\delta n_{eff}}{\delta T}\Delta T = \frac{\lambda_{m,T}}{n_{eff,T}}\frac{\delta n_{eff}}{\delta T}\Delta T \quad (5.14)$$

This is exactly the same as Eqn. (5.9) in which the sensitivity of the temperature depends on the wavelength, effective RI, and thermo-optic coefficient.

5.3.2.1 Effect of wavelength

A racetrack resonator with a radius of 60.00 μm, coupling length of 90.00 μm, and gap of 4.00 μm are fabricated. The microchannel is filled with distilled water. Figure 5-30 shows the dependences of the peak shift on temperature in two ranges of the wavelength. A blue shift occurs as the temperature increases due to the negative thermo-optic coefficient of the SU-8. The sensitivity is about -8.78×10^{-2} nm/^{o}C in the range of 1528 - 1538 nm, which rises to -9.16×10^{-2} nm/^{o}C in the range of 1589 - 1599 nm. This result matches Eqn. (5.14) in which the sensitivity is a linear function of the wavelength.

5.3.2.2 Effect of coupling length and gap

Several racetrack resonators with different coupling lengths and gaps have been investigated. Figure 5-31 presents the sensitivities of different samples. The sensitivities are about -8.80×10^{-2} nm/^{o}C which exhibit no obvious dependence on the coupling length and gap.

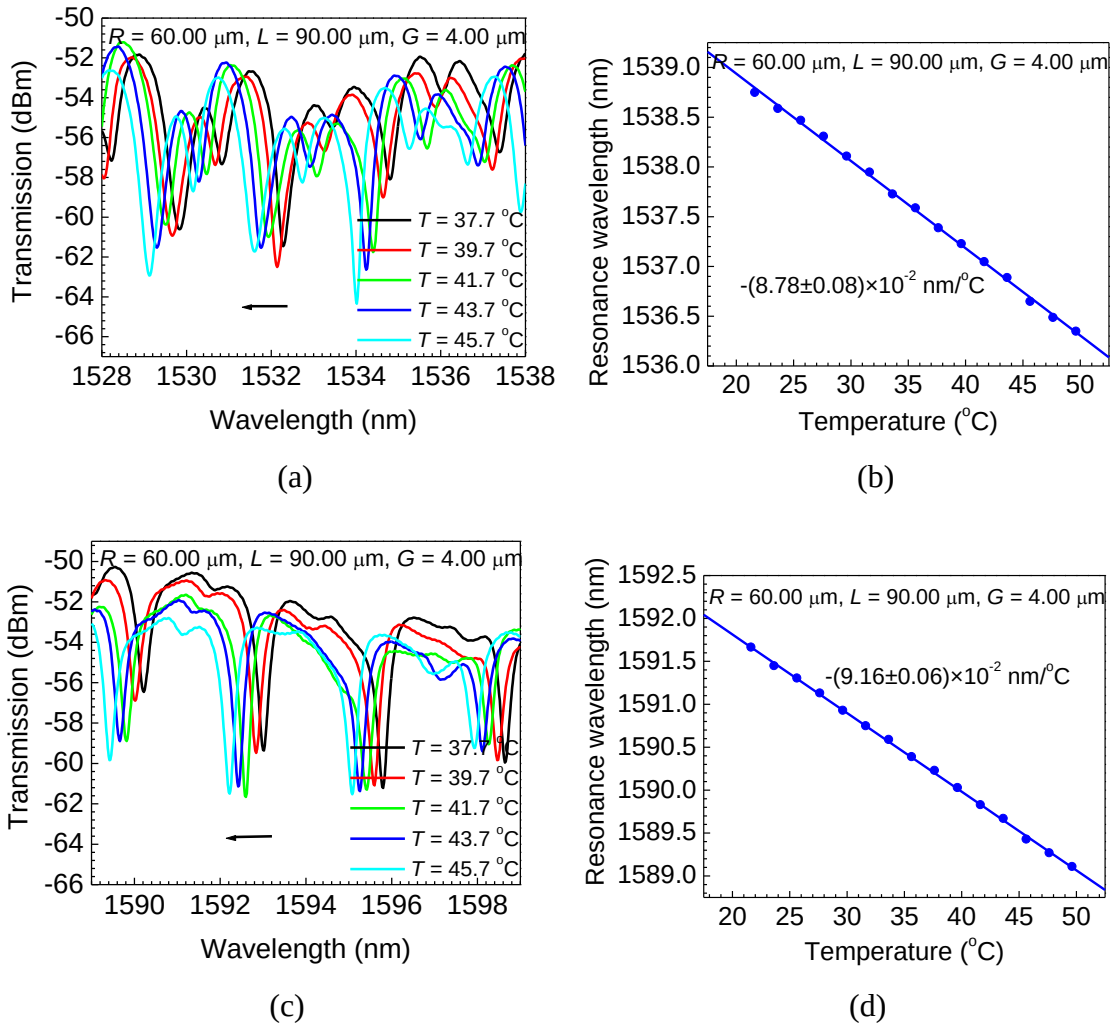

Figure 5-30 Transmission spectra and resonance wavelengths at different temperatures. The racetrack resonator has a radius of 60.00 μm, coupling length of 90.00 μm, and gap of 4.00 μm. The microchannel is filled with distilled water.

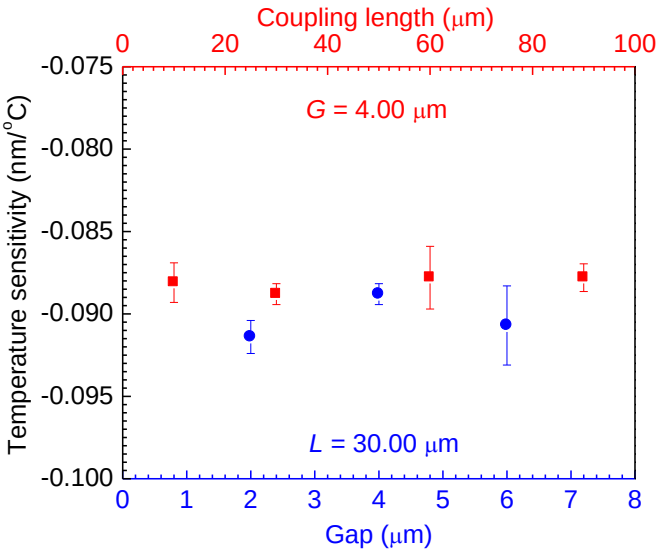

Figure 5-31 Dependence of the temperature sensitivity of racetrack resonators with a radius of 60.00 μm on gap and coupling length

5.3.2.3 Effect of polarization

The temperature sensitivities of the TE and TM modes are also studied. Figure 5-32 shows the simulation on the effective RIs of the TE and TM modes at different temperatures. The core with the cross section of 4.50 μm×4.15 μm is surrounded by water, and the light wavelength is 1550 nm. Both the effective RIs of the TE and TM modes decrease with the increase of the temperature. The slopes (effective thermo-optic coefficients) are almost the same. Figure 5-33 presents the transmission spectra and dependence of the resonance wavelength of a racetrack resonator on temperature. The racetrack resonator has a cross section of 4.50 μm×4.15 μm, radius of 60.00 μm, coupling length of 90.00 μm, and gap of 4.00 μm. The microchannel is filled with distilled water. The sensitivities of the TE and TM resonances have no obvious difference with a value of about -8.80×10^{-2} nm/°C. The reason is that TE and TM modes have the same effective

thermo-optic coefficient according to the simulation, and the effect of the difference in the effective RI can be neglected.

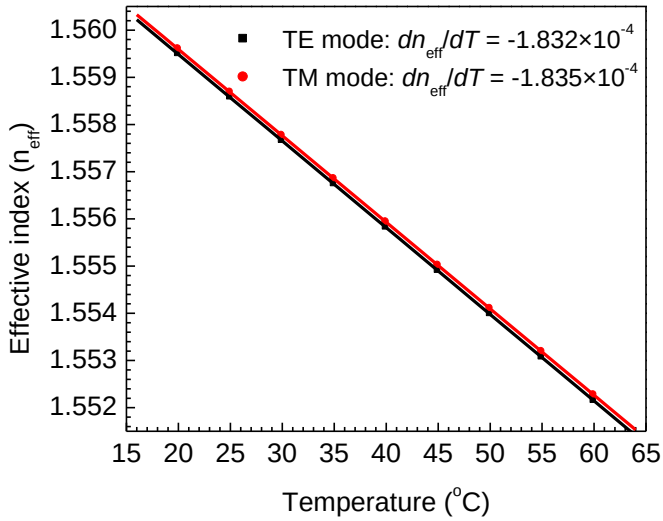

Figure 5-32 COMSOL simulation on effective RIs of the TE and TM modes at different temperatures. The core with a cross section of 4.50 μm×4.15 μm is surrounded by water. The wavelength is 1550 nm.

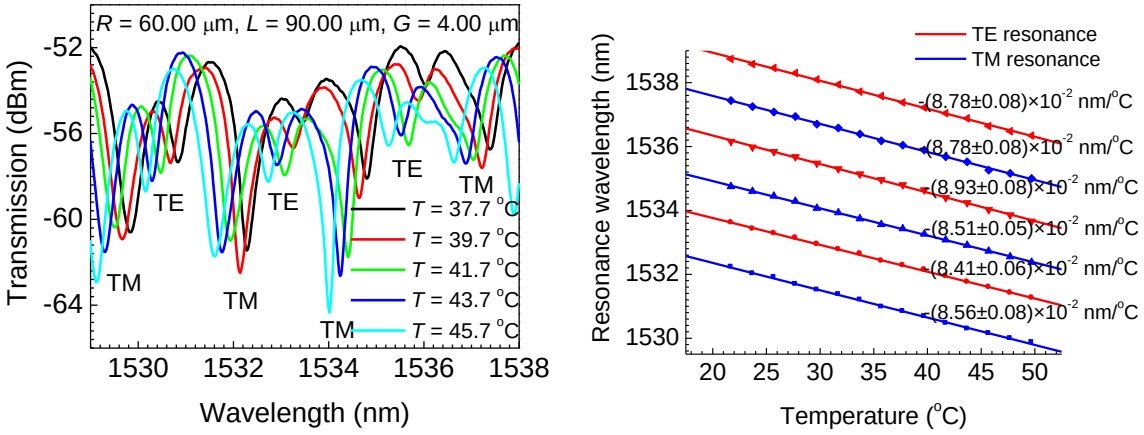

(a) (b)

Figure 5-33 Effect of polarization on temperature sensing: (a) transmission spectra of a racetrack resonator with a core cross section of 4.50 μm×4.15 μm, radius of 60.00 μm, coupling length of 90.00 μm, and gap of 4.00 μm at different temperatures, and (b) dependence of the TE and TM resonance wavelength on temperature.

5.3.3 Racetrack resonator based refractive index sensing

The equation for RI sensing can be described as follows:

$$\Delta\lambda_{m,n} = \lambda_{m,n'} - \lambda_{m,n} = \frac{2\pi R + 2L}{m}(n_{eff,n'} - n_{eff,n}) = \frac{2\pi R + 2L}{m}\delta n_{eff,n} = \frac{\delta n_{eff,n}\lambda_{m,n}}{n_{eff,n}} \qquad (5.15)$$

This is exactly the same as Eqn. (5.10), in which the sensitivity of the RI depends on the wavelength, effective RI, and RI difference.

5.3.3.1 Effect of wavelength

Figure 5-34 shows the dependence of the peak shift on the RI in two different wavelength ranges for a resonator with a radius of 60.00 μm, coupling length of 30.00 μm, and gap of 4.00 μm. A red shift occurs with the increasing RI which has been proved in the ring resonator in section 5.2.3. The sensitivities are about 25.34 nm/RIU in the wavelength range of 1528 - 1540 nm and 28.37 nm/RIU in the wavelength range of 1588 - 1600 nm. Measurement performed at a longer resonance wavelength possesses a higher sensitivity of RI.

5.3.3.2 Effect of coupling length and gap

The RI sensitivities for the samples with different gaps and coupling lengths have also been studied, which is shown in Fig. 5-35. The sensitivities of the RI remain 25 nm/RIU regardless of the coupling length and gap. The sensitivity of a resonator with a coupling length of 30.00 μm and gap of 2.00 μm drops to 16 nm/RIU (red dot circle) due to polarization which will be discussed in the following section 5.3.3.3.

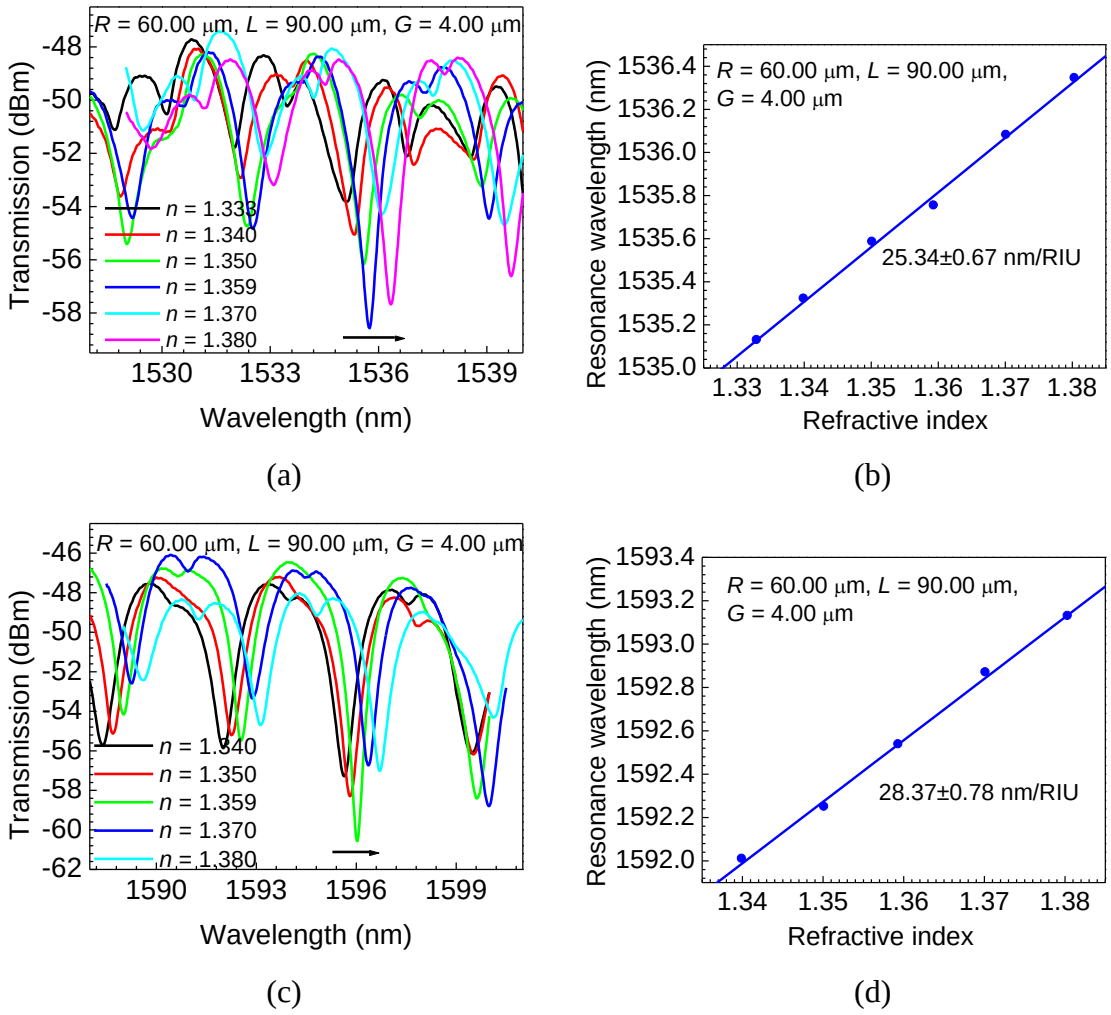

Figure 5-34 Transmission spectra and resonance wavelengths in different RI liquids. The racetrack resonator has a radius of 60.00 μm, coupling length of 30.00 μm, and gap of 4.00 μm.

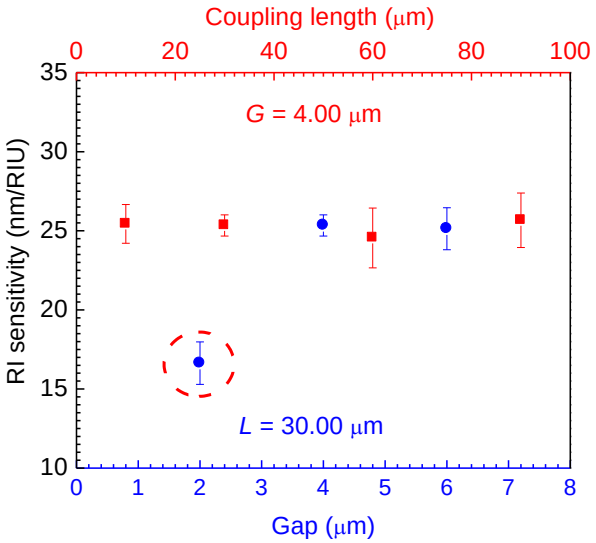

Figure 5-35 RI sensitivities for racetrack resonators with different gaps and coupling lengths.

5.3.3.3 Effect of polarization

Figure 5-36 presents the simulation on the effective RIs of the TE and TM modes surrounded by different liquids. Both the effective RIs of the TE and TM modes increase with the increase of the liquid RI. However, unlike the temperature changes, the effective RI of the TE mode is more sensitive to the changes of the liquid RI than that of the TM mode due to the fact that for a strip waveguide, the TE light which transmits in the transverse direction interacts with the liquid from left and right surfaces, whereas the TM light which transmits in the horizontal direction interacts with the liquid from the top surface. The RI sensitivities for the TE and TM modes have a great difference according to the experimental results shown in Fig. 5-37. The sensitivity of the TM mode is about 16 nm/RIU, and the sensitivity of the TE mode is about 25 nm/RIU. TE resonances present a higher RI response than TM resonances. This is the reason that the RI sensitivity

of the resonator with a coupling length of 30.00 μm and gap of 2.00 μm drops to 16 nm/RIU (TM modes) when the other RI sensitivities are 25 nm/RIU (TE modes) in Fig. 5-35.

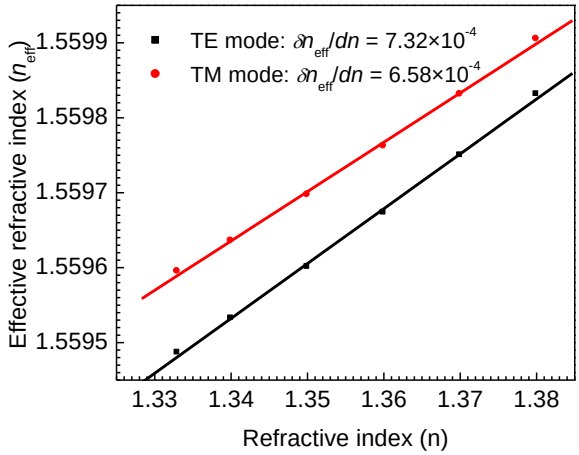

Figure 5-36 COMSOL simulation on effective RIs of the TE and TM modes in different RI liquids. The core has a cross section of 4.50 μm×4.15 μm, and the wavelength is 1550 nm.

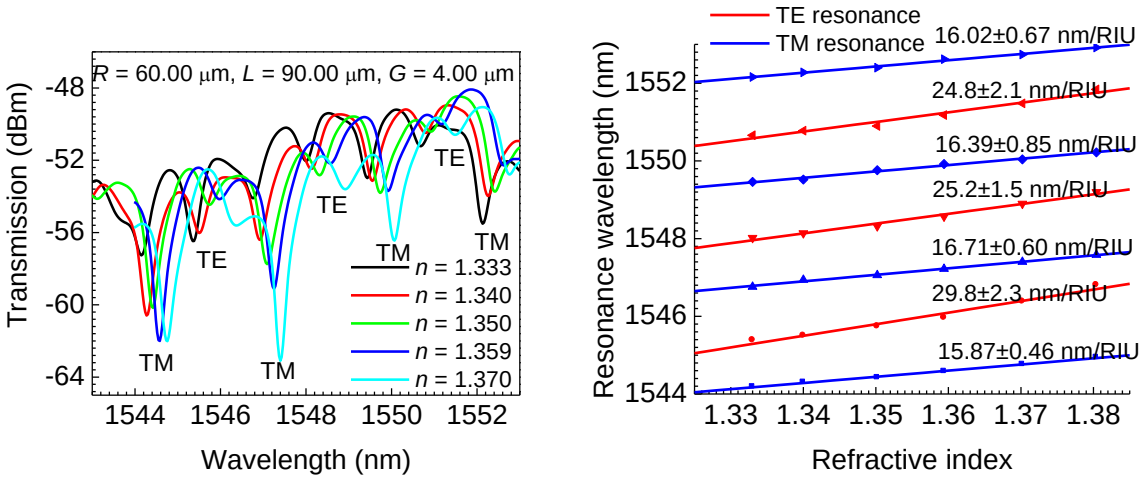

(a) (b)

Figure 5-37 Effect of polarization on RI sensing: (a) transmission spectra of a racetrack resonator with a cross section of core of 4.50 μm×4.15 μm, radius of 60.00 μm, coupling length of 90.00 μm, and gap of 4.00 μm in different RI liquids, and (b) dependence of the TE and TM resonance wavelengths on RI.

5.3.4 Simultaneous refractive index and temperature sensing with a two-racetrack resonator

A two-racetrack resonator has been fabricated on a bus waveguide. One of the racetracks is covered with a PDMS layer for temperature sensing, and the other one is covered with a microchannel for RI sensing. Figure 5-38(a) depicts the schematic illustration of the structure, and (b) presents the transmission spectrum of a two-racetrack resonator with a radius of 60.00 μm, coupling length of 30.00 μm, and gap of 4.00 μm. The microchannel is filled with an NaCl solution with an RI of 1.370. Two series of resonances appear on the spectrum, in which the group marked with red stars comes from the resonator covered with PDMS layer, whereas the other group marked with blue dots comes from the resonator covered with an NaCl solution.

5.3.4.1 Refractive index sensing

NaCl solutions with different RIs are infused into the microchannel in turn to measure the shifts of the resonance wavelengths. As shown in Fig. 5-39, the resonance wavelengths induced by the temperature sensing racetrack are unchanged, whereas a red shift appears in the resonance wavelengths induced by the RI sensing racetrack with the increase of the liquid RI. The RI sensitivity is about 16.46 nm/RIU.

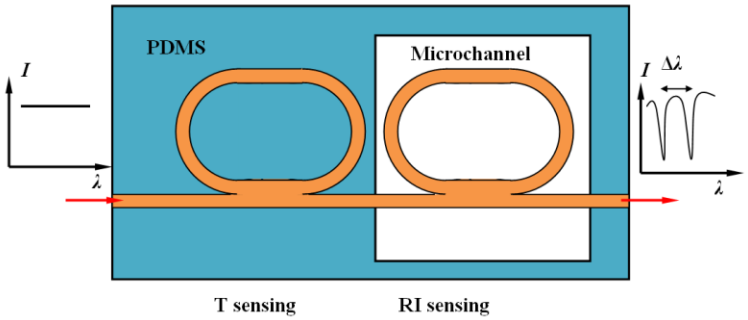

(a)

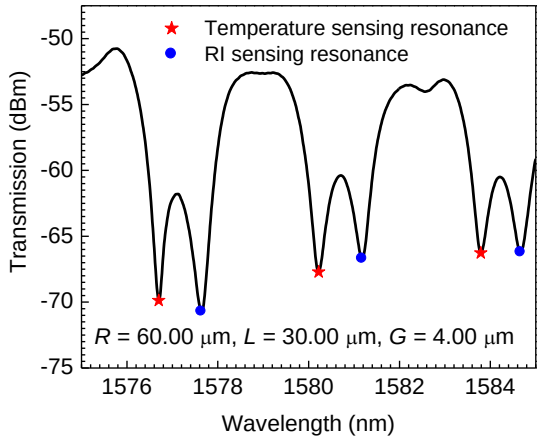

(b)

Figure 5-38 Two-racetrack resonator: (a) a schematic illustration of a two-racetrack resonator, and (b) a transmission spectrum of a two-racetrack resonator with a radius of 60.00 μm, coupling length of 30.00 μm, and gap of 4.00 μm.

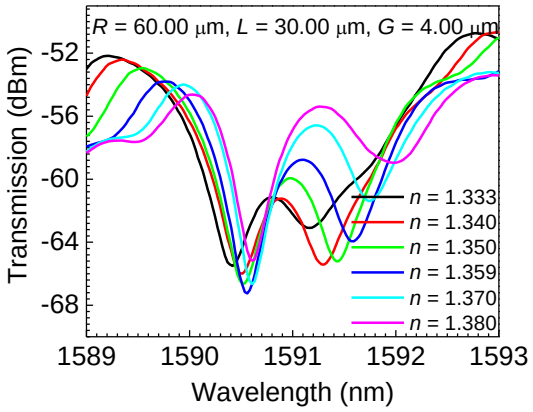

(a)

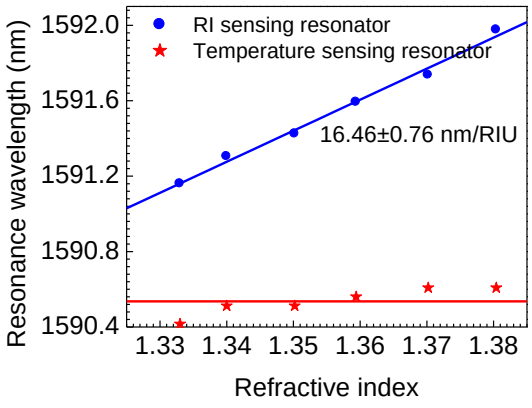

(b)

Figure 5-39 RI sensing with a two-racetrack resonator. The two-racetrack resonator has a radius of 60.00 μm, coupling length of 30.00 μm, and gap of 4.00 μm.

5.3.4.2 Temperature sensing

The microchannel is filled with distilled water, and the chip is heated on a small hotplate. The temperature of the resonator varies following the change in the temperature of the hotplate. As shown in Fig. 5-40, the resonance wavelengths induced by two racetracks both move to the blue side with almost the same sensitivities of -10.10×10^{-2} and -10.16×10^{-2} nm/°C.

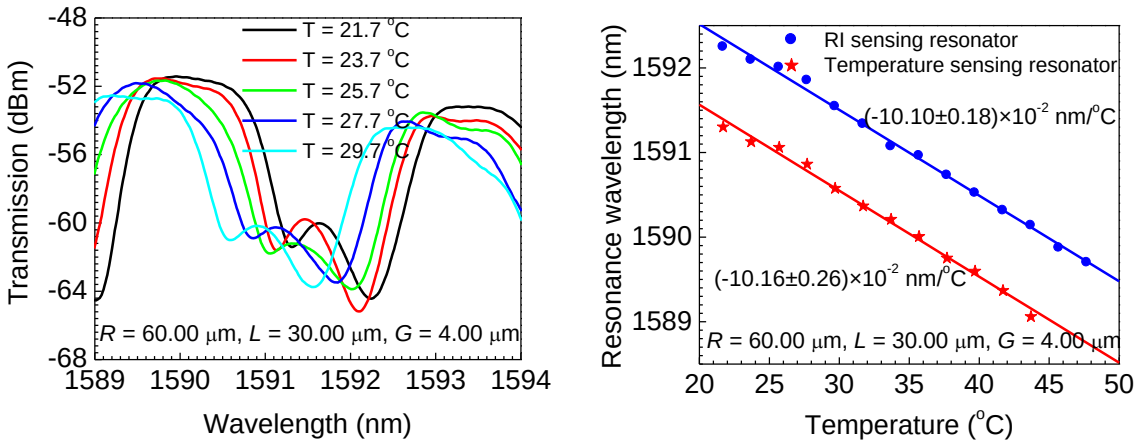

(a) (b)

Figure 5-40 Temperature sensing with a two-racetrack resonator. The two-racetrack resonator has a radius of 60.00 μm, coupling length of 30.00 μm, and gap of 4.00 μm.

5.3.4.3 Simultaneous refractive index and temperature sensing

From the experimental results described above, the relationship between the resonance wavelength and the changes in the temperature and RI of a liquid can be expressed with a matrix equation:

$$\begin{bmatrix}\Delta T\\ \Delta n\end{bmatrix}=\begin{bmatrix}-10.10\times10^{-2} & 0\\ -10.16\times10^{-2} & 16.46\end{bmatrix}^{-1}\begin{bmatrix}\Delta\lambda_{Air}\\ \Delta\lambda_{Liquid}\end{bmatrix} \tag{5.16}$$

where $\Delta\lambda_{Air}$ and $\Delta\lambda_{Liquid}$ are the resonance wavelength shifts of the temperature sensing and RI sensing resonances, respectively, and ΔT and Δn stand for the changes in the temperature and RI, respectively. Figure 5-41 presents transmission spectra of the two-racetrack resonator under different environmental conditions. The comparision of actual and test values is listed in Table 5-2. The maxium error is only 2.40% which demonstrates that the experimental results agree with the matrix equation.

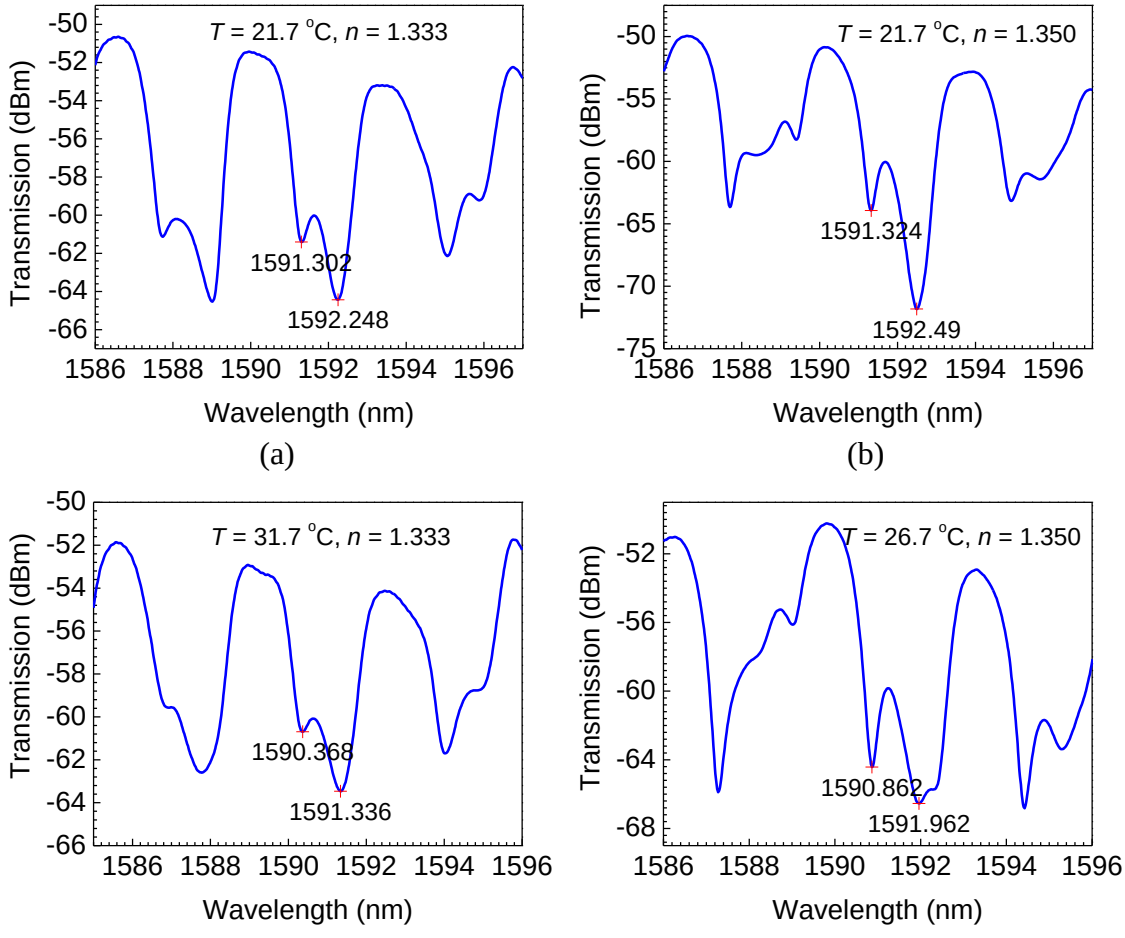

Figure 5-41 Transmission spectra of a two-racetrack resonator with a radius of 60.00 μm, coupling length of 30.00 μm, and gap of 4.00 μm under different environmental conditions

Table 5-2 Comparison of actual values and test values in different environment for a two-racetrack resonator with a radius of 60.00 μm

Sample	Actual value		Peak shift		Test value		Error%	
	T(°C)	RI(RIU)	$\Delta\lambda_{Air}$(nm)	$\Delta\lambda_{Liquid}$(nm)	T(°C)	RI(RIU)	T	RI
1 (Refer)	21.7	1.333	0	0	-	-	-	-
2	21.7	1.350	0.024	0.242	21.46	1.3462	1.11%	0.28%
3	31.7	1.333	-0.934	-0.912	30.95	1.3332	2.37%	0.02%
4	26.7	1.350	-0.440	-0.286	26.06	1.3425	2.40%	0.56%

Figure 5-42 presents the transmission spectrum of another two-racetrack resonator with a radius of 50.00 μm, coupling length of 30.00 μm, and gap of 4.00 μm. The microchannel is filled with distilled water. Two groups of resonances appear in the spectrum. The resonance wavelengths marked with red stars are induced by the racetrack covered with PDMS layer, and the resonance wavelengths marked with blue dots are induced by the racetrack covered with distilled water.

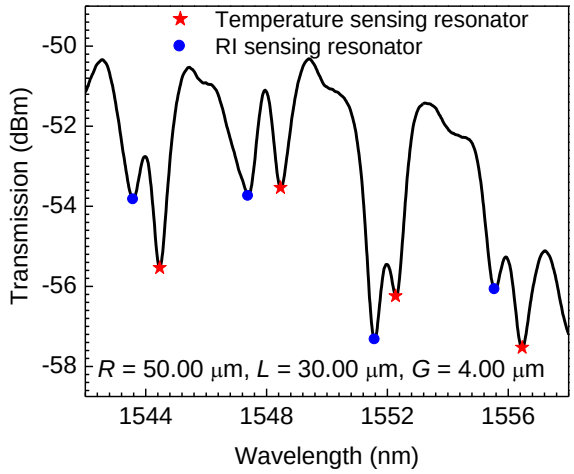

Figure 5-42 Transmission spectrum for a two-racetrack resonator with a radius of 50.00 μm, coupling length of 30.00 μm and gap of 4.00 μm

Figures 5-43 and 5-44 show the RI and temperature sensing of this two-racetrack resonator. The experimental results are similar to those of the last sample. The RI sensitivity is about 17.22 nm/RIU, and the temperature sensitivities are about -8.41×10^{-2} nm/^{o}C and -8.20×10^{-2} nm/^{o}C. Therefore, the relationship between the resonance wavelength and the changes in the temperature and RI of the liquid can be expressed with a matrix equation:

$$\begin{bmatrix}\Delta T\\ \Delta n\end{bmatrix}=\begin{bmatrix}-8.41\times10^{-2} & 0\\ -8.20\times10^{-2} & 17.22\end{bmatrix}^{-1}\begin{bmatrix}\Delta\lambda_{Air}\\ \Delta\lambda_{Liquid}\end{bmatrix} \tag{5.17}$$

Figure 5-45 presents transmission spectra of the two-racetrack resonator under different environmental conditions. The comparision of actual and test values is listed in Table 5-3. The maxium error is only 3.08% which demonstrats that the experimental results agree with the matrix equation. The resonance wavelength for RI sensing is smaller than the resonance wavelength for temperature sensing in two adjacent resonances. The resonance interval will decrease with the increase of the liquid RI. As a result, two resonance wavelengths could be overlapped for some liquids.

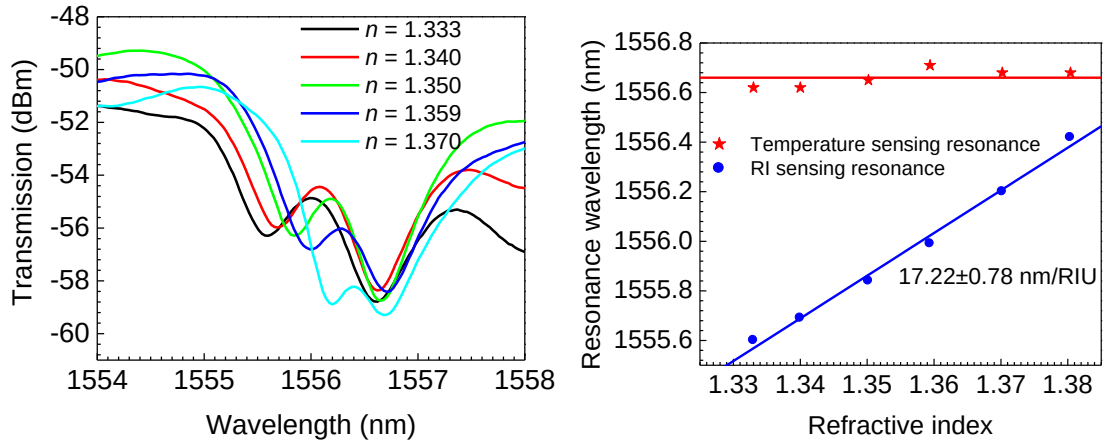

(a) (b)

Figure 5-43 RI sensing of a two-racetrack resonator with a radius of 50.00 μm, coupling length of 30.00 μm, and gap of 4.00 μm

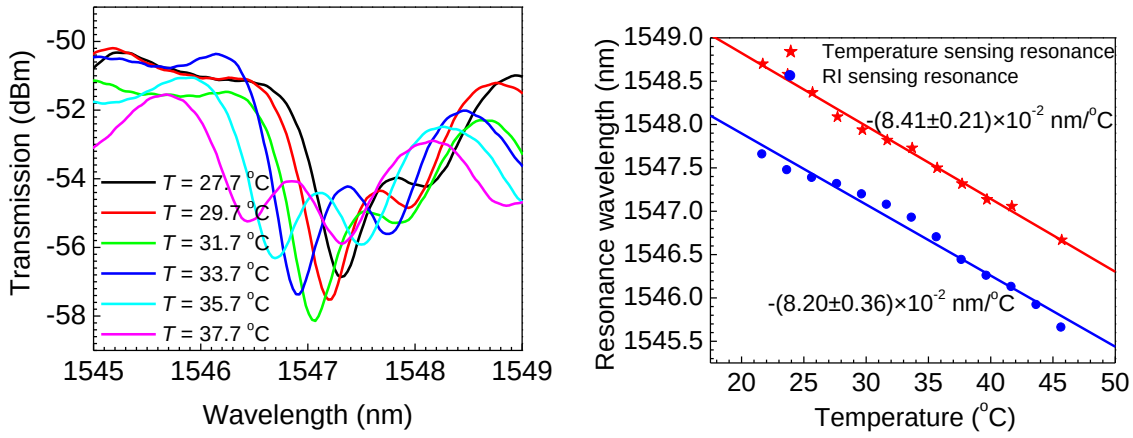

(a) (b)

Figure 5-44 Temperature sensing of a two-racetrack resonator with a radius of 50.00 μm, coupling length of 30.00 μm, and gap of 4.00 μm

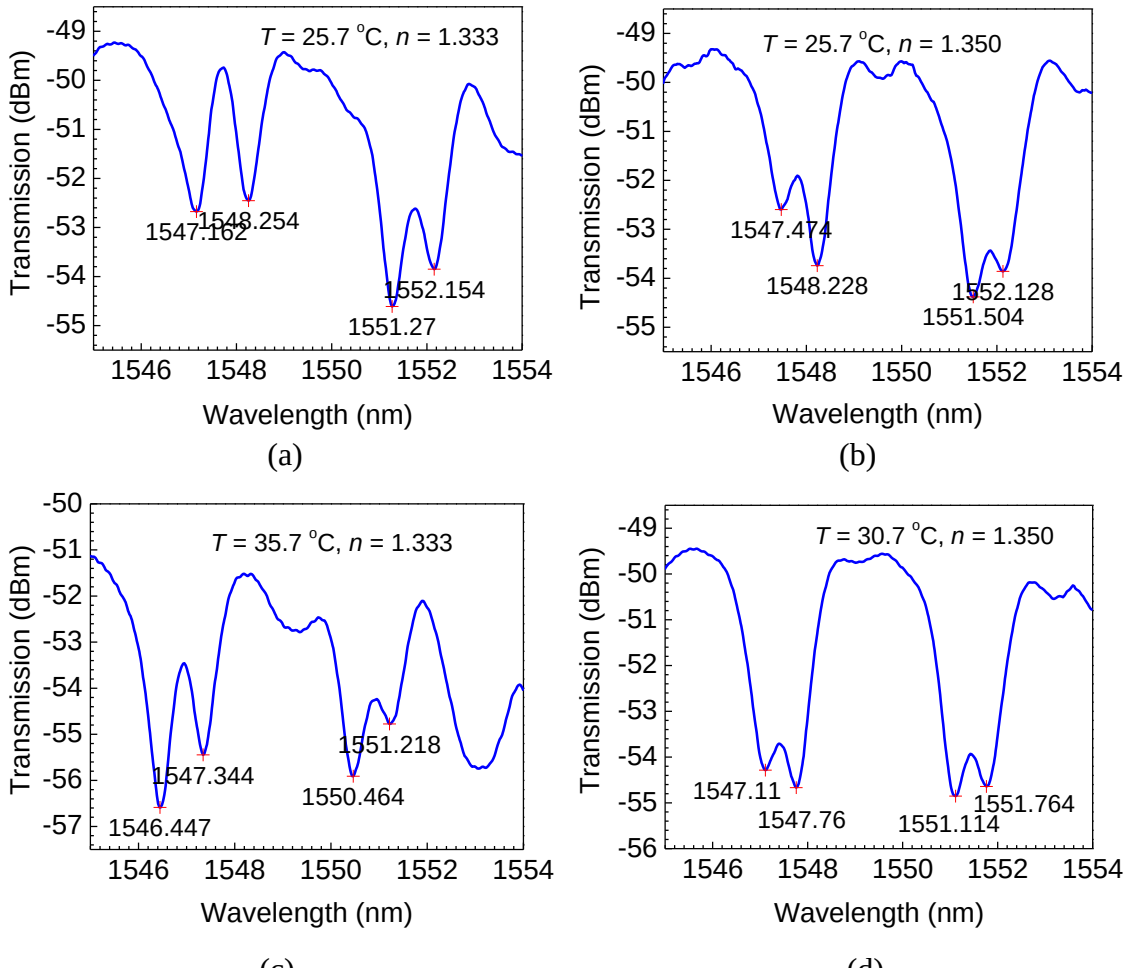

Figure 5-45 Transmission spectra of a two-racetrack resonator with a radius of 50.00 μm, coupling length of 30.00 μm, and gap of 4.00 μm under different environmental conditions

Table 5-3 Comparison of actual values and test values in different environment for a two-racetrack resonator with a radius of 50.00 μm

Sample	Actual value		Peak shift		Test value		Error%	
	T(°C)	RI(RIU)	$\Delta\lambda_{Air}$(nm)	$\Delta\lambda_{Liquid}$(nm)	T(°C)	RI(RIU)	T	RI
1 (Refer)	25.7	1.333	0	0	-	-	-	-
2	25.7	1.350	-0.026	0.226	26.0	1.3476	1.17%	0.18%
3	35.7	1.333	-0.936	-0.806	36.8	1.3392	3.08%	0.47%
4	30.7	1.350	-0.390	-0.156	30.3	1.3460	1.30%	0.30%

5.3.5 Simultaneous refractive index and temperature sensing for multiple liquid samples

Triple-racetrack resonator is designed as shown in Fig. 5-46. One of the racetracks which is covered with PDMS layer is used for temperature sensing, and the other two racetracks which are covered with microchannels are used for RI sensing. Therefore, two kinds of liquid samples can be infused into the microchannels to measure the temperature and RIs at the same time. This will markedly decrease the testing cost. As it is known that each of the racetracks generates one series of resonance pattern, in order to avoid overlapping three series of resonance patterns, the perimeters of three racetracks are slightly changed. Figure 5-47(a) presents the transmission spectrum of a triple-racetrack resonator with a radius of 60.00 μm, gap of 4.00 μm, and coupling lengths of 25.00, 30.00 and 35.00 μm, respectively. The resonator with a coupling length of 25.00 μm is covered with a PDMS layer, and the resonators with the coupling lengths of 30.00 and 35.00 μm are covered with microchannels which are filled with distilled water. Three series of resonances can be clearly distinguished. Figure 5-47(b) shows that the free spectral ranges are 3.522, 3.585 and 3.687 nm, respectively.

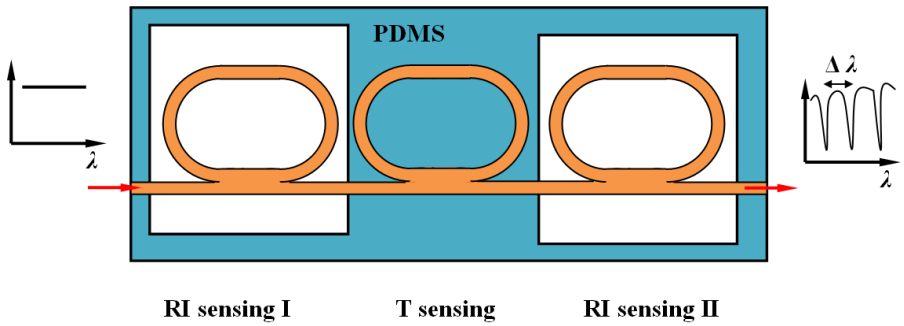

Figure 5-46 Schematic illustration of a triple-racetrack resonator for simultaneous RI and temperature sensing for multiple liquid samples

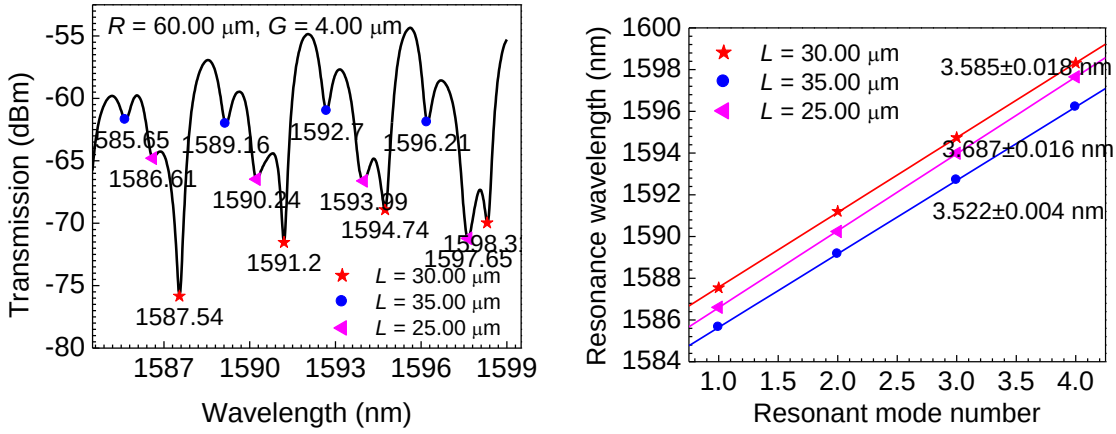

(a) (b)

Figure 5-47 Transmission spectrum and free spectral ranges for a triple-racetrack resonator with a radius of 60.00 μm, gap of 4.00 μm, and coupling lengths of 25.00, 30.00 and 35.00 μm, respectively.

The racetrack with a coupling length of 25.00 μm is labelled as T sensing, and racetracks with coupling lengths of 30.00 and 35.00 μm are marked with RI sensing I and RI sensing II, respectively. Figure 5-48(a) shows the transmission spectrum at a temperature of 21.7 ^{o}C when both microchannels are filled with distilled water. Figure 5-48(b) shows the dependence of the resonance wavelength on RI when the RI sensing I is filled with different salt solutions. The temperature sensing and RI sensing II resonance wavelengths do not change, whereas the RI sensing I resonance exhibits a linear response with a sensitivity of 28.2 nm/RIU. When the RI sensing II resonator is filled with different RI salt solutions, similar results have been obtained as shown in Fig. 5-48(c). The sensitivity of the RI sensing II resonance is about 24.2 nm/RIU. If the chip is heated on a hotplate, all series of resonance wavelengths exhibit blue-shifted. The sensitivities are about -8.65×10^{-2}, -7.12×10^{-2} and -10.52×10^{-2} nm/^{o}C, respectively.

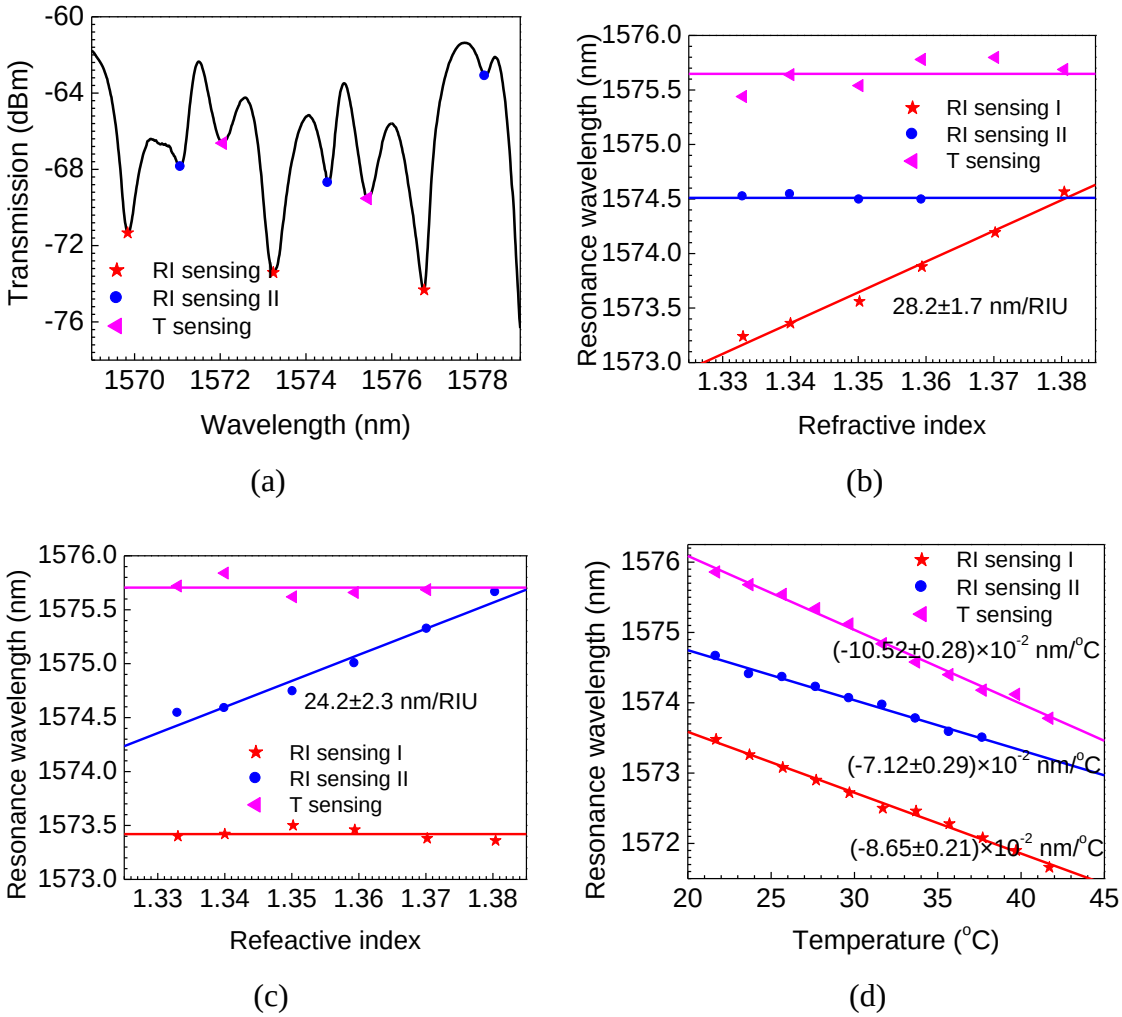

Figure 5-48 RI and temperature sensing with a triple-racetrack resonator. The triple-racetrack resonator has a radius of 60.00 μm, gap of 4.00 μm and coupling lengths of 25.00, 30.00 and 35.00 μm.

As shown in the experimental results described, the relationship between the resonance wavelength and the changes in the temperature and RI of the two liquids can be expressed with a matrix equation:

$$\begin{bmatrix} \Delta T \\ \Delta n_1 \\ \Delta n_2 \end{bmatrix} = \begin{bmatrix} -10.52\times10^{-2} & 0 & 0 \\ -7.12\times10^{-2} & 24.2 & 0 \\ -8.65\times10^{-2} & 0 & 28.2 \end{bmatrix}^{-1} \begin{bmatrix} \Delta\lambda_{Air} \\ \Delta\lambda_{Liquid1} \\ \Delta\lambda_{Liquid2} \end{bmatrix} \tag{5.18}$$

where $\Delta\lambda_{Air}$, $\Delta\lambda_{Liquid1}$ and $\Delta\lambda_{Liquid2}$ are the resonance wavelength shifts of the temperature sensing and RI sensing resonances, respectively, and ΔT, Δn_1 and Δn_2 stand for the changes in the temperature and RIs, respectively.

In conclusion, optical ring and racetrack resonators have been successfully designed and fabricated using TPP technique. The effects of size of the resonator, wavelength and polarization are investigated. By combining with microchannels, an innovative type of opto-microfluidic sensor for temperature and RI sensing has been achieved. Simultaneous temperature and the RI measurement of salt solutions are implemented. Comparing the ring and racetrack resonators, the racetrack resonator has a higher extinction ratio which makes it easier to distinguish the shifts of the resonance wavelengths. Also, a structure which can simultaneously measure the RI and temperature for two liquid samples has been designed. The technique demonstrated here significantly enhances the capability and efficiency of the testing at a reduced cost.

Chapter 6 Opto-microfluidic devices for particle sorting and refractive index sensing

6.1 Introduction

Flow sorting is a process used to separate special cells or particles from heterogeneous mixtures according to their sizes, RIs, and densities etc. This is a vital technique in biological, chemical and environmental research. Flow cytometry is a well-established technology that identifies and divides particles by their physical or chemical characteristics, and is used in clinical diagnostics and biomedical research. First, particles carried by a flow stream pass through lasers one by one. At this moment, the scattered light and fluorescence signals are collected, measured and analyzed. According to the analysis results, the fluid stream is ejected into the air and breaks up into droplets which contain one particle for each droplet. The droplets carry a positive charge, negative charge, or remain uncharged depending on the characteristics of the particles. Then the charged droplets pass through a high power static electrical field and are displaced into different containers. The advantages of this technology are high accuracy and efficiency. However, the high cost and large volume of equipment limit applications for wider fields. With the development of microfluidic technologies in the past two decades, microfluidic sorters have drawn much attention due to the advantages of simplicity, lower cost, portability and less sample consumption [133, 134]. Various microfluidic sorters based on different flow separation methods have been reported such as dielectrophoresis (DEP),

optical force and magnetic force, etc. Different kinds of microfluidic sorters are listed in Table 6-1.

Table 6-1 List of microfluidic sorters based on separation methods

Method	Characteristics of particle	Disadvantages	External instrument requirement	Ref.
Gravity	Density, size	Low resolution	None	135
Filtration	Size	Clogging	Pump	62,63,136,137
Laminar flow	Size	Shear stress	Pump	142-147
Dielectrophoresis (DEP)	Size, permittivity	Electric field	Pump and voltage generator	148-150
Magnetic force	Size, susceptibility	Magnetic field	Pump, magnetic particles, and magnet	151,152
Optical force	Size, RI	Optical irradiation	Pump and laser	153-157
Acoustic force	Density, size	Temperature increase	Pump and acoustic actuator	158,159

Based on the earth's gravity, Huh *et al.* developed a mass-dependent microfluidic sorting system [135]. Particles with different masses split into different flow paths in the microchannel along the direction of gravity. This simple design has no external instrument requirement, such as fluidic pumps, which avoids any damage to sample particles, especially live cells. However, this method only separates particles with significant differences in mass which limits general applications.

Filtration is a straightforward technique to divide particles based on size. Micro-poles or micro-pores are fabricated in the direction perpendicular to the flow. Particles with sizes smaller than the gap are allowed to pass. Particles with sizes larger than the gap are blocked, and stop at the sieves [62, 63, 136]. Mohamed *et al.* successfully used four groups of sieving arrays with different gaps to separate red blood cells, white blood cells, and neuroblastomas [137]. However, this type of dead-end filtration cannot achieve continuous flow separation due to the clogging and jamming. To relieve clogging, cross flow filtration which combines filtration with hydrodynamics is developed [138-141]. In this method, micro-sieves are fabricated in the direction parallel to the channel. Smaller particles pass through the sieves due to the hydrodynamics, whereas larger particles which are blocked outside of the sieves are flushed into the mainstream fluid instead of being jammed at the sieves. The drawback of this method is that particles flowing with high flow velocity will suffer a strong shear stress which is high enough to damage cells.

Laminar flow is the key flow feature in the microchannel. The Seki group designed a pinched segment in the micochannel based on the laminar flow to separate particles according to their sizes [142, 143]. High speed buffer liquid pushed and aligned the particles against the wall at the narrow pinched segment. The center of the smaller particles was closer to the wall than the center of larger particles due to the smaller radius. Therefore, an individual trajectory was generated based on the size of the particle. In the next widening channel, particles followed the diverged laminar flow streams to move to the respective collecting branch. The Seki group also reported hydrodynamic filtration, which had a similar principle as the pinched flow [144, 145]. Several side channels were

fabricated along the main channel. As liquid continuously leaked to the side channels, particles were pushed and aligned against the wall of the main channel by hydrodynamic force. At the following wider side channel, laminar flow streams forced smaller particles to enter the side channel, whereas larger particles followed their streams and still flowed in the main channel. Utilizing asymmetric bifurcation of laminar flow around obstacles, Sturm *et al.* described size-based particle separation devices [146, 147]. An obstacle matrix was fabricated in the microchannel. The matrix consisted of rows of posts. The gap between the posts in each row was a constant which was larger than the largest particle. However, the locations of the posts were asymmetrical row by row. The posts in each row had a slight shift in comparison to the former row. Smaller particles followed the laminar flow stream, whereas larger particles deflected out of the original laminar flow stream and jumped to another flow stream. However, these laminar flow techniques still cannot get rid of the effect of shear stress.

Polarization occurs in an electric field for dielectric particles. When an inhomogeneous electric field is applied on the particles, they experience repelling or attractive forces along the electric field gradient depending on their dielectric properties. Therefore, DEP is used to manipulate the trajectories of the dielectric particles in the microfluidics. Using microfabrication technology, various metal electrodes are integrated into the microchannel to obtain a highly non-uniform electric field [148-150]. Under the effects of DEP and hydrodynamic forces, particles based on sizes or permittivities are divided. This method makes particles to be exposed to a high electric field which will influence the components of the particles, especially some sensitive cells.

Similar to the DEP method, magnetic forces are designed to separate particles depending on size and susceptibility. However, unlike with DEP, most of cells are not usually magnetic. Magnetic particles are used to bond cells through antigen-antibody interactions [151, 152]. A strong magnet is applied to the side of the microchannel to control the movement of magnetic-labeled particles. This method, by contrast, is safe. But strong magnetic fields still have the risk to induce physiological effects on cells.

When a high-quality laser beam shines on a particle, the highly focused laser generates a strong gradient force to push the particle to the point with the highest energy in the beam (center or waist). This gradient force is called optical force and comes from the interaction of the particle with light such as reflection and refraction. Utilizing optical force, several optical sorting techniques are reported. Optical tweezers are a type of popular design [153-156]. In these designs, optical tweezers replace electrical plates to manipulate particles to respective channels in the flow cytometer. MacDonald *et al.* introduced a 3D optical interference pattern to the microchannel. Special particles followed the energy maxima to move to different flow streams [157]. Optical force is a convincing label-free and non-physical contact approach. But high light intensity can cause damage to biological properties.

Acoustic force is another interesting method. An acoustic standing wave is generated between the side walls of a channel by a small transducer. Based on the density or size, particles are driven toward the channel center (nodal plane) by the acoustic force with different velocities, and then laminar flow pushes them to separation channels [158, 159].

Ultrasonic vibration causes an increase of temperature. Therefore, acoustic force also risks damaging biological samples.

Compared with the methods listed in Table 6-1, filtration and laminar flow are simpler methods due to the fact that fewer external instruments are required. Therefore, devices are cheap and highly portable. They offer widespread potential for clinical applications and environmental research in the field. High precision TPP microfabrication by the femtosecond laser can easily produce complicated 3D microstructures such as micropoles, micropores and sieve arrays from the microscale to the nanoscale.

In the following sections, particle sorters fabricated by a femtosecond laser will be described. The separation function of the particle sorters is simulated by COMSOL software and tested with microspheres. By integration with an optical component, opto-microfluidic devices which can realize simultaneous particle sorting and RI sensing are developed.

6.2 Opto-microfluidic devices based on cross flow filtration and racetrack resonator

6.2.1 Particle sorter

6.2.1.1 Design

Figure 6-1 illustrates the schematic structure of this opto-microfluidic device that was constructed in the current work, which consists of one main channel and two side channels. The particle sorting system consists of two sets of micropillars which are produced at the junctions of the main channel and side channels. The micropillars are obliquely located in the main channel

against the flow direction. These two sets of pillars, labelled as Sieve I and Sieve II, are designed to separate microbeads (Thermo Scientific™, USA) with the diameters of 10 and 5 μm. Particles with a diameter of 10 μm are blocked by Sieve I and swept into the outlet I channel. At the same time, particles with a diameter of 5 μm pass through Sieve I and flow to Sieve II. Then these particles are blocked at Sieve II and flushed into the outlet II channel. The purpose of the slope sieves is to generate a bigger drag force parallel to the sieves which can flush blocked particles into the side flow to avoid clogging.

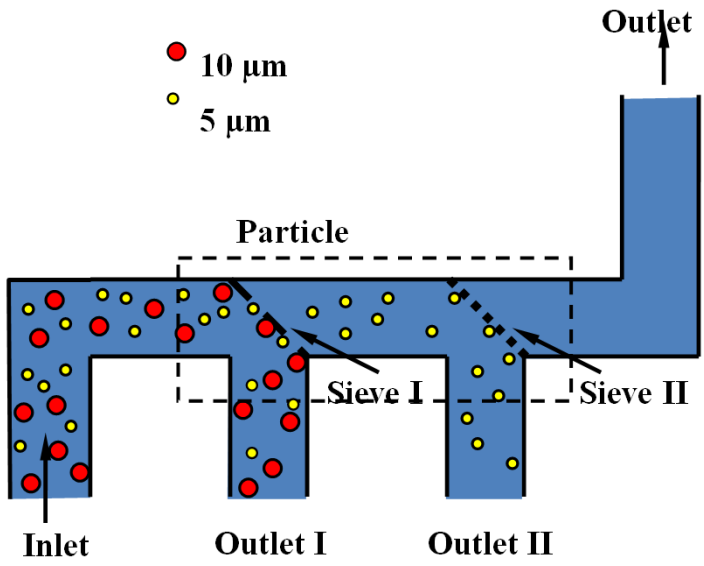

Figure 6-1 Schematic illustration of an opto-microfluidic device for particle sorting

Photoresist materials SU-8-2 and SU-8-3050 with a mixed volume ratio of 1:1 (Microchem®) are spin-coated and dried on a pre-cleaned glass substrate by standard procedures. The thickness is about 15.00 μm. The micropillars are written by femtosecond lasers. The typical width of a single-scan line with the scan speed of 5 μm/s is 4.00 μm. A multi-scan with a step of

2.00 μm is applied to these structures to generate sturdy micropillars which can resist the strong flow pressure from the suspension. Figure 6-2 presents two sets of micropillars, in which (a) and (b) show a row of micropillars with a slit of 6.50 μm and deviation of 5.00 μm between the adjacent pillars. This set of pillars is used to block particles with a diameter of 10 μm and is labelled as Sieve I. Figure 6-2(c) and (d) show a row of pillars with a slit of 3.50 μm and deviation of 3.00 μm between the adjacent pillars. This set of pillars is used to block particles with a diameter of 5 μm and is labelled as Sieve II. The size of pillars is 15.00 μm×10.00 μm×15.00 μm (length × width × height). The distance between Sieve I and Sieve II is 5.00 mm. A PDMS microchannel is produced by a standard soft lithographic method. Then the microchannel is bonded on the glass slide by careful alignment. Figure 6-3 exhibits the morphologies of Sieve I and Sieve II aligned with a microchannel. The size of the main channel is 300.00 μm× 15.00 μm× 16.00 mm (width × height × length), and the cross section of the side channel is 125.00 μm×15.00 μm. The micropillars can perfectly connect the top of the microchannel without any interspace. These two sieves are very suitable to separate white blood cells (10-15 μm) and red blood cells (6-8 μm).

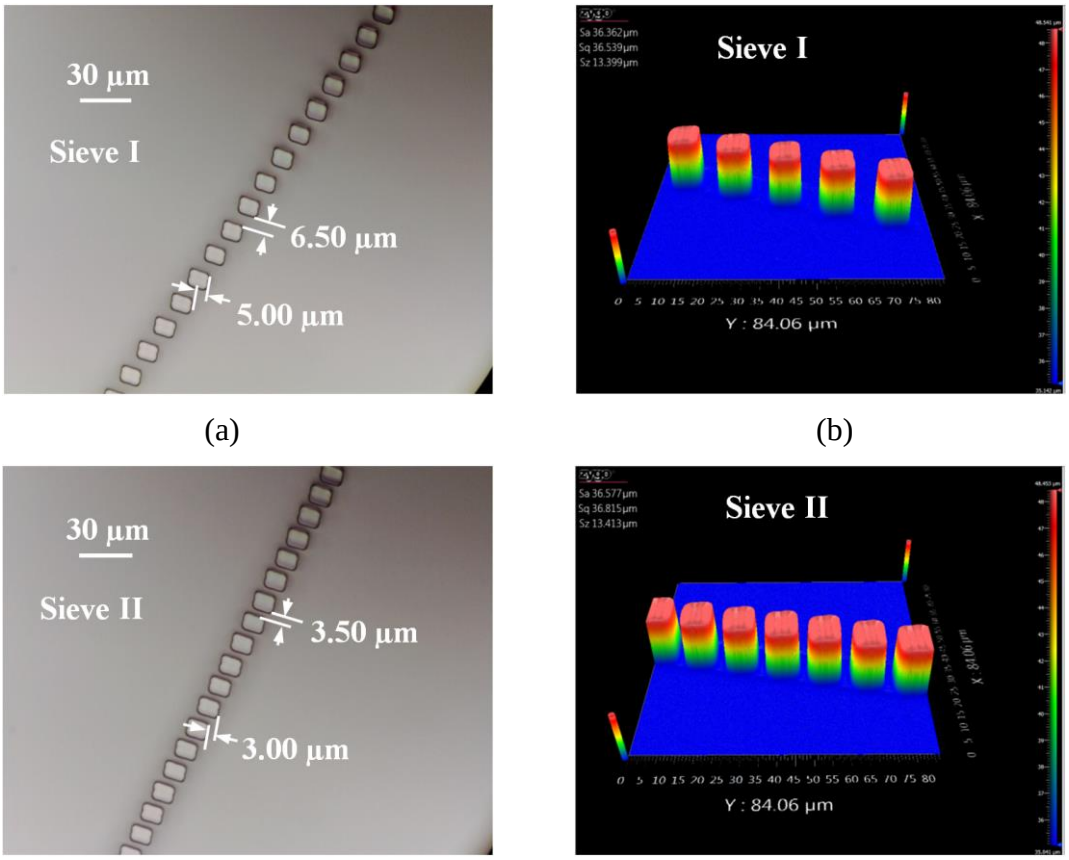

(a) (b)

(c) (d)

Figure 6-2 Structures of two sets of micropillars: (a) the morphology of Sieve I, (b) the 3D profile of Sieve I, (c) the morphology of Sieve II, and (d) the 3D profile of Sieve II. The size of pillars is 15.00 µm×10.00 µm×15.00 µm (length × width × height).

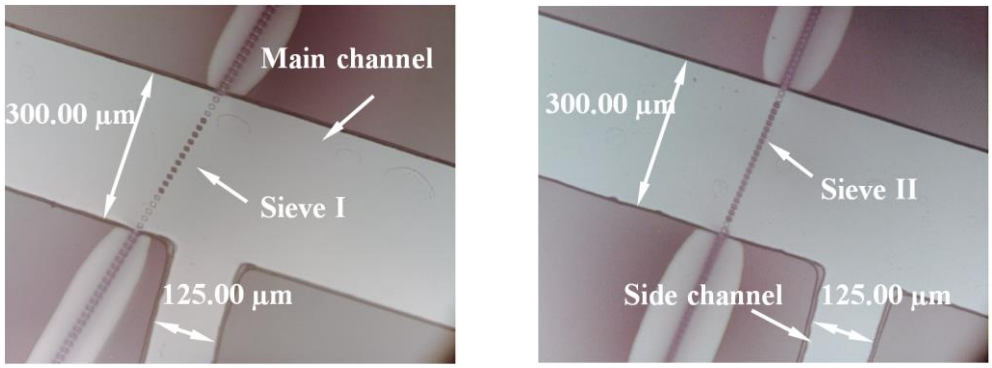

(a) (b)

Figure 6-3 Morphologies of Sieve I and Sieve II aligned with a microchannel. The size of the main channel is 300.00 µm× 15.00 µm× 16.00 mm (width × height × length), and the cross section of the side channel is 125.00 µm×15.00 µm.

6.2.1.2 Simulation

The liquid flow and particle trajectories in the microchannel are simulated by COMSOL software. Figure 6-4 shows the streamlines in the flow field which represent the trajectories of massless particles moving in the flow field. The parameters of the microchannel and sieves are exactly the same as the device structures. Liquid flows into the microchannel from the inlet channel with a velocity of 40 mm/s which means the flow rate is 10 μL/min. Figure 6-5 describes the simulation on trajectories of particles. The coloured background shows the magnitude of the flow velocity. Red colour stands for a higher flow speed, whereas blue colour represents a lower flow speed. 100 particles with the diameters of 10 and 5 μm are uniformly released from the inlet port, respectively. As time passes, most of the larger particles flow into the outlet I channel (Fig. 6-5(a)) and 13 larger particles are blocked at Sieve I (Fig. 6-5(b)). However, the shear force pushes most of the blocked particles to gather at the branch side of Sieve I (Fig. 6-5(c)). For smaller particles, 13 particles pass through Sieve I (Fig. 6-5(d)). As time passes, 9 particles flow into the Outlet II channel and 4 particles jam at Sieve II (Fig. 6-5(e) and (f)). According to the simulation, the separation rate (defined as the ratio of particle number before and after the sieve) is 13%. The particle trajectories at the flow rate of 200 mm/s (50 μL/min) are also simulated as shown in Fig. 6-6. Comparing to the simulation at a lower flow rate, particles use shorter time to arrive at the same place, and more particles are flushed to the branch side of sieves by the crossflow forces, whereas the separation rate does not change.

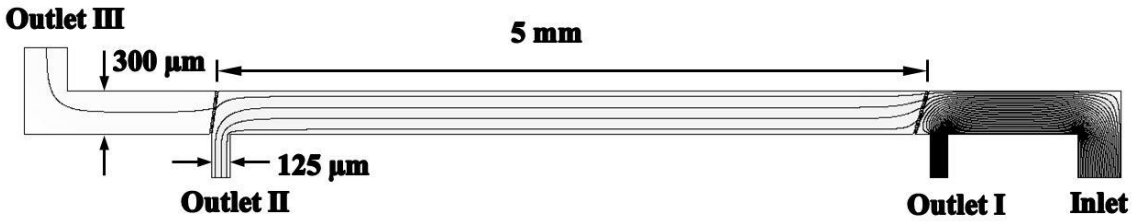

Figure 6-4 COMSOL simulation on streamlines in the flow field

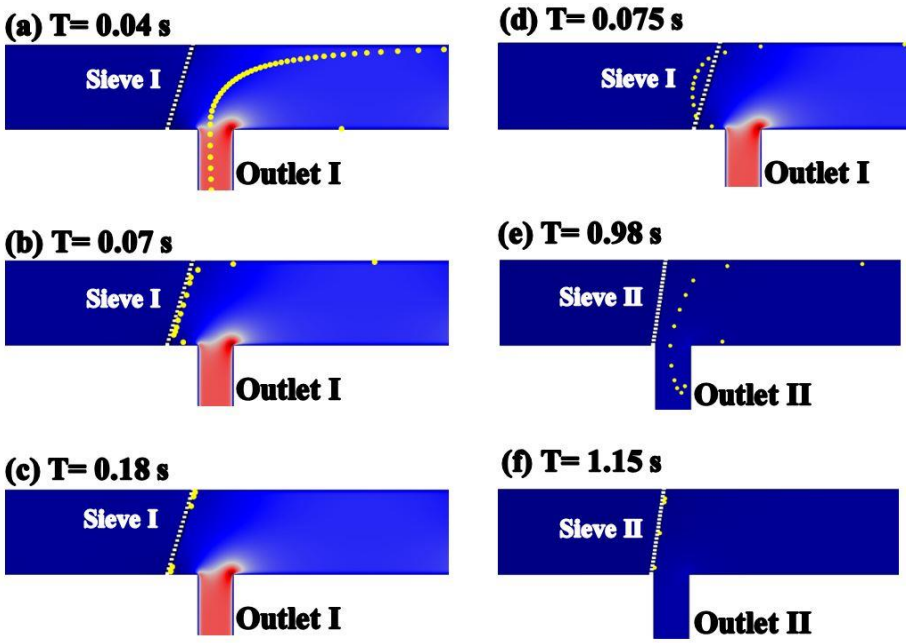

Figure 6-5 COMSOL simulation on particle trajectories: (a), (b) and (c) larger particles, and (d), (e) and (f) smaller particles. The flow rate at the inlet channel is 40 mm/s.

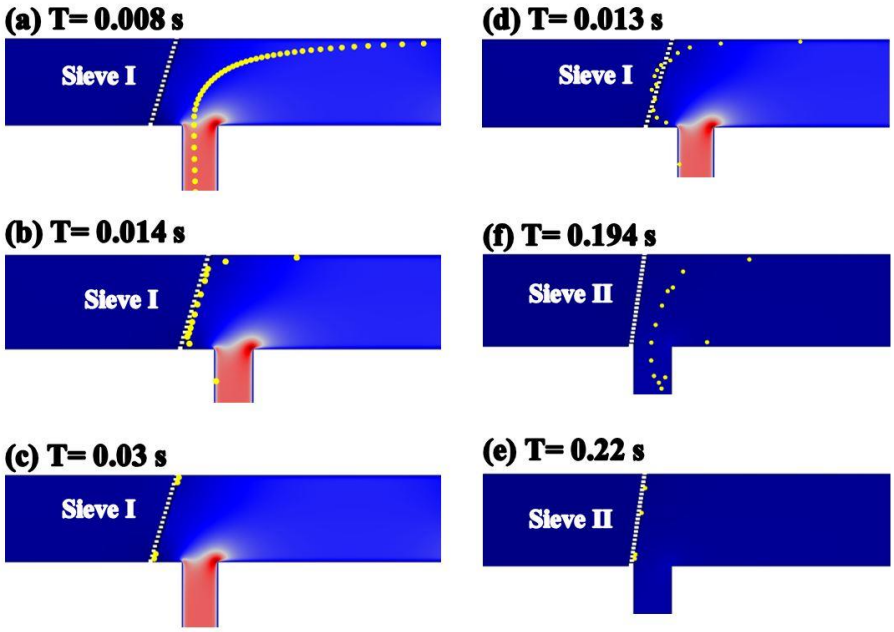

Figure 6-6 COMSOL simulation on particle trajectories: (a), (b) and (c) larger particles, and (d), (e) and (f) smaller particles. The flow rate at the inlet channel is 200 mm/s.

6.2.1.3 Experimental results

The polystyrene microbeads (10 or 5 μm) are originally packaged as aqueous suspensions with 1% solid mass, respectively. Two microsphere suspensions with a volume ratio of 1:1 are mixed and diluted with deionized water with a volume ratio of 1:900. The concentrations are 21 particles/μL for the 10 μm particles and 112 particles/μL for the 5 μm particles. The mixed suspensions are pushed into the microchannel with the flow rate of 10 μL/min. Figure 6-7 shows the morphologies of sieves captured by a Panasonic CCD camera at different times. At the beginning, sieves are clean, as illustrated in Fig. 6-7(a) and (d). A larger particle appears at the right side of Sieve II which is caused by a contamination (Fig. 6-7(d)). For Sieve I, smaller particles pass through and larger particles stop. As more larger particles stack at Sieve I, nearby streams at Sieve I are

changed which makes the smaller particles lack sufficient drag force to move away. As a result, a slight jam happens at 274 s. We also notice that a larger particle is flushed to the branch side of Sieve I by the shear force, as indicated by a dash arrow in Fig. 6-7(b) and (c). For Sieve II, smaller particles are blocked and a particle-free liquid passes through. More smaller particles stopping at the branch side of Sieve II with time is also observed in Fig. 6-7(e) and (f). These experimental results prove that this type of particle sorter is practicable.

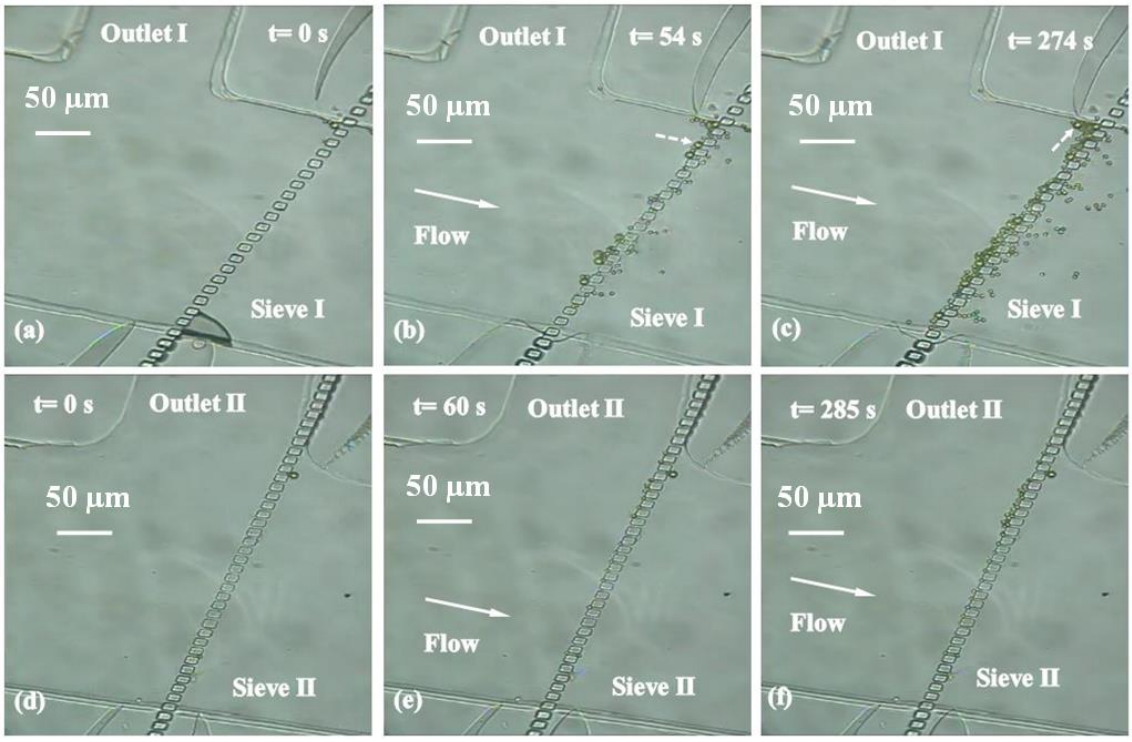

Figure 6-7 Experimental results of particle sorting: (a), (c) and (e) Sieve I at different times of 0, 54 and 274 s, and (b), (d) and (f) Sieve II at different times of 0, 60 and 285 s.

6.2.2 Refractive index sensing

As the research results show in section 5.3, the racetrack resonator is a type of simple and highly effective structure for RI sensing. Hence, we use a racetrack resonator to test the RI of mixed suspensions in this section. As mentioned above, a particle-free liquid is obtained after the suspension passes through Sieve II. Therefore, after the two sieves are fabricated, a thin SU-8-2 layer is coated on the substrate and a racetrack waveguide is written. The cross section of the waveguide is 4.12 μm×5.00 μm. The radius, coupling length and gap of the racetrack resonator are 60.00, 30.00 and 4.00 μm, respectively. The size of the microchannel must be carefully designed according to the location of the racetrack waveguide. In order to make the alignment easier, the main channel at the outlet section is broadened to 1.00 mm. To avoid the collapse of the top wall due to the elasticity of PDMS, the height of this part is also increased from 15.00 μm to 50.00 μm. A photo of an opto-microfluidic chip is shown in Fig. 6-8. The inset is the morphology of the racetrack resonator aligned with the microchannel. The length of the chip is 30.00 mm.

To test the practicality of this device, two sample suspensions are used. Sample I is a mixed distilled water suspension. In Sample II, sodium chloride is added to the mixed distilled water suspension to obtain a solution with a concentration of 9.8% and RI of 1.350. In the experiment, different salt solutions with known RIs are first infused into the microchannel in turn to calibrate the RI. After washing several times with distilled water to get rid of the remaining salt solution, the device is infused with sample suspensions. The output results are compared with the calibration results, and then the RI of the sample solutions is calculated. Figure 6-9 presents the experimental results. The RI sensitivity of

this racetrack resonator is about 21.8 nm/RIU. The measured results show that the first sample solution has an RI of 1.3387, and the second sample has an RI of 1.3523. The errors are 0.43% and 0.16%, respectively.

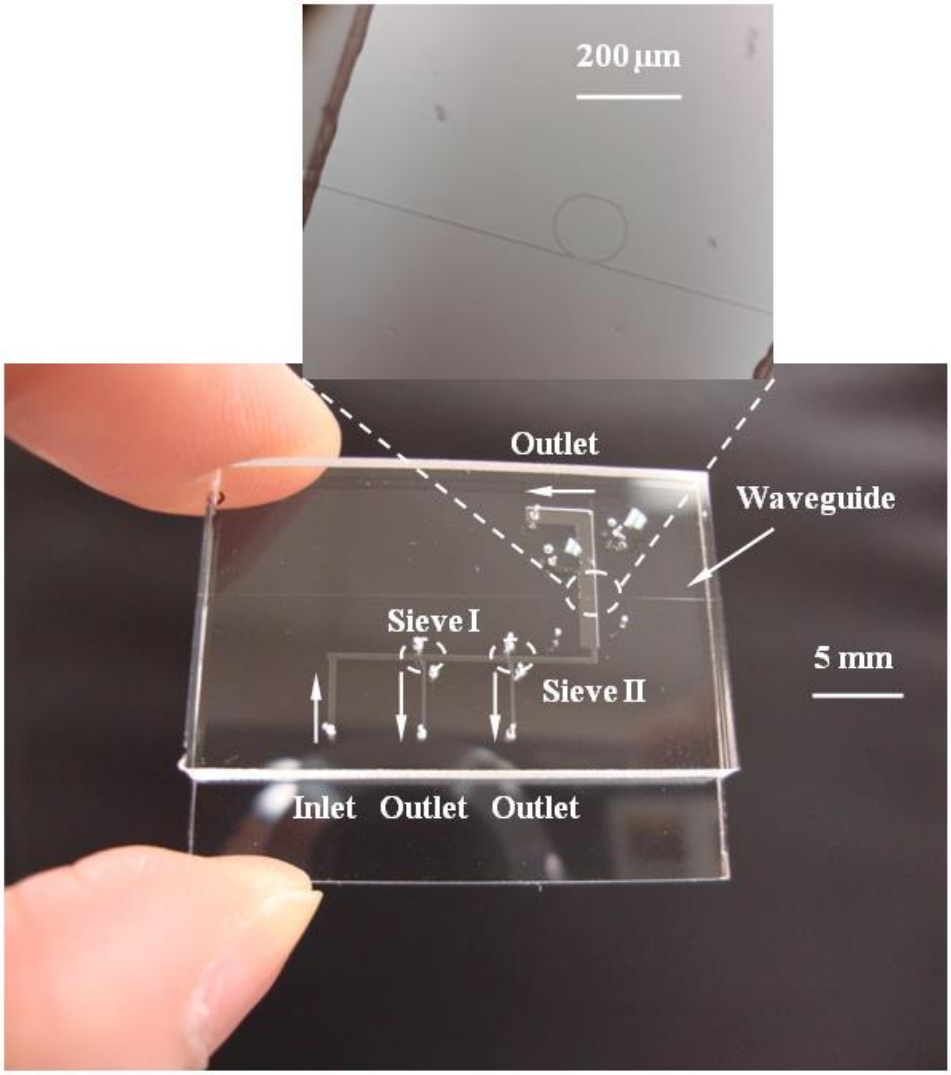

Figure 6-8 Photo of the opto-microfluidic chip for particle sorting and RI sensing. The inset is the morphology of a racetrack resonator.

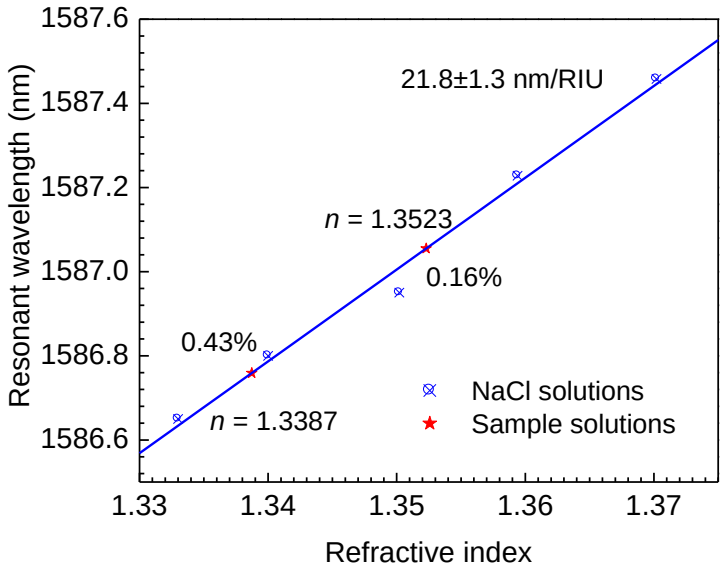

Figure 6-9 Dependence of the resonance wavelength on RI. The racetrack resonator has a waveguide cross section of 4.12 μm×5.00 μm, radius of 60.00 μm, coupling length of 30.00 μm, and gap of 4.00 μm.

This type of opto-microfluidic device successfully realizes simultaneous separation of particles and measurement of the RI of solutions. The primary disadvantage of this device is the low separation rate. Another drawback of this device is that it requires a highly precise alignment technique which makes the sieves as close to the corner of the side channels as possible. Considering the factors above, a type of opto-microfluidic device based on hydrodynamic filtration and diffraction grating will be introduced in the following section.

6.3 Opto-microfluidic devices based on hydrodynamic filtration and diffraction grating

6.3.1 Particle sorter I

6.3.1.1 Design

In this section, innovative filtrations are designed to improve the separation rate. As shown in Fig. 6-10, this sorter consists of one main channel and two side channels. The main channel is arrayed with two sets of microsieves along the direction of the main channel wall: Sieve I and Sieve II. Sieve I is a row of periodic small pillars with the slit size smaller than the diameter of the smaller particles. Therefore, particle-free liquid is obtained from Sieve I by blocking all particles. Sieve II is a row of small pillars with a larger space between the slits. Smaller particles can pass through the slits, whereas larger particles are blocked. Few jams happen in this type of device due to a longer filtration length and a larger shear force along the main microchannel which pushes the blocked particles into the mainstream fluid.

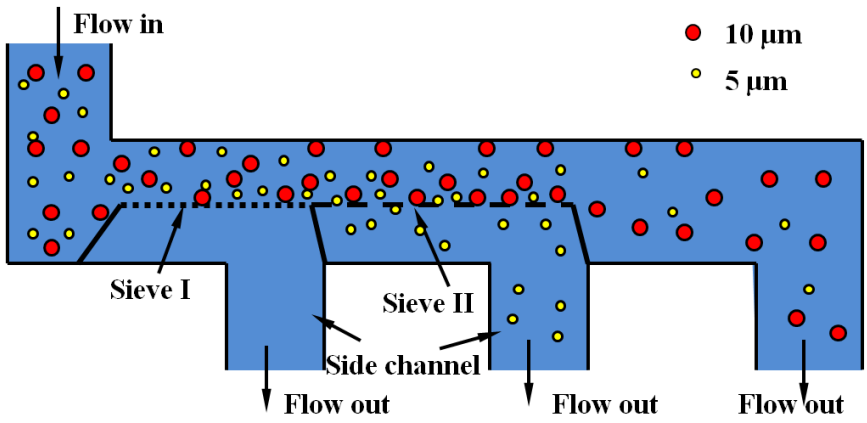

Figure 6-10 Schematic illustration of a particle sorter

6.3.1.2 Simulation

COMSOL software is used to simulate the liquid flow and particle trajectories in the microchannel. Figure 6-11 shows the simulation on streamlines in the flow field. In the simulation, the length of the microchannel is set at 3.00 mm, and the width of the microchannels is 300.00 μm. The size of pillars is 23.00 μm×7.00 μm. For the Sieve I structure, the slit between the pillars is 4.00 μm. For Sieve II, the slit size is 7.00 μm. The lengths of Sieve I and Sieve II are 700 and 900 μm (labelled as filter length I). The flow rate at the inlet channel is 40 mm/s. Figure 6-12 describes the particle trajectories of larger particles (10 μm). 50 particles with a diameter of 10 μm are released from the inlet port. As time passes, 94% of the larger particles jam at Sieve II, 6% of the larger particles flow to the main outlet channel, and no larger particles stop at Sieve I. Figure 6-13 describes the particle trajectories of smaller particles (5 μm). As time passes, 70% of the smaller particles jam at the Sieve I, 24% of the particles pass through Sieve II, and 6% of the particles flow to the main outlet channel. According to the simulation results, the separation rate reaches 24% for smaller particles and most of the particles clog at the sieves. The coloured background in these two figures shows the velocity magnitude of the flow velocity. The maximum flow rate in this situation is 0.23 m/s.

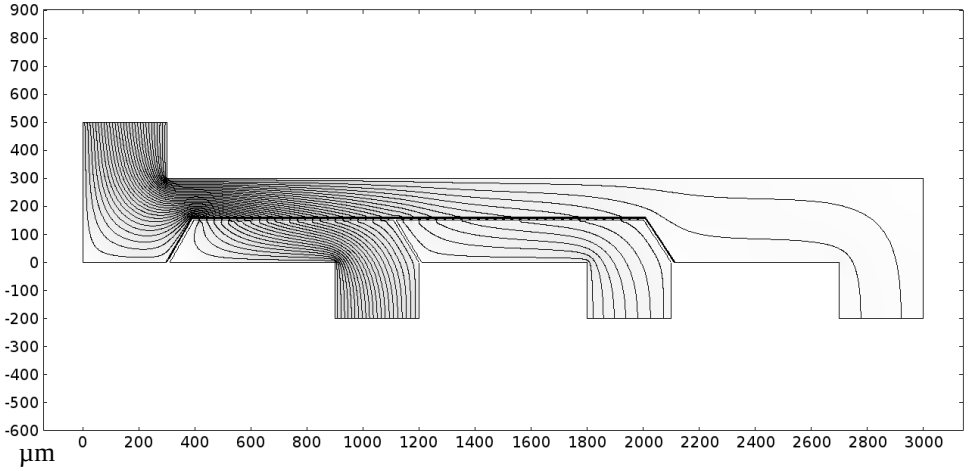

Figure 6-11 COMSOL simulation on streamlines in the velocity field. Particle sorter I has a microchannel length of 3.00 mm and the width of 300.00 µm. The lengths of Sieve I and Sieve II are 700 and 900 µm, respectively.

The characterization of flow velocity and particle trajectories for a longer sieve length (1400 µm for Sieve I and 1800 µm for Sieve II labelled as filter length II) is also simulated. Figure 6-14 presents the simulation on distribution of particles in different situations. For a longer sieve length, more particles jam at Sieve I due to the fact that the hydrodynamic force along the direction of the main channel is lower in a longer microchannel.

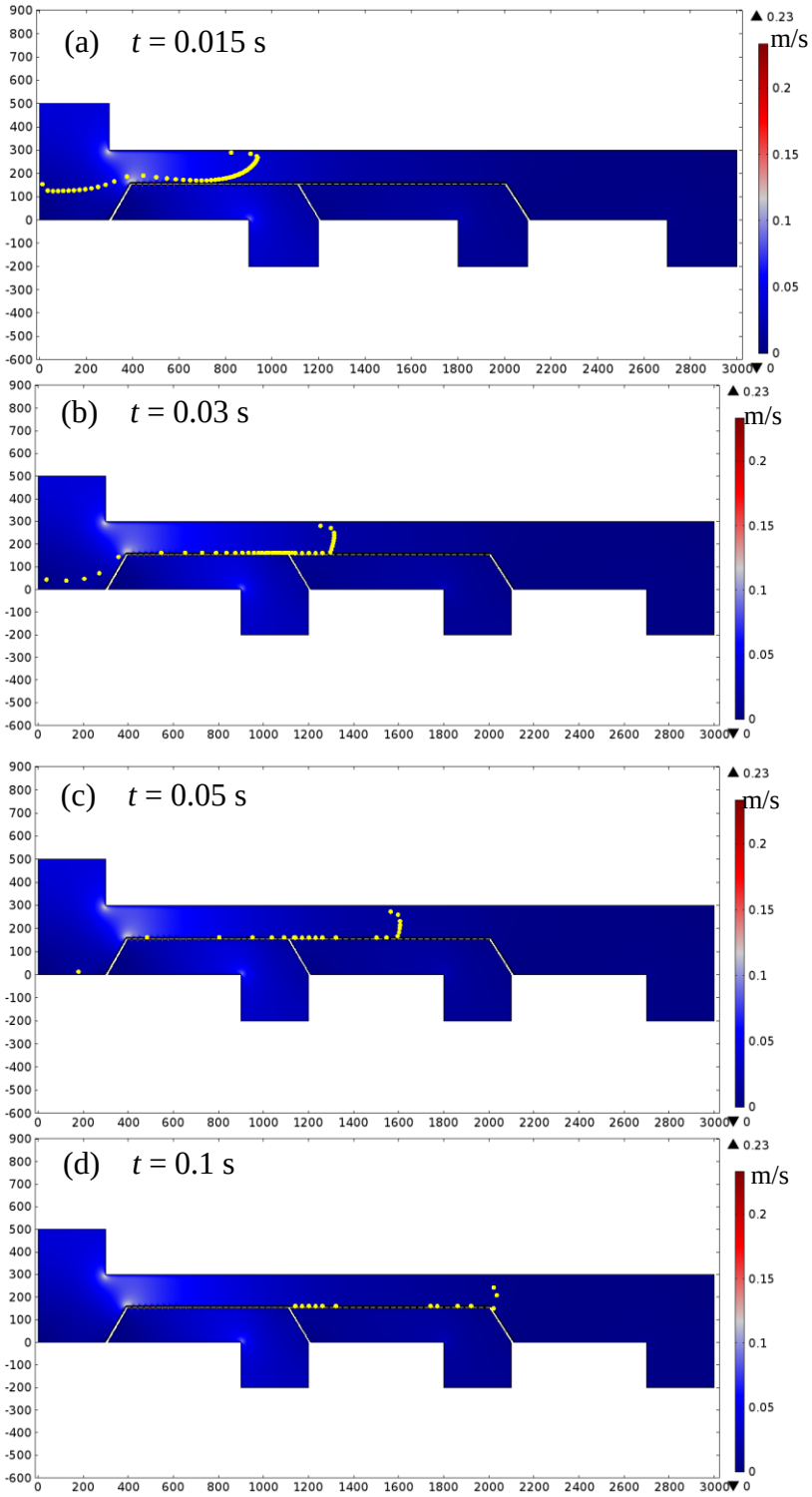

Figure 6-12 COMSOL simulation on particle trajectories of larger particles in particle sorter I

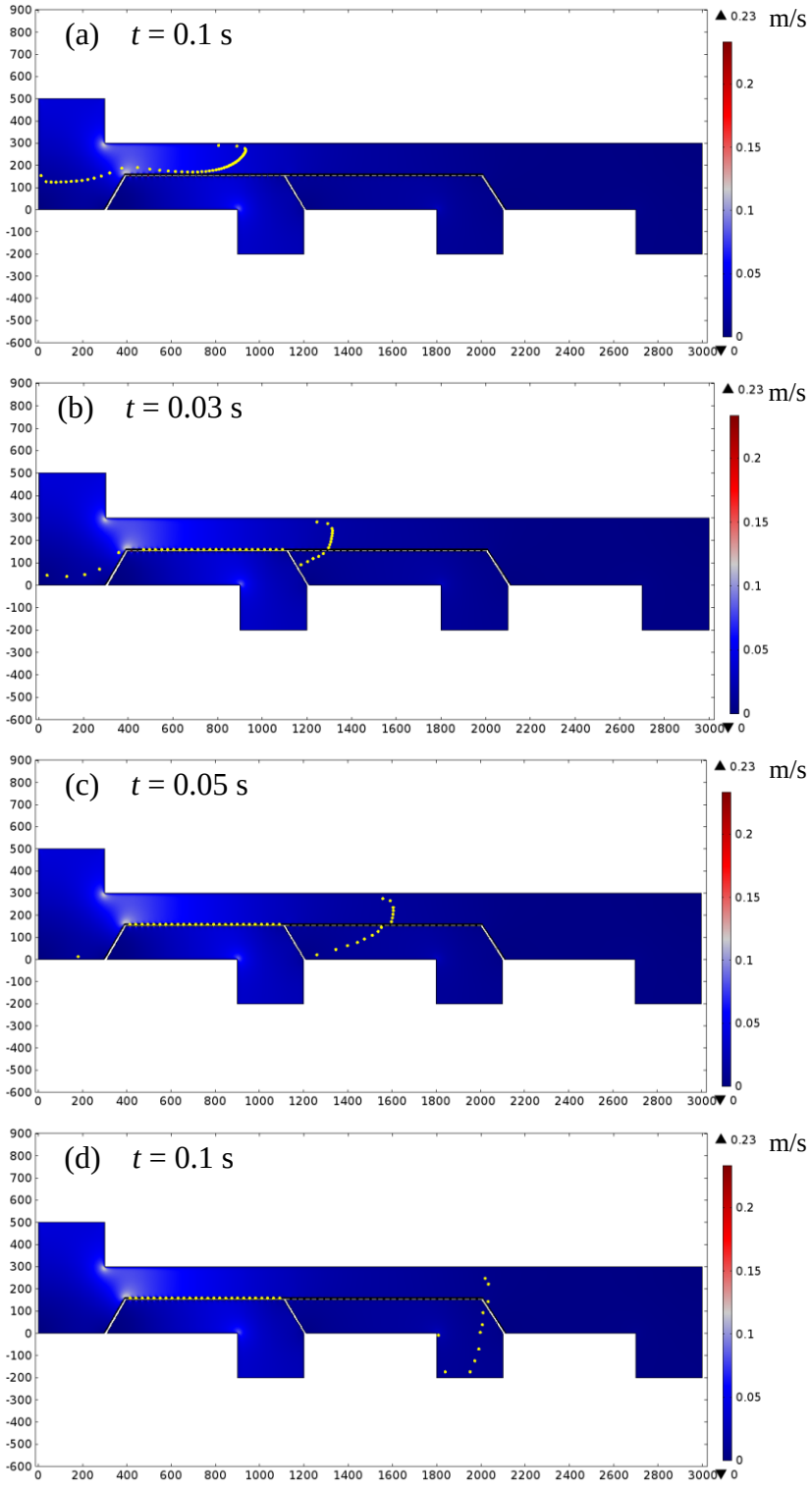

Figure 6-13 COMSOL simulation on particle trajectories of smaller particles in particle sorter I

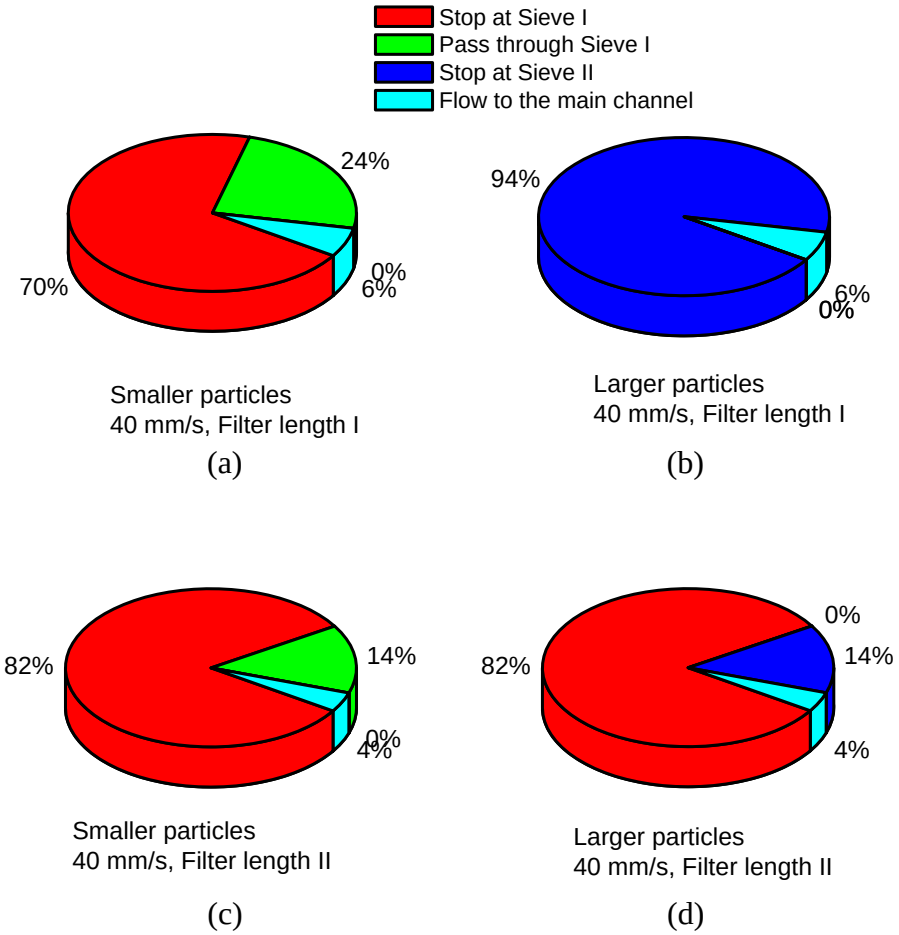

Figure 6-14 Simulation on particle distribution of particle sorter I in the filter length I and II situations with the inlet flow rate of 40 mm/s

6.3.1.3 Experimental results

The same techniques for SU-8 pillar and microchannel fabrication are used in this section. Figure 6-15(a) and (b) present 3D profiles of Sieve I and Sieve II. The size of the periodic micropillar is 23.00 μm×7.00 μm×15.00 μm (length × width × height). The slits between the two adjacent pillars of Sieve I and II are 4.00 and 7.00 μm, respectively. Figure 6-15(c), (d) and (e) show the morphologies of the microsieve structures. The lengths of Sieve I and Sieve II are 5.00 mm, respectively. Microchannels are carefully aligned and

bonded with the sieves as shown in Fig. 6-15(f)-(h). The height of the microchannel is also 15.00 μm. The widths of the main channel and side channels are all 300.00 μm.

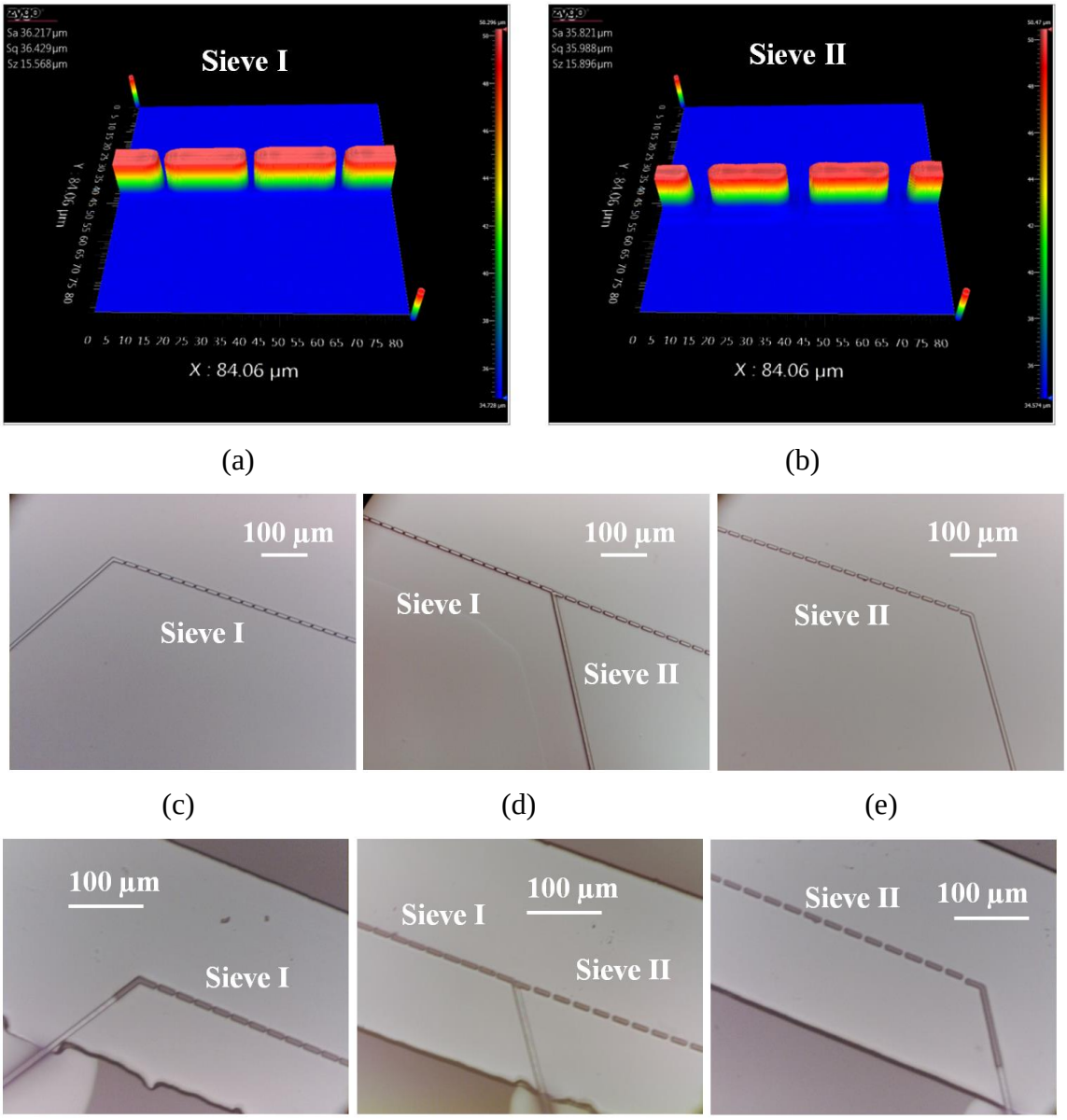

Figure 6-15 Structures of microsieves: (a) and (b) 3D profiles of Sieve I and II, respectively, (c)-(e) morphologies of sieves under microscope, and (f)-(h) morphologies of sieves integrated with microchannels.

The same suspensions are used in this section. The mixed suspensions are injected into the microchannel with a flow rate of 10 μL/min. Figure 6-14 shows the morphologies of the sieves after they work for 10 minutes. Particles are blocked and jammed at Sieve I because the slit of the micropillars is smaller than 5 μm (Fig. 6-16(a) and (b)). When remaining suspensions flow to Sieve II, parts of smaller particles pass through it and the other particles are blocked and jammed at Sieve II. Comparing to the COMSOL simulation results, the experimental results show that some smaller particles jam at Sieve II. The reason is that the blocked Sieve II changes the nearby streams which makes the smaller particles lack sufficient drag force to move away. However, it can still be observed that more larger particles stack at Sieve II than at Sieve I which agrees with the simulation.

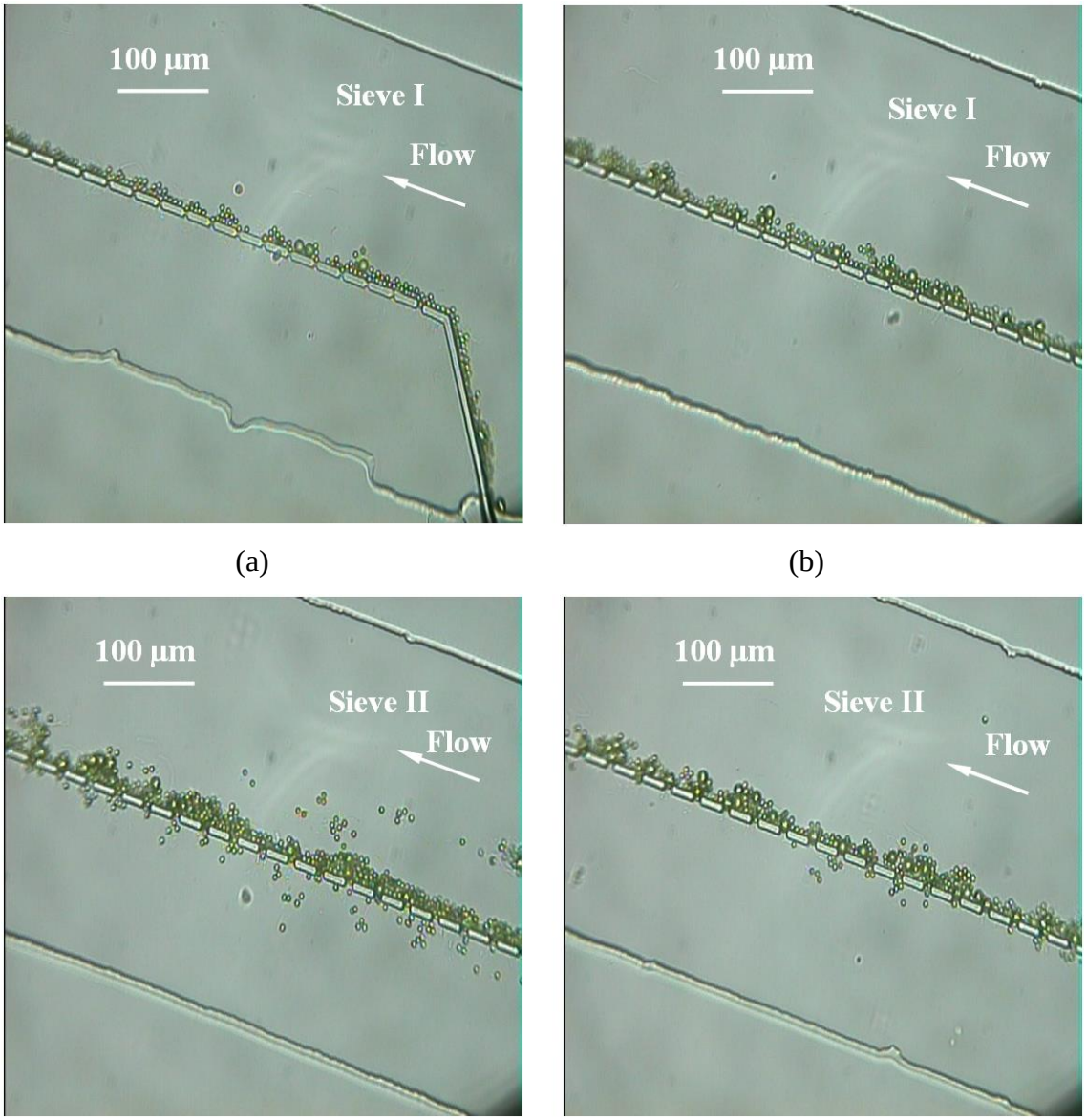

Figure 6-16 Particle sorter I: (a) and (b) Sieve I after it works for 10 minutes, and (c) and (d) Sieve II after it works for 10 minutes.

6.3.2 Particle sorter II

6.3.2.1 Designs and simulation

According to the simulation on the particle sorter I, the separation rate is low due to the fact that most of the smaller particles jam at Sieve I. Therefore, the design here is slightly revised to increase the separation rate. As shown in Fig. 6-17, the functions of Sieve I and II are switched. Sieve I is used to separate smaller particles from the mixture, whereas Sieve II is used to obtain particle-free liquid. Figure 6-18 describes the simulation on streamlines in the flow field. The simulation parameters of this sorter are the same as for Fig. 6-11 except that Sieve I has a slit size of 7.00 μm and Sieve II has a slit size of 4.00 μm. Figure 6-19 shows the particle trajectories of larger particles (10 μm). 100 particles with a diameter of 10 μm are released from the inlet port. As time passes, 78% of the larger particles jam at Sieve I, 22% of the larger particles flow to the main outlet channel, and no larger particles stop at Sieve II. Figure 6-20 shows the particle trajectories of smaller particles (5 μm). 100 particles with a diameter of 5 μm are released from the inlet port. As time passes, 77% of the smaller particles pass through Sieve I, 17% of the particles jam at the Sieve II, and 6% of the particles flow to the main outlet channel. According to the simulation results, the separation rate reaches 77% for smaller particles. The maximum flow rate is 0.19 m/s.

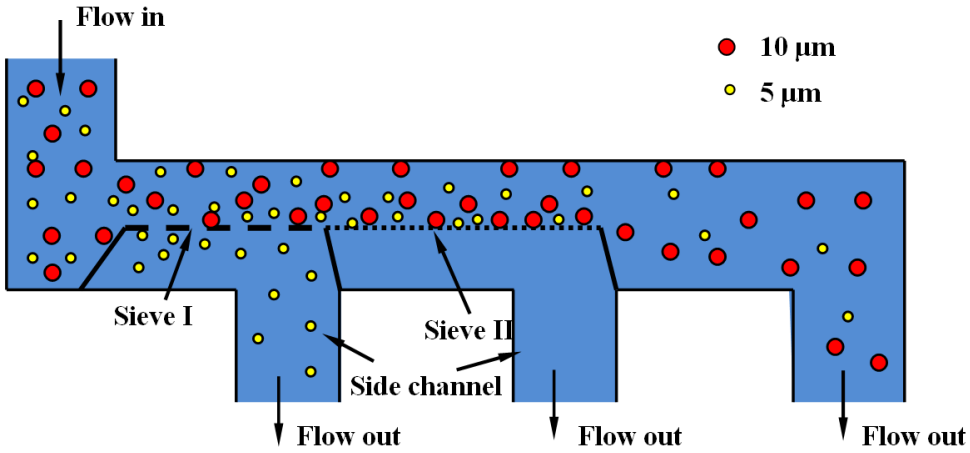

Figure 6-17 Schematic illustration of a particle sorter

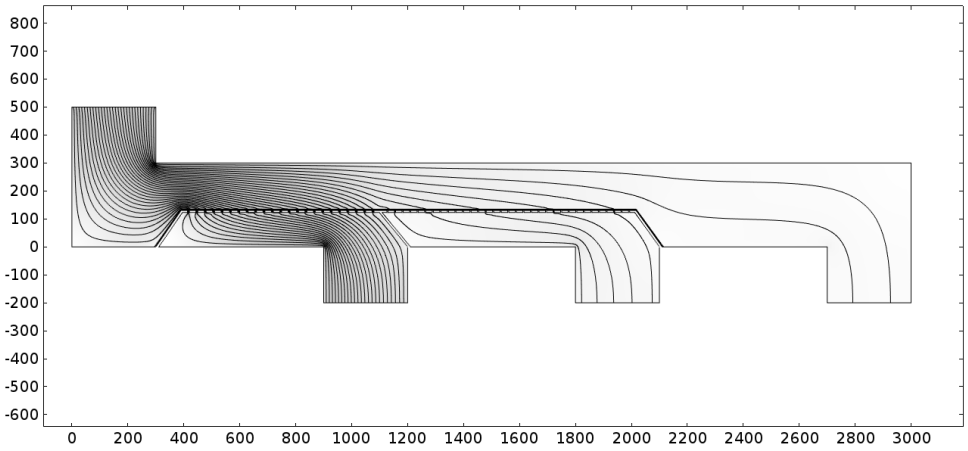

Figure 6-18 COMSOL simulation on streamlines in the velocity field. Particle sorter II has a microchannel length of 3.00 mm and the width of 300.00 µm. The lengths of Sieve I and Sieve II are 700 and 900 µm, respectively.

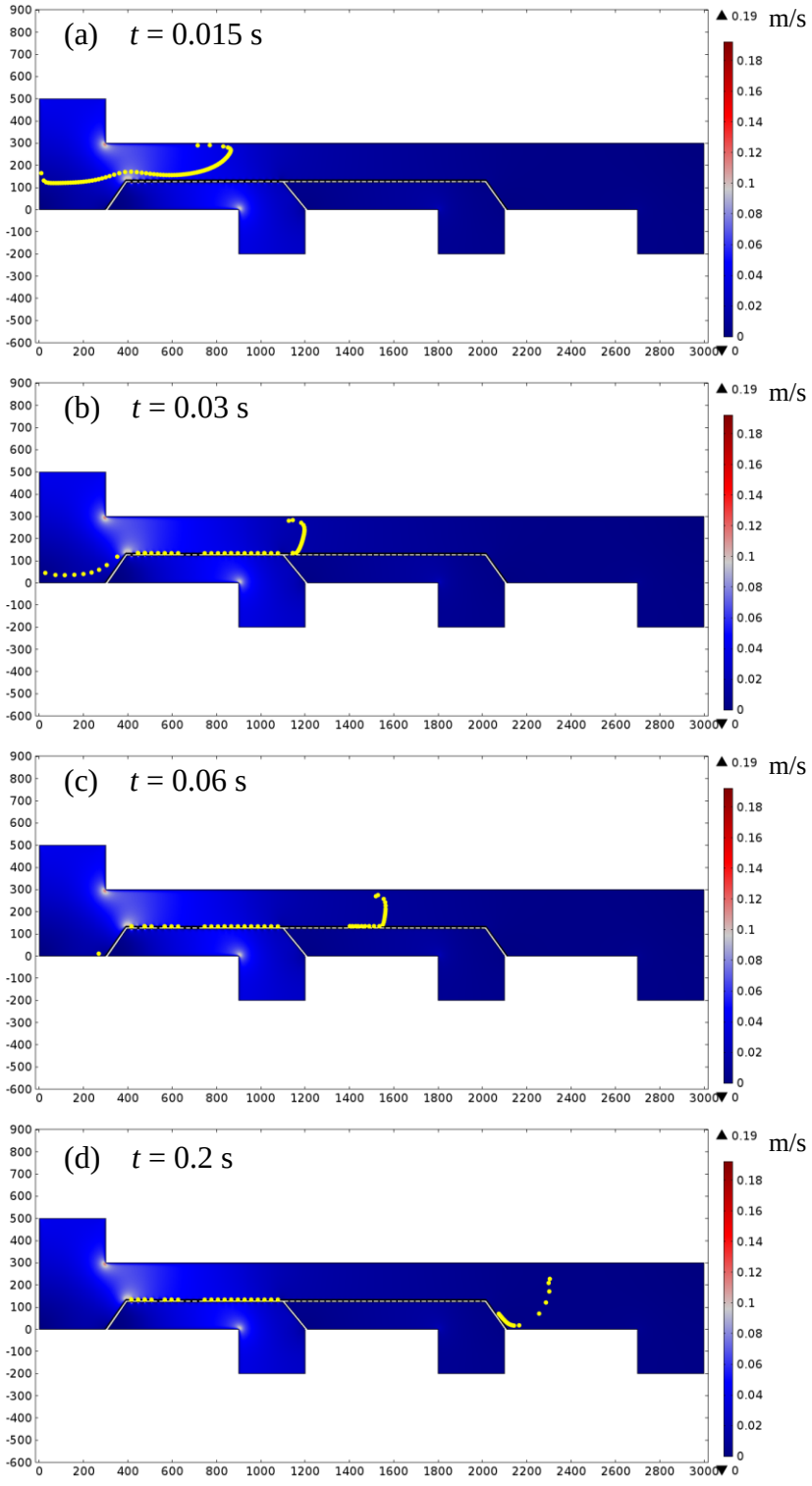

Figure 6-19 COMSOL simulation on particle trajectories of larger particles in particle sorter II

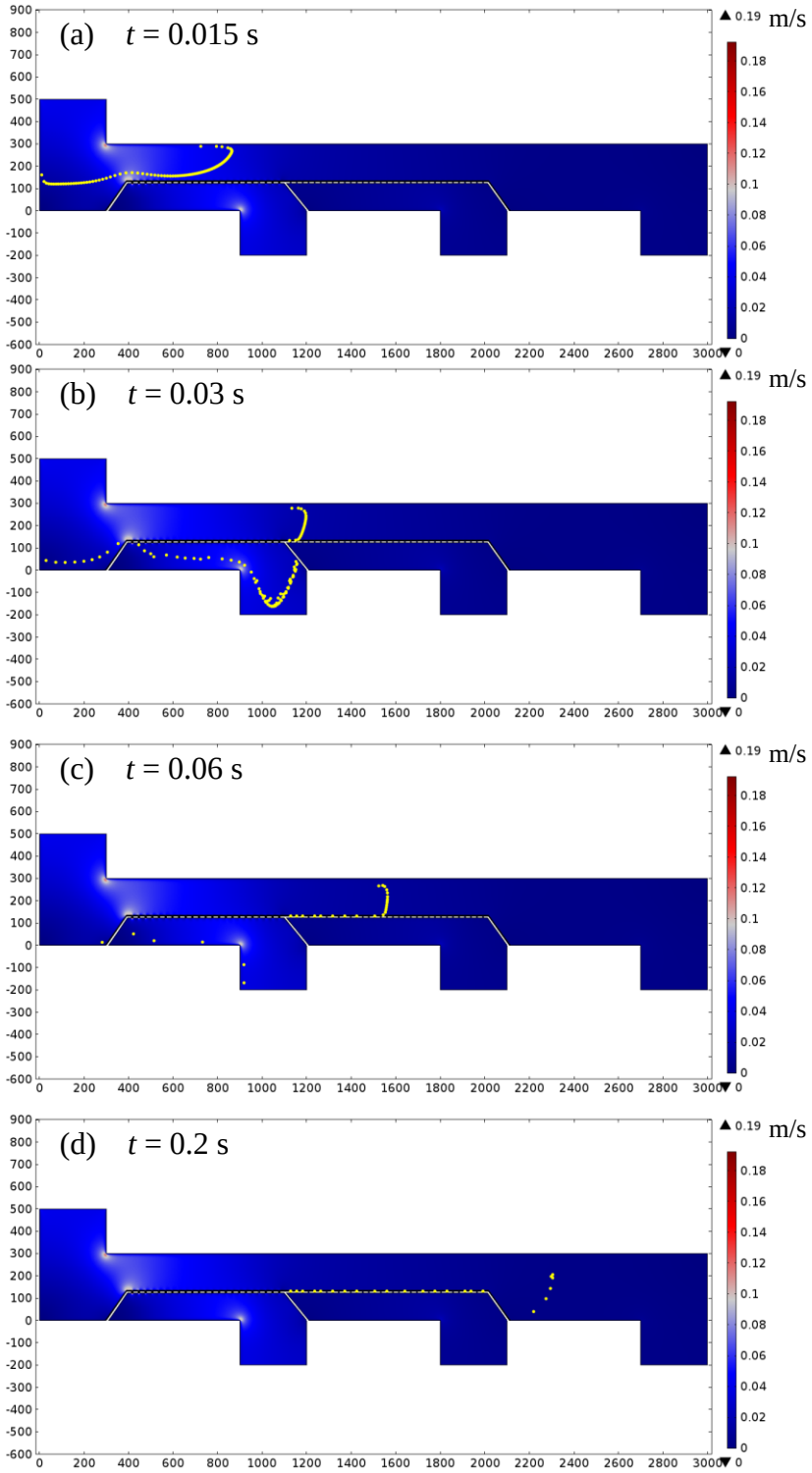

Figure 6-20 COMSOL simulation on particle trajectories of smaller particles in particle sorter II

The characterization of particle sorter II with a longer sieve length (1400 μm for Sieve I and 1800 μm for Sieve II labelled as filter length II) is also simulated. Figure 6-21 presents the simulation on distribution of particles in different situations. For a longer sieve length, more smaller particles pass through Sieve I and larger particles stack at Sieve I.

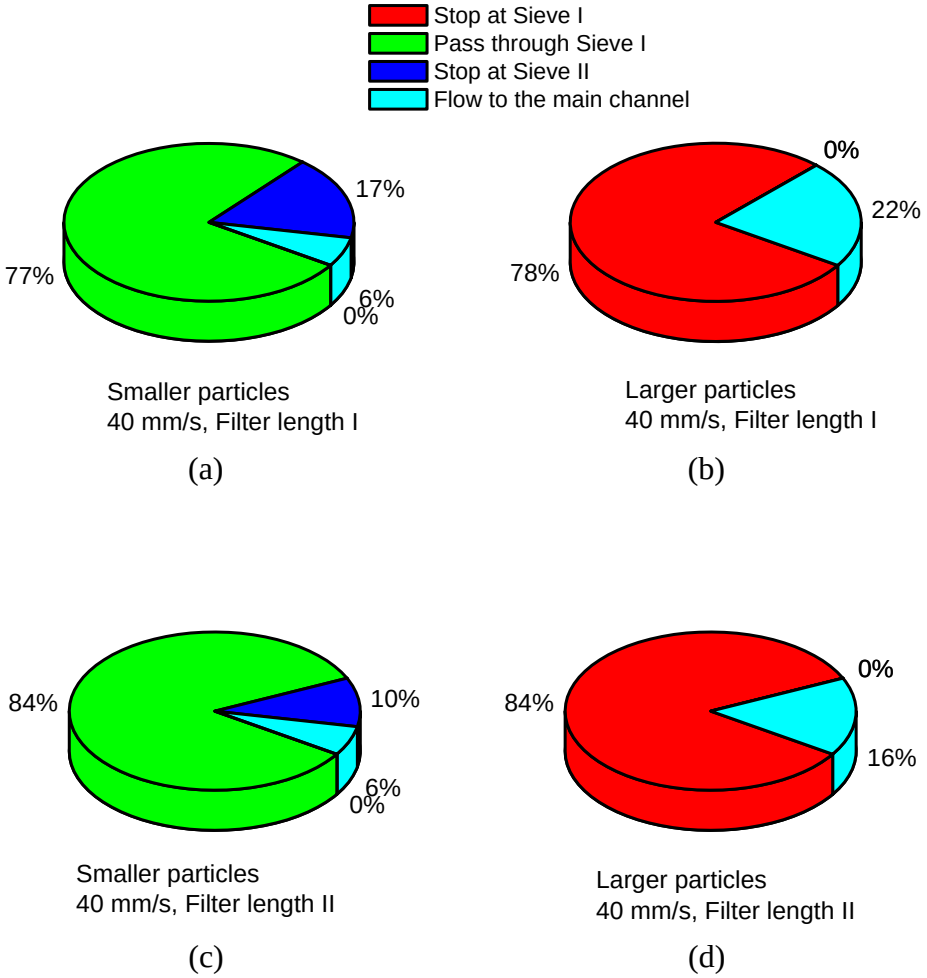

Figure 6-21 Simulation on particle distribution of particle sorter II in the filter length I and II situations with a inlet flow rate of 40 mm/s

6.3.2.2 Experiments

Figure 6-22 shows the morphologies of sieves after they work for 10 minutes. Smaller particles pass through Sieve I, and larger particles are blocked, which agrees with the simulation. Although this design allows more particles to be separated, larger particles will block all the slits of Sieve I and smaller particles will block all the slits of Sieve II as time passes. The blocked sieves alter the streams which makes the sorter lose its function. As a result, smaller particles pile on Sieve I and larger particle stacks at Sieve II. In order to achieve a continuous sorting, particles must be swept away from the sieves by a strong shear force. Therefore, in the following section, the shapes of the microchannel are modified to increase the shear force significantly.

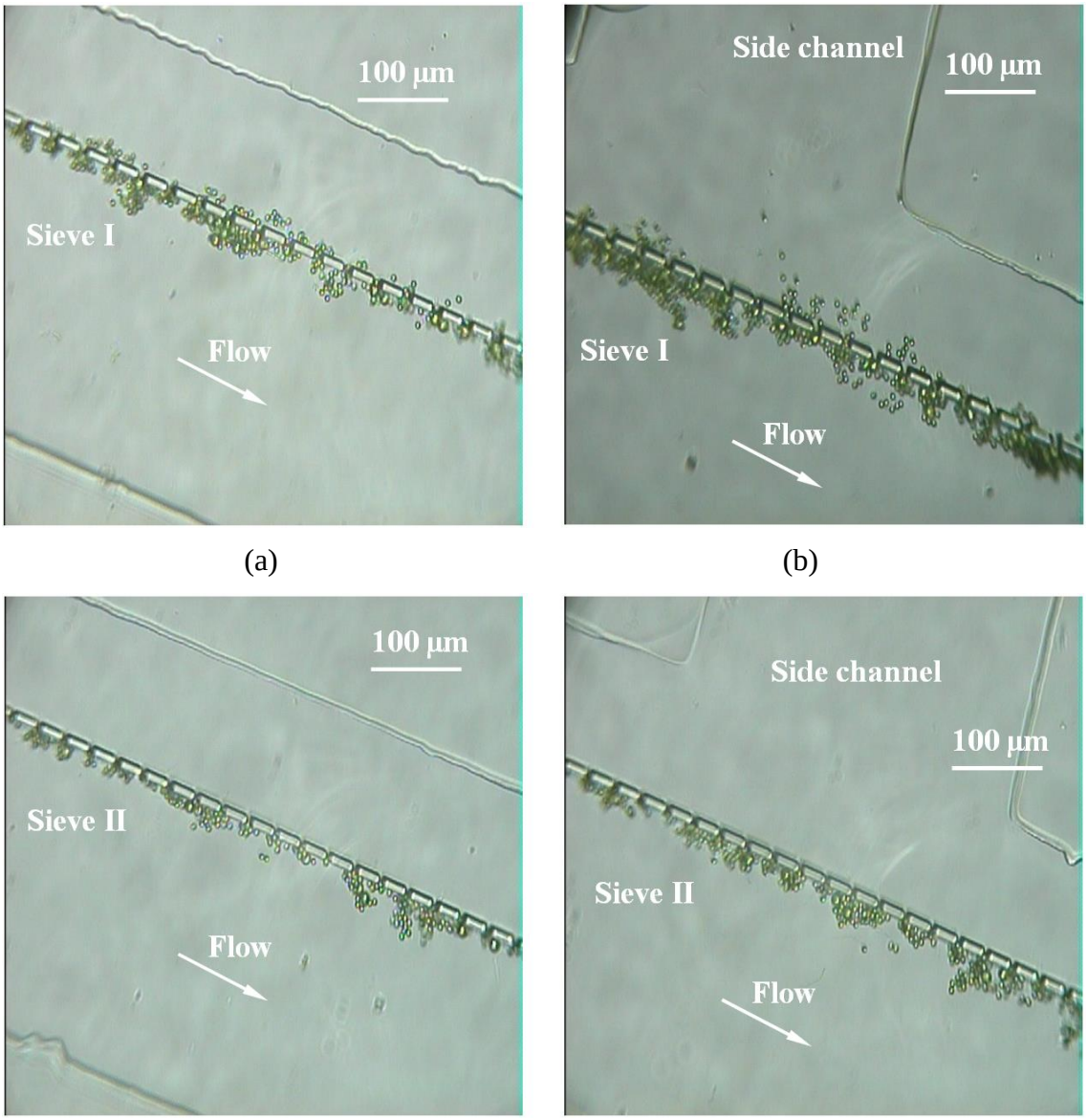

Figure 6-22 Particle sorting II: (a) and (b) Sieve I after it works for 10 minutes, and (c) and (d) Sieve II after it works for 10 minutes.

6.3.2.3 Modified particle sorter II

An internal wall is fabricated opposite the sieves to narrow the microchannel as shown in Fig. 6-23. When liquid flows to the narrow channel, a larger flow pressure is generated which more easily flushes stacked particles away by a strong hydrodynamic force. Figure

6-24 is the morphologies of a modified particle sorter. The width of the microchannel is 300.00 μm and the distance between the sieve and the internal wall is 50.00 μm. Figure 6-25 illustrates the simulation on streamlines in the flow field. Figure 6-26 shows the particle trajectories of larger particles (10 μm). 30 particles with a diameter of 10 μm are released from the inlet port. As time passes, 97% of the larger particles jam at Sieve I, 3% of the larger particles flow to the main outlet channel, and no larger particles stop at Sieve II. However, unlike larger particles in particle sorter II (Fig. 6-19), in which larger particles disperse throughout Sieve I, these larger particles only stack at the location near the side channel. Figure 6-27 describes the particle trajectories of smaller particles (5 μm). 30 particles with a diameter of 5 μm are released from the inlet port. As time passes, 97% of the smaller particles pass through Sieve I, 3% of the particles jam at Sieve II, and no particles flow to the main outlet channel. According to the simulation results, the separation rate reaches 97% for smaller particles. The maximum flow rate is 0.45 m/s.

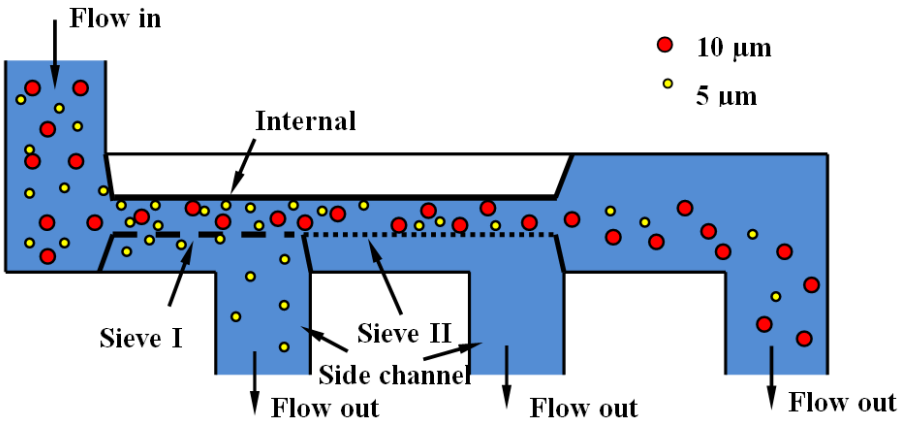

Figure 6-23 Schematic illustration of a modified particle sorter

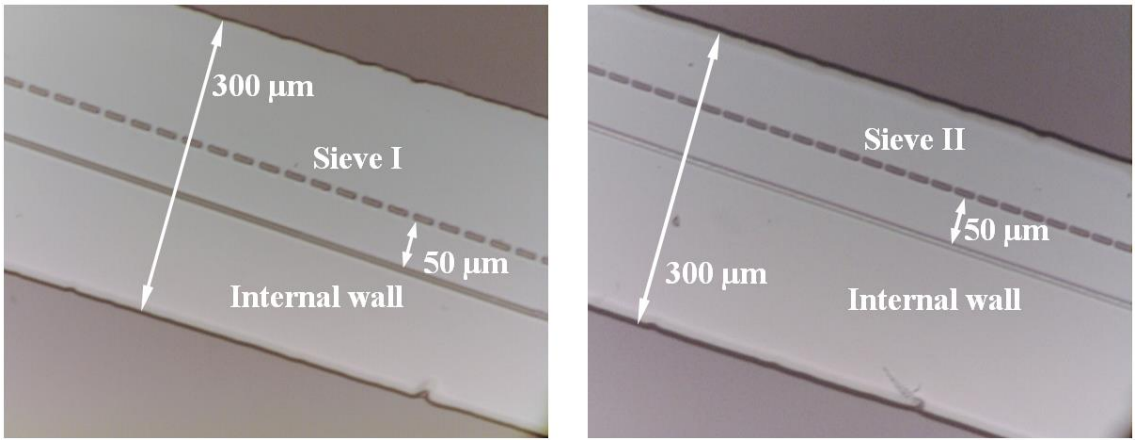

(a) (b)

Figure 6-24 Morphologies of sieves integrated with a microchannel

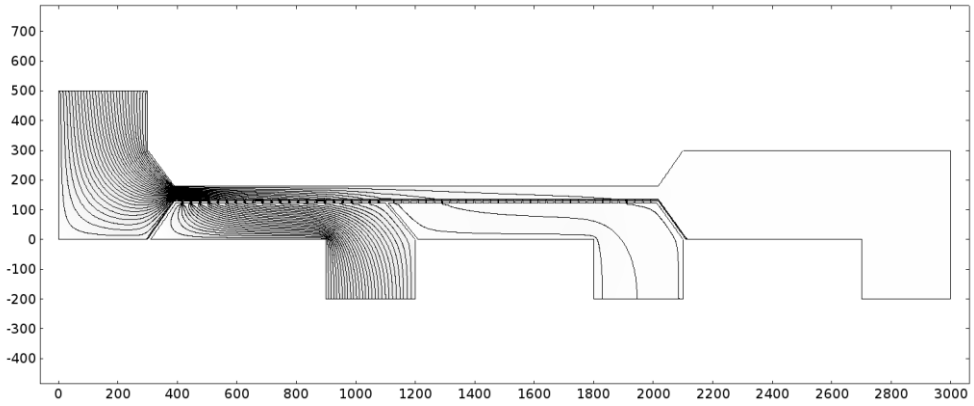

Figure 6-25 COMSOL simulation on streamlines in the velocity field. Modified particle sorter II has a microchannel length of 3.00 mm and the width of internal microchannels of 50.00 µm. The lengths of Sieve I and Sieve II are 700 and 900 µm, respectively.

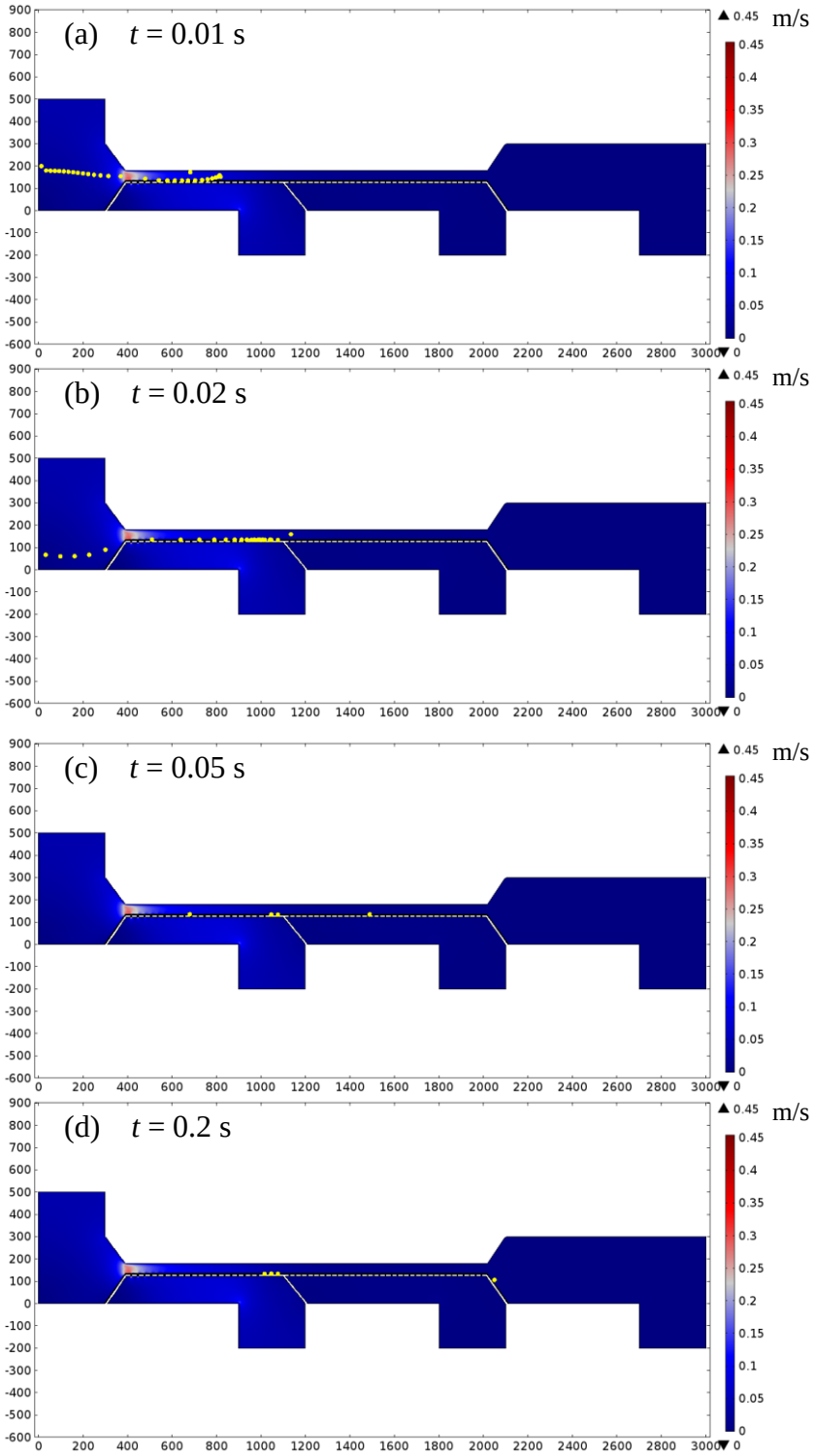

Figure 6-26 COMSOL simulation on particle trajectories of larger particles in modified particle sorter II

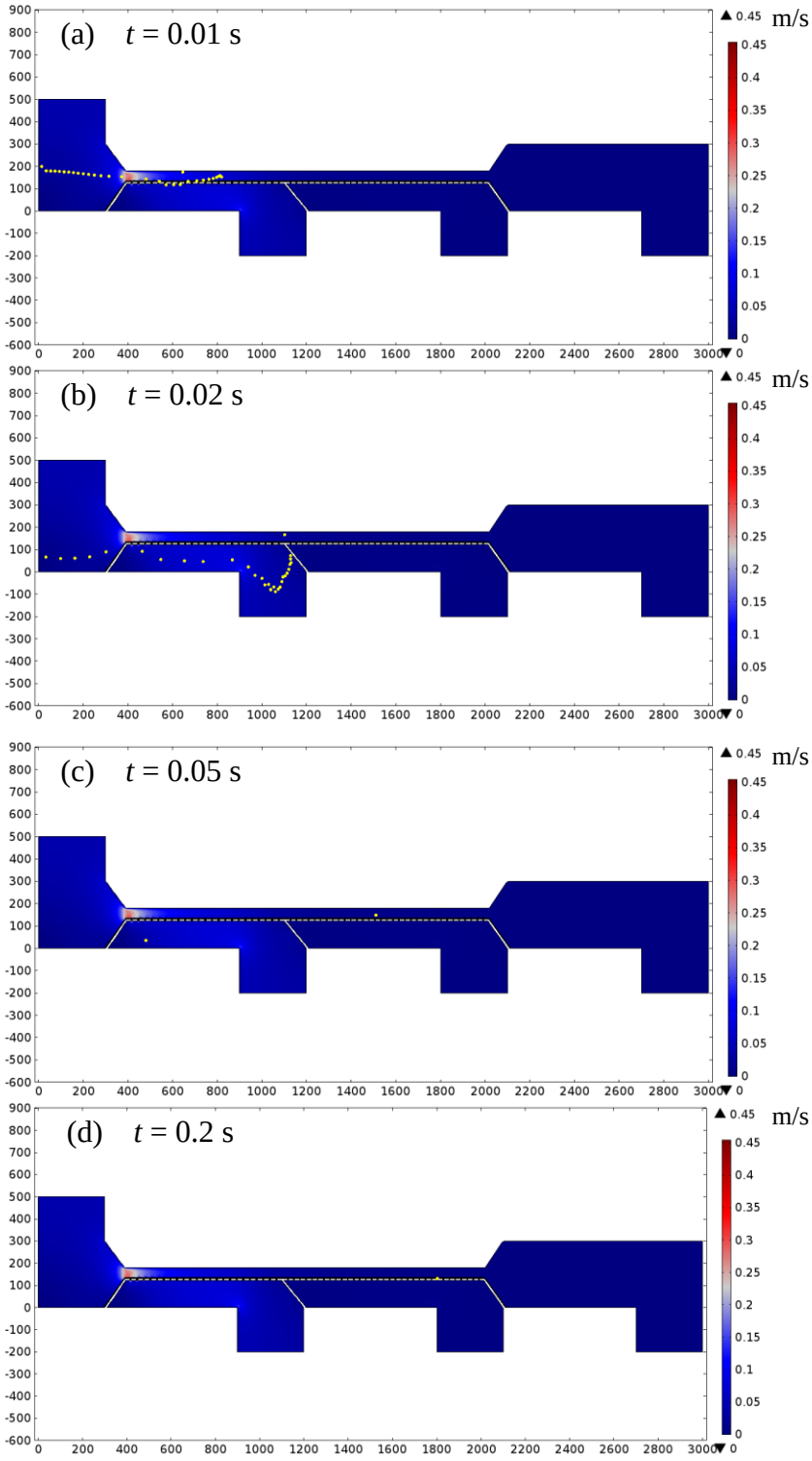

Figure 6-27 COMSOL simulation on particle trajectories of smaller particles in modified particle sorter II

The mixed suspensions are injected into the microchannel with a flow rate of 10 μL/min. The morphologies of the device after it works for 10 minutes are presented in Fig. 6-28. Suspensions flow in the middle of the channel. At the front segment of Sieve I (Fig. 6-28(a)), only several smaller particles can be observed and no larger particles appear. However, at the segment of Sieve I opposite to the first side channel (Fig. 6-28(b)), a lot of larger particles are piled up. At Sieve II, both types of particles are rare. The experimental results completely agree with the simulation. This means that this sorter is a functional device with an ultrahigh separation rate and continuous sorting capability. Of course, we can also design a narrow microchannel to achieve the same filtration function. However, a narrow microchannel will definitely increase the difficulty of alignment. Fabrication of internal walls to control the liquid flow is much easier by TPP with the femtosecond laser.

Depending on the simulation results, the separation rate of this sorter should be larger than 97%. Comparing the performance of this sorter with those of other reported filtration methods, such as the hydrodynamic filtration structure in Ref. [144] with a separation rate of 60% and the cross flow filtration in Ref. [140] with a maximum separation rate of 95%, our sieving method has a higher separation rate. Although Wei *et al.* reported that their porous membrane strtructure [136] can reach a separation rate of 99.9%, the complex structure and operation procedures increase the labour costs and limit applications for wider fields.

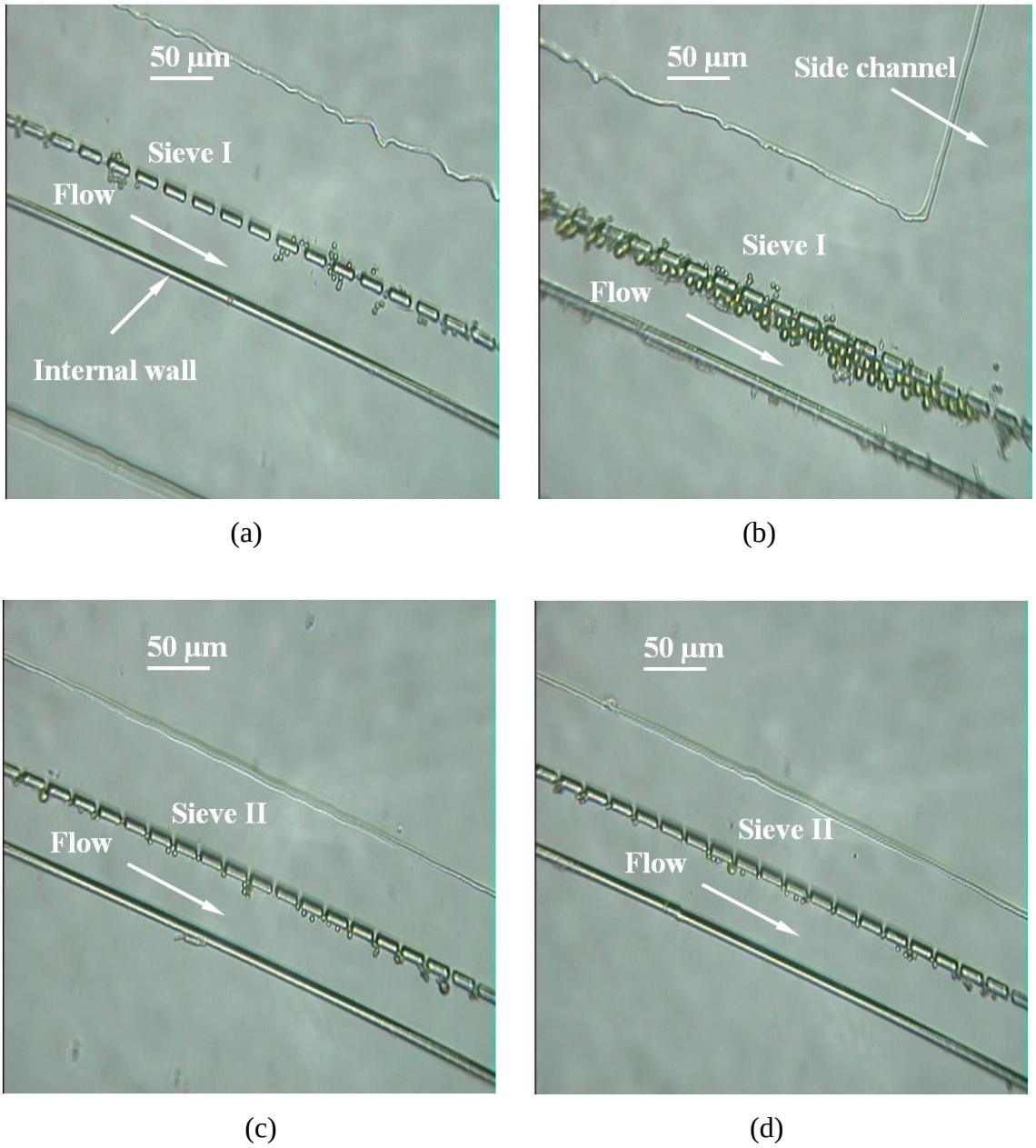

Figure 6-28 Modified particle sorting II: (a) and (b) Sieve I after it works for 10 minutes, and (c) and (d) Sieve II after it works for 10 minutes.

6.3.3 Refractive index sensing

As shown in section 3.4.2, diffraction gratings are reliable structures for RI sensing. In this section a diffraction grating is produced on the glass substrate to test the RI. Comparing this structure to the racetrack resonator, the fabrication is easier than the former design. The grating can be produced at the same layer of the filters and there is no need to coat another SU-8 layer as in the former design. Figure 6-29 presents a 3D profile of a diffraction grating. The height of the grating is about 15.63 μm, the width is 5.10 μm, and the periodicity is 12 μm. Figure 6-30 describes the transmission spectrum of this diffraction grating surrounded by air in the range of 450 - 1250 nm. 14 resonance modes are observed from this diffraction grating. The transmission spectra of the diffraction grating surrounded by different salt solutions are shown in Fig. 6-31. A blue shift occurs with the increase of the RI of the liquid. Figure 6-32 presents the sensitivities of this diffraction grating at the corresponding resonance mode. An inverse proportional fit is applied to the data. The fit result shows that the height of the grating is 15.85 μm which is very close to the measured value of 15.63 μm.

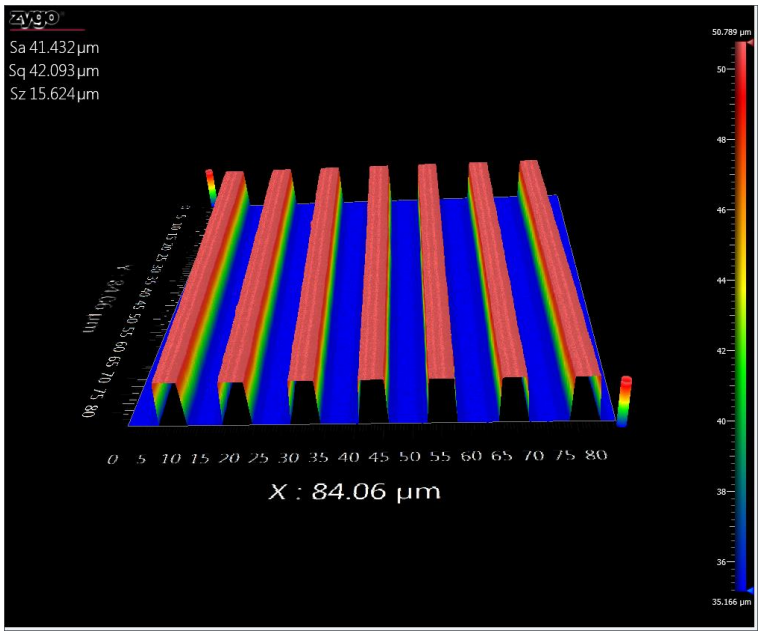

Figure 6-29 3D profile of a diffraction grating with a height of 15.63 µm, width of 5.10 µm, and periodicity is 12 µm.

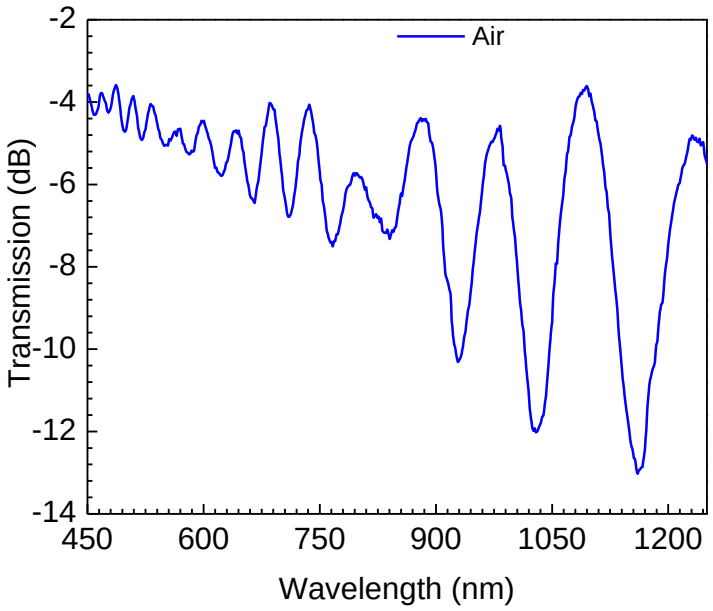

Figure 6-30 Transmission spectrum of an air-surrounded diffraction. The height of the grating is 15.63 µm.

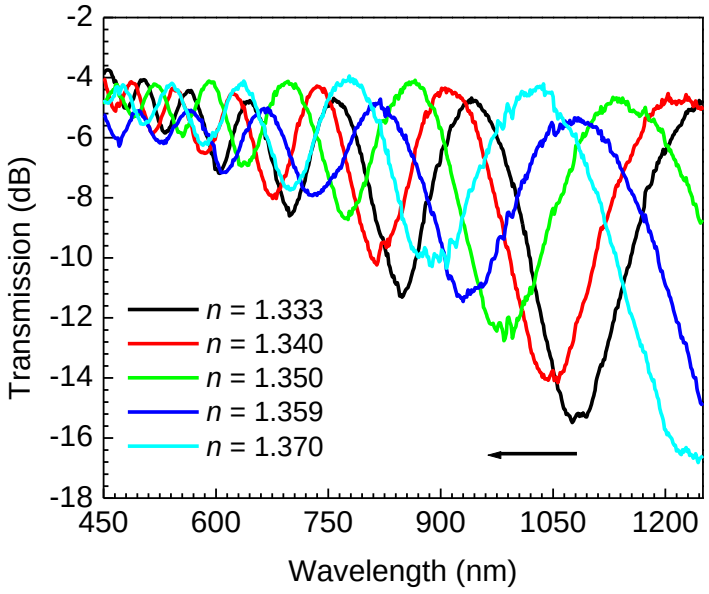

Figure 6-31 Transmission spectra of a diffraction grating surrounded by different salt solutions. The height of the grating is 15.63 μm.

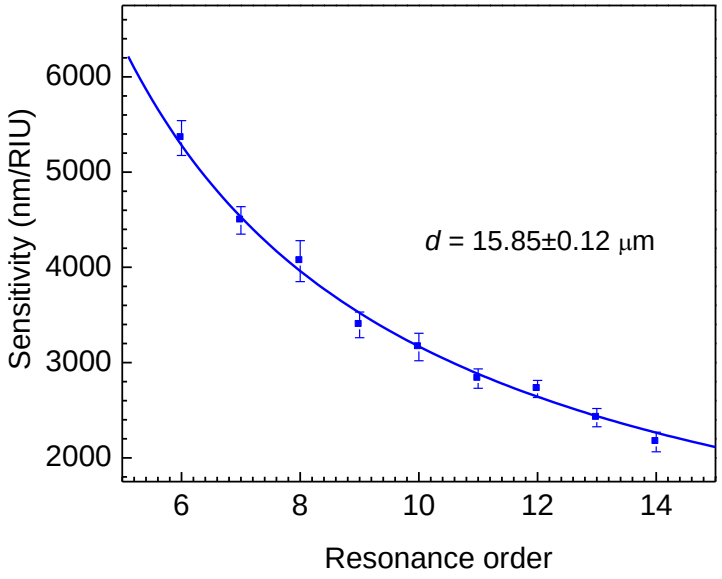

Figure 6-32 RI sensitivities of different resonance orders. The measured height of the grating is 15.63 μm.

In order to make a liquid flow around the diffractive grating, the size of the side channel in which the particle-free liquid flows (the first side channel in particle sorter I or the second side channel in particle sorter II) is widened from 300.00 μm to 1.00 mm and thickened from 15.00 μm to 50.00 μm. The diffraction grating and sieves are aligned and bonded with the microchannel. Figure 6-33 shows an opto-microfluidic chip for particle sorting (particle sorter I) and RI sensing. The cross sections of the main channel and the second side channel are 300.00 μm×15.00 μm (width × height), the cross section of the first side channel is 1.00 mm×50.00 μm, and the length of the main channel is 16.00 mm. The inset is the morphology of the diffraction grating. Salt solutions with known RIs are infused into the microchannel to calibrate the RI, and two sample suspensions are injected into the microchannel in turn as explained in section 6.2.2. Figure 6-34 presents the experimental results. The sensitivity of the resonance mode is 3.80×10^{3} nm/RIU. The measured results show that the first sample solution has an RI of 1.3343, and the second sample has an RI of 1.3513. The errors are 0.10% and 0.08%, respectively.

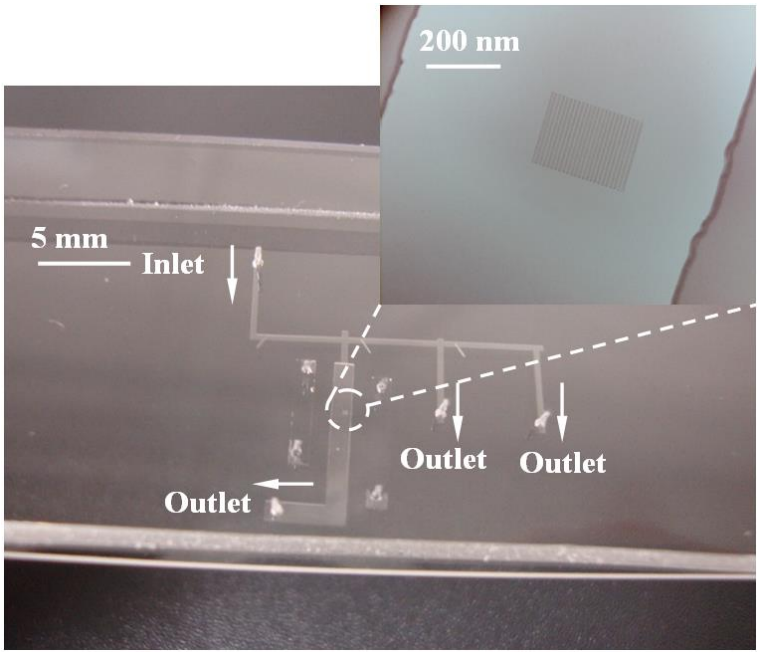

Figure 6-33 Opto-microfluidic chip for particle sorting and RI sensing. The inset is the morphology of the diffraction grating with a height of 15.63 μm, width of 5.10 μm, and periodicity of 12 μm.

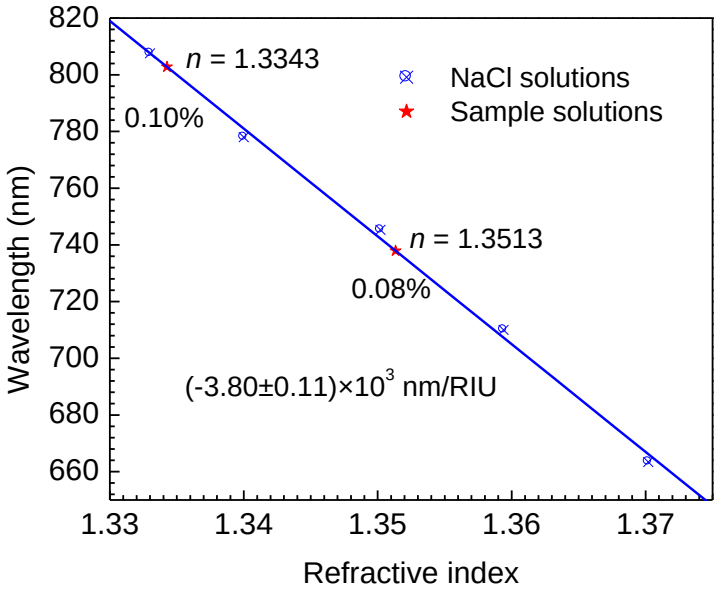

Figure 6-34 Dependence of the peak wavelength on RI

In this chapter, four types of particle sorters based on filtration have been presented. The particle trajectories are simulated to facilitate the understanding of the characterization of the sorters. The sorting functions are tested with a mixed particle solution. A continuous particle sorter with an ultrahigh separation rate is demonstrated. Opto-microfluidic devices are fabricated by integrating the particle sorters with optical structures (microring resonator and diffractive grating) which can achieve simultaneously particle separation and RI analysis. These highly efficient and accurate opto-microfluidic devices exhibit a promising prospect in biological and chemical applications.

Chapter 7 Conclusions

Opto-microfluidic devices have been demonstrated to be powerful miniaturized devices for optical sensing, biological analysis and medical testing. The optical structures in these opto-microfluidic devices are usually produced by several fabrication techniques, such as MEMS, soft lithography and hot-embossing. However, these techniques need highly accurate masks during the fabrication. As a result, the optical patterns are limited by the shapes of the masks. Laser fabrication technique can effectively overcome this drawback with the unique advantages of high precision, flexibility, and 3D capability. In this Ph.D. thesis, several opto-microfluidic devices for RI sensing, temperature measurement, and particle sorting are proposed and fabricated by combining the femtosecond laser induced TPP technique with soft lithography. Simultaneous multiple-operation and multiple-measurement have been achieved in these integrated miniature lab-on-a-chip devices.

The feasibility of microfabrication with femtosecond laser induced TPP technique in an SU-8 layer is systematically explored. The characterization of voxels fabricated by different exposure parameters such as focusing position, exposure time and pulse energy, have been carefully investigated. The results show that a longer exposure time and larger pulse energy increase the size of the voxel and make the edges of a fabricated pattern more uniform. In addition, a high pulse energy poses a risk of damage to the SU-8 layer due to the fact that the pulse energy could be well over the SU-8 ablation threshold. Therefore, depending on specific applications, the exposure conditions should be carefully chosen in order to obtain optimized results.

Grating-based opto-microfluidic devices have been proposed and demonstrated. Gratings with different periodicities and thickness are fabricated on glass substrates. This type of SU-8 grating successfully diffracts light in different diffractive directions. As an application of this grating, colour filters are designed. Gratings with a thickness ranging from 1.50 to 2.00 μm are fabricated on the substrates. Various colours are exhibited from the zeroth diffraction light which can be easily observed from microscope. Another application for this grating is the RI sensor. Different liquids are introduced into the SU-8 grating through a microchannel. The zeroth transmission spectrum shifts according to the RI of the liquid. An RI sensor with a sensitivity of -3.59×10^{3} nm/RIU (blue shift) is obtained in a grating with a thickness of 3.60 μm. The experimental results also prove that a grating with a larger thickness possesses a higher sensitivity.

An approach to achieve an MZI has been proposed using a waveguide and a glass substrate. Two beams split from an SMF propagate in the waveguide and glass substrate, respectively. The interference occurs when the two beams are collected by another SMF. Different interferential spectra have been obtained in chips with different lengths. A longer waveguide chip has a smaller interferential periodicity. An application for this MZI chip is the RI sensor. Liquids are infused into a microchannel which surrounds the SU-8 core. The effective RI of the core changes according to the RI of the liquid, thus resulting in a shift of the spectrum. We investigate the peak shifts in chips with different microchannel lengths and chip lengths. An RI sensor with a sensitivity of 96.8 nm/RIU (red shift) has been obtained in an MZI chip with a microchannel length of 8.00 mm and

chip length of 16.17 mm. The sensitivity increases with the increase of the microchannel length and decrease of the chip length.

An MZI using a waveguide with an SU-8 core and SU-8 cladding has been proposed. Beams split from an SMF pass through the core and cladding, respectively. The interference occurs when the beams are recombined by another SMF. Different interferential spectra are obtained in chips with different lengths. A chip with a longer waveguide has a smaller interferential periodicity. Temperature and RI sensing are measured. By raising the environmental temperature, a variation between the effective RI of the core and cladding results in a red shift of the transmission spectrum. The sensitivity reaches 0.849 nm/^{o}C in a chip with a core size of 2.80 μm ×5.50 μm× 22.92 mm (width × height × length), and cladding size of 125.00 μm ×11.50 μm × 22.92 mm. Different liquids change the effective RI of the cladding which induces a peak shift of the transmission spectrum. A blue shift occurs with the increase of the RI of the liquid. A sensitivity of -132.6 nm/RIU is achieved in a chip with a core size of 5.00 μm ×5.50 μm× 22.66 mm, cladding size of 125.00 μm ×11.50 μm × 22.66 mm, and microchannel size of 1.00 mm× 75.00 μm× 16.00 mm. We also modify this structure by adding one connector, two connectors or a gap in the core. Dissimilar beams propagate in the core and cladding all the time in the former design, light which first propagates in the core is scattered into the cladding at the modified structures (connector or gap). The effects of shape and size of the connector and interval distance of the gap are explored. Optimal parameters are chosen for fabricating three types of MZI-based opto-microfluidic devices to achieve RI

and temperature sensing. The sensing results are similar to those for the opto-microfluidic device mentioned above.

Optical ring resonators are common optical structures in optofluidic devices. We first study a ring resonator structure. The effects of radius, wavelength, core size, number of rings, and polarization are studied. A resonator with a larger radius has a smaller free spectral range, and a resonator with a smaller core has a larger free spectral range. We also find that the transmission spectrum depends on the polarization of the light. For temperature sensing, a blue shift occurs with rising temperature. For RI sensing, a red shift occurs with the increase of RI. The temperature sensitivity is about 9.10×10^{-2} nm/^{o}C, and the RI sensitivity is about 24.2 nm/RIU for a ring resonator with a cross section of 4.48 μm×4.23 μm (width × height) and radius of 60.00 μm. When two rings are integrated in a bus waveguide, simultaneous temperature and RI measurement can be accomplished, in which one of the rings is used for temperature calibration and the other ring is used for RI sensing. A racetrack resonator is another structure studied. Comparing to a ring resonance, the racetrack resonance has a larger extinction ratio. The maximum extinction ratio can reach 30 dB for a racetrack resonance with a radius of 60.00 μm, gap of 4.00 μm, and coupling length of 30.00 μm. A strong dependence of the polarization on RI sensing is found. For a TM mode, the sensitivity is 16 nm/RIU, whereas for a TE mode, the sensitivity increases to 25 nm/RIU. Multiple-RI sensing is also proved by integrating multiple racetracks into the device.

By combining the optical structures mentioned above with the principle of a laminar flow in the microchannel, two types of innovative functional opto-microfluidic devices for simultaneous RI sensing and particle sorting have been demonstrated. One device is based on a cross flow filtration and racetrack resonator. Two sorts of filters with different sieve sizes are fabricated in the main channel close to the branches. Particles are separated by the sieves according to their sizes. Finally, a particle-free liquid flows to the output part of the main channel in which a racetrack resonator is integrated. By testing with two mixed sample suspensions, the experimental results agree with the simulation, and the RI sensing errors are 0.43% and 0.16%, respectively. The second type of device is based on a hydrodynamic filtration and diffraction grating. Two sorts of filters with different sieve sizes are fabricated in the main channel in a parallel direction to the main channel. Particle jamming is effectively decreased due to the fact that a hydrodynamic force parallel to the main channel flushes piled particles away. A particle-free liquid is induced into a side channel in which a diffraction grating is integrated. By testing with two mixed sample suspensions, the experimental results agree with the simulation, and the RI sensing errors are 0.10% and 0.08%, respectively.

Bibliography

1. G. M. Whitesides, "The origins and the future of microfluidics," Nature **442,** 368-373 (2006).
2. J. C. McDonald, D. C. Duffy, J. R. Anderson, D. T. Chiu, H. Wu, O. J. Schueller, and G. M. Whitesides, "Fabrication of microfluidic systems in poly(dimethylsiloxane)," Electrophoresis **21,** 27-40 (2000).
3. C. Monat, P. Domachuk, and B. J. Eggleton, "Integrated optofluidics: A new river of light," Nat. Photonics **1**, 106-114 (2007).
4. D. Psaltis, S. R. Quake, and C. Yang, "Developing optofluidic technology through the fusion of microfluidics and optics," Nature **442,** 381-386 (2006).
5. Y. Fainman, L. P. Lee, D. Psaltis, and C. Yang, *Optofluidics : fundamentals, devices, and applications* (McGraw-Hill, 2010).
6. D. Zhang, L. Men, and Q. Chen, "Microfabrication and applications of opto-microfluidic sensors," Sensors (Basel) **11,** 5360-5382 (2011).
7. X. M. Zhao, Y. Xia, and G. M. Whitesides, "Fabrication of three-dimensional micro-structures: Microtransfer molding", Adv. Mater. **8**, 837-840 (1996).
8. J. G. Fleming, S. Y. Lin, I. El-Kady, R. Biswas, and K. M. Ho, "All-metallic three-dimensional photonic crystals with a large infrared bandgap," Nature **417,** 52-55 (2002).
9. S. Shoji and S. Kawata, "Photofabrication of three-dimensional photonic crystals by multibeam laser interference into a photopolymerizable resin," Appl. Phys. Lett. **76,** 2668-2670 (2000).
10. J. Chen, W. Jiang, X. Chen, L. Wang, S. Zhang, and R. T. Chen, "Holographic three-dimensional polymeric photonic crystals operating in the 1550nm window," Appl. Phys. Lett. **90,** 093102 (2007).
11. K. Lee, R. H. Kim, D. Yang, and S. H. Park, "Advances in 3D nano/microfabrication using two-photon initiated polymerization," Prog. Polym. Sci. **33**, 631-681 (2008).
12. M. Goppert-Mayer, "Uber elementarakte mit zwei quantensprungen," Ann. Phys. **9**, 273-294 (1931).
13. W. Kaiser and C. G. B. Garrett, "Two-photon excitation in CaF_2:Eu^{2+}," Phys. Rev. Lett. **7**, 229-231 (1961).
14. K. D. Belfield, "Observation of fluorescence excitation through the path of a laser beam" (Jan 20, 2013), retrieved from http://chemistry.cos.ucf.edu/belfield/research-1.php
15. W. Denk, J. H. Strickler, and W. W. Webb, "Two-Photon Laser Scanning Fluorescence Microscopy," Science **248,** 73 (1990).

16. J. E. Ehrlich, X. L. Wu, I. Y. Lee, Z. Y. Hu, H. Rockel, S. R. Marder, and J. W. Perry, "Two-photon absorption and broadband optical limiting with bis-donor stilbenes," Opt. Lett. **22,** 1843-1845 (1997).

17. C. Soeller, M. B. Cannell, "Two-photon microscopy: imaging in scattering samples and three-dimensionally resolved flash photolysis," Microsc. Res. Tech. **47**, 182-195 (1999).

18. P. T. So, C. Y. Dong, B. R. Masters, and K. M. Berland, "Two-photon excitation fluorescence microscopy," Annu. Rev. Biomed. Eng. **2,** 399-429 (2000).

19. C. E. Olson, M. J. Previte, and J. T. Fourkas, "Efficient and robust multiphoton data storage in molecular glasses and highly crosslinked polymers," Nat. Mater. **1,** 225-228 (2002).

20. J. Liu, Y. W. Zhao, J. Q. Zhao, A. D. Xia, L. J. Jiang, S. Wu, L. Ma, Y. Q. Dong, and Y. H. Gu, "Two-photon excitation studies of hypocrellins for photodynamic therapy," J. Photochem. Photobiol. B **68**, 156 (2002).

21. S. Maruo, O. Nakamura, and S. Kawata, "Three-dimensional microfabrication with two-photon-absorbed photopolymerization," Opt. Lett. **22,** 132-134 (1997).

22. S. Kawata, H. B. Sun, T. Tanaka, and K. Takada, "Finer features for functional microdevices," Nature **412,** 697-698 (2001).

23. J. Serbin, A. Ovsianikov, and B. Chichkov, "Fabrication of woodpile structures by two-photon polymerization and investigation of their optical properties," Opt. Express **12,** 5221-5228 (2004).

24. H. B. Sun, T. Kawakami, Y. Xu, J. Y. Ye, S. Matuso, H. Misawa, M. Miwa, and R. Kaneko, "Real three-dimensional microstructures fabricated by photopolymerization of resins through two-photon absorption," Opt. Lett. **25,** 1110-1112 (2000).

25. P. Galajda and P. Ormos, "Complex micromachines produced and driven by light," Appl. Phys. Lett. **78,** 249-251 (2001).

26. S. M. Kuebler, M. Rumi, T. Watanabe, K. Braun, B. H. Cumpston, A. A. Heikal, L. L. Erskine, S. Thayumanavan, S. Barlow, S. R. Marder, and J. W. Perry. "Optimizing two-photon initiators and exposure conditions for three-dimensional lithographic microfabrication," J. Photopolym. Sci. Technol. **14**, 657-668 (2001).

27. R. Guo, S. Xiao, X. Zhai, J. Li, A. Xia, and W. Huang, "Micro lens fabrication by means of femtosecond two photon photopolymerization," Opt. Express **14,** 810-816 (2006).

28. W. Haske, V. W. Chen, J. M. Hales, W. Dong, S. Barlow, S. R. Marder, and J. W. Perry, "65 nm feature sizes using visible wavelength 3-D multiphoton lithography," Opt. Express **15,** 3426-3436 (2007).

29. Y. Liu, D. D. Nolte, L. J. Pyrak-Nolte, "Large-format fabrication by two-photon polymerization in SU-8," Appl. Phys. A **100**, 181-191 (2010).

30. W. H. Teh, U. Dürig, U. Drechsler, C. G. Smith, and H. -. Güntherodt, "Effect of low numerical-aperture femtosecond two-photon absorption on (SU-8) resist for ultrahigh-aspect-ratio microstereolithography," J. Appl. Phys. **97,** 054907 (2005).

31. M. Straub, L. H. Nguyen, A. Fazlic, and M. Gu, "Complex-shaped three-dimensional microstructures and photonic crystals generated in a polysiloxane polymer by two-photon microstereolithography," Opt. Mater. **27,** 359-364 (2004).

32. L. H. Nguyen, M. Straub, and M. Gu, "Acrylate-based photopolymer for two-photon microfabrication and photonic applications," Adv. Funct. Mater. **15**, 209-216 (2005).

33. S. Wu, M. Straub, and M. Gu, "Single-monomer acrylate-based resin for three-dimensional photonic crystal fabrication," Polymer **46,** 10246-10255 (2005).

34. S. Maruo and H. Inoue, "Optically driven micropump produced by three-dimensional two-photon microfabrication," Appl. Phys. Lett. **89,** 144101 (2006).

35. A. Ovsianikov, J. Viertl, B. Chichkov, M. Oubaha, B. MacCraith, I. Sakellari, A. Giakoumaki, D. Gray, M. Vamvakaki, M. Farsari, and C. Fotakis, "Ultra-low shrinkage hybrid photosensitive material for two-photon polymerization microfabrication," ACS Nano **2**, 2257-2262 (2008).

36. A. Ovsianikov, S. Passinger, R. Houbertz, and B. N. Chichkov, "Three dimensional material processing with femtosecond lasers," Springer Series in Optical Sciences, Laser Ablation and its Applications, 121-157 (2007).

37. B. N. Chichkov, J. Koch, A. Ovsianikov, S. Passinger, C. Reinhardt, and J. Serbin, "Direct-Write Micro- and Nanostructuring with Femtosecond Lasers," MRS Proc. **850,** MM2.5.1 (2004).

38. A. Ovsianikov, S. Schlie, A. Ngezahayo, A. Haverich, and B. N. Chichkov, "Two-photon polymerization technique for microfabrication of CAD-designed 3D scaffolds from commercially available photosensitive materials," J. Tissue Eng. Regen. Med. **1,** 443-449 (2007).

39. T. Wei, G. Hildebrand, R. Schade, and K. Liefeith, "Two-photon polymerization for microfabrication of three-dimensional scaffolds for tissue engineering application," Eng. Life Sci. **9**, 384-390 (2009).

40. P. Tayalia, C. R. Mendonca, T. Baldacchini, D. J. Mooney, and E. Mazur, "3D cell-migration studies using two-photon engineered polymer scaffolds," Adv. Mater. **20**, 4494-4498 (2008).

41. S. D. Gittard, A. Ovsianikov, B. N. Chichkov, A. Doraiswamy, and R. J. Narayan, "Two-photon polymerization of microneedles for transdermal drug delivery," Expert Opin. Drug Deliv. **7**, 513-533 (2010).

42. A. Ovsianikov, B. Chichkov, O. Adunka, H. Pillsbury, A. Doraiswamy, and R. J. Narayan, "Rapid prototyping of ossicular replacement prostheses," Appl. Surf. Sci. **253,** 6603-6607 (2007).

43. S. Maruo, K. Ikuta, and H. Korogi, "Submicron manipulation tools driven by light in a liquid," Appl. Phys. Lett. **82,** 133-135 (2003).
44. S. D. Gittard, A. Nguyen, K. Obata, A. Koroleva, R. J. Narayan, and B. N. Chichkov, "Fabrication of microscale medical devices by two-photon polymerization with multiple foci via a spatial light modulator," Biomed. Opt. Express **2,** 3167-3178 (2011).
45. M. Farsari, A. Ovsianikov, M. Vamvakaki, I. Sakellari, D. Gray, B. N. Chichkov, and C. Fotakis, "Fabrication of three-dimensional photonic crystal structures containing an active nonlinear optical chromophore," Appl. Phys. A **93**, 11-15 (2008).
46. H. Sun, V. Mizeikis, Y. Xu, S. Juodkazis, J. Ye, S. Matsuo, and H. Misawa, "Microcavities in polymeric photonic crystals," Appl. Phys. Lett. **79,** 1-3 (2001).
47. K. Kaneko, H. Sun, X. Duan, and S. Kawata, "Submicron diamond-lattice photonic crystals produced by two-photon laser nanofabrication," Appl. Phys. Lett. **83,** 2091-2093 (2003).
48. K. K. Seet, V. Mizeikis, S. Matsuo, S. Juodkazis, and H. Misawa, "Three-dimensional spiral-architecture photonic crystals obtained by direct laser writing," Adv. Mater. **17**, 541-545 (2005).
49. M. Deubel, M. Wegener, A. Kaso, and S. John, "Direct laser writing and characterization of "Slanted Pore" Photonic Crystals," Appl. Phys. Lett. **85,** 1895-1897 (2004).
50. A. Ledermann, L. Cademartiri, M. Hermatschweiler, C. Toninelli, G. A. Ozin, D. S. Wiersma, M. Wegener, and G. von Freymann, "Three-dimensional silicon inverse photonic quasicrystals for infrared wavelengths," Nat. Mater. **5,** 942-945 (2006).
51. J. Ishihara, K. Komatsu, O. Sugihara, and T. Kaino, "Fabrication of three-dimensional calixarene polymer waveguides using two-photon assisted polymerization," Appl. Phys. Lett. **90,** 033511 (2007).
52. S. Klein, A. Barsella, H. Leblond, H. Bulou, A. Fort, C. Andraud, G. Lemercier, J. C. Mulatier, and K. Dorkenoo, "One-step waveguide and optical circuit writing in photopolymerizable materials processed by two-photon absorption," Appl. Phys. Lett. **86,** 211118 (2005).
53. M. Malinauskas, A. Zukauskas, V. Purlys, K. Belazaras, A. Momot, D. Paipulas, R. Gadonas, A. Piskarskas, H. Gilbergs, A. Gaidukeviciute, I. Sakellari, M. Farsari, and S. Juodkazis, "Femtosecond laser polymerization of hybrid/integrated micro-optical elements and their characterization," J. Opt. **12**, 124010 (2010).
54. T. Sherwood, A. C. Young, J. Takayesu, A. K. Jen, L. R. Dalton, and Antao Chen, "Microring resonators on side-polished optical fiber," IEEE Photon. Technol. Lett. **17,** 2107-2109 (2005).
55. S. Yokoyama, T. Nakahama, H. Miki, and S. Mashiko, "Fabrication of three-dimensional microstructure in optical-gain medium using two-photon-induced photopolymerization technique," Thin Solid Films **438–439,** 452-456 (2003).

56. C. F. Li, X. Z. Dong, F. Jin, W. Jin, W. Q. Chen, Z. S. Zhao, and X. M. Duan, "Polymeric distributed-feedback resonator with sub-micrometer fibers fabricated by two-photon induced photopolymerization," Appl. Phys. A **89**, 145-148 (2007).

57. G. Kumi, C. O. Yanez, K. D. Belfield, and J. T. Fourkas, "High-speed multiphoton absorption polymerization: fabrication of microfluidic channels with arbitrary cross-sections and high aspect ratios," Lab. Chip **10,** 1057-1060 (2010).

58. S. Jariwala, B. Tan, and K. Venkatakrishnan, "Micro-fluidic channel fabrication via two-photon absorption (TPA) polymerization assisted ablation," J. Micromech. Microeng. **19,** 115023 (2009).

59. S. Jariwala, K. Venkatakrishnan, and B. Tan, "Single step self-enclosed fluidic channels via Two Photon Absorption (TPA) polymerization," Opt. Express **18,** 1630-1636 (2010).

60. S. Maruo, K. Ikuta, and H. Korogi, "Force-controllable, optically driven micromachines fabricated by single-step two-photon microstereolithography," J. Microelectromech. Syst. **12,** 533-539 (2003).

61. S. Maruo, A. Takaura, and Y. Saito, "Optically driven micropump with a twin spiral microrotor," Opt. Express **17,** 18525-18532 (2009).

62. L. Amato, Y. Gu, N. Bellini, S. M. Eaton, G. Cerullo, and R. Osellame, "Integrated three-dimensional filter separates nanoscale from microscale elements in a microfluidic chip," Lab. Chip **12,** 1135-1142 (2012).

63. J. Wang, Y. He, H. Xia, L. G. Niu, R. Zhang, Q. D. Chen, Y. L. Zhang, Y. F. Li, S. J. Zeng, J. H. Qin, B. C. Lin, and H. B. Sun, "Embellishment of microfluidic devices via femtosecond laser micronanofabrication for chip functionalization," Lab. Chip **10,** 1993-1996 (2010).

64. D. Wu, Q. D. Chen, L. G. Niu, J. N. Wang, J. Wang, R. Wang, H. Xia, and H. B. Sun, "Femtosecond laser rapid prototyping of nanoshells and suspending components towards microfluidic devices," Lab. Chip **9,** 2391-2394 (2009).

65. S. H. Park, D. Y. Yang, and K. S. Lee, "Two-photon stereolithography for realizing ultraprecise three-dimensional nano/microdevices," Laser Photon. Rev. **3**, 1-11 (2009).

66. K. S. Lee, D. Y. Yang, S. H. Park, and R. H. Kim, "Recent developments in two-photon polymerization for 2D and 3D microfabrications," Polym. Adv. Technol. **17**, 72-82 (2006).

67. G. Witzgall, R. Vrijen, E. Yablonovitch, V. Doan, and B. J. Schwartz, "Single-shot two-photon exposure of commercial photoresist for the production of three-dimensional structures," Opt. Lett. **23,** 1745-1747 (1998).

68. B. A. Grzybowski, D. Qin, and G. M. Whitesides, "Beam redirection and frequency filtering with transparent elastomeric diffractive elements," Appl. Opt. **38,** 2997-3002 (1999).

69. J. Ihlemann, S. Muller, S. Puschmann, D. Schafer, M. Wei, J. Li, and P. R. Herman, "Fabrication of submicron gratings in fused silica by F_2-laser ablation," Appl. Phys. A **76**, 751-753 (2003).

70. H. Y. Zheng, W. Zhou, H. X. Qian, T. T. Tan, and G. C. Lim, "Polarisation-independence of femtosecond laser machining of fused silica," Appl. Surf. Sci. **236,** 114-119 (2004).

71. P. Äyräs, J. T. Rantala, S. Honkanen, S. B. Mendes, and N. Peyghambarian, "Diffraction gratings in sol–gel films by direct contact printing using a UV-mercury lamp," Opt. Commun. **162,** 215-218 (1999).

72. M. Lai, G. M Sridharan, G. Parish, S. Bhattacharya, and A. Keating, "Multilayer porous silicon diffraction gratings operating in the infrared," Nanoscale Res. Lett. **7**:645 (2012).

73. S. Na, S. Kim, J. Jo, S. Oh, J. Kim, and D. Kim, "Efficient polymer solar cells with surface relief gratings fabricated by simple soft lithography," Adv. Funct. Mater. **18**, 3956-3963 (2008).

74. W. Wang, C. Zhou, and W. Jia, "High-fidelity replication of Dammann gratings using soft lithography," Appl. Opt. **47,** 1427-1429 (2008).

75. C. David, P. Häberling, M. Schnieper, J. Söchtig, and C. Zschokke, "Nano-structured anti-reflective surfaces replicated by hot embossing," Microelectronic Eng. **61–62,** 435-440 (2002).

76. P. W. Leech and R. A. Lee, "Hot embossing of grating-based optically variable images in thermoplastic acrylic lacquer," J. Mater. Sci. **42**, 4428-4434 (2007).

77. Y. Xia and G. M. Whitesides, "Soft lithography," Angew. Chem. Int. Ed. Engl. **37**, 550-575 (1998).

78. P. Garstecki, M. J. Fuerstman, H. A. Stone, and G. M. Whitesides, "Formation of droplets and bubbles in a microfluidic T-junction-scaling and mechanism of break-up," Lab. Chip **6,** 437-446 (2006).

79. Z. Shen, Y. Zou, and X. Chen, "An integrated microfluidic signal generator using multiphase droplet grating," Microfluid Nanofluid **14**, 809-815 (2013).

80. J. Q. Yu, Y. Yang, A. Q. Liu, L. K. Chin, and X. M. Zhang, "Microfluidic droplet grating for reconfigurable optical diffraction," Opt. Lett. **35,** 1890-1892 (2010).

81. M. Hashimoto, B. Mayers, P. Garstecki, and G. M. Whitesides, "Flowing lattices of bubbles as tunable, self-assembled diffraction gratings," Small **2**, 1292-1298 (2006).

82. O. J. A. Schueller, D. C. Duffy, J. A. Rogers, S. T. Brittain, and G. M. Whitesides, "Reconfigurable diffraction gratings based on elastomeric microfluidic devices," Sensor. Actuat. A: Phys.**78,** 149-159 (1999).

83. L. Lei, H. Li, J. Shi, and Y. Chen, "Microfluidic refractometer with integrated optical fibers and end-facet transmission gratings," Rev. Sci. Instrum. **81,** 023103 (2010).

84. Z. G. Li, Y. Yang, X. M. Zhang, A. Q. Liu, J. B. Zhang, L. Cheng, and Z. H. Li, "Tunable visual color filter using microfluidic grating," Biomicrofluidics **4,** 043013 (2010).

85. K. Hosokawa, K. Hanada, and R. Maeda, "A polydimethylsiloxane (PDMS) deformable diffraction grating for monitoring of local pressure in microfluidic devices," J. Micromech. Microeng. **12**, 1-6 (2002).

86. Y. Chen, Z. Li, M. D. Henry, and A. Scherer, "Optofluidic circular grating distributed feedback dye laser," Appl. Phys. Lett. **95,** 031109 (2009).

87. S. Balslev and A. Kristensen, "Microfluidic single-mode laser using high-order Bragg grating and antiguiding segments," Opt. Express **13,** 344-351 (2005).

88. Z. Li, Z. Zhang, T. Emery, A. Scherer, and D. Psaltis, "Single mode optofluidic distributed feedback dye laser," Opt. Express **14,** 696-701 (2006).

89. T. Smith and J Guild, "The C.I.E. colorimetric standards and their use," Trans. Opt. Soc. **33**, 73-134 (1931).

90. T. C. Sum, A. A. Bettiol, J. A. van Kan, F. Watt, E. Y. B. Pun, and K. K. Tung, "Proton beam writing of low-loss polymer optical waveguides," Appl. Phys. Lett. **83,** 1707-1709 (2003).

91. R. C. Weast and D. R. Lide, *Handbook of chemistry and physics* (CRC press, 2004).

92. X. Fang, C. R. Liao, and D. N. Wang, "Femtosecond laser fabricated fiber Bragg grating in microfiber for refractive index sensing," Opt. Lett. **35,** 1007-1009 (2010).

93. Y. Wang, M. Yang, D. N. Wang, S. Liu, and P. Lu, "Fiber in-line Mach–Zehnder interferometer fabricated by femtosecond laser micromachining for refractive index measurement with high sensitivity," J. Opt. Soc. Am. B **27**, 370-374 (2010).

94. P. Dumais, C. L. Callender, J. P. Noad, and C. J. Ledderhof, "Integrated optical sensor using a liquid-core waveguide in a Mach-Zehnder interferometer," Opt. Express **16,** 18164-18172 (2008).

95. A. Crespi, Y. Gu, B. Ngamsom, H. J. Hoekstra, C. Dongre, M. Pollnau, R. Ramponi, H. H. van den Vlekkert, P. Watts, G. Cerullo, and R. Osellame, "Three-dimensional Mach-Zehnder interferometer in a microfluidic chip for spatially-resolved label-free detection," Lab. Chip **10,** 1167-1173 (2010).

96. M. I. Lapsley, I. K. Chiang, Y. B. Zheng, X. Ding, X. Mao, and T. J. Huang, "A single-layer, planar, optofluidic Mach-Zehnder interferometer for label-free detection," Lab. Chip **11,** 1795-1800 (2011).

97. A. Densmore, D. X. Xu, S. Janz, P. Waldron, T. Mischki, G. Lopinski, A. Delage, J. Lapointe, P. Cheben, B. Lamontagne, and J. H. Schmid, "Spiral-path high-sensitivity silicon photonic wire molecular sensor with temperature-independent response," Opt. Lett. **33,** 596-598 (2008).

98. C. Grillet, P. Domachuk, V. Ta'eed, E. Magi, J. Bolger, B. Eggleton, L. Rodd, and J. Cooper-White, "Compact tunable microfluidic interferometer," Opt. Express **12,** 5440-5447 (2004).

99. J. Hong, J. S. Choi, G. Han, J. K. Kang, C. M. Kim, T. S. Kim, and D. S. Yoon, "A Mach-Zehnder interferometer based on silicon oxides for biosensor applications," Anal. Chim. Acta **573-574,** 97-103 (2006).

100. B. Drapp, J. Piehler, A. Brecht, G. Gauglitz, B. J. Luff, J. S. Wilkinson, and J. Ingenhoff, "Integrated optical Mach-Zehnder interferometers as simazine immunoprobes," Sensor. Actuat. B: Chem. **39,** 277-282 (1997).

101. R. Bruck, E. Melnik, P. Muellner, R. Hainberger, and M. Lämmerhofer, "Integrated polymer-based Mach-Zehnder interferometer label-free streptavidin biosensor compatible with injection molding," Biosens. Bioelectron. **26,** 3832-3837 (2011).

102. B. Sepúlveda, J. Sánchez del Río, M. Moreno, F. J. Blanco, K. Mayora, C. Domínguez and L. M. Lechuga, "Optical biosensor microsystems based on the integration of highly sensitive Mach–Zehnder interferometer devices," J. Opt. A: Pure Appl. Opt. **8,** S561 (2006).

103. N. Xie, T. Hashimoto, and K. Utaka, "Very low power operation of compact MMI polymer thermooptic switch," *IEEE Photon. Technol. Lett.* **21**, 1335-1337 (2009).

104. A. Ghatak and K. Thyagarajan, *An introduction to fiber optics* (Cambridge university press 1998).

105. F. G. Della Corte, G. Cocorullo, M. Iodice, and I. Rendina, "Temperature dependence of the thermo-optic coefficient of InP, GaAs, and SiC from room temperature to 600 K at the wavelength of 1.5 μm," Appl. Phys. Lett. **77,** 1614-1616 (2000).

106. G. Cocorullo, F. G. Della Corte, and I. Rendina, "Temperature dependence of the thermo-optic coefficient in crystalline silicon between room temperature and 550 K at the wavelength of 1523 nm," Appl. Phys. Lett. **74,** 3338-3340 (1999).

107. G. Ghosh, "Thermo-optic coefficients of LiNbO(3), LiIO(3), and LiTaO(3) nonlinear crystals," Opt. Lett. **19,** 1391-1393 (1994).

108. X. Quan and E. S. Fry, "Empirical equation for the index of refraction of seawater," *Appl. Opt.*, **34,** 3477-3480 (1995).

109. K. De Vos, I. Bartolozzi, E. Schacht, P. Bienstman, and R. Baets, "Silicon-on-Insulator microring resonator for sensitive and label-free biosensing," Opt. Express **15,** 7610-7615 (2007).

110. D. Dai, "Highly sensitive digital optical sensor based on cascaded high-Q ring-resonators," Opt. Express **17,** 23817-23822 (2009).

111. Q. Xu, D. Fattal, and R. G. Beausoleil, "Silicon microring resonators with 1.5-microm radius," Opt. Express **16,** 4309-4315 (2008).

112. N. A. Yebo, P. Lommens, Z. Hens, and R. Baets, "An integrated optic ethanol vapor sensor based on a silicon-on-insulator microring resonator coated with a porous ZnO film," Opt. Express **18,** 11859-11866 (2010).

113. D. Dai, B. Yang, L. Yang, Z. Sheng, and S. He, "Compact microracetrack resonator devices based on small SU-8 polymer strip waveguides," IEEE Photon. Technol. Lett. **21**, 254-256 (2009).

114. D. Dai and S. He, "Highly-sensitive sensor with large measurement range realized with two cascaded-microring resonators," Opt. Commun. **279,** 89-93 (2007).

115. G. Testa, Y. Huang, P. M. Sarro, L. Zeni, and R. Bernini, "Integrated silicon optofluidic ring resonator," Appl. Phys. Lett. **97,** 131110 (2010).

116. M. H. Salleh, A. Glidle, M. Sorel, J. Reboud, and J. M. Cooper, "Polymer dual ring resonators for label-free optical biosensing using microfluidics," Chem. Commun. (Camb) **49,** 3095-3097 (2013).

117. A. M. Armani and K. J. Vahala, "Heavy water detection using ultra-high-Q microcavities," Opt. Lett. **31,** 1896-1898 (2006).

118. L. Jin, M. Li, and J. He, "Highly-sensitive silicon-on-insulator sensor based on two cascaded micro-ring resonators with vernier effect," Opt. Commun. **284,** 156-159 (2011).

119. U. Levy, K. Campbell, A. Groisman, S. Mookherjea, and Y. Fainman, "On-chip microfluidic tuning of an optical microring resonator," Appl. Phys. Lett. **88,** 111107 (2006).

120. J. K. Poon, L. Zhu, G. A. DeRose, and A. Yariv, "Transmission and group delay of microring coupled-resonator optical waveguides," Opt. Lett. **31,** 456-458 (2006).

121. C. Chao and L. J. Guo, "Biochemical sensors based on polymer microrings with sharp asymmetrical resonance," Appl. Phys. Lett. **83,** 1527-1529 (2003).

122. P. Rabiei, W. H. Steier, C. Zhang and L. R. Dalton, "Polymer micro-ring filters and modulators," J. Lightw. Technol. **20**, 1968-1975 (2002).

123. J. D. Suter, W. Lee, D. J. Howard, E. Hoppmann, I. M. White, and X. Fan, "Demonstration of the coupling of optofluidic ring resonator lasers with liquid waveguides," Opt. Lett. **35,** 2997-2999 (2010).

124. K. Scholten, X. Fan, and E. T. Zellers, "Microfabricated optofluidic ring resonator structures," Appl. Phys. Lett. **99,** 141108 (2011).

125. X. Tu, X. Wu, M. Li, L. Liu, and L. Xu, "Ultraviolet single-frequency coupled optofluidic ring resonator dye laser," Opt. Express **20,** 19996-20001 (2012).

126. J. D. Suter, D. J. Howard, H. Shi, C. W. Caldwell, and X. Fan, "Label-free DNA methylation analysis using opto-fluidic ring resonators," Biosens. Bioelectron. **26,** 1016-1020 (2010).

127. Y. Sun, J. Liu, D. J. Howard, G. Frye-Mason, A. K. Thompson, S. J. Ja, and X. Fan, "Rapid tandem-column micro-gas chromatography based on optofluidic ring resonators with multi-point on-column detection," Analyst **135,** 165-171 (2010).

128. C. Chao, W. Fung and L. J. Guo, "Polymer microring resonators for biochemical sensing applications," IEEE J. Select. Topics Quantum Electron. **12**, 134-142 (2006).

129. M. S. Nawrocka, T. Liu, X. Wang, and R. R. Panepucci, "Tunable silicon microring resonator with wide free spectral range," Appl. Phys. Lett. **89,** 071110 (2006).

130. D. Dai, L. Yang, Z. Sheng, B. Yang and S. He, "Compact microring resonator with 2×2 tapered multimode interference couplers," J. Lightw. Technol. **27**, 4878-4883 (2009).

131. J. Teng, P. Dumon, W. Bogaerts, H. Zhang, X. Jian, X. Han, M. Zhao, G. Morthier, and R. Baets, "Athermal Silicon-on-insulator ring resonators by overlaying a polymer cladding on narrowed waveguides," Opt. Express **17,** 14627-14633 (2009).

132. X. Zhao, J. M. Tsai, H. Cai, X. M. Ji, J. Zhou, M. H. Bao, Y. P. Huang, D. L. Kwong, and A. Q. Liu, "A nano-opto-mechanical pressure sensor via ring resonator," Opt. Express **20,** 8535-8542 (2012).

133. N. Pamme, "Continuous flow separations in microfluidic devices," Lab. Chip **7,** 1644-1659 (2007).

134. H. Tsutsui and C. M. Ho, "Cell Separation by Non-Inertial Force Fields in Microfluidic Systems," Mech. Res. Commun. **36,** 92-103 (2009).

135. D. Huh, J. H. Bahng, Y. Ling, H. H. Wei, O. D. Kripfgans, J. B. Fowlkes, J. B. Grotberg, and S. Takayama, "Gravity-driven microfluidic particle sorting device with hydrodynamic separation amplification," Anal. Chem. **79,** 1369-1376 (2007).

136. H. Wei, B. Chueh, H. Wu, E. W. Hall, C. Li, R. Schirhag, J. Lin and R. N. Zare, "Particle sorting using a porous membrane in a microfluidic device," Lab Chip **11**, 238-245 (2011).

137. H. Mohamed, L. D. McCurdy, D. H. Szarowski, S. Duva, J. N. Turner, and M. Caggana, "Development of a rare cell fractionation device: application for cancer detection," IEEE Trans. Nanobioscience **3,** 251-256 (2004).

138. X. Chen, D. Cui, and J. Chen, "Design, fabrication and characterization of nano-filters in silicon microfluidic channels based on MEMS technology," Electrophoresis **30,** 3168-3173 (2009).

139. X. Chen, D. F. Cui, C. C. Liu, and H. Li, "Microfluidic chip for blood cell separation and collection based on crossflow filtration," Sensor. Actuat. B: Chem. **130,** 216-221 (2008).

140. H. M. Ji, V. Samper, Y. Chen, C. K. Heng, T. M. Lim, and L. Yobas, "Silicon-based microfilters for whole blood cell separation," Biomed Microdevices **10,** 251-257 (2008).

141. V. VanDelinder and A. Groisman, “Separation of plasma from whole human blood in a continuous cross-flow in a molded microfluidic device,” Anal. Chem. **78**, 3765-3771 (2006).

142. M. Yamada, M. Nakashima, and M. Seki, “Pinched flow fractionation: continuous size separation of particles utilizing a laminar flow profile in a pinched microchannel,” Anal. Chem. **76**, 5465-5471 (2004).

143. J. Takagi, M. Yamada, M. Yasuda, and M. Seki, “Continuous particle separation in a microchannel having asymmetrically arranged multiple branches,” Lab Chip **5**, 778-784 (2005).

144. M. Yamada and M. Seki, “Hydrodynamic filtration for on-chip particle concentration and classification utilizing microfluidics,” Lab. Chip **5,** 1233-1239 (2005).

145. M. Yamada and M. Seki, “Microfluidic particle sorter employing flow splitting and recombining,” Anal. Chem. **78,** 1357-1362 (2006).

146. L. R. Huang, E. C. Cox, R. H. Austin, and J. C. Sturm, “Continuous particle separation through deterministic lateral displacement,” Science **304,** 987-990 (2004).

147. K. J. Morton, K. Loutherback, D. W. Inglis, O. K. Tsui, J. C. Sturm, S. Y. Chou, and R. H. Austin, “Hydrodynamic metamaterials: microfabricated arrays to steer, refract, and focus streams of biomaterials,” Proc. Natl. Acad. Sci. U. S. A. **105,** 7434-7438 (2008).

148. J. G. Kralj, M. T. Lis, M. A. Schmidt, and K. F. Jensen, “Continuous dielectrophoretic size-based particle sorting,” Anal. Chem. **78,** 5019-5025 (2006).

149. S. Choi and J. K. Park, “Microfluidic system for dielectrophoretic separation based on a trapezoidal electrode array,” Lab. Chip **5,** 1161-1167 (2005).

150. I. Doh and Y. Cho, “A continuous cell separation chip using hydrodynamic dielectrophoresis (DEP) process,” Sensor. Actuat. A: Phys. **121,** 59-65 (2005).

151. N. Xia, T. P. Hunt, B. T. Mayers, E. Alsberg, G. M. Whitesides, R. M. Westervelt, and D. E. Ingber, “Combined microfluidic-micromagnetic separation of living cells in continuous flow,” Biomed. Microdevices **8,** 299-308 (2006).

152. N. Pamme and C. Wilhelm, “Continuous sorting of magnetic cells via on-chip free-flow magnetophoresis,” Lab. Chip **6,** 974-980 (2006).

153. A. Y. Lau, L. P. Lee, and J. W. Chan, “An integrated optofluidic platform for Raman-activated cell sorting,” Lab. Chip **8,** 1116-1120 (2008).

154. M. M. Wang, E. Tu, D. E. Raymond, J. M. Yang, H. Zhang, N. Hagen, B. Dees, E. M. Mercer, A. H. Forster, I. Kariv, P. J. Marchand, and W. F. Butler, “Microfluidic sorting of mammalian cells by optical force switching,” Nat. Biotechnol. **23,** 83-87 (2005).

155. R. Applegate Jr, J. Squier, T. Vestad, J. Oakey, and D. Marr, "Optical trapping, manipulation, and sorting of cells and colloids in microfluidic systems with diode laser bars," Opt. Express **12,** 4390-4398 (2004).

156. T. D. Perroud, J. N. Kaiser, J. C. Sy, T. W. Lane, C. S. Brand, A. K. Singh, and K. D. Patel, "Microfluidic-based cell sorting of Francisella tularensis infected macrophages using optical forces," Anal. Chem. **80,** 6365-6372 (2008).

157. M. P. MacDonald, G. C. Spalding, and K. Dholakia, "Microfluidic sorting in an optical lattice," Nature **426**, 421-424 (2003).

158. M. Kumar, D. L. Feke, and J. M. Belovich, "Fractionation of cell mixtures using acoustic and laminar flow fields," Biotechnol. Bioeng. **89,** 129-137 (2005).

159. F. Petersson, L. Aberg, A. M. Sward-Nilsson, and T. Laurell, "Free flow acoustophoresis: microfluidic-based mode of particle and cell separation," Anal. Chem. **79,** 5117-5123 (2007).